Production-related Characterization of the Thermal Transport Properties of Battery Electrodes via Laser Flash Analysis and Guarded Hot Plate Method

Zur Erlangung des akademischen Grades einer

DOKTORIN DER INGENIEURWISSENSCHAFTEN

von der KIT-Fakultät für Chemieingenieurwesen und Verfahrenstechnik des Karlsruher Instituts für Technologie (KIT)
genehmigte

DISSERTATION

von

Julia Celina Gandert, M. Sc.

aus Rheinfelden (Baden)

Tag der mündlichen Prüfung: 15.04.2026

Erstgutachter: Prof. Dr.-Ing. Thomas Wetzel

Zweitgutachter: Prof. Odne Stokke Burheim

Kurzfassung

Lithium-Ionen Batterien sind aus mobilen Anwendungen nicht mehr wegzudenken. Als elektrochemische Energiespeicher werden sie jedoch hauptsächlich in Bezug auf ihre elektrochemischen Eigenschaften optimiert, während das thermische Verhalten meistens außer Acht gelassen wird.

In den vergangenen Jahren hat sich jedoch gezeigt, dass die thermischen Gradienten in Batteriezellen einen wesentlichen Einfluss auf deren Leistungsfähigkeit und Alterungsverhalten haben. Das zunehmende Interesse am thermischen Verhalten zeigt sich auch in der steigenden Anzahl an Publikationen, die den Wärmetransport in Batterien in ihren Simulationen und Experimenten betrachten. In zahlreichen Studien wurden die thermischen Transporteigenschaften von Anoden, Kathoden und Separatoren untersucht, die aus kommerziellen Zellen entnommen wurden. Für eine Optimierung des thermischen Verhaltens der Batteriezellen ist es jedoch erforderlich, den Einfluss der Prozessschritte der Elektrodenproduktion zu verstehen, da diese sowohl die Mikrostruktur als auch die thermischen Transporteigenschaften der einzelnen Elektroden beeinflussen können. Bisher ist keine Studie bekannt, die sich in ausreichendem Umfang mit diesem Thema beschäftigt.

Die Elektrodenproduktion beginnt mit dem Trockenmischen der einzelnen Komponenten. Für den slurry-basierten Prozess, werden diese anschließend in einem Lösungsmittel dispergiert und das erzeugte Slurry wird auf eine Ableiterfolie beschichtet. Nach dem Trocknen der Beschichtung werden die Elektroden im Prozess des Kalandrierens auf ihre finale Dicke und Porosität komprimiert. Ein alternativer Prozessweg der Elektrodenproduktion besteht im Trockenprozessieren.

Dabei wird die trockene Pulvermischung zwischen zwei erhitzten Walzen komprimiert und dadurch direkt und ohne den Gebrauch von Lösungsmittel auf die Ableiterfolie beschichtet.

Mit Ausnahme des Trockenmischens werden alle genannten Produktionsschritte in der vorliegenden Arbeit behandelt und bezüglich ihres Einflusses auf die thermischen Transporteigenschaften der Elektrodenbeschichtungen untersucht. Zudem werden verschiedene Arten und Partikelgrößen des Aktivmaterials verglichen. Die Ergebnisse zeigen keinen wesentlichen Einfluss der Produktionsparameter beim Mischen und Trocknen auf. Eine erhöhte Beschichtungsdicke weist eine Tendenz zu einer geringeren Wärmeleitfähigkeit auf, was mit der stärkeren Bindermigration erklärt werden kann. Der stärkste Einfluss auf die thermischen Transportparameter zeigt sich beim Kalandrieren. Ein höherer Kalandriergrad führt zu einer höheren Wärmeleitfähigkeit der Beschichtung. Ein positiver Einfluss auf die Wärmeleitfähigkeit kann auch für eine zunehmende Größe der Aktivmaterialpartikel beobachtet werden.

Darüber hinaus wird in der Arbeit ein Vergleich der Laser-Flash-Analyse (LFA) und der Zwei-Platten-Methode (engl. Guarded Hot Plate Method, GHP) durchgeführt, welche die am häufigsten verwendeten Verfahren zur Messung der Wärmeleitfähigkeit von Batterieelektroden sind. Die Ergebnisse zeigen erhebliche Unterschiede in der Wärmeleitfähigkeit, die zudem mit dem Kalandriergrad variieren. Die LFA weist allgemein höhere gemessene Wärmeleitfähigkeiten auf als die GHP Methode. Eine detaillierte Analyse möglicher Fehlerquellen beider Methoden liefert Empfehlungen für ihre Anwendbarkeit und gibt Hinweise auf die wahren Werte der Wärmeleitfähigkeit.

Als erste umfassende Studie zu diesem Thema, bildet die vorliegende Arbeit die Grundlage für die angemessene Berücksichtigung des thermischen Verhaltens bei der ganzheitlichen Auslegung von Batterieelektroden.

Abstract

Lithium-ion batteries have become indispensable for mobile applications. As electrochemical storage devices, they are primarily designed with regard to their electrochemical properties, while the thermal behavior is usually of secondary interest.

However, it was shown in recent years that the thermal gradients in batteries have a significant influence on their performance and aging. Consequently, an increasing number of research groups consider the thermal transport in their model and experiments. There are now numerous studies that investigated the thermal transport properties of the different battery components extracted from commercially produced cells, including both anodes and cathodes as well as separators. For an optimization of the thermal transport behavior of the batteries, it is crucial to understand the impact of the process steps of electrode production as these define the microstructure and thermal transport properties of the single electrodes. Hitherto, there is now study known to the author that covers this topic in an adequate manner.

The electrode production process starts with the dry mixing of the components. For the slurry-based processing route, these are then dispersed in a solvent and the obtained slurry is coated onto a current collector foil. After the subsequent drying of the coating, the electrodes are compressed to their final thickness and porosity in the so-called calendering step. An alternative processing route is the dry manufacturing, where the dry mixture is coated onto the current collector by compression between two heated rolls without the use of any solvent.

With the exception of the dry mixing, all the mentioned production steps are investigated in the present work with respect to their impact on the thermal

transport properties of the electrode coatings. Moreover, different active material types and particle sizes are compared. The results show no significant impact of the production parameters varied during mixing and drying. An increased coating thickness shows a tendency towards lower thermal conductivity values, potentially caused by binder migration. The most pronounced influence is found for the calendering step. A higher degree of calendering results in a higher thermal conductivity of the coating. A positive influence on the thermal conductivity can also be seen for an increased size of the active material particles.

Furthermore, a comparison of the laser flash analysis (LFA) and the guarded hot plate method (GHP) as most common measuring methods for the thermal transport properties of battery electrodes is conducted. The results show significant differences that vary in their extent for the differently calendered electrodes. Generally, the LFA leads to higher measured thermal conductivity values than the GHP method. An in-depth analysis of potential error sources for both methods provides recommendations for their applicability and gives insight on the true values of the thermal conductivity.

Being the first of its kind, this study forms the basis for the consideration of the thermal behavior during the holistic design of battery electrodes.

Acknowledgements

This PhD thesis is based on the work conducted during my employment as a research associate at the Institute of Thermal Process Engineering (TVT) at the Karlsruhe Institute of Technology (KIT) from July 2020 till March 2025. I want to express my gratitude to my supervisor Prof. Dr.-Ing. Thomas Wetzel for making this PhD possible and for giving me the freedom to take the time and find a research topic that I am truly interested in. Above all, I am very grateful to have been given the opportunity to visit the Norwegian University of Science and Technology (NTNU) in Trondheim for a research stay from April 2024 till June 2024. Thank you for making this possible!

In this context, I would like to sincerely thank Prof. Odne Burheim for welcoming me at NTNU and later taking on the task of becoming the co-supervisor and co-examiner for my PhD. I will not only remember the great scientific collaboration resulting in a joint publication, but also the numerous bouldering sessions and the time spent with your family on constitution day. Thank you for making me feel so welcome! I will always think back to my time at NTNU with joy and Trondheim has become dear to my heart.

In this regard, the Karlsruhe House of Young Scientists (KHYS) at KIT is greatly acknowledged for funding the research stay at NTNU. The Research Council of Norway is acknowledged for the support to the Norwegian Micro- and Nano-Fabrication Facility, NorFab, which enabled the profilometer measurements conducted in this work.

Moreover, the German Federal Ministry of Education and Research (BMBF) and the Baden-Württemberg Ministry of Science, Research and Art (MWK) are acknowledged for funding the project AgiloBat.

I would like to thank all the colleagues at TVT. Nicole Feger for aiding with all the organizational matters. Sabrina Herberger for conducting numerous measurements featured in this work and the support with many additional experimental investigations. And the whole TVT workshop – Stefan Böttle, Stephan Fink, Max Renaud, and Michael Wachter – for the manufacturing of parts and fetching liquid nitrogen over and over again.

The investigations featured in this work are a result of numerous cooperations with partners at KIT and beyond. Without the connections I made via the project AgiloBat and their openness to collaborate, this work would not have been possible. I am very grateful to have met so many great people.

First of all, I want to thank Marcus Müller who has accompanied this work from the very start by calendering the first set of samples and has since then been part of almost all of the sub-projects. Thank you for providing so many samples, for calendering countless electrode sheets, for preparing the SEM images featured in this work and for the discussions and revisions of our shared papers.

Moreover, I want to thank Julian Klemens, David Burger, Linus Janning, Kevin Ly, Andreas Gyulai, Pirmin Koch and Juan Meza Gonzalez for providing samples, making measurement devices available and for the discussions of the results. I really appreciate the time you took to manufacture all these electrodes for me.

My work on the project AgiloBat and for this thesis was greatly supported by various student projects. Thank you to David Seifert, Helene Reppich, Saskia Müller, Maximilian Birkle, Moritz Link, Luca Graf, Simon Pelzer, Adrian Reyes Mayorga, Martin Böhm, Yasmin Grübbel, Paul Heinold, Anastasia Schmidt Gallegos and Malte Keller.

Thank you to Lisa Cloos, Oliver Queisser and Daniel Werner for the great scientific discussions that significantly enhanced my work.

A big thank you also to Sabine Paarmann for her mentorship and friendship even beyond her time at TVT. I am grateful for your support and advice in so many ways.

Thank you to the 10.94 crew for adopting us and making 2023 survivable. And thank you to the TFT for the best lunch breaks and parties. I will miss you!

I also want to thank all the colleagues and friends at NTNU who adopted me so well. Anders, Silje, Vitor, Sam, Pauline, Mahshid, Ge, and most of all, Simon and Ida. I really want to come back for one of those taco nights!

But most importantly, I am grateful to my friends and my family – most of all, my parents – for their continuous support. 2025 has not been the easiest year, but I guess sometimes that's what brings you closer. Thank you for being here for me always!

And finally, Jonas. Thank you for everything!

Contents

Kurzfassung . . . . . **i**

Abstract . . . . . **iii**

Acknowledgements . . . . . **v**

List of Symbols . . . . . **xiii**

List of Acronyms . . . . . **xvii**

1 Introduction **1**

2 State of the Art **5**
2.1 Electrode Analysis 5
2.1.1 Microstructural Investigations 6
2.1.2 Mechanical Investigations 14
2.1.3 Electrical Investigations 18
2.1.4 Thermal Investigations 21
2.2 Electrode Production 36
2.2.1 Formulation 38
2.2.2 Dry Mixing 45
2.2.3 Wet Mixing 47
2.2.4 Wet Coating 50
2.2.5 Drying 52
2.2.6 Calendering 60
2.2.7 Dry Manufacturing 68

3 Experimental Methods **71**
3.1 Manufacturing of the Electrodes 71

3.2 Laser Flash Analysis . . . 76
3.3 Differential Scanning Calorimetry . . . 79
3.4 Gas Pycnometry . . . 80
3.5 Geometrical and Gravimetrical Analysis . . . 81
3.6 Guarded Hot Plate Method . . . 86
3.7 Scanning Electron Microscopy . . . 88
3.8 Electrical Resistance Measurements . . . 88
3.9 Profilometer . . . 89

4 Modeling . . . 91
4.1 Analytical Model by Oehler . . . 91
4.2 FEM Simulation of the LFA Measurements . . . 94

5 Results and Discussion . . . 99
5.1 Formulation . . . 100
5.2 Wet Mixing . . . 104
5.3 Wet Coating . . . 106
5.4 Drying . . . 107
5.5 Calendering . . . 109
5.5.1 LFA Measurements . . . 109
5.5.2 Comparison with Model-Based Thermal Conductivities . . . 118
5.5.3 Applicability of the LFA and GHP Method . . . 122
5.5.4 Impact of the Electrolyte and Transfer to the Cell Level . . . 142
5.5.5 Electrical Resistance Measurements . . . 146
5.6 Dry Manufacturing . . . 148
5.7 Summary of the Separate Investigations . . . 149

6 Conclusion . . . 153

Bibliography . . . 159

List of Publications . . . 199

List of Supervised Theses . . . 203

A Appendix **205**
A.1 Additional Data 205
A.2 Additional Figures 219

List of Figures **225**

List of Tables **235**

List of Symbols

Latin Symbols

Symbol	Unit	Meaning
A	m^2	Area
c	-	Particle distance parameter
c_p	$\mathrm{J{\cdot}kg^{-1}{\cdot}K^{-1}}$	Specific heat capacity at constant pressure
d	m	Diameter
D_s	m	Outer screw diameter
f	-	Factor in the Hamilton-Crosser model
$F_\mathrm{t,max}$	N	Maximum tensile force
h	m	Indentation depth
M	kg	Mass
n	s^{-1}	Rotation speed
n_layers	-	Number of layers
p	$\mathrm{N{\cdot}m^{-2}}$	Pressure
P	N	Force
$\dot{q}$	$\mathrm{W{\cdot}m^{-2}}$	Heat flux
r	m	Radius
R	$\mathrm{m^2{\cdot}K{\cdot}W^{-1}}$	Thermal resistance
s	m	Thickness
T	K	Temperature
t	s	Time
$t_{1/2}$	s	Half-time of the heat-up
V	m^3	Volume
$\dot{V}$	$\mathrm{m^3{\cdot}s^{-1}}$	Volume flow rate

Latin Symbols – continued from previous page

Symbol	Unit	Meaning
V_A	m^3	Added volume
V_C	m^3	Volume of the measurement chamber
W_e	J	Elastic indentation work
W_p	J	Plastic indentation work
W_t	J	Total indentation work
x	m	Coordinate

Greek Symbols

Symbol	Unit	Meaning
α	$W{\cdot}m^{-2}{\cdot}K^{-1}$	Heat transfer coefficient
α (Model DO)	-	Particle contact parameter
β	$K{\cdot}s^{-1}$	Heating Rate
γ	$N{\cdot}m^{-1}$	Surface tension
γ_c	$N{\cdot}m^{-1}$	Compaction resistance
Δ	-	Difference
κ	$m^2{\cdot}s^{-1}$	Thermal diffusivity
λ	$W{\cdot}m^{-1}{\cdot}K^{-1}$	Thermal conductivity
ν	-	Volume fraction
ρ	$kg{\cdot}m^{-3}$	Density
ρ_{el}	$\Omega{\cdot}m$	Electrical resistivity
σ	$N{\cdot}m^{-2}$	Adhesion strength
σ_{el}	$S{\cdot}m^{-1}$	Specific electrical conductivity
θ	$^\circ$	Contact angle
τ	-	Tortuosity
ϕ	-	Porosity
Π_c	-	Compression rate

Indices

Symbol	Meaning
Al-sample	Contact between aluminum (rig) and sample
AM	Active material
after	Measured after the GHP measurement
b	Base
BCB	Binder-carbon black phase
before	Measured before the GHP measurement
calc	Calculated
CB	carbon black
cc	Current collector
co	Active material coating
D	Drying
dry	Dry electrodes
eff	Effective value
f	Fluid phase
g	Gaseous phase
gr	Gravimetrical
Hg	Mercury intrusion
ideal	Ideal path
KIT	Measured at KIT
lower	Lower piston
m	Mean
NTNU	Measured at NTNU
P	Pore(s)
PM	Polymer, binder phase
piston	Piston, in general
pressure	Measured within the GHP rig under pressure
ref	Reference
s	Solid phase
sample	Sample
soaked	Electrodes soaked with electrolyte solvent

Indices – continued from previous page

Symbol	Meaning
th	Thermal
total	Total value
upper	Upper piston
0	Initial value

List of Acronyms

AM	active material
BCB	binder-carbon black
BOL	beginning of life
CB	carbon black
CC	commercial
CG	conductive graphite
CMC	carboxymethyl cellulose
DEM	discrete element method
DOD	depth of discharge
DSC	differential scanning calorimetry
EDX	energy dispersive x-ray spectroscopy
EFC	equivalent full cycle
EIS	electrochemical impedance spectroscopy
GHP	guarded hot plate method
Gr	graphite
HC	hard carbon
IAM	Institute for Applied Materials at KIT

IAM-ESS Institute for Applied Materials – Energy Storage Systems at KIT

IM inactive material

IR infrared

KHYS Karlsruhe House of Young Scientists

KIT Karlsruhe Institute of Technology

LCO lithium cobalt oxide

LFA laser flash analysis

LFP lithium iron phosphate

LIB lithium-ion battery

LIBS laser-induced breakdown spectroscopy

LMO lithium manganese oxide

LNMO lithium nickel-manganese oxide

LTO lithium titanium oxide

MVM Institute of Mechanical Process Engineering and Mechanics at KIT

NCA lithium nickel-cobalt-aluminum oxide

NMC lithium nickel-manganese-cobalt oxide

NMP N-Methyl-2-pyrrolidone

NTNU Norwegian University of Science and Technology

OCV open-circuit voltage

PB prussian blue

PBA prussian blue analogue

PTFE polytetrafluoroethylene

PTL	porous transport layer
PVDF	polyvinylidene fluoride
SBR	styrene-butadiene-rubber
SEI	solid electrolyte interface
SEM	scanning electron microscopy
SFL	specific feed load
SIB	sodium-ion battery
Si-C	silicon-graphite
SOC	state of charge
s-s	sample-sample
TFT	working group Thin Film Technology at KIT
TSE	twin-screw extruder
TVT	Institute of Thermal Process Engineering at KIT
ZBS	Zehner, Bauer, and Schlünder
1D	one-dimensional
3D	three-dimensional

1 Introduction

Lithium-ion batteries (LIBs) have become an integral part of mobility. However, as electrical energy storage devices they are still primarily designed with regard to their electrochemical properties, while the thermal behavior is usually of secondary interest. This approach is already reflected in the production and analysis of the intermediate products. Even the differently coated, dried and calendered samples are currently only examined and optimized with regard to their electrical and mechanical parameters.

However, in recent years it has been shown that the thermal transport parameters and the resulting temperature gradients in batteries have a significant influence on the performance and aging of batteries [1–9]. In this context, electrothermal models have been developed to reproduce the thermal transport and electrochemical performance of the batteries [10–12]. Usually homogenized thermal transport properties are used in these models. Consequently, an increasing number of studies provide corresponding data by measuring the specific heat capacity and thermal conductivity directly on cell level [13–23]. For an optimization, however, the knowledge of the limiting factor for the thermal transport is crucial. Especially perpendicular to the stacked electrode layers, the component with the lowest thermal conductivity constitutes a significant bottleneck for the thermal transport. It is therefore important to understand the influence of the production processes on the thermal transport parameters in order to better predict and optimize the thermal behavior of electrodes and battery cells.

This does not only include the production itself but also involves the choice of the used formulation like the choice in active material and binder, the content of binder and conductive additive as well as the particle size distribution of

the material. When these configurations are defined, the production starts with the dry mixing of the components, which – for wet-processed electrodes – is followed by the dispersion of the dry mixture in a solvent and the formation of a slurry. This slurry is then applied to a metallic current collector foil during the coating process. The subsequent drying step leads to the build-up of the porous microstructure of the electrodes. In a last step, the so-called calendering, the electrodes are compressed between two heated rolls to reduce the thickness and porosity. [24]

A novel approach for electrode production is the dry manufacturing of electrodes [25]. This way, the process chain is shortened and it only takes one or two steps of calendering from the dry mixture to the final electrode.

The electrodes can then be cut, stacked between separator layers and eventually enclosed in the cell housing. The filling with electrolyte and formation of the cells – an initial charging and discharging with very low currents – leads to the activation of the battery cells.

Hitherto, there is no study known that covers the impact of the whole electrode production sequence on the thermal material properties and the interconnection of the single steps in this context. Previous studies have focused on the investigation of the thermal transport properties of electrodes extracted from commercial cells. The studies used either the laser flash analysis (LFA) [26–37] or guarded hot plate method (GHP) [38–44] for the determination of the thermal conductivity, making them the two most common measuring methods in this context. However, the results in the literature largely differ for the two methods, giving rise to the question, which method's results are closer to the true value.

Aim of this thesis

Against this background, the present work aims to shed light on the impact of the different electrode production steps on the thermal transport properties of the interim and final products. Moreover, the two most common measurement methods for the thermal conductivity – the laser flash analysis and the guarded

hot plate method – are applied to the differently calendered samples to narrow down the range of the real value. The primary research questions therefore are:

How do the different production parameters influence the thermal transport in battery electrodes?

Do production steps aimed at achieving optimal capacity and electrical transport properties also lead to optimal thermal transport properties?

What are important effects to be considered when determining the thermal transport properties using LFA and GHP?

The key measure herein is the effective thermal conductivity of the porous coatings, which is investigated for different electrodes directly after drying or at varied degrees of calendering.

In a first step, a thorough analysis of the state of the art is conducted to provide a solid basis for the interpretation and discussion of the results obtained later on. This includes a breakdown of the measuring methods most commonly used for the determination of the thermal transport properties and an overview on the thermal conductivity values obtained for battery electrodes available in the literature. Moreover, observations of the microstructural, mechanical and electrical effects made in former studies are discussed to examine to what extent they are transferable to the thermal behavior observed in the present study.

Secondly, an experimental matrix with a large parameter variation for the produced electrodes is determined. This way, potential influences of the wet mixing, coating, drying, calendering and dry manufacturing steps are investigated for several different active materials.

Lastly, the results of the measured thermal conductivity are discussed in consideration of the known literature. The main focus herein is on the calendering process, which is investigated in most detail and accounts for the majority of this work. While the impact of the other production steps and influencing factors are only measured with the LFA, the varyingly strong calendered electrodes are measured

with both, the LFA and GHP. This allows a comparison of the two methods with equal electrodes. The challenges and the applicability of both methods are discussed.

Moreover, the thermal conductivity values measured with the LFA are used for the comparison with the analytical model developed by Oehler in a previous work [34]. The model is used for the theoretical calculation of the effective thermal conductivity of electrode coatings. It considers the influence of the applied active material, composition and porosity of the electrodes. Thus, the newly obtained experimental results provide an interesting data set for the comparison with the model.

2 State of the Art

There are various review articles and books that describe the basics of lithium- and sodium-ion batteries in great detail. These include the design and operating principles [45, 46] as well as comprehensive summaries of the production processes currently used and anticipated to be implemented in the future [24, 25, 46–48].

As a consequence, this section does not seek to reproduce the fundamentals. Instead, the focus lies on the analysis methods used to evaluate the intermediate products of the whole electrode production chain and thus the influence of the single production steps on the behavior of the final electrodes and cells. Therefore, the microstructural, mechanical, electrical and thermal effects are considered.

With a general understanding of the analysis methods, the quantified influences of the production processes are then discussed in the second part.

2.1 Electrode Analysis

To understand the impact of different production settings, a general knowledge of the applied analysis methods is needed. These include methods for the determination of the thermal material properties as well as the microstructural, mechanical and electrical properties. The latter give further insight into the changes obtained by the processes and allow for a meaningful comparison with the newly obtained thermal transport properties. For the thermal properties themselves of the different intermediate products or samples with similarly set properties only few studies exist so far [26, 49].

2.1.1 Microstructural Investigations

The microstructure presents a very broad field of properties. It can stand for the most basic descriptions of the morphology like porosity and tortuosity or can go far into detail describing locally varying compositions and particle and pore size distributions. In the context of battery electrodes, great emphasis is for example also put on the distribution of the binder and the particle size and de-agglomeration of conductive additives. The pore structure is of importance for the electrochemical performance of the cells built from these electrodes. Often mechanical and electrical investigations are actually used to obtain underlying information on the microstructure and distribution of the single components, which makes the explicit division into the different categories difficult.

The porosity ϕ as one of the most important characteristics describes the void fraction within the electrodes and is defined according to Equation (2.1) with the absolute volume of all pores V_{P} and the total volume of the electrode coating V_{co} including both particles and pores. The values assigned to ϕ are in the range of 0 to 1.

$$\phi = \frac{V_{\mathrm{P}}}{V_{\mathrm{co}}} \tag{2.1}$$

As the porosity only poses an overall mean value and gives no information about the distribution of the pores, there are additional variables describing the local microstructure. The tortuosity τ describes the ratio of the effective path lengths through the pores $L_{\mathrm{P,eff}}$ to the shortest, ideal path length $L_{\mathrm{P,ideal}}$ as given in Equation (2.2). As $L_{\mathrm{P,eff}} \geq L_{\mathrm{P,ideal}}$ is valid here, the tortuosity obtains values of $\tau \geq 1$.

$$\tau = \frac{L_{\mathrm{P,eff}}}{L_{\mathrm{P,ideal}}} \tag{2.2}$$

Owing to the scarcity of empirical methods for the direct determination of the tortuosity, it is often calculated from the known porosity. Most common for this

is the Bruggemann correlation as given in Equation (2.3) [50]. However, more complex equations were developed in recent years [50] to describe the tortuosity more accurately.

$$\tau = \frac{1}{\sqrt{\phi}} \tag{2.3}$$

The tortuosity is especially relevant in the context of solvent evaporation during drying and the lithium-ion diffusion during the operation of the batteries. In both cases, a low tortuosity is advantageous.

Another interesting variable for the analysis of the electrodes is the knowledge of the particle size distribution. It provides qualitative information on the number and size of particle-particle contacts in the conduction pathways. Furthermore, it is closely related to the pore size distribution, which defines the pathways for ionic conduction.

In the following, several methods for the characterization of the microstructure and an assessment of the above mentioned properties are described.

Laser Diffraction Analysis

Two methods for the measurement of particle size distributions are considered in this work. The first one is the laser diffraction method also known as angular scattering. Here, the particle mixture is dispersed in a liquid, usually water. A laser beam is expanded and passed through the suspension. The particles within the sample diffract the light with a certain angle which depends on the size of the particles. The smaller the particles are, the larger is the diffraction angle. On the backside of the sample suspension, the diffracted light is focused onto a detector. This way, the main beam of the light is focused on a point in the center of the receiver, while the scattered light creates a diffraction pattern in the form of an angular variation in the light intensity. This pattern only depends on the particle size distribution and is not influenced by the particle movement. [51]

The calculation of the size of the particles responsible for the scattering intensity pattern can either be conducted according to the Fraunhofer diffraction theory or the Lorenz-Mie scattering theory. The former is only valid for particles that are significantly larger than the wavelength of the light source ($d > 10\lambda$). As this is typically between 400 nm and 700 nm, for battery electrodes including the active material with a particle size of 1 µm to 20 µm and additives with common particle sizes below 1 µm, the Lorenz-Mie theory is preferred. [52]

Light Extinction Method

The second method for the measurement of particle size distributions discussed in this work is the light extinction method, sometimes also named total light scattering. The method follows a similar set-up as the laser diffraction with a beam of monochromatic light pointed at a particle suspension. The intensity of the transmitted light diminishes along the thickness of the sample according to Beer's law. The evaluation also follows the Lorenz-Mie theory. [53]

However, for multi-material systems as present for electrode slurries, the results have to be considered carefully as the different materials have different extinction coefficients [54].

With both of these methods for the measurement of the particle size distribution, diluted electrode slurries can be investigated. This gives an insight into the impact of the mixing process and thereby the de-agglomeration of carbon black secondary particles or the fragmentation of active material particles.

Mercury Intrusion

The mercury intrusion provides a rough estimate of the electrode's porosity and tortuosity. Moreover, it gives information on the pore size distribution, either incremental or cumulative, the absolute and specific pore volume and the inner coating surface [50].

The measuring device consists of a penetrometer made of glass wherein a specific pressure can be set. For the measurement, the electrodes with current collector are cut into small pieces to fit into the sample container. The penetrometer is first evacuated and then filled with mercury with increasing pressure.

The theory behind the mercury intrusion was first noted by Washburn in 1921 [55] as a method for determining the pore size distribution in porous materials. Due to its non-wetting properties (contact angle $\theta \geq 90°$) the mercury has to be forced into the pores with a pressure p [50]. The required pressure difference is directly correlated to the radius r_P or diameter d_P of the intruded pores according to the Washburn equation given in Equation (2.4) [55]. Thus, the smaller the pore size, the higher the pressure needed to intrude them.

$$\Delta p = -\frac{2 \cdot \gamma \cdot \cos(\theta)}{r_\mathrm{P}} = -\frac{4 \cdot \gamma \cdot \cos(\theta)}{d_\mathrm{P}} \tag{2.4}$$

A constant surface tension of $\gamma = 0.485\ \mathrm{N \cdot m^{-1}}$ of the intruded mercury [50] and a contact angle of $\theta = 140\,°$ independent of the surface composition are assumed for the evaluation [50, 56]. By slowly increasing the pressure and measuring the volume filled in each pressure range, the size of the pores and their ratio can be detected, providing a pore size distribution.

Result of the mercury intrusion is the filled volume as a function of the applied pressure from which the pore size distribution can be derived. The pore size distribution may be presented either in an incremental way, featuring a maximum at the predominant pore size, or in a cumulative way from 0 to the total pore volume.

A more common approach is to plot the derivative $-\mathrm{d}V/\mathrm{d}(d_\mathrm{P})$ versus the pore diameter d_P as shown in Figure 2.1 (a). In this, the pore diameter is plotted on a logarithmic scale and the volume is usually normalized to the sample weight and thus given in $\mathrm{cm^3 \cdot g^{-1}}$ to make the results comparable [50]. This depiction shows at least one peak (monomodal distribution), though it may also have two (bimodal) or more peaks for battery materials. In this, the peak at higher pore

diameters refers to the pores between the comparably large active material (AM) particles, while the peak at smaller pore diameters is predominantly caused by the pores in the binder phase.

The second option is to plot the pore volume distribution sum [50], which is also plotted versus the logarithmic pore diameter as shown in Figure 2.1 (b). The cumulative sum runs from 0 to the maximum value. Depending on the form of depiction this maximum can either be the absolute pore volume in cm^3, the specific pore volume in $cm^3 \cdot g^{-1}$ or simply 1 for the normalized case.

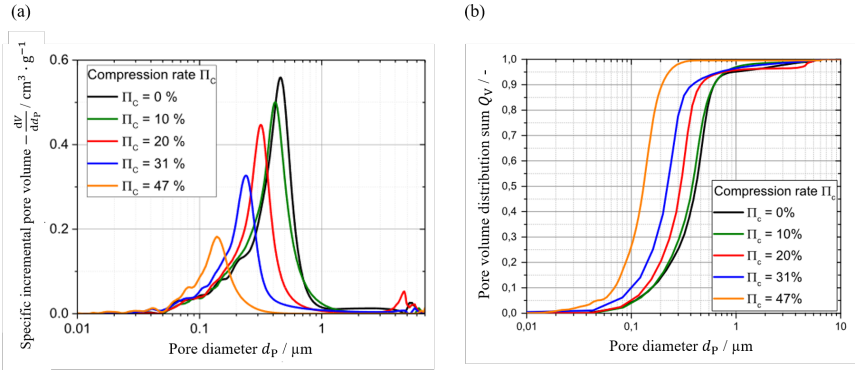

Figure 2.1: Examples for (a) an incremental and (b) a cumulative pore size distribution for graphite electrodes at different compression rates (adjusted from Froboese et al. [50], Copyright 2017, Elsevier, reproduced under the license number 6135241071637).

The sum of all pores allows the calculation of the porosity in accordance with Equation (2.1). For the mercury intrusion the equation can be modified to Equation (2.5) with the used volume of mercury V_{Hg}, the total volume of the electrode stack V_{stack} consisting of coating and current collector and the current collector volume V_{cc}.

$$\phi_{Hg} = \frac{V_{Hg}}{V_{stack} - V_{cc}} \tag{2.5}$$

A general constraint of the mercury intrusion is that closed pores are not accessible for the mercury and, thus, are not included in the recorded pores. Therefore, the volume of the closed pores is missing for the calculation of the porosity.

Furthermore, when measuring battery electrodes, the mercury can react with the aluminum or copper of the current collectors to amalgam [50]. This results in a volume generation which distorts the measurement results. For aluminum this is said to be especially important in the higher pressure range above 375 kPa [57] which corresponds to pores ≤ 4.0 µm.

Another concern is the choice of the maximum pore size for the evaluation of the porosity. Choosing a value too high might include the volume between the sample pieces [50]. However, too low values might lead to the neglection of a part of the pore volume. Froboese et al. [50] recommend an upper limit of 7 µm and a lower limit of 10 nm for graphite-based battery electrodes. The choice of those boundaries leads to a significant uncertainty in the porosity determined from the mercury intrusion measurements. That is why the method is mostly used for the determination of pore size distributions, but not necessarily for the absolute porosity.

Instead or additionally, a gravimetrical determination of the porosity is reasonable. When the densities of the current collector and the mixed solid components of the AM coating as well as their layer thicknesses are known, the porosity can be calculated for a sample with defined area. For a circular sample of a single-sided coated electrode with a diameter d the calculation follows Equation (2.6).

$$\phi_{\mathrm{gr}} = 1 - \left[\frac{m_{\mathrm{stack}}}{\left(\frac{\pi \cdot d^2}{4} \cdot s_{\mathrm{co}}\right)} - \rho_{\mathrm{cc}} \cdot \frac{s_{\mathrm{cc}}}{s_{\mathrm{co}}} \right] \cdot \rho_{\mathrm{s,co}}^{-1} \tag{2.6}$$

Herein, m_{stack} is the mass of the two-layer sample, s_{co} and s_{cc} are the thicknesses of the AM coating and the current collector, respectively, and $\rho_{\mathrm{s,co}}$ and ρ_{cc} are the mean density of the solid mixture of the coating and the density of the current collector. The solid density of the coating is often measured with gas pycnometry. It is possible that part of the pores are not accessible for the gas and thus the mass

is referred to a too large volume resulting in a slightly lower density value than in reality.

The most important error source of the gravimetrical determination of the porosity is the measurement of the sample thickness. Due to the generally small thickness of the electrodes in the range of tens to hundreds of micrometers, the relative error is highly significant here and directly impacts the uncertainty of the porosity. The uncertainty also increases with increasing degree of calendering as the thickness of the electrodes is reduced leading to a higher relative uncertainty with the same absolute error of the measurement.

Scanning Electron Microscopy

The scanning electron microscopy (SEM) is used as imaging technique to get a qualitative impression of the electrode structure. For this, a focused electron beam scans the surface to be investigated in a raster pattern. The sample within the device is under vacuum to prevent interactions between the electrons and gas atoms and molecules. Depending on the interaction with the examined material different signals are obtained. Either the electron beam shoots an electron out of the valence bands of the atoms at the top surface of the sample. These electrons ejected from the upper 1 nm of the surface are called secondary electrons. They have a much lower kinetic energy compared to the beam electrons and thereby those areas appear darker in the final image. The ejections of electrons and, thus, the darker color in the SEM image is a sign for lower density materials. The second form of interaction of the electron beam with the material surface are electrons that stem from the original beam and are only reflected at the surface. These are called backscattered electrons. The higher the density of the material that is shot by the electron beam, the higher is the proportion of reflected electrons and the brighter the material appears in the final image. Moreover, edges appear brighter than smooth surfaces. SEM allows the high resolution imaging of samples in the nm to µm range. However, it requires the material to be electrically conductive, which is the case for battery electrodes. Otherwise this could be obtained by sputtering the material with a thin conductive coating. [58]

For electrodes, usually either the surface is examined with SEM or a cross section is created by ion-etching with argon. The surface investigation gives insight into potential depositions caused by the cycling and aging of the batteries or the formation of cracks [59]. The cross-section views for example provide information on particle cracks and particles that are pressed into the current collector [60]. Moreover, they give a qualitative impression of the binder distribution within the electrodes [61].

Energy Dispersive X-ray Spectroscopy

In combination with the SEM, the energy dispersive x-ray spectroscopy (EDX) – sometimes termed EDS is the literature – can be used to obtain insights into the elements present in the sample and their concentration. For this, electron beams with a very high voltage of several kV are shot onto the sample. This way, electrons from further inside of the sample are ejected. The evaluation of the received intensity vs. energy spectra of the electron beams with their element specific peaks provides information of the present elements and their concentration. The energy of the electron depends on the shell of the atom it was removed from. [58, 62]

In the context of the electrode production, EDX is often used to investigate the distribution of the polyvinylidene fluoride binder by measuring the fluorine concentration [63, 64].

Laser-induced Breakdown Spectroscopy

An alternative to EDX is the laser-induced breakdown spectroscopy (LIBS). It exhibits a direct method for the determination of the element distribution within electrodes. Here, a laser is shot onto the electrode surface and a thin layer of material is transformed into a plasma. The plasma is analyzed regarding its composition and delivers information of the binder concentration in that area. Applying more and more shots on the exact same spot of the electrode, they cut

deeper and deeper into the material. This way, the concentration at different thickness coordinates can be analyzed, delivering an impression of the binder distribution along the thickness of the electrode. [64]

Profilometer

Measurements with an optical or stylus profilometer are used to estimate the surface roughness and differences in height of electrodes. They provide a meaningful addition to the SEM images of the electrode surface. The optical profilometer uses the interference patterns of light to scan the electrode surface without physically touching it. In the stylus profilometer, a stylus with a tip radius usually in the range of 100 nm to 20 µm scans the sample surface. A slight weight of a few mg is applied to the stylus. While it is moved along the surface with a constant speed in horizontal direction, the vertical deflection of the stylus is recorded. [65]

2.1.2 Mechanical Investigations

Investigations of the microstructure and mechanical properties are often closely connected. This section focuses on the stability of the electrode layer and structure analyses that are obtained by mechanical measurements such as adhesion strength measurements and deformation energy measurements.

Adhesion Strength Measurements

The adhesion strength is considered an important parameter for the early prediction of the quality and lifetime of the battery cells built from the considered electrodes. A higher adhesion strength between the electrode coating and the current collector indicates a better long time performance of the batteries. [66]

Moreover, the adhesion strength is used as a measure for the amount of binder at the coating-current collector interface and the consequential binder distribution.

The testing methods for the adhesion strength can be divided into pull-off tests and peel tests. As the former refers to the areal removal of the electrode coating while the latter means the one-dimensional removal with a line load, a quantitative comparison between the two methods is not possible. However, it can be assumed that the same qualitative effects are found with both methods. Both tests are conducted with single-sided coated electrodes.

The pull-off test was introduced for the use on battery electrodes by Haselrieder et al. [66]. In this, a rectangular or circular sample with a defined area is fixed to both base plates of a uni-axial material testing machine with double-sided adhesive tape. The electrode is compressed in a defined manner to create a reproducible bond towards the adhesive. Haselrieder et al. [66] recommend a pressure of 0.6 $\mathrm{N{\cdot}mm^{-2}}$, a time of 7 s for the pressure build-up and a hold time of 30 s. The pressure used is substantially lower than the one applied during calendering and is too low to cause a significant plastic deformation of the electrode. Therefore, the measurement procedure is also applicable for uncalendered samples.

Subsequently, the actual pull-off test is conducted by moving the base plates in opposite directions at a defined velocity while measuring the tensile strength. The adhesion strength σ is in this case defined as the maximum tensile force $F_{\mathrm{t,max}}$ divided by the area of the sample A as described in Equation (2.7) and, thus, is given in Pa.

$$\sigma = \frac{F_{\mathrm{t,max}}}{A} \tag{2.7}$$

Furthermore, three different failure mechanisms are distinguished: adhesion failure, cohesion failure and failure of the adhesive, which are schematically shown in Figure 2.2. The adhesion failure that is desired during the measurement describes the breakage of the interface between coating and current collector. In the case of a cohesion failure or a failure of the adhesive, no exact value of the adhesion strength is measurable. It is only shown that the adhesion strength is higher than the strain measured for the failure occurred. Thus, if the quality of the interface is of interest for the investigations, only the results of the real adhesion failures

may be considered and an optical breakage analysis after the pull-off test needs to be conducted.

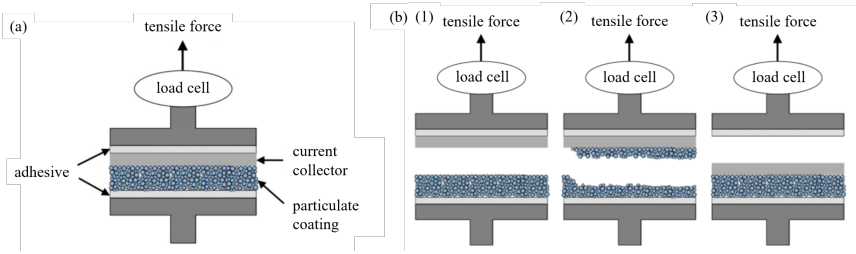

Figure 2.2: Schematic depiction of (a) the pull-off test and (b) possible failure mechanisms: (1) adhesion failure, (2) cohesion failure and (3) failure of the adhesive (adjusted from Haselrieder et al. [66], Copyright 2015, Elsevier, reproduced under the license number 6135250046122).

The second, commonly used method to determine the adhesion between electrode coating and current collector is the peel test. For this, electrode strips with a defined width usually between 5 mm and 30 mm [67–75] are cut and the coated side is fixed to the base plate of the measurement device with double-sided adhesive tape. The sample is pressed on with a defined force to ensure a uniform contact towards the adhesive tape [74] and subsequently the current collector is peeled off with an angle of either 90 ° [71–74] or 180 ° [67–70, 75]. The velocity should be kept constant while the used force is recorded. Usual values for the velocity in literature vary strongly between 6 mm $\cdot$ min^{-1} and 600 mm $\cdot$ min^{-1} [70, 71, 75]. The adhesion strength is defined as the maximum tensile force divided by the width of the sample and, therefore, poses a line load with the unit N $\cdot$ m^{-1}.

Deformation Energy Measurements

Another method to draw conclusions about the binder distribution in the coating is the measurement of the elastic and plastic deformation energy. This approach is based on the investigations of carbon coatings with nanoindentation by Bartali et al. [76]. At this, an indenter with a defined tip is pressed into the coating surface

with increasing force and then retracted. The force P and indentation depth h are recorded during loading and unloading and may be plotted according to Figure 2.3. The occurrence of plastic deformation provokes a hysteresis between the two curves.

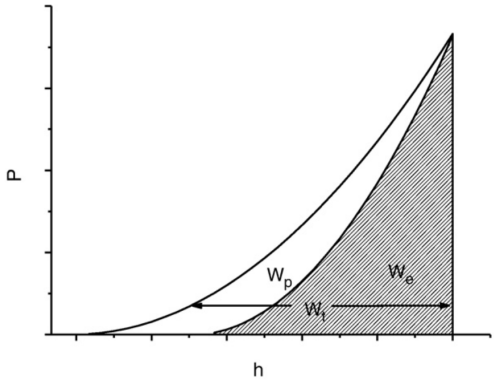

Figure 2.3: Connection between the force P during loading and unloading and the indentation depth h. The areas under the curves represent the total (W_t), plastic (W_p) and elastic (W_e) indentation work (reproduced from Bartali et al. [76], Copyright 2010, Elsevier, reproduced under the license number 6135250724496).

The total deformation work W_t is defined as the area under the loading curve and the elastic deformation work W_e is defined as the area under the unloading curve. As a result, the plastic deformation work W_p is equivalent to the difference of $W_\mathrm{t} - W_\mathrm{e}$ [76].

Tran et al. [77], Westphal and Kwade [64] and Scheffler et al. [78] used the nanoindentation method for the investigation of the production processes for batteries. They all recommended a circular flat punch indenter but used different procedures. Westphal and Kwade [64] applied a maximum indentation depth of 10 % of the electrode thickness which is approached with a defined velocity. This way, the force varies between different samples. Tran et al. [77], however, applied a defined maximum force of 8 mN, so that the indentation depth is varied instead.

Although both approaches allow similar statements about the investigated sample, a comparison among each other is difficult. For a good comparability between the measurements, they should be conducted at a defined temperature with the same indenter geometry as well as indentation speed and the same approach of path- or force-controlled indentation.

As a result of the measurements, Westphal and Kwade [64] and Scheffler et al. [78] mapped the cumulative distribution curves of the total, plastic and elastic deformation work from 80 measurements. Opposed to using just the mean values of the measurements, the distribution curves give insight into an increasing inhomogeneity in the electrode in the form of a lower slope and wider curve.

The ratio of elastic deformation gives indications on the binder fraction in the upper part of the electrode coating. Moreover, insight into the elastic deformation process might be interesting for understanding and optimizing the calendering of different electrode compositions as a highly elastic behavior suggests a stronger springback after releasing the calendering force again.

2.1.3 Electrical Investigations

This section aims at explaining the basics of the measurement of the electrical, ionic and electrochemical properties of electrodes and cells.

Electrical Resistance Measurements

On electrode level, the electrical resistance is often measured as first indicator of the electrical and electrochemical performance. However, investigations into this topic in the literature often focus on different variables. Some studies present the absolute resistance in Ω [79, 80], others the resistivity – or alternatively termed volume resistance – in $\Omega \cdot m$ [61, 72, 81], and some even the specific electrical conductivity in $S \cdot m^{-1}$ [82, 83] which is the reciprocal of the resistivity. Additionally, the interface resistance in $\Omega \cdot cm^2$ was investigated in some studies

[84, 85], giving an insight into the quality of the electrical contact between coating and current collector.

The most common approach for the measurement of the electrical resistance of thin layers is the current transit method [79, 86]. It uses four measuring tips arranged along a line. A defined current applied between the outer two tips while the voltage drop along the conduction path is measured at the inner tips [87]. More novel methods use higher numbers of probes and include a numerical simulation of the voltage distribution during the evaluation for a more precise analysis of the resistivity and interface resistance [61, 81, 88].

The electrical conductivity is not the only criterion for the electrochemical performance. The ionic conductivity is inversely impacted by changes in the microstructure and is thus often investigated as well. While the reduction of the electrode porosity generally results in an enhancement of the electrical conductivity, it leads to a reduction in the ionic conductivity [82].

Cell Tests

Another important investigation of the produced electrodes is the measurement of the available discharge capacity at different C-rates. These measurements are often simply termed cell tests. However, some researchers use the term cell test in a much wider range for measurements of the open-circuit voltage (OCV) or the entropy coefficient among other forms.

The C-rate in h^{-1} is a normalized current and describes the reciprocal of the time it takes to fully charge or discharge the cell. It is usually referred to the nominal capacity of the cell. A C-rate of 1C, for example, means that the cell is fully charged or discharged within one hour. Thus, the applied current is equal to the nominal capacity per hour. Higher C-rates, thus, mean that higher currents are applied and a shorter time is needed for the charging or discharging process.

Cell tests can be conducted with either half cells, where the anode or cathode is measured against lithium metal, or full cells consisting of anode and cathode.

In case of full cells, the tested setup can vary depending on the focus of the investigation. For the analysis of the impact of different production parameters, experimental coin cells are usually used with electrode discs of 18 mm in diameter. However, equivalent tests and especially the aging tests can also be conducted on pouch cell level [89].

The cell tests give insight into the usable capacity at different currents applied. In general, the discharge capacity drops with increasing C-rate [90] due to the rising overvoltage which results in a faster reaching of the voltage limit. In a comparison of different production parameters, the absolute capacity values define the quality of the electrodes. The extent of the capacity drop with increasing C-rate decides on the applicability of the electrodes for high-power applications. An exemplary depiction of the discharge capacity in dependence on the C-rate is given in Figure 2.4 (a).

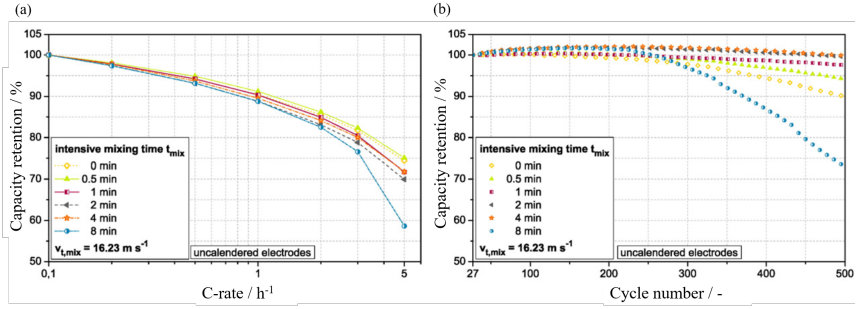

Figure 2.4: Capacity retention of a full cell: (a) percentage of the usable discharge capacity at different C-rates referred to the capacity at C/10 and (b) percentual capacity retention of different cells after cyclization with 1C (adjusted from Bockholt et al. [80], Copyright 2016, Elsevier, reproduced under the license number 6135251325427).

Another common approach for the quality assessment of novel materials or process routes is to increase the C-rate in the first few cycles and to run five to ten cycles per C-rate. Common C-rates here range from C/20 to 5C [71, 72, 83, 91, 92].

To analyze the long-term stability of cells and electrodes, aging tests with an increased number of cycles are conducted. At this, the remaining discharge capacity is depicted against the cycle number as shown in Figure 2.4 (b). In case the aging is conducted with a depth of discharge (DOD) < 1 – meaning that the cell is not discharged to 0 % SOC and/or not charged up to 100 % SOC – the data is generally plotted against equivalent full cycles (EFCs).

2.1.4 Thermal Investigations

There are different approaches for the measurement of the thermal transport properties of battery components, which are mainly performed on electrodes extracted from commercial lithium-ion batteries.

Generally, a distinction must be made between methods for the direct determination of the thermal conductivity and measurements of the thermal diffusivity. The latter require the knowledge of the mean density ρ and specific heat capacity c_p of the sample for a subsequent calculation of the thermal conductivity. Therefore, additional measurements are necessary, which cause an increased uncertainty by error propagation. The density and specific heat capacity are both interesting to determine for different battery electrodes. However, they are only influenced by the specified composition and not by the microstructure formed by different production processes and, thus, are not of interest for comparing the impact of different processes.

Furthermore, the methods can be divided into stationary and transient methods. For stationary methods, the thermal gradient over the sample is measured in a steady state. Here, the sample is cooled from one side and heated from the other, provoking a heat flow through the sample. For transient methods, the sample is heated by a pulse for a very short time. The heat is conducted through the material and the temperature response on the backside of the sample over time is used to determine the thermal transport properties.

Both approaches have not only been applied on the electrode level, but have also been used for the determination of the effective thermal transport properties of pouch cells [13–15, 21, 22] as well as prismatic and cylindrical hard-case cells [18–20]. However, the present work focuses on dry battery electrodes and, thus, the application for whole cells is not discussed further.

The most common measuring methods for dry battery components that allow the subsequent calculation of the thermal conductivity are the stationary, contact-based guarded hot plate method (GHP) [38–44] and the transient, optical laser flash analysis (LFA) [26–35, 37]. So far, no use of those methods for the investigation of specifically the impact of the production steps or even a comparison of the two methods in view of this specific application is known. Both are used and compared in this work and shall be explained in detail. The following section gives a summary on the literature on this matter and is based on the former publication by Gandert et al. [93].

Guarded Hot Plate Method

The guarded hot plate method – also known as the 1D thermal conductivity meter or the constant heat flux method – was introduced for the first time at the beginning of the 20th century [94, 95]. It was applied to fuel cell and battery components in several studies within the last two decades [39, 41–44, 96].

The general setup of the GHP rig is depicted in Figure 2.5. Here, the sample is clamped between two metallic pistons with a known thermal conductivity which are often made of stainless steel. The sample can consist of one or multiple layers. While the top of the upper piston is heated, the bottom of the lower piston is cooled which provokes a heat flux through the sample. Along the height, thermocouples are incorporated into the pistons at defined positions with constant distances. As the steel exhibits a comparably low thermal conductivity, the thermal gradients within the pistons adopt quantifiable values that enable the calculation of the heat flow through the setup. The pistons are encased in an insulation tube to minimize parasitic heat flows. [96]

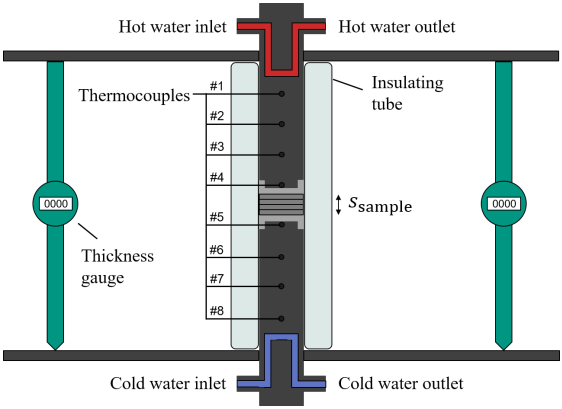

Figure 2.5: Schematic depiction of the measurement device used for the guarded hot plate method (reproduced from Gandert et al. [93], Creative Commons Attribution 4.0 License CC BY).

For the determination of the effective thermal conductivity of the sample, the constant areal heat flux through the pistons, the sample thickness and the temperature difference along the sample are needed. The sample thickness during clamping is measured by one or two micrometers. The areal heat flux can be calculated from the temperatures within the piston according to Equations (2.8) to (2.10) with λ_{piston} being the thermal conductivity of the piston.

$$\dot{q}_{\text{upper}} = \lambda_{\text{piston}} \cdot \frac{T_1 - T_3}{\Delta x_{1-3}} \tag{2.8}$$

$$\dot{q}_{\text{lower}} = \lambda_{\text{piston}} \cdot \frac{T_6 - T_8}{\Delta x_{6-8}} \tag{2.9}$$

$$\dot{q}_{\text{sample}} = \frac{\dot{q}_{\text{upper}} + \dot{q}_{\text{lower}}}{2} \tag{2.10}$$

The numerical indices refer to the thermocouples as specified in Figure 2.5. The underlying assumption of a linear temperature profile is only valid for a sufficient insulation to the environment. Thus, even though the evacuated glass tube provides a fairly good insulation, a mean value of the heat flux in the upper and lower piston should be used [96] to minimize errors from potential heat losses.

The temperature gradient within the sample is equated with the temperature difference between T_4 and T_5 at the tip of the pistons. This is justified by the use of highly conducting plates made of aluminum at the surface of the pistons [96]. The total resistance of the sample including all the contact resistances – towards the apparatus and between the single stacked layers – results from Equation (2.11) [96].

$$R_{\text{total}} = \frac{T_4 - T_5}{\dot{q}_{\text{sample}}} \tag{2.11}$$

Assuming the contact resistances between the different layers of one sample are negligible as stated by Burheim et al. [39, 97], the total resistance can also be described as the sum of the thermal resistance of the sample itself R_{sample} and the contact resistances towards the aluminum plates of the apparatus $R_{\text{Al-sample}}$ as shown in Equation (2.12).

$$R_{\text{total}} = R_{\text{sample}} + 2 \cdot R_{\text{Al-sample}} \tag{2.12}$$

The thermal conductivity of the sample $\lambda_{\text{sample}} = \lambda_{\text{stack}}$ then follows from the thermal resistance and the thickness of the sample according to Equation (2.13).

$$\lambda_{\text{stack}} = \lambda_{\text{sample}} = \frac{\Delta x_{\text{sample}}}{R_{\text{sample}}} \tag{2.13}$$

The stacking of multiple layers and measuring of numerous samples results in a linear system of equations which enables the calculation of the thermal conductivity of the electrode stack λ_{stack}.

Opposed to the LFA, the GHP method has the significant advantage that no knowledge of the mean density and specific heat capacity of the electrode material is required for the calculation of the thermal conductivity [96]. However, the samples need to be stacked and clamped in the apparatus which results in a number of contact resistances between the single layers and components [39]. For a realistic value of the sample's thermal conductivity, these contact resistances need to be quantified or minimized down to a negligible level.

Laser Flash Analysis

Due to the seemingly simple application of the commercially available measuring devices, the LFA found use for the determination of the thermal transport properties of electrodes in recent years [26–35, 37].

However, the general principle behind the LFA was already introduced in 1961 by Parker et al. [98]. In most applications a xenon lamp – as opposed to the laser giving the method its name – shoots a light pulse onto one side of the sample for a short amount of time in the µs-range. Thereby, the surface of the formerly tempered sample heats up and the heat is conducted through the material driven by the now existing temperature gradient. An infrared sensor detects the temperature change on the backside of the sample over the course of time. A schematic of the measurement setup is given in Figure 2.6 (a) beside an exemplary progression of the voltage signal of the detector in Figure 2.6 (b). Herein, the voltage is directly proportional to the temperature change on the backside of the sample.

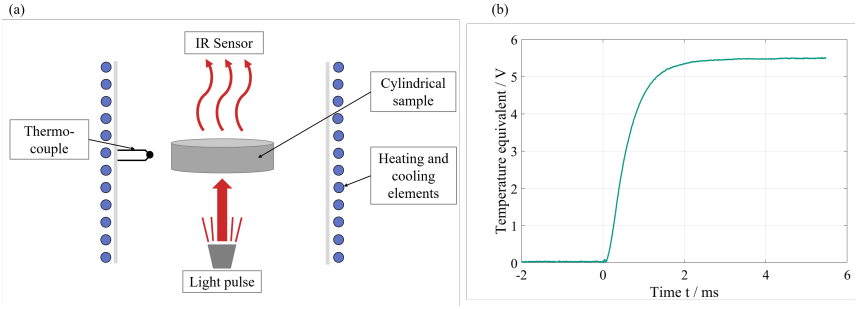

Figure 2.6: Schematic depiction of the laser flash method (a, reproduced from Gandert et al. [93], Creative Commons Attribution 4.0 License CC BY) and exemplary voltage profile which is directly proportional to the temperature change on the backside of the sample (b).

With the derived temperature profile and the known sample thickness, the effective thermal diffusivity κ of the sample can be calculated using Equation (2.14) according to Parker et al. [98].

$$\kappa = \frac{1.38 \cdot s^2}{\pi^2 \cdot t_{1/2}} \tag{2.14}$$

In this, s describes the thickness of the sample and $t_{1/2}$ stands for the half time of the heat-up on the backside of the sample, which is equivalent to the time passed until half of the maximum temperature rise is reached [98]. The half time is derived from the function $T(t)$ that is fitted to the experimental data. There are several approaches for the fit function for T. The most basic approach was developed by Parker et al. [98] for adiabatic conditions. Within the consecutive years, it was extended to account for the impact of convective and radiative heat losses [99, 100]. Further advancements in the 1990s also considered the duration and shape of the light pulse [101], radiative heat transfer in transparent or translucent samples [102] and the light penetration into porous samples [103]. In the latter case, the heat is not absorbed exclusively at the surface but in part also within the material. This kind of absorption entails a non-uniform temperature profile at the start and is also expected for the measurement of battery components like the electrodes or the separator due to their porous character.

Regardless of the model applied for the evaluation of the thermal diffusivity, the effective thermal conductivity λ can be calculated according to Equation (2.15). For this, the mean specific heat capacity c_p and the mean density ρ of the material need to be known.

$$\lambda = \kappa \cdot \rho \cdot c_\mathrm{p} \tag{2.15}$$

An adjusted form of this approach for the application on one-sided coated electrodes is given in Equation (2.16).

$$\lambda_\mathrm{stack} = \kappa_\mathrm{stack} \cdot \left[\rho_\mathrm{s,co} \cdot c_\mathrm{p,s,co} \cdot (1-\phi) \cdot \frac{s_\mathrm{stack} - s_\mathrm{cc}}{s_\mathrm{stack}} + \rho_\mathrm{cc} \cdot c_\mathrm{p,cc} \cdot \frac{s_\mathrm{cc}}{s_\mathrm{stack}} \right] \tag{2.16}$$

It considers the porosity and the more complex geometry of the two-layer sample consisting of different materials. For better understanding, a one-sided coated electrode is schematically depicted in Figure 2.7. In the present case, the pore volume was neglected in the calculation of the mean volumetric heat capacity $\rho \cdot c_\mathrm{p}$ within the square brackets, which is valid for dry electrode samples due to the low density of the gas phase within the pores. Here, the index 'co' describes the coating, 'cc' the current collector, 'stack' the combination of those two and 's' the solid material. The symbol s stands for the thickness of the different components.

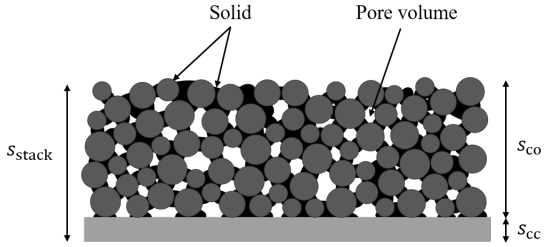

Figure 2.7: Schematic depiction of a one-sided coated electrode consisting of the active material coating and the current collector.

From this, the effective thermal conductivity of the coating λ_co of a one-sided coated electrode can be calculated according to Equation (2.17). It is based on a serial connection of the thermal resistances under neglection of the thermal contact resistance between coating and current collector. Equation (2.17) is also applicable for the calculation of the coating thermal conductivity from the stack thermal conductivity obtained with the GHP method.

$$\lambda_\mathrm{co} = \frac{s_\mathrm{co}}{\frac{s_\mathrm{stack}}{\lambda_\mathrm{stack}} - \frac{s_\mathrm{cc}}{\lambda_\mathrm{cc}}} \tag{2.17}$$

Differential Scanning Calorimetry

As mentioned above, the mean specific heat capacity and density of the electrode material are needed to enable the use of the LFA for the determination of the

thermal conductivity of the electrodes. A common method for the measurement of the specific heat capacity is the differential scanning calorimetry (DSC). The method discussed in the following is the so-called heat flux DSC [104].

The general setup of the measuring chamber is given in Figure 2.8. The measurement chamber has two platforms which carry a sample crucible filled with the material to be investigated and an empty reference crucible. Both crucibles are connected to the heating block denoted as base [104]. Inside the chamber there is an inert atmosphere, usually realized with nitrogen.

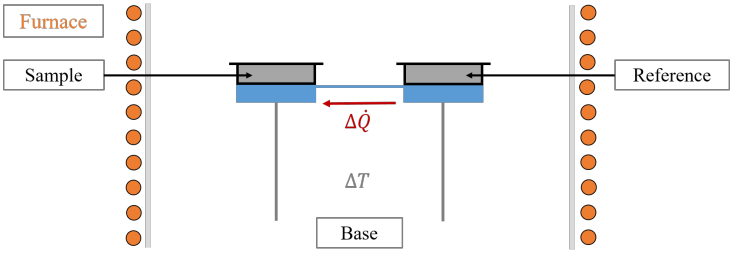

Figure 2.8: Schematic depiction of the DSC setup and operating principle (inspired by NETZSCH-Gerätebau GmbH [105]).

Area thermocouples within the platforms measure the temperature of the sample (T_{sample}) and the reference (T_{ref}), while a third thermocouple measures the temperature at the base (T_{b}). Both crucibles are heated with the same heat flux. However, due to its lower heat capacity, the reference crucible heats up faster which results in a temperature gradient between the sample and the reference. This temperature difference leads to a balancing heat flow between the two crucibles. This heat flow can be calculated according to Equation (2.18). [104]

$$\begin{aligned}\Delta\dot{Q} = &- \frac{T_{\text{sample}} - T_{\text{ref}}}{R_{\text{th}}} + (T_{\text{b}} - T_{\text{sample}}) \cdot \left(\frac{R_{\text{ref}} - R_{\text{sample}}}{R_{\text{ref}} \cdot R_{\text{sample}}} \right) \\ &+ (C_{\text{ref}} - C_{\text{sample}}) \cdot \frac{\mathrm{d}T_{\text{sample}}}{\mathrm{d}t} - C_{\text{ref}} \cdot \frac{\mathrm{d}\left(T_{\text{sample}} - T_{\text{ref}}\right)}{\mathrm{d}t}\end{aligned} \tag{2.18}$$

In this, R_{sample} and R_{ref} describe the thermal resistances between the furnace and the sample crucible or the furnace and the reference crucible, respectively. C_{sample} and C_{ref} describe the absolute heat capacity of the sample and reference crucible, respectively. [104]

The crucibles are identical within the scope of the manufacturing variability. Thus, the difference in the heat capacity stems only from the sample. The calculation of the specific heat capacity of the material follows Equation (2.19) with the sample mass m_{sample}, the heating rate β and the balancing heat flow $\Delta\dot{Q}$. [106]

$$c_{p,\text{sample}} = \frac{1}{m_{\text{sample}}} \cdot \frac{\Delta\dot{Q}}{\beta} \tag{2.19}$$

Gas Pycnometry

The gas pycnometry is often used for the indirect determination of the solid density of powdery materials. In this case, *indirect* means that the method itself allows the measurement of the volume of a sample under deduction of the cavity volume [107], which in combination with the known mass of the sample delivers the solid density of the powder. The mass is usually determined with a high-precision scale.

A schematic of the general operating principle is given in Figure 2.9. The setup consists of two well-defined volumes of the measurement chamber V_{C} and an added volume V_{A}. Prior to the measurement, the whole setup – thus, both V_{C} and V_{A} – is evacuated. The measurement is conducted with inert gas to avoid adsorption [108]. Usually nitrogen or helium are applied for this.

First, the gas is injected through the valve V1 until the desired pressure p_1 is set. After closing V1, the second valve V2 is opened and the gas can expand into the added volume. The occurring pressure p_2 can then be measured and allows the

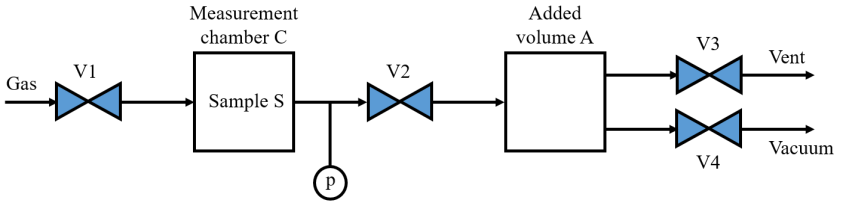

Figure 2.9: Schematic depiction of the setup and operating principle of the gas pycnometry (inspired by Lowell et al. [108].

calculation of the sample volume. For the evaluation, the inert gas is treated as ideal gas, so that the sample volume V_{sample} follows Equation (2.20) [108].

$$V_{\text{sample}} = V_{\text{C}} + \frac{V_{\text{A}}}{1 - \frac{p_1}{p_2}} \tag{2.20}$$

The solid density of the sample then results from Equation (2.21) with the knowledge of the sample mass m_{sample}.

$$\rho_{\text{s,sample}} = \frac{m_{\text{sample}}}{V_{\text{sample}}} \tag{2.21}$$

It should be noted that closed pores within the material are not detected by this method and might lead to minor errors. That is why the powdery sample should not be compressed within the sample holder. [107]

The Different Methods and Conditions in the Literature

A number of analyses of the data for the thermal conductivity of battery electrodes available in the literature have been conducted by several working groups [32, 44, 109–111]. However, the comparability of the values obtained by different measurement methods still poses a large uncertainty. To the best knowledge of the author, no electrode was investigated with more than one measurement method in a comparable way. The only known study using two different methods

for determining the thermal conductivity of battery electrodes is the one by Koo et al. [28]. Here, the LFA technique was used to determine the through-plane value and the "hot disk" method was used to measure the in-plane value. As battery electrodes coated on metallic current collectors show a highly anisotropic behavior, those measurements do not provide meaningful data for the comparison of the measurement methods.

To give a basis for the analysis conducted in the present study, an overview of the literature data shall be given. As the LFA is in the focus of this work and compared to the GHP as alternative method, particularly values obtained by those two methods were gathered for the comparison. In case several data points were available from one source, values at room temperature of 20 °C to 25 °C and a state of charge (SOC) of 0 % were preferred. The samples were assumed to be at beginning of life (BOL) if not stated otherwise, as they were either taken from new commercial cells or directly from the production line. Furthermore, only values obtained for dry electrodes were used and the effective thermal conductivity of the AM coatings was compared. If only the through-plane thermal conductivity for the electrode stack with the current collector was given, the coating value was calculated assuming a serial connection of the resistances and a thermal conductivity of the current collector foil of 236 $\mathrm{W{\cdot}m^{-1}{\cdot}K^{-1}}$ for aluminum and 400 $\mathrm{W{\cdot}m^{-1}{\cdot}K^{-1}}$ for copper.

The collected data are depicted in Figure 2.10, divided by the AMs used in the electrode coatings [26, 30–34, 39, 41–44, 110, 112, 113]. At this, it is distinguished between lithium cobalt oxide (LCO) and lithium nickel-manganese-cobalt oxide (NMC) as cathode AMs and graphite (Gr) as anode AM. NMC summarizes different compositions like NMC111 and NMC622. The single data points used and their individual references are given in the Tables A.1, A.2 and A.3 in the Appendix.

The evaluation shows a tendency towards higher values obtained with the LFA in comparison to the GHP method. However, the strong scattering of the literature data makes a sound statement difficult. In general, it can be assumed that the employed additives, the present particle size distribution and electrode porosity

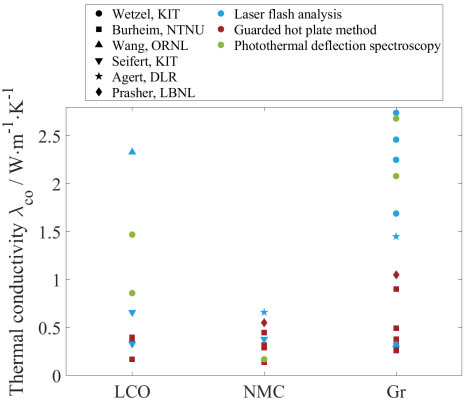

Figure 2.10: Literature data for the thermal conductivity of the dry electrode coating of battery electrodes measured with LFA, GHP and photothermal deflection spectroscopy [26, 30–34, 39, 41–44, 110, 112, 113] (reproduced from Gandert et al. [93], Creative Commons Attribution 4.0 License CC BY).

have a stronger impact on the effective thermal conductivity than the AM itself. This information is, however, often not known for the literature data.

For the LFA samples a porosity range of 19 % to 46 % can be assumed from the few known values [31, 33]. This already strong variation is further enhanced by the large uncertainty of porosity values in battery research as discussed in Section 2.1.1.

Furthermore, the composition is unknown for most of the electrode samples. Thus, it is unclear if the tendency in Figure 2.10 stems from the differences in the measurement methods or rather the variation in the samples. This question shall be elucidated within this thesis.

Additionally, Figure 2.10 shows an especially strong scattering for the values obtained by LFA. Some authors questioned the validity of LFA measurements of electrode materials [39, 114]. However, it is yet to be clarified, if the possible errors just originated from the stacking of the different materials or if the LFA

measurements in general lead to unrealistic values for the porous battery components. Thus, this study aims at giving a better insight into the application of the LFA for the investigation of battery components.

In addition to the discussed impact of the measurement method, the pore-filling fluid has a significant influence on the measured thermal conductivity. Several authors compared the thermal conductivity of dry and soaked electrodes extracted from the same cell [39, 41–44]. Electrolyte or just the electrolyte solvent within the pores leads to higher values than a gaseous phase in general. The data from the literature for electrode coatings is depicted in Figure 2.11. A breakdown of the single data points and references is given in Table A.2 in the Appendix.

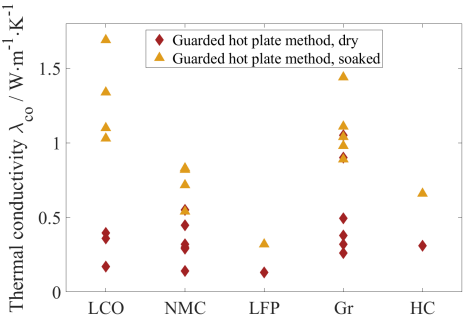

Figure 2.11: Literature data for the thermal conductivity of the dry and soaked electrode coating of battery electrodes measured with the GHP [39, 41–44].

Here, only data measured with the GHP method were chosen, as it was shown above that the measurement method might have a significant impact on the obtained results and the most data is available for GHP. Wherever possible the values for electrodes at BOL and an SOC of 0 % were used in compliance with the analysis above. The publications provide data for LCO, NMC, and lithium iron phosphate (LFP) as cathode active materials.Figure 2.11 shows that the measured thermal conductivity of soaked electrodes is generally higher than that of the dry electrodes. This is also true for all the single values from the mentioned studies

[39, 41–44]. In extreme cases the values of the soaked electrodes are a factor of 6 higher than the dry values for cathodes. This maximum factor is 4.3 for anodes. The same influence was investigated by Bazinski et al. [15] on cell level, which showed the same effect of a higher effective thermal conductivity with electrolyte in comparison to the dry state.

Furthermore, in various studies the pressure applied to the electrodes during thermal conductivity measurements with the GHP method was varied [41, 42, 44]. In this, both dry and soaked electrodes were compared. The collected data is shown in Figure 2.12. The single data points and according references are given in Table A.4 and Table A.5 in the Appendix.

In accordance with Figure 2.11 the soaked electrodes have significantly higher absolute values of the thermal conductivity as demonstrated in Figure 2.12 (a) and (c). The relative evolution of the thermal conductivity with increasing pressure normalized to the thermal conductivity at the lowest available pressure of 2 bar or 2.3 bar, respectively, is given in Figure 2.12 (b) and (d). Especially the normalized plot suggests an increase of the thermal conductivity with increasing pressure for both the dry and soaked electrodes. However, the relative increase in thermal conductivity is significantly higher for the dry electrodes with up to 100 % increase between 2 bar and 11.5 bar for graphite in comparison to only up to 55 % increase for the soaked electrodes. From the depiction it is evident that the better conducting materials – namely graphite and LCO – in general experience a stronger relative increase in thermal conductivity.

The significance of the electrolyte for the thermal conductivity is made clear in Figure 2.13, which exhibits the relative increase in thermal conductivity by adding electrolyte solvent for different active materials and at different pressures. It should be noted that all soaked measurements have been conducted with the GHP method and that the comparison is only valid for this method.

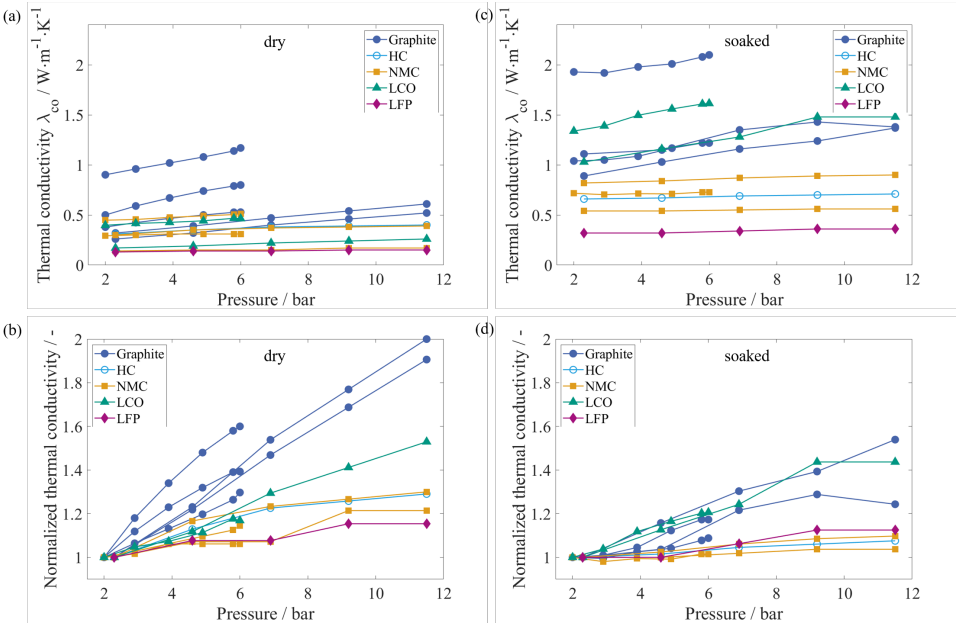

Figure 2.12: Evaluation of literature data for the thermal conductivity of electrode coatings at different pressures measured with the guarded hot plate method. (a) Absolute values and (b) data normalized to the thermal conductivity at 2 bar or 2.3 bar of the dry electrodes. (c) Absolute values and (d) data normalized to the thermal conductivity at 2 bar or 2.3 bar of the soaked electrodes.

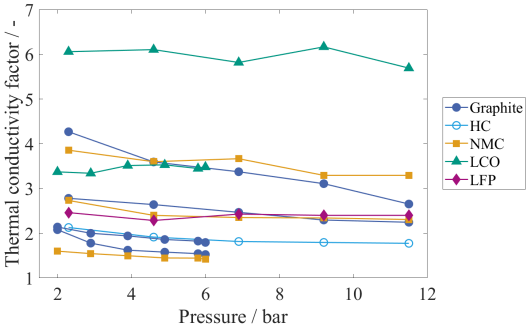

Figure 2.13: Thermal conductivity factor of the electrodes measured with the GHP method in the literature describing the ratio of the thermal conductivity of the electrodes soaked with electrolyte solvent to the thermal conductivity of the dry electrodes $\lambda_{co,soaked}/\lambda_{co,dry}$.

2.2 Electrode Production

The following section will provide an overview on the production steps from the raw materials to the final electrode. There are multiple review papers on the production steps themselves and possible developments in the future [25, 47, 48], however, in this work not only the state-of-the-art materials and process parameters shall be considered, but also their impact on the final electrode in view of their thermal transport properties. This includes the investigation of the microstructure as well as mechanical and electrical properties of the electrodes presented in the previous section, as those represent the microstructural changes in the material that occur during the process and might explain the thermal behavior as well. Furthermore, the few known approaches to describe the impact of the production steps on the thermal conductivity are discussed.

The sequence of the single steps of electrode production is given in Figure 2.14. Before the actual production, the formulation needs to be specified. This includes the selection of the AM, the binder system and the conductive additive, as well as the definition of the target composition and solvent amount and potentially the choice of a specific mean particle size of the AM. The production is started with

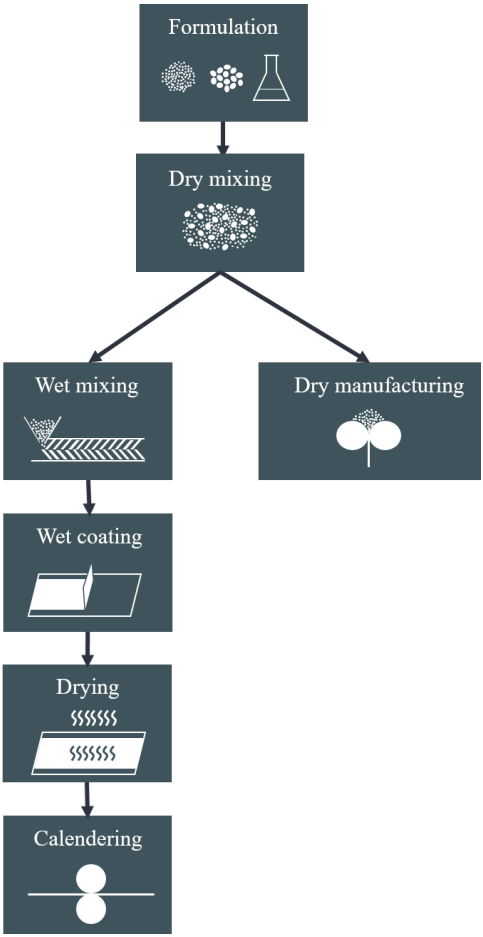

Figure 2.14: Schematic depiction of the sequence of the processes used for electrode production. Left: wet processing route. Right: dry manufacturing.

the mixing of the dry components. For the conventional electrode production, the dry mixture is then dissolved in a solvent, which in some cases already contains the polymeric binder. The slurry obtained from the wet mixing process is then coated onto an aluminum or copper foil. During the drying, the porous electrode structure is formed and the AM particles are fixated by the binder phase. After the drying, the electrodes still have a relatively high thickness and porosity. To increase the energy density of the electrodes, the dried electrodes are subsequently compressed in the calendering step, reducing both, the thickness and porosity of the electrodes.

An alternative processing route is the dry manufacturing of the electrodes. In this case, the dry mixture is directly coated onto the current collector without adding any solvent. This work only considers dry manufacturing approaches using a calender.

As some process steps influence each other and are investigated in combination in some sources, it is in parts difficult to discuss them individually. E. g. an effect can originate from the formulation but its influence is only truly reflected in a later step. In these cases, the influencing factors are explained later on.

2.2.1 Formulation

Although the formulation does not constitute an actual production step, the regulation of the slurry composition has a significant impact on the properties of the final electrode. In the following, common constituents of lithium-ion battery (LIB) and sodium-ion battery (SIB) electrodes are introduced and their impact on the microstructure and mechanical, electrical and thermal properties of the electrodes is discussed.

The anodes of LIBs are usually made of graphite as AM. Here, a distinction is made between natural and synthetic graphite [115]. While both types of graphite generally consist of polycrystalline particles, the single crystals in natural graphite show an orientation in a particular direction while those in synthetic graphite are

more randomly oriented [115]. The properties and advantages of both forms are discussed in detail in the study by Gottschalk et al. [116].

The composition applied in commercial batteries is slowly transforming from pure graphite anodes to silicon-graphite (Si-C) electrodes, with a low, but in recent years increasing fraction of silicon added to the graphite to increase the capacity [78]. However, due to its huge volume expansion during cycling [117, 118] and the consequential fracture of the active material particles [119] and capacity fade [120], Si still poses challenges for industrial and long-term use.

In the case of stationary applications or very strict safety requirements, lithium titanium oxide (LTO) is more often used as anode active material due to its higher intrinsic safety [24]. LTO, however, has only approx. half the theoretical specific capacity of the commonly used graphite [121].

Another anode material, that has been applied for both, LIB and SIB applications, is hard carbon. For LIBs it is generally coated on a copper current collector, while for SIBs it is coated on aluminum. In comparison to the layered structure of graphite, hard carbon has a highly disordered structure of graphene layers, which results in a higher theoretical capacity [122]. Hybrid anodes made of graphite and hard carbon showed a potential for high-power applications due to their great long-term cycling performance during fast-charging [123].

Standard active materials of LIB cathodes are lithium metal oxides. Those include lithium cobalt oxide (LCO), lithium manganese oxide (LMO), lithium nickel-manganese oxide (LNMO), lithium nickel-manganese-cobalt oxide (NMC), and lithium nickel-cobalt-aluminum oxide (NCA) as well as blends of the different materials. Due to the resource scarcity – mainly concerning cobalt [124, 125] – and the inferior performance of LMO in terms of capacity [126] and lifetime [127], the trend is going towards nickel-rich cathode materials. This leads to a change in composition from NMC111 over NMC532 and NMC622 to NMC811 and beyond with the numbers describing the molar fractions of the single metal oxide components. Furthermore, lithium iron phosphate (LFP) is experiencing a comeback as cobalt-free AM [128, 129]. While it has a significantly lower energy

density than the layered oxides, it shows advantages with a good rate capability and a much better material availability [129].

The fraction of the AM within the coating usually makes up between 80 wt.% and 96 wt.% depending on the AM itself, the used production processes and the intended application [47, 48]. The highest fractions are achieved with commercial electrodes, while electrodes produced on lab-scale often have lower AM fractions. The additional share is taken up by the binder, possibly in combination with a thickener, and conductive additives. Industrial production generally works with AM fractions in the upper range.

The most common binder for water-based electrode slurries is styrene-butadiene-rubber (SBR) in combination with the thickener carboxymethyl cellulose (CMC), which is mainly used for anode materials like graphite, Si-C and hard carbon [73, 78, 130]. The processing of many cathode active materials with water still poses challenges like the corrosion of the aluminum current collector foil due to the high pH of the slurries [131–135]. Although pH-control during water-based processing of nickel-based cathodes led to promising results [131, 134, 135], a combination of N-Methyl-2-pyrrolidone (NMP) as solvent with polyvinylidene fluoride (PVDF) as binder still constitutes the default processing route.

To enhance the electrical conduction through the otherwise fairly insulating binder phase, conductive additives are added to the slurry. The most important and widely spread additive is carbon black (CB), which exists in many different forms [136]. The significantly smaller particle size in comparison to the active material particles allows the formation of good particle-particle contacts and the establishment of new pores in the order of 40 nm to 300 nm depending on the degree of dispersion of the carbon black agglomerates [80]. Especially for cathodes, e. g. NMC as AM, carbon black is sometimes complemented by conductive graphite (CG) [61, 80, 137, 138]. Due to its larger particle size in comparison to CB [61, 130, 137], it helps to build long-range pathways and thereby enhances the electrical conductivity of the electrodes [138].

As binder and conductive additives constitute electrochemically inactive material (IM) and thus reduce the capacity and energy content of the electrode and

thus the whole battery cell, the fraction of those components should ideally be low. However, they are indispensable to reach a decent mechanical stability, electrochemical performance and thus a good long-term stability of the electrodes [139, 140]. Deficient amounts of binder lead to handling difficulties [140] as they can result in the delamination or breakage of the coating, whereas reduced amounts of carbon black and conductive graphite entail a higher electrical resistance [61]. It is especially important to set the ratio of those two components right, as the binder has an electrically isolating effect and may even counteract the positive effect of the carbon black. Therefore, there is several research known investigating the impact of a variation of the IM fraction of the whole system as well as a variation of the ratio between binder and carbon black on the electrochemical performance and processability of the electrodes [61, 90, 141, 142].

The applied fraction of binder and conductive additives varies widely in the literature. Common values lie between 2 wt.% and 10 wt.%, respectively [143, 144], whereby the ratio of CB to binder usually is in the range of 0.2:1 to 1:1.

Another parameter that is defined by the material composition, is the particle size of the active material and its distribution. Here, it is crucial to find a good compromise between larger and smaller particles because both have their own benefits. The particle size distribution also has a significant impact on the effects occurring during the mixing, drying and calendering process.

Microstructural Effects

A lower mean particle size of the AM generally results in a significantly reduced modal value of the pore size [73] and a lower electrode porosity after drying [73, 116]. This is, though, also dependent on the width of the particle size distribution, with a wider distribution generally resulting in a lower porosity [145]. The same appears for a bimodal mixture of the larger and smaller particles [116].

The studies in the literature are inconclusive regarding the impact of the binder and additive fractions on the porosity of the dry electrode. While a higher binder-carbon black (BCB) fraction led to a reduced porosity in the study by Meyer et

al. [140], a higher additive fraction led to an increased porosity in the study by Bauer et al. [61]. Either the binder and CB particles fill the voids between the AM particles since they are much smaller than the AM particles. This often results in a bimodal pore size distribution with pores in the µm-range between the AM particles and much smaller pores in the 100 nm-range within the BCB network [80, 146]. Or the binder and CB accumulate at the contact points between the AM particles and thereby increase the distance between the particles and thus the porosity.

Some studies also investigated graphite as conductive additive in NMC cathodes. The graphite particles have a mean particle size in the lower µm-range and thus lie between the AM and BCB particles in size. Therefore, they fit well into the spaces between the NMC particles resulting in a reduction of the modal value of the pore size. Moreover, the overall porosity of the electrodes is reduced. [90]

Mechanical Effects

The impact of the mean particle size of the active material on the mechanical properties still raises questions. As shown in Figure 2.15, Klemens et al. [73] demonstrated a higher adhesion strength between coating and current collector for smaller particles of hard carbon and especially when dried at high drying rates.

Gottschalk et al. [116] showed the exact opposite. Here, smaller particles of graphite as AM resulted in a lower adhesion strength between coating and current collector. This suggests that the effect of the particle size might depend on the material investigated.

The choice in the binder also has a significant impact on the mechanical stability of the final electrode. Polymer binders with higher molecular weights tend to build more complex binder networks [47] and are less prone to binder migration away from the current collector. Therefore, electrodes produced with binders with a higher molecular weight exhibit a higher adhesion strength between coating and current collector [66].

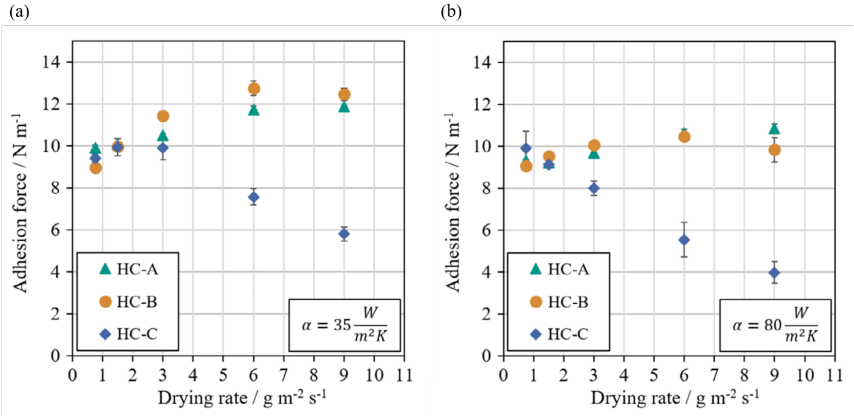

Figure 2.15: Adhesion strength of HC anodes with different AM particle sizes (HC-A < HC-B < HC-C) dried with different drying rates and constant heat transfer coefficients of (a) 35 $W \cdot m^{-2} \cdot K^{-1}$ and (b) 80 $W \cdot m^{-2} \cdot K^{-1}$ (reproduced from Klemens et al. [73], Creative Commons Attribution 4.0 License CC BY).

Moreover, the amount of binder effects the adhesion strength as well. Several studies investigated the impact of the binder content. While increasing the IM content, they kept the mass ratio of CB to binder constant at 1:1 [140] or 0.5:1 [64]. Meyer et al. [140] were able to show an increase of the adhesion strength with increasing IM content. However, the results by Westphal and Kwade [64] suggest that the adhesion strength not only increases but approaches an asymptote with increasing IM content. Thus, at some point a further increase is not beneficial. Besides that, too high IM contents lead to an impaired electrochemical performance.

The influence of a varied additive content can also be observed in the elastic deformation work, which also increases and approaches an asymptote with increasing IM content [64]. This is in line with the assumption that a higher binder content in the top layer of the coating results in a higher elasticity and thus a higher ratio of the elastic deformation work in the measurement. However, this effect also seems to be limited at some point.

Electrical Effects

From an electrical point of view, smaller AM particles are often detrimental. Within the same path length, smaller particles exhibit a higher number of particle-particle contacts which leads to higher overall contact resistances within the electrode and therefore a reduced electrical conductivity [116]. In addition, smaller AM particles also entail a lower mean pore size, which increases the resistances for the ion transport. The use of smaller AM particles thus results in a lower ionic conductivity [116].

Furthermore, the enhanced active surface area of the smaller AM particles leads to a higher non-reversible lithium loss during the formation of the solid electrolyte interface (SEI), as Kumberg et al. [83] discovered for graphite anodes. A similar effect of an increased capacity loss for smaller AM particles was also observed for hard carbon SIB anodes by Klemens et al. [73].

However, smaller AM particles can also be of advantage at higher C-rates. For the electrodes with the larger AM particles, the ion transport is more and more controlled by the solid-state diffusion with increasing C-rate. Due to their shorter paths for solid-state diffusion the electrodes with smaller AM particles exhibit a much higher discharge capacity at C-rates up to 5C. [147]

While the binder content is of high importance for the mechanical stability of the electrodes, the additive content is crucial for a good electrochemical performance. Uncalendered NMC electrodes without any CB did not show a reasonable cycling behavior due to the high electrical resistances [90]. This was also true for electrodes in which graphite has been applied as conductive additive instead [90].

Bauer et al. [61] investigated the electrical resistance of NMC electrodes produced with different compositions. An increase of the CB content from 5 wt.% to 9 wt.% resulted in a significant reduction of the electrical resistivity for the whole porosity range investigated. An increase of the content of the graphite additive from 5 wt.% to 10 wt.% with a constant CB content of 4 wt.% showed a similar, however, less pronounced effect.

Westphal and Kwade [64] increased both the CB and binder content with a constant weight ratio of 0.5:1. They also observed a decreasing absolute electrical resistance with increasing CB content for electrodes with a constant thickness.

Thermal Effects

In terms of the thermal effects, Maleki et al. [26] and Sangrós et al. [49] were able to demonstrate an impact of the mean particle size on the effective thermal conductivity of electrode coatings. Both showed an increase of the thermal conductivity with increasing particle size for graphite as AM. The study of Maleki et al. [26], moreover, exhibits that this increase is less pronounced for higher fractions of CB in the electrode mixture, as the resistances between the AM particles are thereby reduced.

2.2.2 Dry Mixing

Concerning the dry mixing step, two purposes can be distinguished. On the one hand, dry mixing of the powdery materials is used as pre-homogenization for the subsequent wet mixing step [66, 80, 148, 149]. On the other hand, by dry mixing, a homogeneous powder is prepared for a following dry manufacturing process [92, 150, 151].

In both application cases, dry mixing with a sufficient speed of the mixing tool results in the de-agglomeration of the carbon black [61, 66, 80, 148, 149, 152]. Kumberg et al. [83] showed that dry mixing in a kneader can also result in the reduction of the size of the AM particles.

Before the mixing step, CB is usually present in a highly agglomerated form and the secondary particles need to be broken down into finer particles. Performing a longer dry mixing step is expected to result in a more homogeneous distribution of the CB. Opposed to the larger secondary CB particles which fill the space

between the AM particles and accumulate at the electrode surface, the highly de-agglomerated CB particles rather deposit at the surface of the AM particles. SEM images for the different dry mixing times are given in Figure 2.16. The electrodes produced with dry preprocessing show a much more homogeneous distribution of the binder [61]. A similar behavior was found by Bockholt et al. [80].

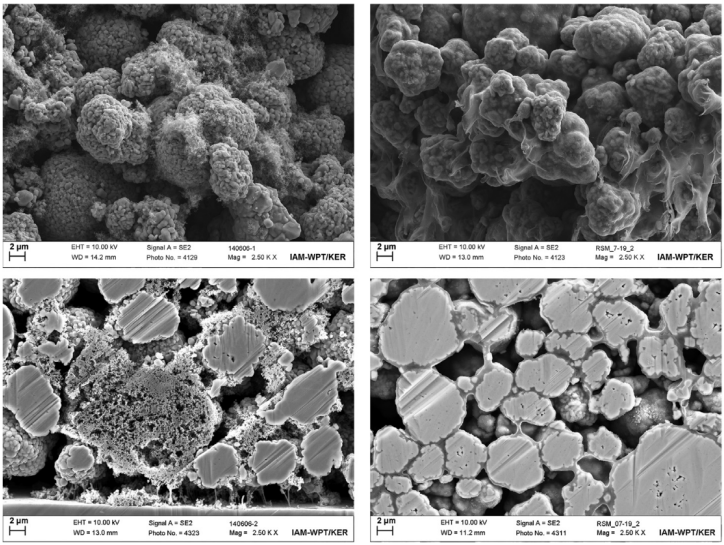

Figure 2.16: SEM images of a ruptured surface (top) and an ion-etched cross-section (bottom) of NMC cathodes produced with conventional dissolver mixing (left) and additional dry preprocessing (right) of the NMC and CB (reproduced from Bauer et al. [61], Copyright 2015, Elsevier, reproduced under the license number 6135260942067).

The de-agglomeration of the carbon black, furthermore, leads to changes in the bimodal pore size distribution of the produced electrodes. The peak describing the pores between the CB particles in the pore size distribution gets smaller and moves to smaller pore diameters with increasing dry mixing time. At the same time, the peak of the pores between the AM particles moves to higher pore diameters and the larger pores become predominant [148].

This was found to enhance the cohesion of the electrode [80] and is thus preferable from a mechanical point of view. However, the electrical properties are impaired by excessive mixing. Bauer et al. [61] and Bockholt et al. [80] showed that although intensive dry mixing results in a lower electrical resistivity on powder level, it entails an increase in the electrical resistivity on electrode level.

Moreover, the intensive dry mixing resulted in a drop of the specific discharge capacity of uncalendered NMC cathodes [90]. The electrodes with only CB and no graphite as conductive additive showed no reasonable cycling performance due to a lack of long-range electric pathways [90].

For the dry mixing as preparation for the dry manufacturing not many studies are known. Gyulai et al. [92] only measured the resistivity of the powder mixtures which is not representative for the final electrode [61, 80]. However, they also conducted cell tests which revealed the highest discharge capacity for the electrode made from the powder mixed with the highest intensity for the whole range of C-rates from C/20 to 3C.

2.2.3 Wet Mixing

The wet mixing of the slurry is generally conducted with dissolvers with sawtooth impellers or planetary mixers [152–154]. Here, the solvent, binder and powder mixture are mixed and homogenized in a batch process. This approach has proven efficient and is common in commercial battery production at present.

However, new processing approaches gained interest in recent years. Those include the slurry mixing with extruders. In contrast to the above mentioned procedures, this production process can be operated continuously [154]. Thereby, it allows an optimum inter-connection with the subsequent continuous steps of coating, drying and calendering and leads to significant cost savings [155] as well as a reduction in the process time by a factor of 6 [154]. Moreover, the solvent content can be reduced in comparison to the dissolver mixing, resulting in reduced material costs and energy savings during the drying step [156, 157].

The focus of the present work is on the extruder mixing as it poses the leading-edge approach for the mixing of electrode materials. Thus, only studies on extruder mixing or the results of studies on conventional mixing that are assumed to be transferable to extruder mixing are discussed here.

Microstructural Effects

The mixing step influences the distribution of the binder and additives in the final electrode [66]. A good embedment of the AM particles within the BCB matrix is much more relevant for the cathode since the specific electrical conductivity of graphite as most commonly used anode material is much higher than that of typical cathode AMs [146].

Meza Gonzalez et al. [54] demonstrated that the screw design and rotation speed have a significant impact on the filling degree and material distribution within the extruder during mixing and thereby influence the dispersion and de-agglomeration of the particles. An increased rotation speed of the screws results in an increased specific energy input [158] and a stronger de-agglomeration of the CB particles which is reflected in the particle size distribution by an increased peak for particles with a diameter lower than 1 µm also called fines [54, 159].

Suspensions with a high solid content that exhibit a high viscosity might be of advantage for the extrusion process. The high particle concentration prevents significant sedimentation of the large AM particles due to the increase in viscosity [155] and enables a sufficient de-agglomeration of the CB secondary particles. Moreover, the high viscosity entails a good edge contour accuracy during coating [160] and restricts the binder migration during drying [155].

In this context, Haarmann et al. [155] demonstrated an increasing de-agglomeration of the CB with increasing solid content of the slurry. The highest tested solid content of 80 %, however, resulted in the attachment of the small CB particles onto the surface of the larger NMC particles. In the particle size distribution, this is reflected by a much smaller CB peak in comparison to the mixtures with lower solid content.

Mechanical Effects

In accordance to the microstructural properties, the adhesion strength is influenced by the screw design and rotation speed as well [158]. In the case of the binder being presolved in the solvent before being fed to the extruder, which is in line with the investigations conducted in the present work, a higher rotation speed seems to be beneficial.

For NMC cathodes with PVDF binder, Haarmann et al. [155] showed that an increase of the solid content from 65 % to 75 % results in an enhanced cohesion of the coating and is thus beneficial from a mechanical perspective.

Electrical Effects

With the de-agglomeration of the CB, the mixing process also influences the CB distribution within the electrode and the formation of an electrically conductive network [61]. A sufficient dispersion of the CB is crucial for the electrochemical performance of the electrodes and might even allow the application of a lower binder content [161]. However, former studies that did not use extruder mixing suggest that an excessive dispersion results in a higher electrical resistance of the electrodes [61, 80] and a poor cycling performance [90] and should thus be avoided.

The specific electrical resistance of the uncalendered electrodes decreases with increasing solid content from 65 % to 75 % according to Haarmann et al. [155]. However, electrodes produced from a slurry with a solid content of 80 % showed a resistance as high as that of the 65 % electrodes. This might be explained by the attachment of the CB particles to the AM particle surface [155].

Thermal Effects

No investigation of the impact of variations in the wet mixing process on the thermal transport properties are known to the author.

2.2.4 Wet Coating

The wet coating of electrodes using doctor blades or slot dies presents the main procedure for the setting of the electrode coating thickness according to the aspired application. While the wet film thickness is directly determined by the gap of the doctor blade or the volume flow through the slot die, the thickness of the dried coating highly depends on the solvent content within the slurry and the porosity of the formed dry layer. By fabricating thicker layers of the electrochemically active coating and keeping the thicknesses of the inactive separator and current collector constant, higher energy densities can be reached [47]. However, higher coating thicknesses result in a higher electrical resistance of the electrode, which is why an optimum needs to be found for every particular application. Electrodes used in high-power cells are rather thin and porous, combined with comparatively thick current collectors, leading to lower electrical resistances but also lower energy densities, while high-energy cells usually come with thick electrode coatings with relatively low porosities [162].

Coating and drying are closely linked processes. Many influencing factors only become apparent after the drying of the electrodes and are also impacted by the drying conditions. Therefore, they are discussed in the subsequent section.

Microstructural Effects

Several studies indicate a decreasing porosity of the dried coating with an increasing coating thickness [74, 140, 163, 164]. In the most recent study, Klemens et al. [74] stated that this effect is not influenced by the drying rate. Instead, it is assumed that the gravimetrically obtained porosity is defined by the edge effects at the bottom and top of the coating [74]. At the bottom, the particle structure is constricted by the current collector, leading to a less dense package and a higher porosity in this area. A similar behavior can be found at the surface of the coating although it has no physical restriction. The thicker the coating is, the less significant does this effect get, leading to a reduction of the porosity and the approaching of an asymptotic value.

Mechanical Effects

It was found that the mass loading, which is directly proportional to the coating thickness, has an impact on the adhesion strength [64, 66, 74, 79, 140, 165] and elastic deformation work [64] of the electrodes. Klemens et al. [74], for example, have shown that the adhesion strength drops with increasing coating thickness, in case of Figure 2.17 represented as the areal capacity.

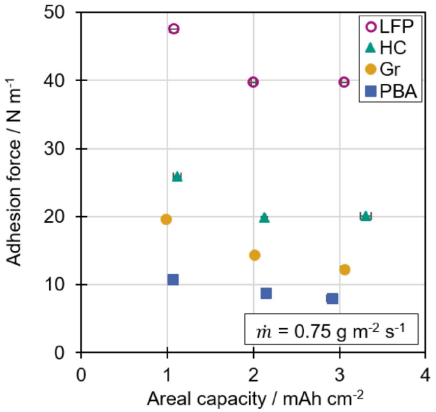

Figure 2.17: Adhesion strength of hard carbon (HC), prussian blue analogue (PBA), LFP and graphite electrodes (reproduced from Klemens et al. [73], Creative Commons Attribution 4.0 License CC BY).

However, this impact of the coating thickness only becomes apparent during drying and the severity of the mechanical effects is determined by the drying conditions. This is why these effects are mainly discussed in Section 2.2.5 in the context of the drying process.

Electrical Effects

Westphal and Kwade [64] observed an influence of the mass loading and, thus, the coating thickness on the specific electrical resistance of the electrodes. However,

this is again also dependent on the drying conditions and is therefore covered in the following section.

While the theoretical capacity of the electrodes is increased with an increasing AM mass loading, the usable capacity depends on the structure of the electrode and the applied C-rate. Thicker electrodes exhibit longer paths for both the lithium-ions and the electrons, which reflects in elevated ionic [166] and electrical resistances. For higher C-rates, this leads to a plummeting of the specific discharge capacity with increasing electrode thickness [167–170]. The general influence of longer pathways is accompanied by superimposing effects of the drying process as discussed below.

Thermal Effects

At present, no investigation of the impact of variations in the coating process on the thermal behavior of the electrode is known to the author.

2.2.5 Drying

As already mentioned in Section 2.2.4, low coating thicknesses are desired for high-power cells, while high electrode thicknesses are common for high-energy cells [162]. However, the latter ones – equated with high mass loadings – pose challenges for the drying process.

Besides the formation of cracks within the coating, the pivotal, undesired effect occurring during the drying of battery electrodes is the so-called binder migration presented in Figure 2.18 [64, 171, 172]. Binder migration means the effect that the binder and other additives are dragged towards the surface of the electrode during drying, leading to a concentration gradient within the coating [173]. This effect is increasingly strong for higher mass loadings, as the time to fixation and structure immobilization is longer [79]. Some influencing factors from the formulation to the coating step only become evident during drying, as the severity of binder

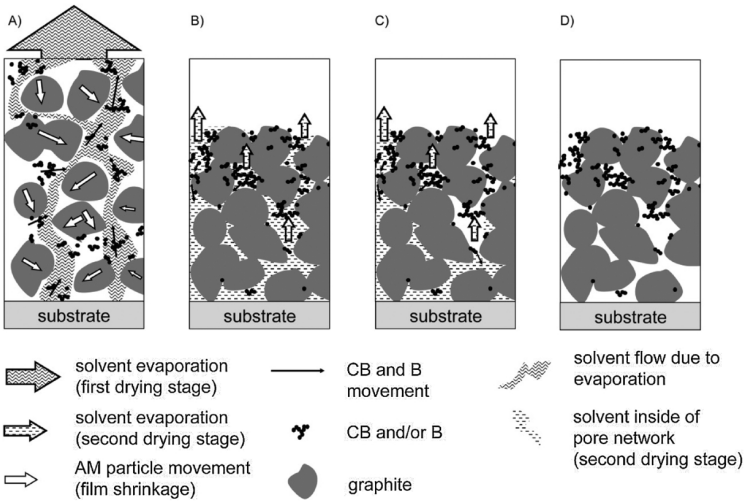

Figure 2.18: Schematic depiction of the binder migration during electrode drying (reproduced from Westphal and Kwade [64], Copyright 2018, Elsevier, reproduced under the license number 6135261301190).

migration varies, e. g. with coating thickness and the particle size of the active material. Furthermore, the extent of binder migration can vary with the used binder and active material [48, 74]. The binder migration can be substantiated by several experimental methods. It is especially important for the electrochemical performance of the battery cells due to its impairment of the electrical and ionic conduction within the electrodes.

As the drying process poses the most energy-intense production step, several new drying technologies – such as infrared (IR) or radiation drying [174] – have been developed and tested in recent years to reduce the energy consumption [175]. They might also lessen the binder migration [174]. However, the focus of most published research is still on convective drying with a preheated gas flow and/or on a heated plate as the standard method, which is also the common drying method used for the electrodes investigated in this work.

The drying rate may either be set by adjusting the volume flow and thereby the heat transfer coefficient or the temperature of the air flow and thereby the thermal gradient as driving force for the evaporation of the solvent.

Microstructural Effects

Müller et al. [63] and Westphal and Kwade [64, 176] used EDX in combination with SEM to visualize the distribution of PVDF binder within graphite electrodes. In doing so, a positive gradient of the binder concentration from substrate to surface was found as shown in Figure 2.19.

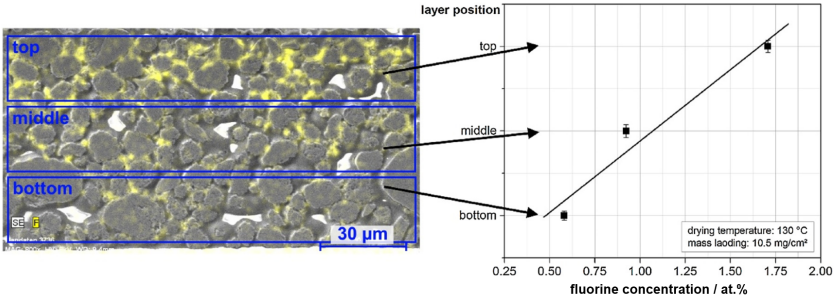

Figure 2.19: Results of the EDX analysis of a graphite anode showing the distribution of fluorine from the PVDF binder within the coating and the derived concentration within the different layers (adjusted from Westphal and Kwade [64], Copyright 2018, Elsevier, reproduced under the license number 6135261301190).

Müller et al. [63] compared two samples produced at different drying rates of 1 $g \cdot m^{-2} \cdot s^{-1}$ and 2.8 $g \cdot m^{-2} \cdot s^{-1}$ and comparably high dry film thicknesses of 400 µm. The sample dried with a high rate showed an increased fluorine – and thus binder – concentration at the surface and a lower concentration at the interface towards the current collector in comparison to the sample dried with a low rate. Investigations at different drying temperatures by Westphal [176] indicate higher gradients for $T \geq 110\,°C$ in comparison to 80 °C at a constant mass loading of 10.5 $mg \cdot cm^{-2}$. Those results were also validated with LIBS [64].

This concentration gradient could be found for different binder systems like PVDF and CMC-SBR [63, 64, 79, 171, 177]. It is expected that the findings are adaptable to different recipes as long as the dominant forces and interactions between the different particles and materials are comparable. Thus, they are assumed to also apply to the recipes used in this work.

However, EDX and LIBS present two elaborate methods. As an alternative, adhesion strength measurements are solely used in most studies.

Mechanical Effects

The most common method to investigate the mechanical effect of drying is the measurement of the adhesion strength between the coating and the current collector. As described in Section 2.1.2 there are different approaches to quantify the adhesion strength. Those methods are not distinguished or put in relation here, but in general show similar effects.

It is difficult to differentiate between the influences of drying rate, drying temperature, mass loading and other contributing factors like particle size and particle structure as they all interact with each other [64, 71, 73, 74, 79, 172, 176].

If the surrounding conditions are not adjusted accordingly, an increase in the temperature is accompanied by an increase in the drying rate. Initial studies in this context [79, 172] suggested a decrease of the adhesion strength with an increasing temperature and drying rate for both, PVDF and CMC-SBR binder systems. Further studies indicate a more complex behavior with respect to a variation of the mass loading. Westphal conducted a comprehensive study on graphite anodes with PVDF binder and considered seven different mass loadings from 2.7 $mg{\cdot}cm^{-2}$ up to 12 $mg{\cdot}cm^{-2}$ and three different drying temperatures [176]. The results are reproduced in Figure 2.20. At the lowest temperature of 80 °C no significant difference in adhesion strength could be found for the variation in mass loading. It is assumed that the driving force for the movement of the binder towards the surface of the coating is not sufficient for a segregation of the components here [176].

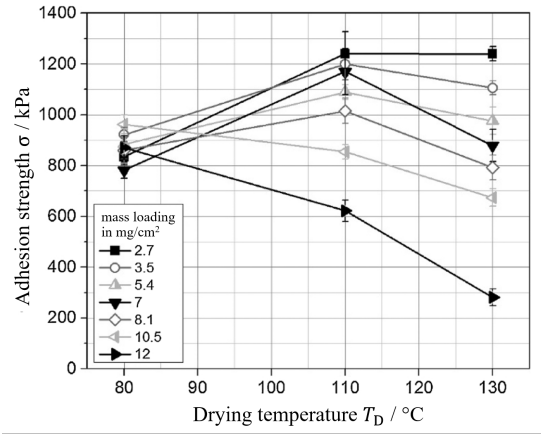

Figure 2.20: Adhesion strength of graphite anodes with PVDF binder processed with different mass loadings and drying temperatures (adjusted from Westphal and Kwade [64], Copyright 2018, Elsevier, reproduced under the license number 6135261301190).

With increasing temperature (110 °C) an increase in adhesion strength can be observed for the samples with a mass loading <10.5 mg·cm^{-2}. It is assumed that the rise in temperature increases both, the driving force for the solvent evaporation and the cross-linking between the coating and current collector. While the former enhances the segregation, the latter entails an increase in adhesion strength. At lower mass loadings and moderate temperature rises, the positive influence on the adhesion strength appears to predominate. At higher mass loadings, the drying time is longer, which on the one hand impairs the fixation of the polymer entanglements of the binder and on the other hand results in increased solvent transport to the surface and thus greater segregation.

With an even higher drying temperature of 130 °C a growing importance of the driving force for solvent evaporation can be observed. Consequently, a stronger segregation can already be observed for lower mass loadings. This is reflected by a decline in adhesion strength for all samples except for the one with the lowest mass loading of 2.7 mg·cm^{-2}. Higher mass loadings entail higher drying times and, thus, higher times for the binder to migrate towards the surface and away from the interface to the current collector [64, 140].

A similar behavior was also shown for an increasing air flow, which is directly connected to an enhancement of the drying rate, which also leads to a drop in adhesion strength for high mass loadings [79].

As a result, the mass loading does not seem to have a significant impact at lower temperatures and drying rates. However, at sufficiently high temperatures increased mass loadings and thus increased coating thicknesses result in higher binder gradients and therefore a lower adhesion strength [64, 74, 165, 178]. Consequently, the maximum of the adhesion strength is at different temperatures depending on the mass loading of the coating. This also explains why other studies showed a peak of the adhesion strength at higher temperatures [47].

Klemens et al. [74] investigated the impact of the drying rate on the adhesion strength of electrodes with equal areal capacities but different active materials. Here, it should be noted, that the electrodes do not have the same thickness. The results of the adhesion strength are given in Figure 2.21. The behavior of the adhesion strength varies between almost constant values for HC and a strong decrease with an increasing drying rate for graphite.

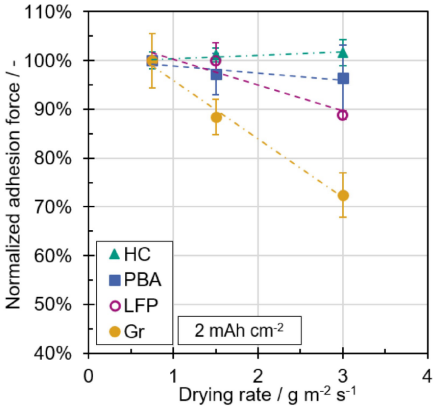

Figure 2.21: Adhesion strength of HC, PBA, LFP and graphite electrodes referred to the value at the lowest drying rate (reproduced from Klemens et al. [74], Creative Commons Attribution 4.0 License CC BY).

Besides the type of AM, the particle size of the AM also seems to have an impact on the binder migration. For investigations with HC and a stronger variation of the drying rate up to 9 $g \cdot m^{-2} \cdot s^{-1}$, the larger particles showed a decrease in the adhesion strength, while the smaller particles even showed an increase in adhesion strength with an increasing drying rate [73].

A change in the particle size distribution caused by different mixing devices with graphite as AM, however, did not show this behavior [83]. The binder dispersion for different mixing approaches might be the dominating impact in this context.

Furthermore, the measurement of the elastic deformation work may be used for comparing the severity of the binder migration in different electrodes. Westphal et al. [79] found an increasing elastic deformation work with an increased drying temperature for electrodes with high mass loadings. The electrodes with lower mass loadings did not show significant changes in the elastic deformation work with increased temperature [64]. An enhanced elastic deformation work can be equated with a higher binder concentration at the surface, as the polymer of the binder – opposed to the AMs – is highly elastically deformable [64]. Thus, high values in these investigations correspond to a strong binder migration.

Another mechanical effect that can be observed on a macro-scale is the cracking of the electrodes during drying. Kumberg et al. [179] investigated this behavior in detail on graphite electrodes with a CMC-SBR binder system. They concluded that cracking only happens for higher mass loadings with dry film thicknesses above approx. 325 µm. While no cracking occurred at all for drying rates ≤ 3 $g \cdot m^{-2} \cdot s^{-1}$, the severity of the cracking increases with an increased drying rate. Rollag et al. [170] found a similar tendency towards an elevated crack formation in NMC111 cathodes with an increased mass loading and drying rate.

Electrical Effects

The binder migration can lead to pore blockage close to the surface of the coating and thus an impaired ion diffusion, manifesting in a reduced ionic conductivity [180]. Especially for high mass loadings, this is often accompanied by a decrease

in the electrical conductivity and, thus, an increase in the volumetric resistivity [72, 83, 181]. Similar to the adhesion strength, Westphal and Kwade [64] demonstrated a significant impact of the mass loading in this matter as shown in Figure 2.22. While lower mass loadings exhibited an almost constant electrical resistance for temperatures between 80 °C and 130 °C, the increase in the resistance is particularly strong for high mass loadings.

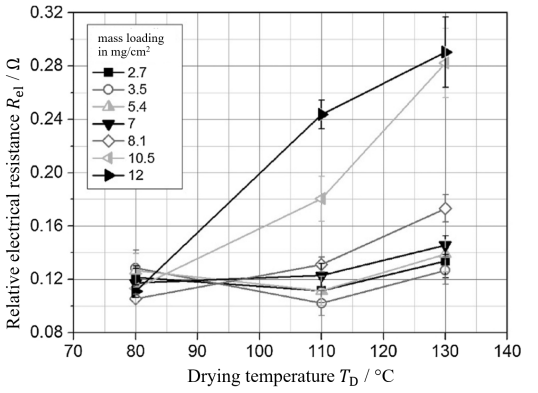

Figure 2.22: Relative electrical resistance of graphite anodes with PVDF binder processed with different mass loadings and drying temperatures (adjusted from Westphal and Kwade [64], Copyright 2018, Elsevier, reproduced under the license number 6135261301190).

Nikpour et al. [182], however, showed a different behavior with an increase in the electrical conductivity when increasing the drying temperature from 24 °C to 80 °C and subsequently a decrease of the electrical conductivity between 80 °C and 232 °C.

The interface resistance between coating and current collector was found to also increase with increasing binder migration caused by a higher drying rate [85] or a higher temperature [182]. This can be explained by the reduced carbon black concentration in the bottom layer and in proximity to the current collector [64, 71, 79, 83].

At large, all these restrictions lead to an impaired electrochemical performance and a reduced lifetime of the battery [171]. The reduction of the specific ionic and electrical conductivity add to the elongated pathways and are a further explanation for the poor electrochemical performance and dropping discharge capacity for the thicker electrodes at high C-rates as discussed in Section 2.2.4.

Thermal Effects

No investigation of the thermal effects is known for the drying process.

2.2.6 Calendering

The calendering process represents a compaction of the electrodes and homogenization of the mechanical structure [183] as the final step of electrode production. By calendering the electrodes, their mechanical stability is enhanced [90] and the lifetime is increased due to an improved adhesion strength and the reduction of aging inhomogeneities [66, 183]. Furthermore, the compaction is aimed to minimize the plastic deformability of the coating [184].

However, the most evident goal of the calendering process is the adjustment of thickness and porosity of the coating, which allows a specific setting for high-energy or high-power cells [147]. The compaction not only reduces the porosity [146] but consequently also increases the tortuosity [140, 146, 185, 186], which lengthens the path for ion transport [186] and reduces the available capacity for high C-rates [162] due to impaired ion diffusion. Thus, the energy density of the electrodes is increased by calendering while an optimum of good electrical conductivity and sufficient ionic conductivity needs to be found. In this context, it is important to know the point at which the ionic conductivity becomes the bottleneck for the electrochemical performance of an electrode [147].

The degree of calendering is generally defined by the compression rate $\Pi_{c,i}$ given in Equation (2.22) following Haselrieder et al. [183]. Here, $s_{co,0}$ stands for the

initial coating thickness of the uncalendered sheets and $s_{\mathrm{co},i}$ describes the coating thickness of the calendered sheet i.

$$\Pi_{\mathrm{c},i} = \frac{s_{\mathrm{co},0} - s_{\mathrm{co},i}}{s_{\mathrm{co},0}} \tag{2.22}$$

Thus, the compression rate is $\Pi_{\mathrm{c},0} = 0$ for uncalendered samples and increases for stronger calendering. It is physically possible for the compression rate to reach values above 0.5 for starting porosities higher than 50 %. However, common values are between 0.25 and 0.45, as there is still a certain porosity needed in the calendered electrode for a reasonable electrochemical performance and since very high line loads are needed for the compression in the low porosity range.

Another important parameter that does not describe the process of calendering itself but rather the capability of an electrode to be calendered is the so-called compaction resistance γ_{c}. It was introduced by Meyer et al. [146] and describes the compressibility of the electrodes in N·mm^{-1}. With the help of the compaction resistance, the resulting coating density $\rho_{\mathrm{co},i}$ for a certain line load q_{L} applied to the electrode during calendering can be estimated according to Equation (2.23) [146].

$$\rho_{\mathrm{co},i} = \rho_{\mathrm{co,max}} - \left(\rho_{\mathrm{co,max}} - \rho_{\mathrm{co},0}\right) \cdot \exp\left(-\frac{q_{\mathrm{L}}}{\gamma_{\mathrm{c}}}\right) \tag{2.23}$$

This correlation involves the maximum coating density $\rho_{\mathrm{co,max}}$ and the initial coating density $\rho_{\mathrm{co},0}$ of the uncalendered electrode. In this, $\rho_{\mathrm{co,max}}$ and γ_{c} are fitting parameters. The compaction resistance is a function of the active material, particle size, mass loading, roll temperature of the calender, BCB phase and the circumferential speed of the calender rolls [78, 146, 163]. Common values lie between 100 N·mm^{-1} and 400 N·mm^{-1}. Graphite generally adopts smaller values than the lithium metal oxides like NMC due to its softer characteristics. As shown by the equation, the coating density $\rho_{\mathrm{co},i}$ asymptotically approaches its maximum value with increasing line load [78, 146].

Meyer et al. [140] showed that an increase in temperature from 25 °C to 90 °C leads to a reduction of the compaction resistance for NMC cathodes with PVDF binder. This can be explained by the thermoplasticity of the PVDF binder. Thereby, the interparticular friction is reduced with increasing temperature. This effect is particularly important for high binder contents [178].

Common circumferential velocities used for calendering in laboratory conditions lie between 0.8 $m \cdot min^{-1}$ and 5 $m \cdot min^{-1}$ [146, 187, 188]. Lippke et al. [189] investigated very high calendering speeds of 50 $m \cdot min^{-1}$ and deduced that the consequent contact times are too short for a sufficient heating of the electrodes.

Beside the changes of the mechanical and electrical material properties [140, 146, 190, 191], calendering can entail different defect patterns [192]. Some defects on the macro-scale are identified by sight analysis. Those include the formation of wrinkles, waves and cracks within the coating as well as the rupture of the substrate foil or coiling up of the electrode [184, 193, 194].

On the micro-scale, too high compression rates can provoke the breakage of particles [193, 195], the penetration of rigid particles like NMC and LFP into the current collector [60, 77, 90, 140, 193, 196–199] and – especially for graphite electrodes – the delamination of the coating. Furthermore, the high tortuosity leads to restrictions in lithium-ion diffusion [190] and wetting problems [146, 184, 200, 201].

On the other hand, low compression rates can be responsible for a poor electrical conductivity [190] and a low adhesion strength [196, 202].

Microstructural Effects

The applied pressure leads to a reduction of the surface roughness [146, 178] and an overall more homogeneous coating with a reduced thickness and porosity. This conversion can on the one hand be observed in SEM images of the cross-sections of differently calendered samples, which not only suggest that the particles on the top are pressed further into the coating, but also that the top particles are deformed

and flattened themselves [178]. Images of this effect can be found in Section 5.5 of the present thesis. This smoothing of the surface is also characterized by an increasing surface sheen of the electrodes [178, 197].

On the other hand, the changes of the coating may be quantified by mercury intrusion [78, 90, 146]. At this, pore size distributions for varyingly strong calendered samples are generally plotted for the different applied forces or the resulting coating densities. While the particulate structure becomes denser due to calendering ($\rho_{\text{co}} \uparrow$) [90], the overall pore volume – and thus the porosity – is reduced. Coating density and porosity show a linear relation according to Equation (2.24) with $\rho_{\text{co,s}}$ representing the density of the solid mixture of the coating [78].

$$\rho_{\text{co}} = \rho_{\text{co,s}} \cdot (1 - \phi) \tag{2.24}$$

The reduction of the porosity is accompanied by a reduction of the predominant pore size, represented by the modal value of the pore size distribution plotted as $-dV/d(d_{\text{P}})$ versus the pore diameter d_{P}. For the presentation of the total intruded pore volume, a shift of the curves to smaller pore diameters is observed [183]. Strong calendering might even result in the creation of new pores in the range of 100 nm to 500 nm due to particle breakage [90].

As mentioned above, particle breakage can occur at high line loads which is particularly common for cathodes [60, 82, 90]. The exact line load or porosity at which this occurs depends heavily on the AM and the binder content. It is suspected that the breakage of particles during calendering results in accelerated aging of the cells manufactured from those electrodes [195].

Another effect investigated for cathodes with rigid active material particles like NMC and LFP is the penetration of those particles into the current collector foil at high applied line loads [60, 77, 140, 193, 196–199] as shown in Figure 2.23. However, this behavior does not seem to have a negative impact on the electrode performance but rather increases the quality of the mechanical and presumably

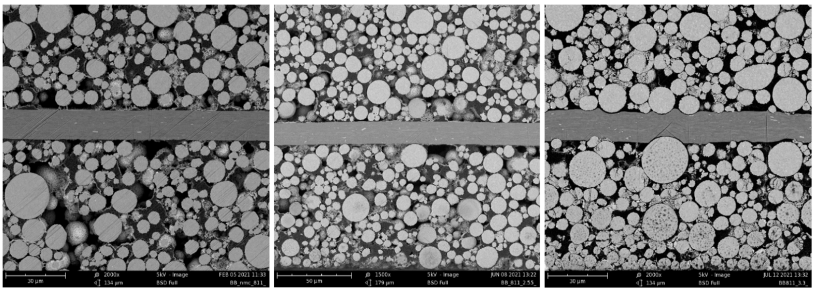

Figure 2.23: SEM images of NMC electrodes with increasing degree of calendering from left to right. A penetration of the AM particles into the current collector foil can be observed for the most strongly calendered electrode (reproduced from Mayer et al. [60], License: Creative Commons Attribution 4.0 License CC BY).

also electrical and thermal contact between coating and current collector [140, 198].

Furthermore, the calendering process is responsible for the breakage and build-up of AM-binder connections [197].

Mechanical Effects

Several authors observed a u-shaped course of the adhesion strength between coating and current collector for cathodes when plotted against the porosity or coating density adjusted by calendering [140, 196, 197]. The minimum of the adhesion strength lies at a porosity around 35 %. For low line loads, it is expected that shear forces occur between the coating and current collector that impair the mechanical contact and thus reduce the adhesion strength [140, 197]. Especially for electrodes with high mass loadings and relatively low amounts of binder, moderate compaction can result in a critical reduction in adhesion strength [140].

For higher line loads, the penetration of the AM particles into the current collector foil can be expected for the cathodes which results in an expansion of the contact area [140] and thus a re-increase of the adhesion strength [197].

Moreover, the temperature applied during calendering has a significant impact on the adhesion strength [140, 197, 202]. Higher temperatures enhance the plasticity of the binder and reduce the defects formed in the coating and at the interface towards the current collector. Furthermore, aluminum exhibits a lower elastic modulus at higher temperatures, facilitating the penetration of the AM particles into the current collector foil [140]. As a results, higher calendering temperatures result in higher adhesion strengths in the low-porosity region [140].

However, most other studies on anodes showed a different behavior of the adhesion strength. A u-shaped slope of the adhesion strength was only observed for the graphite electrode investigated by Scheffler et al. [78]. Under careful consideration of the uncertainty, the Si-C electrodes in the same study only showed a decrease in the adhesion strength with increasing degree of calendering [78]. The graphite electrodes studied by Billot et al. [202], however, presented a tendency towards an increasing adhesion strength with reduced porosity.

Through the calendering process, the extent of plastic deformation is significantly reduced while the elastic properties stay almost equal [77]. This way, the ratio of plastic to elastic deformation work is heavily reduced [77, 197]. This helps in compensating mechanical stress during cycling and enhances the cycling stability of the electrodes [77].

Electrical Effects

Generally, the increasing compression induced by calendering is expected to enhance the electrical conductivity [61, 82, 191] of the electrodes and impair the ionic conductivity. The electrical conductivity – defined as the reciprocal of the resistivity – is specified by the solid pathways through the AM-BCB network. By reducing the porosity and the distance between the AM particles, the resistances along the pathways are lowered. Some studies, however, first showed a decrease in the electrical conductivity (thus, an increase in the resistivity) for slight compressions, before following the expected trend [78, 149]. Similar to the

effect discussed for the mechanical observations, this could be reasoned by small defects and shearing occurring in the range of moderate compression.

The ionic conductivity on the other hand is mainly determined by the lithium-ion diffusion within the electrolyte phase. Due to the compression of the electrodes, the tortuosity is increased and the pores are narrowed. This elongates the pathways for ion diffusion and leads to an impaired ionic conductivity.

According to Meyer et al. [163], the enhancement of the electrical conductivity by calendering usually outweighs the increasing ionic resistance for cathodes [198, 203, 204]. With respect to the resulting discharge capacity, it was shown in the numerical study by Appiah et al. [205] that NMC cathodes with low mass loadings perform best with a porosity around 20 % and for cathodes with higher mass loading a higher porosity around 30 % is preferred. A similar impact was found in the experimental study by Bockholt et al. [90]. For high C-rates the cathodes comparable to the ones with the higher mass loadings from the former study showed a decrease in the discharge capacity with reduced capacity, especially at a porosity between 35 % and 25 %. This is in line with the expectations that high-power cells – exposed to higher current and, thus, higher C-rates – should have higher porosities, while high-energy cells – with low currents and high energy densities – are optimal with low porosities [162]. Although the total discharge capacity might be reduced for strong calendering, the volumetric energy density of the electrodes is increased by calendering [78].

Thermal Effects

At the beginning of this work, there were only few studies on the impact of the calendering on the thermal transport in electrodes.

The most important work to mention here is the study by Sangrós et al. [49]. They used a discrete element method (DEM) simulation to estimate the impact of calendering on the effective thermal conductivity of graphite electrodes with different AM particle sizes. The calculations predict a monotonous increase of

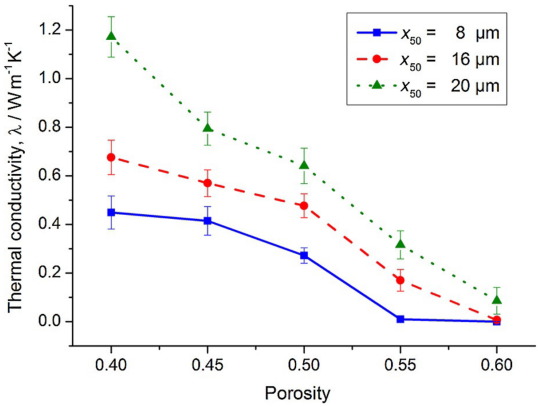

Figure 2.24: Simulated effective thermal conductivity of the electrode coating for different porosities obtained by calendering and different mean particle sizes of the AM (reproduced from Sangrós et al. [49], License: Creative Commons Attribution 4.0 License CC BY-NC).

the thermal conductivity with decreasing porosity as shown in Figure 2.24. This effect is expected to be increasingly strong with elevated particle size.

Moreover, Oehler et al. [32, 34, 113] developed both a numerical model and an analytical model to describe the impact of the porosity, binder and CB content and the thermal conductivity of the single components on the effective thermal conductivity of the porous electrode. Their models also predict a monotonous increase of the thermal conductivity with decreasing porosity.

Maleki et al. [26] measured the thermal conductivity of pellets made from the powder mixture used for anodes. They used different compression pressures which are presumably also reflected in the obtained porosities. An increase in the thermal conductivity is observed with increasing pressure. However, the microstructure of the pellets is not quite comparable with wet-coated, dried and subsequently calendered electrodes.

2.2.7 Dry Manufacturing

As the drying step still represents one of the most energy consuming and thus most expensive steps of battery manufacturing [47, 206, 207], researchers are constantly looking for options to optimize or even eliminate the process [25]. While the reduction of the solvent amount already has beneficial effects on the energy requirements and process costs, the complete elimination of the solvents is preferable. This way, not only the operation costs but also the capital costs can be significantly reduced [208], as the drying process gets removed from the process chain entirely.

Different approaches of dry manufacturing were pursued in recent years. Degen and Krätzig discussed the most promising ones, which – according to their research – are the free-standing electrode fabrication, direct calendering, brush application and electrostatic fluidized bed coating [25]. They all have similar benefits in comparison to the wet coating of electrodes.

Since a detailed explanation of all the different processes would go beyond the scope of this work, the focus of this section is on the free-standing electrode production in a calender, the subsequent lamination onto the current collector as presented by Gyulai et al. [92] as well as the electrode production by direct calendering. The techniques are schematically depicted in Figure 2.25.

In all three cases, a powdery mixture of active material particles, PVDF or polytetrafluoroethylene (PTFE) binder and conductive additives is prepared in a dry mixing process. For the *free-standing electrode production*, this mixture is then fed into the gap between two hot calender rolls by gravitation or additional pressure, e. g. caused by extrusion. Commonly used temperatures for the calender rolls lie between 100 °C and 180 °C [92, 180, 209]. The different rotation speeds applied to the two rolls and the roller surface morphology optimized for adequate friction lead to the envisaged shearing of the powder [92]. This way, especially at higher temperatures, the polymer binders are sheared, resulting in a network of so-called binder fibrils. The fibrillation leads to an increased surface and a fine linkage of the active material particles in contrast to the inhomogeneously

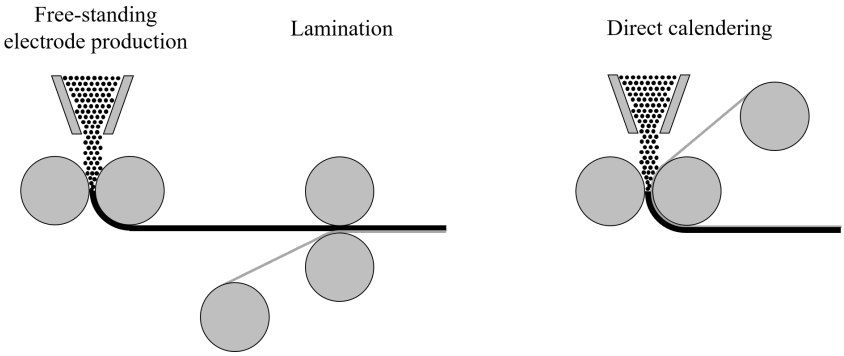

Figure 2.25: Schematic depiction of the free-standing electrode production with subsequent lamination onto the current collector foil and the dry manufacturing by direct calendering of the electrodes (inspired by Degen and Krätzig [25]).

distributed, mossy BCB phase in slurry cast electrodes [92, 180]. Thereby, a better ion diffusion and enhanced discharge capacity can be obtained [180].

In a second step – the *lamination* – the electrodes can be transferred onto the current collector foil by an additional hot calendering step. A primer layer on the current collector is recommended for this [92].

In the *direct calendering* process, the powder mixture is also compressed between two heated rolls, but is directly applied to the current collector foil in a single step. This way, the fragile free-standing electrodes are avoided and higher coating speeds are possible [25].

Dry manufacturing still poses challenges with regard to the flow properties of the applied powder mixtures, the processing speed and the homogeneity of the microstructural and electrochemical properties of the produced electrodes [92]. However, it is a good starting point for further development as it presents considerable opportunities that go beyond the mere reduction of the manufacturing cost and energy consumption [151]. For one thing, toxic solvents like NMP, which is especially applied for the production of NMC cathodes, are used for wet coating. The environmental and health hazards they cause are reduced or even eliminated by avoiding the solvents [47, 151, 210]. Secondly, it prevents the

binder migration during the solvent evaporation of the drying process [171, 210]. This way, dry manufacturing enables high thicknesses and, thus, high areal capacities [210]. In combination with the lower porosities that are obtained by dry processing, significantly higher energy densities can be reached [151] on cell level. Early results also imply an improved capacity retention and overall performance of the dry manufactured electrodes [210]. Matthews et al. [180] also observed an improved mobility of the ions due to the non-existent pore blockage in dry manufactured electrodes with PTFE as binder and a superior capacity at higher C-rates in comparison to the wet-coated electrodes.

3 Experimental Methods

This chapter aims to give an overview of the methods used for the electrode production and the preparation and analysis of the samples applied in this work. For all the production steps, only one-sided coated electrodes with single-layer coatings were investigated.

3.1 Manufacturing of the Electrodes

Not all electrodes could be produced in the same manner due to the use of different materials, different sources and the availability of different machines at the different partner institutes. Thus, this section specifies the applied processes and introduces specific identifiers for the different samples. The complete list of all samples investigated in this work is given in Table A.6 in the Appendix.

After the production, the electrodes were dried in a hot air chamber at a temperature of 50 °C to 60 °C over night before being transferred to an argon-filled glovebox for sample preparation and long-term storage.

For the commercial samples, the exact production procedure of the electrodes is unknown. Only the setting of the degree of calendering was conducted at KIT.

Formulation

The exact formulation and the utilized current collector material of the basic electrodes is given in Table 3.1. In this, MVM, TFT, and IAM describe the partner

institutes, which provided the samples. These include the Institute of Mechanical Process Engineering and Mechanics at KIT (MVM), the working group Thin Film Technology at KIT (TFT) and the Institute for Applied Materials – Energy Storage Systems at KIT (IAM-ESS). CC describes a commercial electrode. The second part of the identifier stands for the active material employed in the sample. In the present work those include graphite, HC, LFP, NMC622 and NMC811. The exact names and manufacturers of the utilized materials can be found in Table A.8 in the Appendix.

The variations conducted with those formulations are given in Table 3.2 and further elucidated in the following sections.

For TFT_LFP and TFT_HC, electrodes with different AM particle sizes were available. LFP200 and LFP400 refer to mean particle sizes x_{50} of 5.8 µm and 11.1 µm, respectively [211]. For both of them, a combined variation of the drying rate and degree of calendering was conducted. HC-A and HC-C have mean particle sizes x_{50} of 3.7 µm and 9.4 µm, respectively [73]. The nomenclature of HC-A and HC-C is derived from the study by Klemens et al. [73]. Furthermore, an electrode with mixed AM particles was produced. The resulting 'HC-Blend' includes 50 % of each, HC-A and HC-C, in the AM fraction. HC was coated on both, copper – generally used for lithium-ion batteries – and aluminum – for sodium-ion batteries.

Mixing

For the MVM samples, the slurry was produced by extruder mixing. Three twin-screw extruders (TSEs) with different screw sizes but equivalent screw geometries (Thermo Scientific Energy 11, Thermo Scientific Process 16 and TSE 24 MC, Thermo Fisher Scientific Inc., USA) were used here. They are specified by TSE11, TSE16, and TSE24 in the identifiers. The number describes the screw diameter in mm. Moreover, an extruder with a differing screw geometry (ZSK-18 MEGAlab, Coperion, Germany) referred to as TSE18 was

Table 3.1: Exact recipe for the different electrode formulations in wt.%.

Formulation	AM	CMC	SBR	PVDF	CB	CG	solid content	current collector
MVM_Graphite [54]	93.00	1.87	3.73	–	1.40	–	43	copper
TFT_Graphite [74]	93.00	1.87	3.73	–	1.40	–	43	copper
TFT_HC [74]	93.00	1.87	3.73	–	1.40	–	43	aluminum / copper
TFT_LFP [74]	93.00	1.87	3.73	–	1.40	–	43	aluminum
IAM_Graphite	96.00	1.25	1.25	–	1.50	–	50	copper
IAM_NMC622	92.00	–	–	3.00	3.00	2.00	68 (wet) | 100 (dry)	aluminum
CC_NMC811	96.00	–	–	2.00	2.00	–	unknown	aluminum

Table 3.2: Conducted variations for the different basic electrode formulations.

Formulation	Particle size AM	RPM extruder	Mass flow extruder	Coating thickness	Drying rate	Dry coating	Degree of calendering
MVM_Graphite		X	X				X
TFT_Graphite				X	X		
TFT_HC	X			X	X		X
TFT_LFP	X			X	X		X
IAM_Graphite				X			X
IAM_NMC622						X	X
CC_NMC811							X

applied. For all of them, the rotation speed and mass flow through the extruder can be varied. The rotation speed was modified between 300 RPM and 900 RPM. At this, the settings were equal for the different extruders. The mass flow is increased with the screw size to obtain a constant specific feed load for the different extruders. Thus, n300, n600, and n900 refer to the rotation speed of the screws in RPM and m0.4, m0.8, etc. specify the mass flow in $kg \cdot h^{-1}$. The exact procedure for the slurry mixing using an extruder was given by Meza et al. [159].

All TFT and IAM slurries were mixed with a dissolver (Dispermat SN-10, VMA Getzmann GmbH Verfahrenstechnik, Germany). The exact procedure for the TFT electrodes was described by Klemens et al. [73]. They all contain a CMC-SBR binder system and thus follow the same mixing procedure. The procedure for the IAM electrodes was described by Müller et al. [81].

Wet Coating

All wet processed electrodes produced at KIT were coated using a doctor blade. All electrodes – including CC_NMC811 – are single-sided coated.

The MVM electrodes were coated on sheets of copper foil with an automatic film applicator (PG-1818V, Thierry GmbH, Germany). The doctor blade was set to a wet film thickness of 180 µm. [159]

The procedure used for the TFT electrodes was described in detail by Klemens et al. [73]. Here, a batch coater is used to produce electrode sheets approx. 1 m in length. The wet film thickness was varied widely.

For the IAM electrodes, a continuous roll-to-roll coater (KTF-S, Mathis AG, Switzerland) with a coating speed of 0.2 $m \cdot min^{-1}$ was used for the slurry-based processing route [81, 92].

For most of the TFT electrodes and the IAM_Graphite electrode, a variation of the coating thickness was conducted. Thus, 58µm, 117µm, etc. describe the thickness of the dried but uncalendered electrode coating in the identifier.

Drying

The MVM electrodes were dried in ambient atmosphere without the application of specific temperature, air flow and humidity conditions. However, as the electrodes of one batch were produced on the same day, they are assumed to be comparable.

The TFT electrodes were dried under an array of 20 slot nozzles as described by Baunach et al. [172]. Both, the velocity and temperature can be adjusted for the air flow. In addition, the temperature of the sample carrier may be set. The applied values for the TFT_Graphite, TFT_HC-C_Al and TFT_LFP400 electrodes, were given by Klemens et al. [73, 74]. In this way, well-defined drying rates and drying temperatures could be achieved. In the identifier DR0.75, DR1.5, etc. specify the drying rate in $g \cdot m^{-2} \cdot s^{-1}$. The drying rate was varied from 0.75 $g \cdot m^{-2} \cdot s^{-1}$ up to 9 $g \cdot m^{-2} \cdot s^{-1}$.

The IAM electrodes were dried within the roll-to-roll coater (KTF-S, Mathis AG, Switzerland). The integrated convective drying stages were set to 80 °C and 120 °C [81, 92].

Calendering

All wet-coated electrodes were calendered at IAM-ESS with the same two-roll laboratory calender (GKL 200, Saueressig Group, Germany) with a width of 400 mm and a roll diameter of 267 mm. The circumferential velocity of the rolls was set to a constant value of 1 $m \cdot min^{-1}$ and the temperature to 50 °C.

The variation of the degree of calendering was conducted for IAM_Graphite_70µm, IAM_Graphite_117µm, IAM_NMC622, CC_NMC811, TFT_HC-C_Cu at drying rates of 0.75 $g \cdot m^{-2} \cdot s^{-1}$ and 6 $g \cdot m^{-2} \cdot s^{-1}$, and TFT_LFP200 and TFT_LFP400, both at drying rates of 0.75 $g \cdot m^{-2} \cdot s^{-1}$ and 3 $g \cdot m^{-2} \cdot s^{-1}$.

The identifiers p1, p2, etc. describe the calendering variation in the order of an increasing degree of calendering and thus a decreasing porosity. This way, p1 always denotes the uncalendered sample.

Dry Manufacturing

The dry processing was carried out at IAM-ESS and was only conducted with NMC622 as active material. For this, a composition equal to the wet-coated IAM_NMC622 electrodes was seeked. The AM, PVDF and additives were premixed in a planetary mixer (Thinky ARV-310, Thinky USA Inc., USA) according to the high-intensity mixing procedure described by Gyulai [212]. For the electrode manufacturing itself, two different production routes were pursued: The free-standing electrode fabrication with potential subsequent lamination and the direct calendering onto the current collector (see Figure 2.25 in Section 2.2.7).

Those yielded three types of electrodes: Free-standing electrodes (without current collector), laminated electrodes, and directly calendered electrodes.

The dry processing was conducted with a two-roll laboratory calender (GK 300 L, Saueressig Group, Germany) with a width of 450 mm and a roll diameter of 200 mm. The temperature of the rolls was set to 180 °C and the circumferential speed to 1 m·min^{-1} and 0.1 m·min^{-1}, respectively. A line load of 225 N·mm^{-1} and a gap width of 60 µm were applied.

In the second step, either discs with 18 mm in diameter were stamped out of the free-standing electrode and were laminated onto a precoated aluminum foil (En'Safe, Armor, France) for the laminated electrodes [212]. Alternatively, the whole electrode sticking to the calender roll was transferred to the precoated aluminum foil for the directly calendered electrodes. In both cases, the gap width was set to $s = (s_{\mathrm{co}} + s_{\mathrm{cc}} - 3\,\mu\mathrm{m})$ here. A line load of 225 N·mm^{-1} and a constant roll speed of 0.1 m·min^{-1} for both rolls were applied.

3.2 Laser Flash Analysis

For most of the samples, the thermal conductivity was only determined by using laser flash analysis. At this, the thermal diffusivity is measured and further evaluated with the results for density and specific heat capacity as described in

Section 2.1.4. A large number of these measurements were conducted by Sabrina Herberger (TVT), Anastasia Schmidt Gallegos and as part of the final thesis projects of Luca Graf, Adrian Reyes Mayorga and Yasmin Grübbel [213–215].

All the measurements were conducted with a LFA 467 HyperFlash® (NETZSCH-Gerätebau GmbH, Germany) with a measurement uncertainty of 3 %. Liquid nitrogen is used for the cooling of both, the IR detector and the sample chamber. The light pulse heating the sample is generated by a xenon flash lamp which has a maximum pulse energy of 10 J. The pulse signal has a triangular shape as a function of time. The magnitude and duration of the light pulse can be adjusted, which is especially important for the comparison of samples with widely varying thickness or material properties. The pulse width can adopt values in the range of 10 µs to 1500 µs. For all measurements conducted in the course of this work, a pulse duration of 50 µs was applied. The ignition voltage of the xenon lamp was set to 150 V. The magnitude was varied for the different samples to be suitable for the respective thicknesses and thermal conductivities. The output of the IR detector as exemplarily shown in Figure 2.6 is displayed in volts. However, the increase in the voltage signal is directly proportional to the temperature increase at the back of the sample.

For the sample preparation, discs with 18 mm or 20 mm in diameter were punched out of the electrodes. The first experiments with IAM_Graphite_70µm, IAM_NMC622 and CC_NMC811 were conducted with 20 mm discs cut out with a hollow punch [213]. However, they showed chipping of the coating along the circumference which was especially strong for the uncalendered, highly porous graphite electrodes [213]. This results in an underestimation of the mass and, thus, an overestimation of the porosity of those samples. Consequently, all subsequent samples were punched out with a high-precision punching tool (EL-Cut, EL-Cell, Germany) with a disc diameter of 18 mm. The measurements for IAM_Graphite_70µm_p1 – the uncalendered graphite electrode from the first experiments – were also repeated with the 18 mm discs to reduce the errors in the measured porosity. The thermal diffusivity and resulting thermal conductivity are expected to not be significantly influenced by the diameter of the samples.

To prevent reflection and increase the absorption and emission of the heat, the metal side of the electrode samples was coated with a thin layer of graphite spray (ÄRONIX Spezialschmierstoffe, Germany). As the spraying is a manual process and is strongly influenced by the viscosity and homogeneity of the spray as well as the operator, the thickness of the graphite spray is expected to vary strongly. SEM images suggest a thickness of up to 10 µm. Assuming a high thermal conductivity of this layer in comparison to the electrode coating, the hereby added resistance may be neglected.

For each electrode sheet in Table A.6 in the Appendix, five samples were measured. For this, the 25.4 mm foil sample holder (NETZSCH-Gerätebau GmbH, Germany) shown in Figure 3.1 was used. The only exception was the TFT_Graphite_700µm sheet which only allowed the measurement of 4 samples with current collector due to material scarcity.

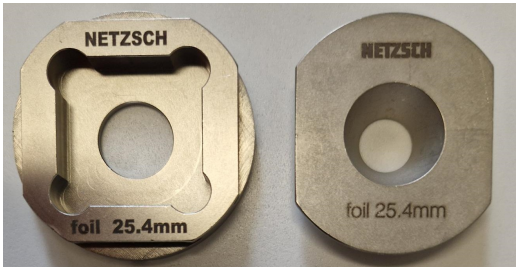

Figure 3.1: Foil sample holder used for all the LFA measurements featured in this work (reproduced from Gandert et al. [216], Creative Commons Attribution 4.0 License CC BY).

All the measurements were carried out on dry samples. No additional pressure was applied during the measurements. Nitrogen was used as protective gas with a volume flow rate of 60 mL·min^{-1}. If not stated otherwise, the measurements were carried out in a helium atmosphere with a volume flow rate of 25 mL·min^{-1}. Some samples were additionally measured in a nitrogen atmosphere with an equal gas flow of 25 mL·min^{-1}. For the electrodes used for the calendering variation in the first published study [36] – IAM_Graphite, IAM_NMC622 and CC_NMC811 – temperature-dependent measurements were conducted in a range of $-20\,^{\circ}$C to

60 °C in 10 K intervals [213]. All other samples were only measured at 20 °C. The set temperature value in the LFA software for this was 19.9 °C to ensure sufficient cooling. For the temperature-dependent measurements, a jump in the thermal diffusivity results could be found between 20 °C and 30 °C (see Figure A.6 in the Appendix). This might be explained by the gas flow present for the measurements at 19.9 °C with an active cooling and the static conditions at 30 °C as described by Lauerer and Lunev [217].

The light flash was shot onto the side with the electrode coating for all samples. There have been some controversies on the impact of the sample orientation on the results. However, a comparison of the results for individual samples measured with either the coating or current collector facing the light pulse did not result in a clear recommendation in this matter (see Figure A.5 in the Appendix). The penetration model by McMasters et al. [103] implemented in the Proteus LFA software (NETZSCH-Gerätebau GmbH, Germany) was used for the evaluation of all measurements.

Except for the IAM_Graphite_58µm and IAM_NMC622 samples all electrodes were measured using the laser flash analysis only.

3.3 Differential Scanning Calorimetry

The DSC was used to measure the specific heat capacity of the electrode materials. For this, the solid mixture of the coating was scraped off of the current collector. The powdery material is compactly pressed into aluminum crucibles. The mass of the empty and filled crucibles was measured with a precision scale (Balance XPE206DR, Mettler-Toledo GmbH, Switzerland) with a measurement uncertainty of 0.015 mg. For each composition, three samples were prepared.

Most of the measurements were conducted with a calorimeter (Q2000, TA Instruments, USA) with a measurement uncertainty of 0.05 %. As measuring gas, nitrogen was used with a flow rate of 50 mL·min^{-1}. A temperature range of −40 °C to 60 °C was run in 2 K steps with a heating rate of 20 K·min^{-1}. The

temperature ramp was performed five times for each sample to allow a sound averaging of the results.

The specific heat capacity of the TFT_LFP200 and MVM_Graphite mixtures was measured with a newer model (DSC 2500, TA Instruments, USA) with the same settings.

Most DSC measurements were conducted and the data made available by Sabrina Herberger (TVT). Some originate from the final thesis project of Luca Graf [213].

For some electrodes with known composition, the specific heat capacity was estimated from literature data or the measurements of the single components instead of measuring the mixture. Below, they are specified as "estimated specific heat capacity" instead of "measured specific heat capacity".

3.4 Gas Pycnometry

The gas pycnometry was applied for the density measurements. It uses the same scraped-off material as the DSC. Three such powder samples were gauged per electrode composition using a gas pycnometer (Ultrapyc 1200e, Quantachrome Instruments, a brand of Anton Paar GmbH, Austria) with a measurement uncertainty of 0.03 %. The mass of the samples was determined using the same precision scale as used for the DSC samples (Balance XPE206DR, Mettler-Toledo GmbH, Switzerland). All measurements were conducted at 25 °C with nitrogen as measuring gas. The measurements were conducted and the data made available by Sabrina Herberger (TVT).

Similar to the specific heat capacity, not all compositions were measured, but some were estimated with the data of the single components.

3.5 Geometrical and Gravimetrical Analysis

The evaluation of the porosity according to Equation 2.6, which requires the measurement of geometrical and gravimetrical variables, was conducted for all the disc samples also used for the LFA measurements.

In doing so, the mass was determined with a precision scale (Balance XPE206DR, Mettler-Toledo GmbH, Switzerland) with a measurement uncertainty of 0.015 mg and the diameter was measured with a digital caliper (digiMax 150D, Wiha Werkzeuge GmbH, Germany) with a measurement uncertainty of 0.05 mm.

The thicknesses of the current collectors and electrode stacks used for the evaluations were measured with a digital micrometer screw (Micromar 40 EWR, Mahr GmbH, Germany) with a flat measuring area and an error margin of 2 µm. Not only does this measurement method in itself show high errors, it also shows large deviations to thickness measurements with different measuring heads. It is important to consider the impact of this thickness uncertainty on the results for the thermal conductivity. In this context, the thickness of a part of the differently strong calendered electrodes – IAM_Graphite_70µm, IAM_NMC622 and CC_NMC811 – was additionally measured with a digital dial indicator (ID-H0530, Mitutoyo Corporation, Japan) with a ball tip measuring head and an accuracy of 1.5 µm. In Figure 3.2 the thickness s_{Mahr} measured with the micrometer screw (Mahr GmbH) and the thickness s_{Mitutoyo} measured with the dial indicator (Mitutoyo Corporation) are compared.

The values measured with the dial indicator are generally lower than those measured with the micrometer screw and show a deviation of up to 23 % for the electrode stack. A similar relative deviation was found for the current collector foils. The deviation between the two methods significantly decreases with increasing degree of calendering. This matter was previously discussed by Gandert et al. [36] and is summarized in the following.

The flat measuring area of the micrometer screw with 33.18 mm^2 and the applied measuring force of 5 N to 10 N [218] result in a maximum pressure of

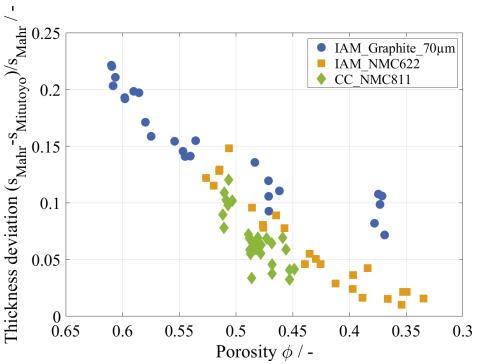

Figure 3.2: Relative deviation of the stack thickness measured with the dial indicator by Mitutoyo Corporation in comparison to the micrometer screw by Mahr GmbH (adjusted from Gandert et al. [36], Creative Commons Attribution 4.0 License CC BY).

0.3014 N·mm^{-2}. It can be assumed that the compression of the electrode coating is marginal under this pressure. Thus, the measurements provide the sample thickness at its highest points without any balancing of the unevenness. The dial indicator, on the other hand, has a ball tip contact element with a diameter of 3 mm and a measuring force of up to 2 N [219]. Due to the significantly smaller contact area of the ball tip for penetration depths in the µm-range, it might measure the thickness in the hollows at the surface. Moreover, the smaller area leads to a higher applied pressure, which might result in a slight compression of the sample. A penetration depth of up to 20 µm in the graphite samples in comparison to the thickness measured with the micrometer screw corresponds to a pressure of at least 10.6 N·mm^{-2}. For the NMC sample and a penetration depths of up to 10 µm the applied pressure is even higher with at least 21.2 N·mm^{-2}.

The fact that the deviation between the two methods declines with decreasing porosity can be attributed to two effects. Firstly, the more compressed layers have a more even surface and smaller hollows that the dial indicator might enter. Secondly, they have already experienced stronger compression; thus, a further pressure application does not have a substantial impact anymore. The strong unevenness of the uncalendered electrodes and the leveling of the surface by calendering were also shown by Meyer et al. [146]. This hypothesis also explains

that the graphite electrode still shows a substantial deviation of approx. 10 % for porosities below 0.4 while the deviation for the NMC electrodes is already below 5 % here. Graphite electrodes have a lower compaction resistance [146], therefore, lower pressures are needed for compression, leading to higher penetration depths of the measuring head.

Thus, while the relative error of the measurement with the micrometer screw increases with increasing degree of calendering assuming a constant error margin of the measurement device, the difference between the two methods decreases with increasing degree of calendering.

An error in the thickness measurement affects the evaluation of the thermal conductivity in different ways. For one thing, it directly impacts the calculation of the thermal diffusivity according to Equation 2.14 as previously discussed by Gandert et al. [36].

Besides the thickness s of the sample, the thermal diffusivity κ is determined by the time $t_{1/2}$ that elapses until half of the measured temperature change is reached [103]. As the time is fixed by the measurement results, a higher assumed thickness entails a higher calculated value of the thermal diffusivity. Higher values of the thermal transport properties are required to conduct heat over a longer distance in the same time.

An attempt to estimate the extent of the error of the thermal diffusivity for an erroneous electrode thickness, the results of selected samples were re-evaluated for a wider range of the thickness. Values of the thickness s_{var} in the range of $0.75 \cdot s_{\text{Mahr}}$ to $1.25 \cdot s_{\text{Mahr}}$ were used, resembling a variation of ± 25 % conform to the deviations observed above. The thermal diffusivity for the varied thicknesses s_{var} normalized to the thickness measured with the micrometer screw s_{Mahr} is displayed in Figure 3.3 (a). The thermal diffusivity was also normalized to the value determined for the thickness obtained with the micrometer screw. The results shown here were established with the uncalendered samples. However, calendered samples led to similar results. The dependency is equal for all the investigated electrodes as only the thickness and no material properties flow into the calculation. Thus, the four graphs lie exactly on top of each other.

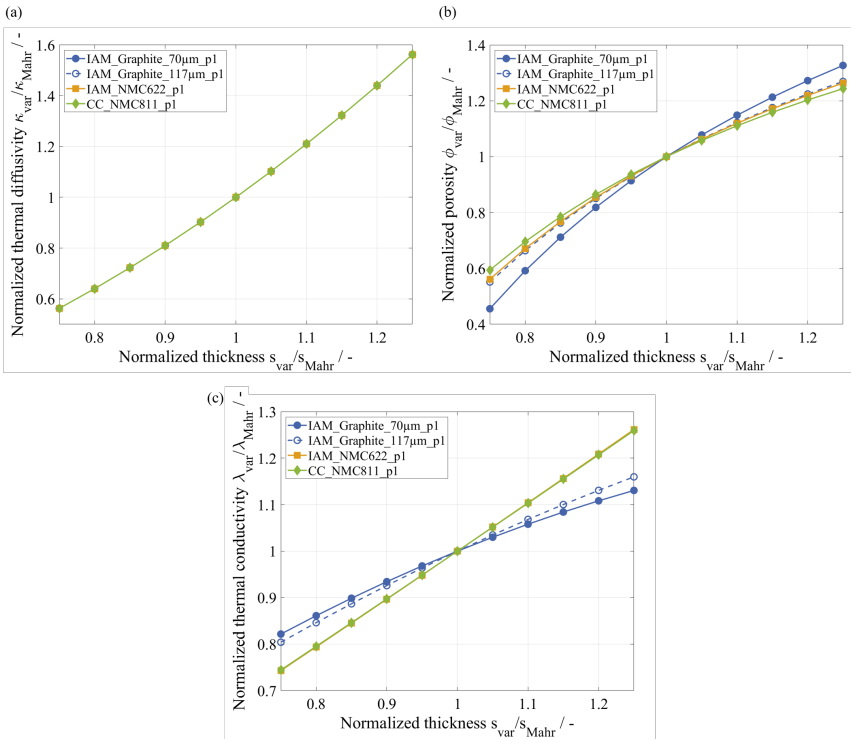

Figure 3.3: Impact of a variation in the thickness of the electrode stack on (a) the effective thermal diffusivity κ, (b) the porosity ϕ and (c) the effective thermal conductivity λ of the electrode stack for the uncalendered electrodes IAM_Graphite_70µm_p1, IAM_Graphite_117µm_p1, IAM_NMC622_p1 and CC_NMC811_p1 (adjusted from Gandert et al. [36, 220], Creative Commons Attribution 4.0 License CC BY).

Moreover, the thickness has a significant influence on the calculated porosity. Keeping the mass, solid density, and diameter of the sample constant, an increase in the thickness results in a higher porosity as the incorrectly higher assumed volume only leads to higher amounts of hollows. The impact of a variation in the sample thickness on the porosity is given in Figure 3.3 (b) normalized to the values based on the micrometer screw.

The thicknesses of the stack and current collector also directly flow into the thermal conductivity through Equation 2.16. In this, only the ratio of the two values is important and not the absolute values. For the present investigation of both the thermal conductivity and porosity, the ratio of s_{cc} to s_{stack} was assumed to remain constant, thus, neglecting the interrelation of measurement uncertainties of the stack and current collector.

When it comes to the calculation of the thermal conductivity, the effects of the thickness on the thermal diffusivity and the porosity counteract each other (see Equation 2.16). The increasing slope of the effective thermal conductivity indicates that the thermal diffusivity has a stronger influence in this relation than the porosity. All things considered, the thermal conductivity shows significantly lower relative variations than the thermal diffusivity due to the counteracting effect of the porosity.

The according depiction of the variation of the thermal conductivity for a varied thickness is given in Figure 3.3 (c). The graphs of NMC811 and NMC622 are almost equal, making the yellow curve for NMC622 barely identifiable. While the tendency is similar, the effect is not equally strong for the different materials, which is attributed to the different porosity of the uncalendered samples.

The conducted analysis leaves open the question of which thickness measurement method should be used for future investigations. For this decision, it is essential to consider the application for which the thickness is being used. All the LFA measurements conducted in this work were evaluated using the penetration model by McMasters et al. [103]. This model is intended for the use on porous samples and takes into account the hollows and how the light beam does not just hit the surface but partially penetrates further into the pores. Since the penetration depth is fitted to the recorded data and is thus corrected automatically by the evaluation software (Proteus LFA Analysis, NETZSCH-Gerätebau GmbH, Germany) [221], the thickness of the highest point should be used for the evaluation of the LFA measurements. Therefore, the values measured with the micrometer screw are preferred in this case.

For the calculation of the porosity, an explicit decision between the two methods is not possible. Assuming that the dial indicator really just measured the lowest points of the coating surface and that the high points and low points balance each other, the mean of both thickness values would be a good estimation for the determination of the averaged porosity. However, it is statistically improbable that the dial indicator only measures the low points of the samples, although we have only measured very few points that were as high as the values of the micrometer screw or even higher (max. of 12.5 % for IAM_NMC622, approx. 0 % for IAM_Graphite_70µm and CC_NMC811). This suggests that the low values mainly originate from the compression of the material. Thus, the resulting thickness values are inapplicable for investigations in which the electrode is not further compressed. Therefore, all further thickness measurements were conducted with the micrometer screw.

The measurement of the diameter with a caliper also poses a great possibility for errors. For one thing, it is improbable to always measure the longest distance of a circle going through the center. Additionally, the measurement is very sensitive to the applied clamping force in radial direction which leads to a deformation of the sample to varying degrees. Thus, the result might vary strongly with the operator. However, for both cases of incorrect application, the result for the diameter is lower than the true value, which leads to an underestimation of the porosity.

3.6 Guarded Hot Plate Method

Similar to the LFA measurements, electrode discs were punched out of the sheets for the GHP measurements. Due to the geometry of the measurement rig, a diameter of 21 mm was used. The sample preparation was conducted in ambient air. After opening the sealed transport pouches, the electrode sheets were stored in a desiccator at the NTNU.

The experimental setup is based on the schematic in Figure 2.5. The pistons are made of stainless steel. The inlet temperatures of the hot water and cold

water stream are controlled with thermostats. The ends of the pistons that are in contact with the sample are covered with thin aluminum plates. With approx. 236 $W \cdot m^{-1} \cdot K^{-1}$, aluminum has a significantly higher thermal conductivity in comparison to steel with approx. 15 $W \cdot m^{-1} \cdot K^{-1}$. Thus, as the thermal gradients within the pistons and the sample are much higher, the temperatures within the aluminum plates can be assumed as spatially constant and define the temperature difference through the sample used in the evaluation. To minimize parasitic heat flows to and from the environment, the pistons and sample are surrounded by an evacuated and mirrored insulation tube made of glass. The sample thickness is measured by the two micrometers on the outside of the rig in relation to their calibration, which is conducted without any sample in the rig. More details on the setup can be found in the study by Burheim et al. [96].

Due to their asymmetry, the one-sided coated electrodes were always measured in pairs. In this setting, the coatings are facing each other while the current collectors are on the outside. This stacking method has shown a tendency towards lower thermal contact resistances between the single layers than the stacking of several samples facing in the same direction. Following this approach, the differently calendered sheets of the IAM_NMC622 and IAM_Graphite_70µm electrodes were measured with two, four and six layers with the electrode coatings facing each other. It should be noted that the most strongly calendered graphite electrode IAM_Graphite_70µm_p6 could not be measured in this setting due to material scarcity.

The thickness of the multi-layer stacks was measured with a micrometer screw (Ironside Group, USA) before they were inserted into the rig. In addition, two micrometers (ID-S1112XB, Mitutoyo Corporation, Japan) with an accuracy of 3 µm are integrated into the rig that measure the thickness variation during the measurement. The mean value of the two micrometers is used in the evaluation for a more precise result.

Different pressures can be applied to the sample in the rig. In the present work, the pressure was varied in a realistic range of 2 bar to 6 bar for the differently calendered samples. Additional investigations of the internal contact resistances

used pressures of 2.5 bar and 5 bar as discussed in detail in Section 5.5.3. The measurements were conducted in air.

The thermal conductivity resulting from the GHP is evaluated with a linear regression of the overall thermal resistances of the measured stacks with varying layer numbers. The reported error bars represent the least square residuals from the linear regression. The thermal conductivity data are reported with double standard deviations.

3.7 Scanning Electron Microscopy

The SEM imaging was conducted by Dr. Marcus Müller at IAM-ESS with a field-emission scanning electron microscope (Supra 55, Zeiss, Germany).

For the cross-section images, the electrode samples were cut with a triple ion beam cutter (EM TIC3X, Leica Mikrosysteme GmbH, Germany). The sample preparation is performed under vacuum with a residual pressure of $2 \cdot 10^{-4}$ mbar of argon. The acceleration voltage for the argon ions is 6 kV to 7 kV and the gun current is 2.2 mA to 2.6 mA.

3.8 Electrical Resistance Measurements

The volumetric resistivity and interface resistance were measured for the IAM_NMC622 and IAM_Graphite_70µm electrodes with an electrode resistance measurement system (RM2610, Hioki E.E., Japan) at IAM-ESS. The room temperature ranged from 18 °C to 20 °C. Five samples were used per degree of calendering and three measurement points were recorded per sample. The LFA samples were used for this investigation. Therefore, the evaluation of the measurements is based on the mean thickness obtained earlier for the LFA. It should be noted, that the electrical resistance measurements were conducted more than two years after the

thermal diffusivity measurements with the LFA. The samples were stored in air during that time.

The results allow the calculation of the specific electrical conductivity, which is used in the comparison below. The specific electrical conductivity is equivalent to the reciprocal of the volumetric resistivity of the coating.

3.9 Profilometer

In the context of the comparison of the LFA and GHP as measuring methods for the thermal conductivity an interest into the surface roughness of the electrodes arose. To investigate this, a profilometer (Dektak 150, Veeco, USA) with a ball-type stylus with a radius of 5 µm was used to record the height profiles of the differently calendered electrodes. The discs measured with the GHP were also used for these investigations. The measurements were conducted in a clean room at NTNU.

The same procedure was applied to all the sheets. Especially the strongly calendered samples are prone to bending. Therefore, the samples were fixated on a specimen slide with adhesive tape to obtain a fairly even surface. Three lines of 500 µm each were scanned within 100 s each at different areas of the sample. A load of 3 mg was applied to the stylus.

The three measurements per sheet can differ strongly depending on the starting point of the measurement which results in a different offset in height. This is why the measurements were each referred to their highest point so that only the relative course along the surface is taken into account. Thereafter, the three measurements per sheet can be combined to one dataset and allow an evaluation of the surface roughness of the different electrodes.

4 Modeling

For the further analysis of the experimental data, two models were considered in this thesis. Firstly, the analytical model introduced by Oehler et al. [32, 34, 113] was implemented in MATLAB for a comparison with the experimental results of the differently calendered electrodes. Secondly, a numerical model representing the thermal transport processes during the LFA measurements was developed to estimate the impact of the radial heat losses on the resulting thermal conductivity.

4.1 Analytical Model by Oehler

Generally known heat conduction models for packed beds cannot reproduce the complex interdependencies of the different components within the microstructure of battery electrodes. Oehler et al. [32, 34, 113] developed an analytical model based on the Zehner, Bauer, and Schlünder (ZBS) model [222–224]. As shown in Figure 4.1, the advanced model considers different heat conduction pathways through the fluid (path 1), through the AM solid (path 2), and through a combined path including the BCB phase (path 3). While the particle size is no contributing factor in this model, it is able to take into account different porosities as well as a variation in the binder and carbon black volume fractions.

The modeling approach was described in detail by Oehler at al. [32, 34]. Therefore, only the most important correlations for the present consideration and the specific settings used for the calculations are discussed here.

Generally, the effective thermal conductivity of the electrode coating is a function of the thermal conductivities of the AM λ_{AM}, the BCB phase λ_{BCB} and the fluid λ_{f}.

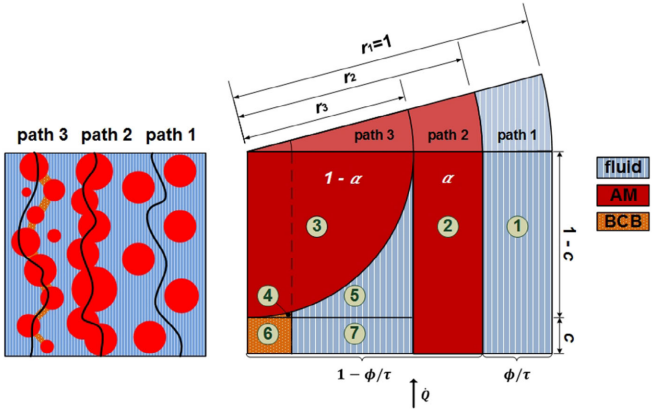

Figure 4.1: Schematic depiction of the model introduced by Oehler et al. [32, 34, 113] (reproduced from Oehler et al. [32], Creative Commons Attribution 4.0 License CC BY).

Moreover, the volume fractions of the AM ν_{AM}, the BCB ν_{BCB}, and the porosity ϕ, which equates the volume fraction of the fluid, are needed. Newly introduced parameters are the particle distance parameter c and the particle contact parameter α. The correlation for the effective thermal conductivity as a parallel connection of the three paths with their respective thermal conductivities λ_{path1}, λ_{path2} and λ_{path3} is given in Equation 4.1. The radii r_2 and r_3 are defined according to the schematic depiction in Figure 4.1.

$$\lambda_{\text{eff}} = f\left(\lambda_{\text{AM}}, \lambda_{\text{BCB}}, \lambda_{\text{f}}, \nu_{\text{AM}}, \nu_{\text{BCB}}, \phi, c, \alpha\right) \tag{4.1}$$

$$= \left(1 - r_2^2\right) \cdot \lambda_{\text{path1}} + \left(r_2^2 - r_3^2\right) \cdot \lambda_{\text{path2}} + r_3^2 \cdot \lambda_{\text{path3}} \tag{4.2}$$

For the detailed derivation of the correlations for the calculation of the thermal conductivities of the three paths, the reader is referred to the publications by Oehler et al. [32, 34].

Inspired by Oehler et al. [32], the particle contact parameter α was set to 0 in the present work, implying that no heat transfer path exists that only passes the AM solid. Thus, heat conduction along path 2 in Figure 4.1 is excluded. This is based on the assumption that all AM particles are surrounded by a layer of BCB phase.

The used compositions comply with those given in Table 3.1. An overview on the specific material properties used for the calculation is given in Table 4.1. The density is used for the conversion of mass fractions into volume fractions.

Table 4.1: Values of the thermal conductivity λ and the density ρ of the materials contained in the investigated electrodes that were used in the model.

Material	λ / W·m^{-1}·K^{-1}	ρ / kg·m^{-3}
Graphite (AM & additive)	139.6 [49, 225, 226]	2115 [115, 227]
NMC622 / NMC811	4.3 [228]	4680 [31]
LFP	0.8 [229]	3350 [74]
HC	5.5 [230]	2062 [74]
PVDF	0.2 [231]	1750 [231]
CMC	0.21 [34, 232]	1595 $\pm$ 6 (measured at TVT by Sabrina Herberger)
SBR	0.206 [232, 233]	940 [234]
Carbon black	24 [34]	2260 [34]
Helium	0.152 [235]	–

The model was applied to all the differently calendered electrodes experimentally investigated in this work. The IAM_NMC622 electrodes contain a graphite additive, which has a significantly higher thermal conductivity than all other included materials and a relatively large particle size. However, it only makes up 2 wt.% of the coating. Additives are usually considered in the BCB phase. In the model by Oehler et al., the thermal conductivity of the BCB phase is calculated according to the model by Hamilton and Crosser [236] given in Equation 4.3. Herein, λ_{PM} refers to the thermal conductivity of the polymer and thus the binder and λ_{CB} stands for the thermal conductivity of the carbon black. For polymer-CB systems, a factor of $f = 3.2$ is recommended [34].

$$\lambda_{\mathrm{BCB}} = \lambda_{\mathrm{PM}} \cdot \frac{(f-1)\cdot\lambda_{\mathrm{PM}} + \lambda_{\mathrm{CB}} - (f-1)\cdot(\lambda_{\mathrm{PM}} - \lambda_{\mathrm{CB}})\cdot\nu_{\mathrm{CB}}}{(f-1)\cdot\lambda_{\mathrm{PM}} + \lambda_{\mathrm{CB}} + (\lambda_{\mathrm{PM}} - \lambda_{\mathrm{CB}})\cdot\nu_{\mathrm{CB}}} \tag{4.3}$$

Including the graphite particles in the BCB phase would require a thorough analysis of their weighting factor in the context of Equation 4.3. Moreover, due to their size, the consideration within the binder phase might not be the right approach. Their size is more similar to that of the NMC particles. Although it is assumed, that the graphite particles lead to an enhancement of the effective thermal conductivity, they do not build continuous heat conduction paths along the coating thickness. Thus, the simple assumption of a parallel connection of both AM materials for the calculation of λ_{AM} strongly overestimates the effective thermal conductivity of the coating. A series connection, on the other hand, results in an underestimation of the effective thermal conductivity. No sufficiently elaborate approach to consider two different kinds of the larger particles exists so far, even though this is also of interest for the modeling of blend electrodes with more than one AM. Instead, the graphite fraction was neglected completely in the modeling of the IAM_NMC622 electrodes in the present work.

4.2 FEM Simulation of the LFA Measurements

A numerical model was implemented in COMSOL Multiphysics® to investigate the error in thermal conductivity caused by radial heat losses in the LFA measurements. The model is realized as a rotationally symmetric 2D geometry with different boundary conditions. The physics module *Heat Transfer in Solids* and a time-dependent solver were applied. This way, the porous electrode coating is regarded as a single phase continuum with uniform, isotropic properties. The following model geometries were considered in this context, which are depicted in Figure 4.2.

- *Reference case:* In this case, only the irradiated and radiating inner circle of the sample is taken into account. This way, the system follows a pure 1D heat conduction and thereby meets the assumptions used for the evaluation. Symmetry is assumed at $r = 0$ mm. The outer surface in radial direction is assumed to be adiabatic. The whole bottom surface is evenly heated and a Dirichlet boundary condition with a heat transfer coefficient

of 5 $W \cdot m^{-2} \cdot K^{-1}$ is assumed at all surfaces in axial direction. An adiabatic Neumann boundary condition was applied to all surfaces in radial direction.

- *18 mm disc:* The name of this case refers to the size of the circular samples, which have a diameter of 18 mm, i. e. a radius of $r = 9$ mm. For this and all the following cases, only the inner circle of 0 mm$\leq r \leq 7$ mm of the bottom surface is irradiated and experiences heat transfer to the surrounding gas phase with 5 $W \cdot m^{-2} \cdot K^{-1}$. For the upper surface, the same heat transfer coefficient applies to a circle of only 0 mm$\leq r \leq 5$ mm following the geometry of the foil sample holder used for the LFA measurements (see Figure 3.1.) For the models without sample holder, adiabatic conditions were assumed at the outer surfaces which corresponds to a Neumann boundary condition.

- *20 mm disc:* This case is almost equal to the *18 mm disc*, except for the disc is 20 mm in diameter here. As some of the experiments were conducted with 20 mm discs instead of 18 mm discs, both cases were considered in the model. To verify the experimental results it is of interest if a change in the sample diameter entails a large deviation in the results.

- *18 mm disc with sample holder and 10 µm He contact resistance:* In this case, a lumped volume with the material properties of stainless steel is added to the 18 mm disc model to take the thermal influence of the sample holder into account. The volume of the upper and lower piece was set to have the same heat capacity as the two pieces of the real sample holder. The sample holder's geometry was simplified for the simulation and is implemented in the form of two metal rings which have the same heat capacity and contact area towards the sample as lower and upper piece of the real sample holder. A 10 µm thick layer of helium (He) representing a potential contact resistance was added between the sample and the sample holder. Its thermal conductivity was set to an approximate value of 0.15 $W \cdot m^{-1} \cdot K^{-1}$ in the model [235].

- *18 mm disc with sample holder and without contact resistance:* In this case, the helium phase and thus the contact resistance is neglected in comparison

to the former model resulting in a better heat conduction and making the additional heat capacity of the sample holder more accessible.

- *20 mm disc with sample holder and without contact resistance:* In the last geometry the disc diameter is again increased to 20 mm. Hereby, the contact area between sample and sample holder is increased as well.

The accessible heat capacity of the whole system and especially the amount of the material outside of the measurement area is gradually increased from the *reference case* to the case of a *20 mm disc with sample holder and without contact resistance*. All geometries were checked for mesh independence by doubling the mesh resolution.

For all the geometries, the sample can consist of either two or three layers: The electrode coating, which is irradiated, and the metallic current collector are present in any case. The optional third layer is a thin layer of graphite spray on the backside of the metal foil as described in Section 3.2. All the thickness values and material properties can be adjusted depending on the assumed AM, current collector material, degree of calendering and for parameter studies for the graphite spray.

For all simulations, the sample was assumed to be ideally centered within the sample holder so that the light flash occurs perfectly centered as well. Of course, this cannot be achieved in experiments due to human error in sample positioning.

The most strongly calendered graphite electrode is used for the analysis as it exhibits the highest in-plane thermal conductivity due to the highest fraction of the thickness of the copper current collector. Therefore, it is expected to experience the strongest errors due to undesired heat conduction in radial direction. As a consequence, the thickness of the coating, current collector and graphite spray were set to 37 µm, 10 µm and 3 µm, respectively. The thermal conductivity was set to 1.6 $W \cdot m^{-1} \cdot K^{-1}$ for the coating, 380 $W \cdot m^{-1} \cdot K^{-1}$ for the copper current collector and 0.2 $W \cdot m^{-1} \cdot K^{-1}$ for the graphite spray.

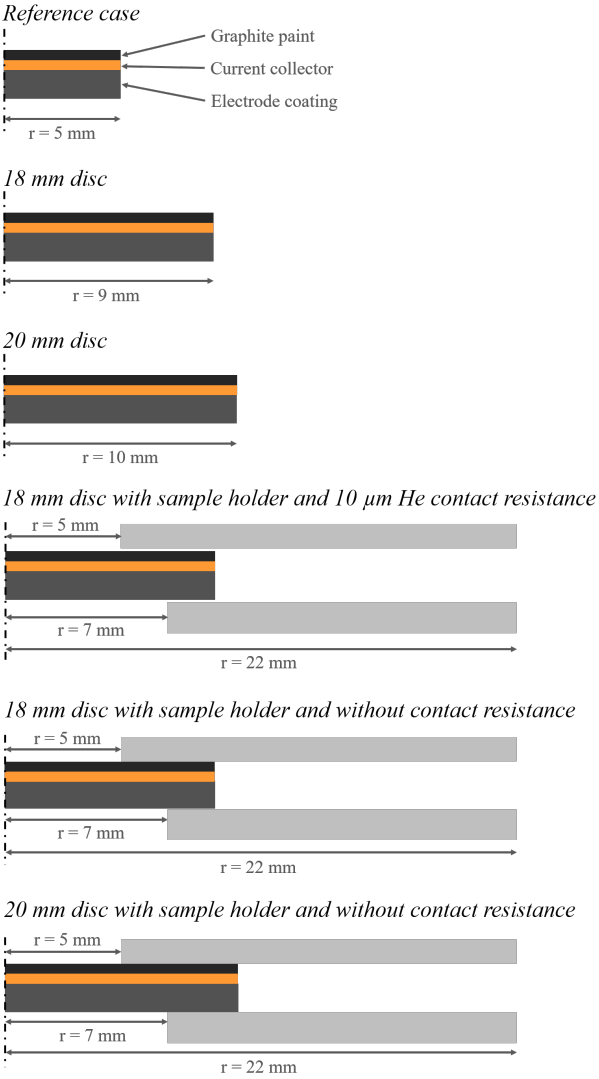

Figure 4.2: Graphic depiction of the considered model geometries. For a better visibility, the thickness ratio of the different components does not reflect the reality. Exemplarily, the different geometries are shown for the cases with graphite paint on the backside of the metal foil (adjusted from Gandert et al. [93], Creative Commons Attribution 4.0 License CC BY).

Based on the assumptions for the evaluation, the heat input is assumed to be a triangular pulse, which is released during the first 0.1 ms of the simulation. The heat input is realized as an areal heat source at the bottom surface of the sample. As the adiabatic fitting approach for solids was used for the evaluation, which assumes a smooth sample surface, light penetration into the porous sample was not considered.

The results of the model are exported in a `.txt` file in the form of a time array and the mean temperature along the radius 0 mm $\leq r \leq 5$ mm on the backside of the sample over time. The evaluation is conducted in MATLAB® with the computational framework by Philipp et al. [237, 238]. The framework automatically chooses the adiabatic fitting approach.

For the evaluation of the coating thermal conductivity according to a series connection, the thickness of the graphite spray was neglected to replicate the procedure used for the evaluation of the experimental LFA data.

5 Results and Discussion

In this chapter, the impact of the different production parameters on the thermal conductivity is analyzed and the correlation with the microstructural, mechanical and electrical changes is discussed.

For this, the effective thermal conductivity of the electrode coating according to Equation 2.17 is taken into account. This way, the impact of different ratios of coating to current collector thickness are eliminated. This allows a better comparison with the literature and of the electrodes investigated here among each other. It should be noted that the calculation according to Equation 2.17 does not take into account the thermal contact resistance between the coating and the current collector as an individual variable. Thus, the contact resistance is included in the coating thermal conductivity and thereby leads to a reduction of the value. However, the order of magnitude of the thermal contact resistance is yet unknown and it is uncertain, if it is even significant in this context.

Unless stated otherwise, mean values are always depicted with a double standard deviation. The standard deviation is calculated according to the statistical uncertainty analysis (type A) and – if applicable – error propagation in compliance with the Guide to the Expression of Uncertainty in Measurement [239]. The approach used for the calculation of the uncertainty of the thermal conductivity obtained with GHP is elaborated in Section 3.6. Moreover, the LFA data were always measured in helium. For a comparison with the GHP, the electrodes calendered to different degrees were additionally measured in nitrogen atmosphere in the LFA.

In particular, the process steps of coating and drying are closely related. Therefore, a strict distinction of the two steps in the discussion of the results is not always possible.

The mean density and specific heat capacity of the particle mixtures of the different electrodes which are needed for the calculation of the thermal conductivity from the thermal diffusivity are given in Table 5.1.

Table 5.1: Solid density and specific heat capacity of the different formulations of the electrode coatings at 20 °C to 25 °C used for the evaluation of the effective thermal conductivity. For the AMs with different particles size, the specific heat capacity was measured separately. The uncertainties of the measured values are given with a coverage factor of $k = 2$.

Formulation	$\rho_{\mathrm{co,s}}$ **/ kg · m**$^{-3}$	$c_{\mathrm{p,co,s}}$ **/ J · kg**$^{-1}$ **· K**$^{-1}$
MVM_Graphite	2136 (estimated)	714.7 ± 13.0 (Herberger, TVT)
TFT_Graphite	2136 [74]	687.0 ± 37.6 (Herberger, TVT)
TFT_HC-A	1873 (estimated)	753.2 ± 9.4 (Herberger, TVT)
TFT_HC-C	1970 [74]	769.5 ± 13.8 (Herberger, TVT)
TFT_LFP200	2992 [74]	795.5 ± 3.7 (Herberger, TVT)
TFT_LFP400	2992 [74]	753.4 ± 15.3 (Herberger, TVT)
IAM_Graphite	2162 ± 5 [213]	701.1 ± 5.4 [213]
IAM_NMC622	4229 ± 7 [213]	785.8 ± 14.4 [213]
CC_NMC811	4474 ± 3 [213]	773.5 ± 10.5 [213]

5.1 Formulation

In terms of the formulation of the electrodes, the mean particle size of the active material particles was varied for HC and LFP. Those include the electrodes TFT_HC-A, TFT_HC-C, TFT_LFP200 and TFT_LFP400. The coating thickness was set to similar values for both HC and LFP electrodes, respectively.

In this section, only the effective thermal conductivity and porosity of the electrodes produced with the lowest drying rate and in the uncalendered state are covered. However, the impact in combination with a variation of the drying rate and the degree of calendering is discussed later on.

Figure 5.1 shows the thermal conductivity of the electrode coating and its porosity with respect to the AM particle size. Herein, it is evident that the effective thermal conductivity increases with increasing mean particle size. The same applies to the porosity which also shows increasing values with increasing particle size. This is in line with the expectations from the literature [73, 116]. However, the porosity does not only depend on the mean particle size x_{50} of the AM particles, but also on the content of binder and CB and the particle size distribution. A wider or even bimodal particle size distribution generally results in a lower porosity as the voids between the larger particles may be filled by the smaller ones. The particle size distributions for the raw AMs discussed here are given in the Figures A.1 and A.2 in the Appendix.

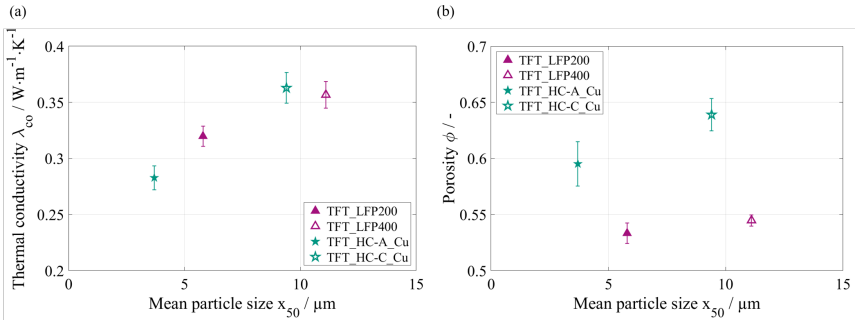

Figure 5.1: Impact of the mean particle size of the active material on (a) the effective thermal conductivity and (b) the porosity of the LFP and HC electrode coatings.

The correlation between the porosity and thermal conductivity is contradictory, as a higher porosity and thus a lower solid fraction is generally expected to result in a lower effective thermal conductivity. Therefore, the results in Figure 5.1 emphasize that the porosity is not the only and often – e. g. in the present case – not even the most important influencing factor on the effective thermal conductivity.

Instead, the observed behavior of the thermal conductivity may be explained by the microstructure of the coating. Larger AM particles result in fewer particle-particle contacts and, thus, less disconnections of the conduction path by the

binder phase, which generally has a significantly lower thermal conductivity than the AM. These particle-particle contacts are expected to also cover a greater area in the case of the larger particles. Consequently, better long-range pathways can be achieved for the thermal conduction in the electrode with larger particles. This influence appears to be similar for both investigated active materials.

When it comes to measurements of dry electrodes, the thermal conductivity of the gas within the pores can also have a significant impact on the resulting values. This, however, is not only dependent on the used medium, but on the pore size as well. The so-called Knudsen or Smoluchowski effect [240, 241] leads to a significant reduction of the thermal conductivity within the pores in comparison to the continuum value. An estimation of the thermal conductivity of the gas within the pores is given in Figure A.4 in the Appendix. The evaluation is based on the assumption of two parallel plates and calculated according to the derivation by Schlünder and Tsotsas [240]. Taking the pore size distributions measured by Klemens et al. [73] for the HC electrodes into consideration (see Figure A.3 in the Appendix), the average reduction of the thermal conductivity of the gas can be estimated. With a modal value of the pore diameter of 2 µm for the HC-C electrode and 0.55 µm for the HC-A electrode, this leads to a reduction of the thermal conductivity of helium by 72 % to 91 % in comparison to the continuum value. While the reduction of the thermal conductivity of the gas is very significant, the influence on the effective thermal conductivity of the electrode coating is not expected to be the most substantial. However, it might in some part also contribute to the deviations reported above.

Additionally, for the LFP electrodes in particular, it cannot be excluded that the differences in the effective thermal conductivity of the coating are due to variations in the thermal conductivity of the AM itself. In this case it is uncertain, if the composition of LFP200 and LFP400 is exactly the same. Usually, small fractions of carbonaceous particles are added during the material synthesis of LFP active material to enhance the electrical conductivity of the final material. According to the manufacturer, the carbon fraction of both AMs are in the same range of 3.5 wt.% to 3.9 wt.% [242, 243], however, more detailed information is missing.

In contrast to the thermal properties, the influence of the particle size on the mechanical behavior seems to depend highly on the AM and the applied drying rate. Klemens et al. [73] measured the adhesion strength and noted an advantage of the smaller particles ($\leq$ 5 µm) for HC, especially for higher drying rates up to 9 $g{\cdot}m^{-2}{\cdot}s^{-1}$. Gottschalk et al. [116] investigated graphite electrodes with different AM particle sizes and bimodal mixtures of them and concluded that a reduction of the mean particle size entails a decrease in the adhesion strength. No detailed information on the applied drying rate was given here. Due to the small number of existing studies on this matter, it is unclear which mechanical behavior can be expected for the electrodes investigated here and whether this depends on the type of AM.

However, Gottschalk et al. [116] also examined the electrical properties. According to their study, smaller particles result in a higher ionic resistance and a lower electrical conductivity. Larger particles are suggested for good electrical conductivity as they result in a lower number of interparticle gaps within the conduction pathways that are filled with the more poorly conducting BCB phase. However, larger particles entail longer paths for the solid state diffusion which is generally slower than the ion diffusion within the electrolyte. Therefore, from an electrical perspective, often there exists a limitation of the maximally allowed particle size.

It can be concluded that the thermal, mechanical and electrical behavior are not always comparable. This makes sense, since the adhesion strength only gives insight into the quality of the contact and the thermal conductivity is mainly a measure for the quality of the coating itself. Electrical and thermal conductivity are expected to show many parallels. However, in the context of binder influences comparisons are challenging, since the binder is electrically insulating, but still allows for a certain heat conduction.

5.2 Wet Mixing

For the variation of the wet mixing, four different extruders were used to produce graphite slurries. The three extruders by Thermo Fisher Scientific (TSE11, TSE16, TSE24) have an equivalent screw geometry and are thereby optimal for scale-up investigations. Moreover, the TSE18 extruder by Coperion with a different screw geometry was also compared to the lab scale extruder TSE11 which presents the initial state for the scale-up. To compare the electrodes produced from slurries mixed with different extruder dimensions, rotation speeds and mass flows within the extruder, a dimensionless number is used. The specific feed load (SFL) describes the filling degree and flow profile within the extruders. The SFL is defined according to Equation 5.1 with the volume flow rate $\dot{V}$, the rotation speed of the screws n and the outer screw diameter D_s. [159]

$$\mathrm{SFL} = \frac{\dot{V}}{n \cdot D_\mathrm{s}^3} \tag{5.1}$$

Six values of SFL as combinations of rotation speed and mass flow were chosen and kept constant during scale-up of the slurry production rate by adjusting the mass flow. For the visualization, the reciprocal of the specific feed load – SFL^{-1} – was used. The SFL^{-1} for all electrode slurries used in the mixing variation are given in Table A.9 in the Appendix.

Generally, higher values of SFL^{-1} represent a lower filling degree within the extruder. Thus, the total energy input is partitioned between a lower amount of material resulting in a higher specific mechanical energy input (SEI) and a stronger fragmentation of the material. This behavior can be seen with the aid of Figure 5.2 (a) which shows the porosity of the electrode coatings with regard to the SFL^{-1} applied during extruder mixing. The porosity of the coating shows a decreasing trend with an increasing SFL^{-1}. The stronger fragmentation and de-agglomeration of the CB particles leads to a higher fraction of smaller particles. These may arrange themselves within the hollows of the larger particles and thereby reduce the overall porosity. Furthermore, the porosity values of the

electrodes are in a similar range for the different extruders applied in the mixing step, when considering their uncertainties.

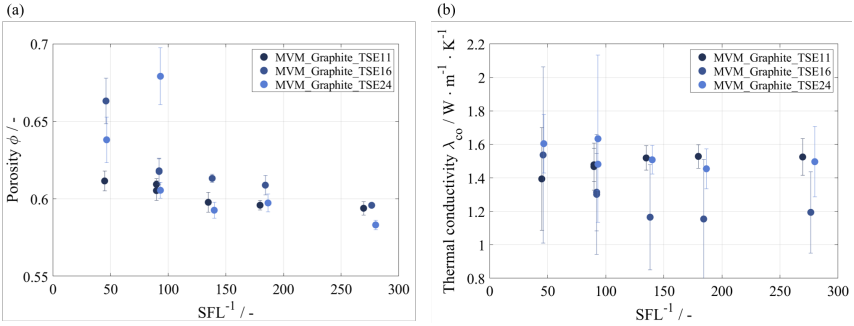

Figure 5.2: Impact of the specific feed load on (a) the porosity and (b) the thermal conductivity of the coating for different extruders by Thermo Fisher Scientific (TSE11, TSE16 and TSE24) and varied settings for the rotation speed and mass flow.

Figure 5.2 (b) exhibits the thermal conductivity of the coatings with respect to the SFL^{-1} during mixing. No significant impact of the rotation speed and mass flow on the thermal transport properties could be found. There are also no significant differences between the different extruder dimensions visible. Therefore it can be concluded that the scaling up of the slurry production rate based on a constant SFL has no considerable impact on the thermal transport properties.

Additionally, a comparison of the TSE11 and TSE18 extruder with different screw geometries was conducted, following the investigation by Meza Gonzalez et al. [159]. The results for the porosity and thermal conductivity of the coating with respect to SFL^{-1} are given in Figure 5.3. The elelctrodes produced with the TSE18 extruder show slightly higher porosities implying an inferior fragmentation of the material in comparison to the TSE11 which is confirmed by the particle size distributions [244]. The thermal conductivity is in a similar range for both extruders.

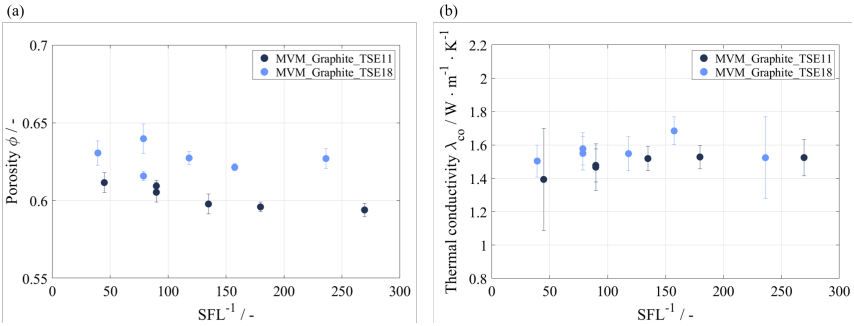

Figure 5.3: Impact of the specific feed load on (a) the porosity and (b) the thermal conductivity of the coating for the TSE11 and TSE18 extruder with different screw geometries.

5.3 Wet Coating

During the coating process, the mass loading and thus the coating thickness of the electrodes was varied. The influence of the coating thickness on the effective thermal conductivity of the uncalendered electrodes is given in Figure 5.4. Especially the graphite electrodes and the HC electrode with the lowest thickness show a strong scattering and therefore a high uncertainty of the thermal conductivity values.

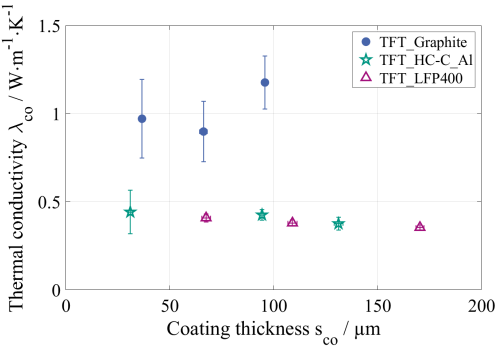

Figure 5.4: Impact of the coating thickness on the effective thermal conductivity of the electrode coating for graphite, HC and LFP processed with a drying rate of 0.75 $g \cdot m^{-2} \cdot s^{-1}$.

For the LFP electrodes, a slight decrease of the thermal conductivity of approx. 13 % can be observed with increasing coating thickness, while graphite and HC show no significant impact of the coating thickness.

The investigations carried out on the same samples by Klemens et al. [74] allow for a comparison with the mechanical properties. Klemens et al. observed a drop in the adhesion strength with increasing coating thickness, which was especially strong for the variation between the lowest and mean thickness (see Figure 2.17). The trend was very similar for the different active materials. It is concluded that the increased drying times for higher coating thicknesses result in a stronger binder migration [74]. Due to the lower concentration of the binder at the coating-current collector interface, the adhesion strength is reduced. However, for the graphite and HC electrode, this effect does not seem to have a significant impact on the effective thermal conductivity in the regarded range of the coating thickness. Changes in the thermal contact resistance at the interface would also show in the resulting thermal conductivity of the coating, which might explain the decrease for LFP with increased coating thickness.

5.4 Drying

During the drying process of the investigated electrodes, the heat transfer coefficient and the film temperature were set to achieve a constant and well defined drying rate. The effective thermal conductivity of the coating is shown in Figure 5.5 as a function of the drying rate. The graphite samples again show a high uncertainty due to strong scattering. All the electrodes show fairly constant values and no significant impact of the drying rate can be found for any AM. The tendency to a higher effective thermal conductivity for electrodes with larger AM particles does not change with higher drying rate. For the LFP electrodes, however, the differences between the LFP200 and LFP400 electrodes become insignificant at higher drying rate.

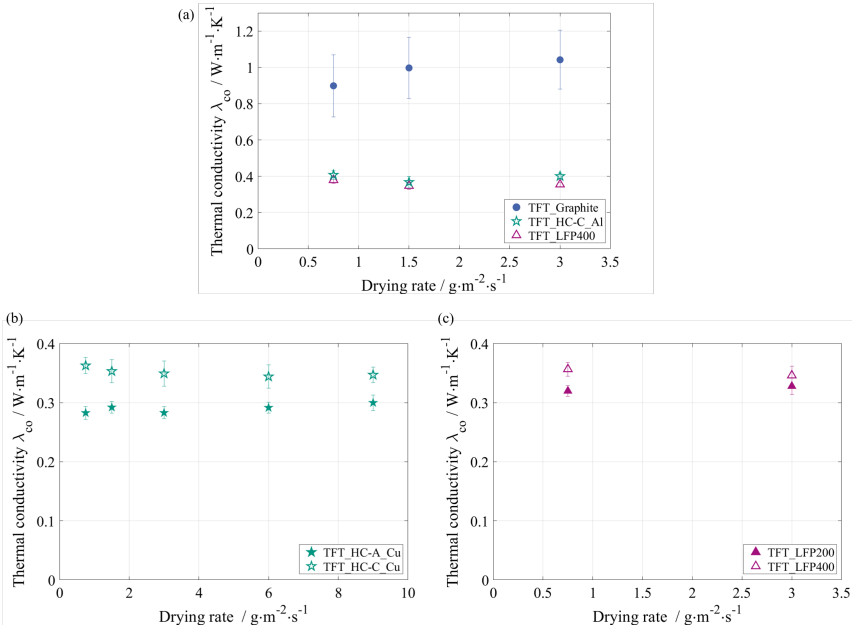

Figure 5.5: (a) Impact of the drying rate on the effective thermal conductivity of the electrode coating with a dry film thickness of approx. 67 µm for graphite, 94 µm for HC and 109 µm for LFP. (b) Combined impact of drying rate and mean particle size on the thermal conductivity of the HC electrodes and (c) the LFP electrodes.

The adhesion strength of the electrodes in Figure 5.5 (a) was previously investigated by Klemens et al. [74]. The results are given in Figure 2.21 in a normalized form. A strong decrease of the adhesion strength with increasing drying rate was observed for the graphite electrodes, while the decrease was moderate for the LFP electrodes and no significant change was visible for the HC-C electrodes. A comparison with the data of a different study by Klemens et al. [73] suggests, that the drop in adhesion strength only happens for higher drying rates for HC-C as was also shown in Figure 2.15.

In terms of the electrical behavior, a decrease in the electrical conductivity – equivalent to an increase in the resistivity – has been observed in the literature [72, 83, 181]. This is also reflected by an increase in the interface resistance

between coating and current collector [85]. The decrease in electrical conductivity can be explained by the more inhomogeneous microstructure with increasing drying rate. Hereby, insulating binder layers are formed in the upper layer of the electrode and the electrical contacts in the bottom layer are impaired due to a reduced concentration of carbon black [71, 79, 83].

Considering the thermal conductivity data, the binder migration does not seem to have a significant impact. It is reasonable that the thermal behavior is different from the electrical behavior here since the binder or rather BCB phase is not completely insulating in terms of heat transport. Although it has a comparably low thermal conductivity and, thus, longer conduction paths through the BCB phase should have a negative impact, the simultaneous increase in the contact area might balance this out. Additionally, the AM particles move closer together in the bottom layer due to the reduced BCB content and, thus, the fraction of the better conducting AM particles in the pathways is increased.

5.5 Calendering

The calendering process represents the production step most extensively studied in this work. The thermal conductivity and thermal resistance depicted in this section are always plotted over a decreasing porosity which complies with an increasing degree of calendering.

5.5.1 LFA Measurements

First investigations on the impact of the calendering were carried our with graphite and NMC electrodes [36]. Opposed to the previously published study, the thermal conductivity of the electrode coating is depicted here instead of the effective value of the whole electrode stack.

The effective thermal conductivity of both NMC cathodes – IAM_NMC622 and CC_NMC811 – is given in Figure 5.6. Both electrodes first show a decrease in the thermal conductivity with decreasing porosity and then an increase.

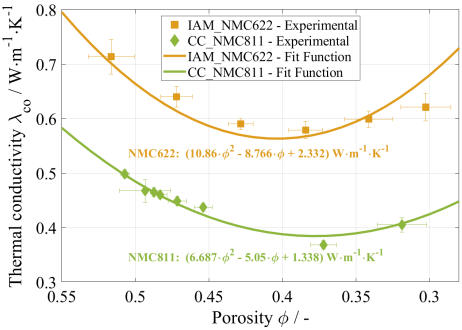

Figure 5.6: Thermal conductivity of the coating of varyingly strong calendered NMC electrodes. Besides the experimental data, quadratic fit functions and the corresponding equations are given.

The adhesion strength between coating and current collector shows a similar behavior for NMC electrodes in studies available in the literature. This means that the adhesion strength also first decreases and then increases again with decreasing porosity with a minimum at approx. 0.35 [140, 196, 197]. However, the starting porosity was also lower than in the present work for most of the electrodes in the literature.

The reduction of the adhesion strength is usually attributed to the shear forces occurring between the two layers during the calendering process and impair the connection [197]. For sufficiently high line loads, the active material particles are then pressed into the relatively soft aluminum current collector foil leading to a larger contact area and a higher adhesion strength [197]. This behavior was observed by several authors for cathodes with rigid active material particles like NMC and LFP [60, 77, 140, 196–199]. It is also evident from the SEM images of the ion-milled cross-sections of the NMC622 electrodes used in this study as depicted in Figure 5.7 (a). While the first two samples do not show any

penetration of the particles into the current collector, the particles are pressed into the aluminum for the most strongly calendered sample.

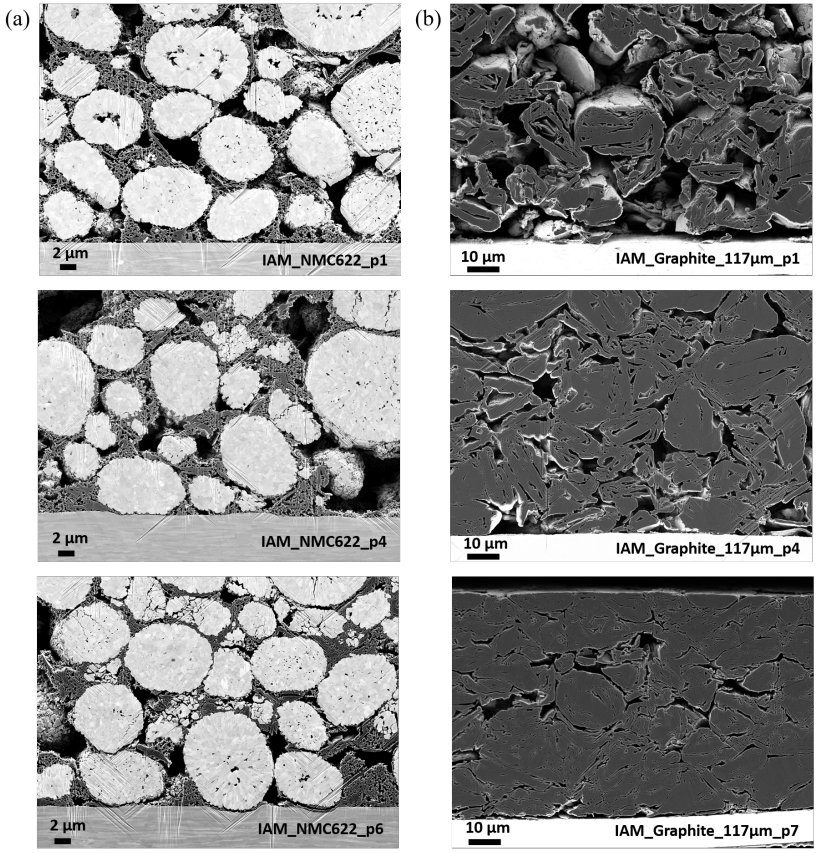

Figure 5.7: SEM images of the ion-milled cross-sections of (a) the IAM_NMC622 cathodes and (b) the IAM_Graphite_117µm anodes: Uncalendered sample (top), sheet at the minimum of the thermal conductivity (center), and most strongly calendered sample (bottom) (adjusted from Gandert et al. [36], Creative Commons Attribution 4.0 License CC BY).

The u-shaped course of the adhesion strength was found for different cathode compositions with PVDF as binder, NMC111 or NMC622 as AM, with and

without graphite additive and with different mass fractions of binder and CB [140, 196, 197]. Assuming that the course can be transferred to the electrodes in this work, these mechanical observations might also explain the change in the effective thermal conductivity. As the thermal contact resistance at the interface is included in the calculation of the thermal conductivity of the coating, a deterioration and subsequent improvement of the contact quality would reflect in a decrease and then increase of the coating's thermal conductivity.

However, the adhesion strength is only a measure for the changes at the interface. Beyond that, there may also be changes happening to the structure of the electrode coating itself. These might include the delamination or breakage of binder connections for minor compression rates. Unfortunately, there is yet no known literature describing this behavior. A more commonly observed behavior is the breakage of particles [82, 245], which can happen for very high line loads. This can also be seen in the SEM images for the most strongly calendered cathode in this study (IAM_NMC622_p6) and can be noticed to some extent for the less strongly calendered sheet IAM_NMC622_p4.

Regarding the influence of the calendering on the electrical properties of the electrodes, Sangrós Giménez et al. [82] have conducted a study with NMC111. Their measurements suggest that the electrical conductivity of the cathode stacks increases with the porosity decreasing from $\phi = 0.417$ to $\phi = 0.270$. In this range of the porosity, the thermal conductivity is increasing as well. However, far higher porosities and even uncalendered samples were investigated in the present study, while the sample with the highest porosity of $\phi = 0.417$ used by Sangrós Giménez et al. was already calendered. Thus, it leaves unclear, if a drop in the electrical conductivity would occur in the range between $\phi = 0.522$ and $\phi = 0.417$ as it does for the effective thermal conductivity in the present work. A similar behavior with a monotonously increasing electrical conductivity with an increasing compaction pressure was found by Zhang et al. [246].

Moreover, using the fit functions for comparison, it is evident from Figure 5.6 that the effective thermal conductivity of the NMC622 electrode coatings is between

36 % and 66 % higher than the effective thermal conductivity of the NMC811 electrode coatings. Regarding the current data situation, it is unclear if the bulk thermal conductivity of the NMC622 particles is higher than that of the NMC811 particles. However, it is assumed that possible differences in the AM thermal conductivity are not the most important contributing factor to the differences in the coating thermal conductivity. Instead, it is assumed that the higher thermal conductivity of the NMC622 coating might stem from the higher fraction of carbon black and the additional use of conductive graphite. They both have a significantly higher thermal conductivity than the NMC and binder with approx. 24 $\mathrm{W{\cdot}m^{-1}{\cdot}K^{-1}}$ for carbon black [113] and a mean value of approx. 139.6 $\mathrm{W{\cdot}m^{-1}{\cdot}K^{-1}}$ [49, 225, 226] for graphite.

With IAM_Graphite_70µm and IAM_Graphite_117µm two anodes with the same composition but different starting thicknesses are investigated. The results for their effective thermal conductivity with respect to a decreasing porosity are given in Figure 5.8. Here, the thermal conductivity also shows a decrease with decreasing porosity and then an even stronger increase going far beyond the initial value. The thermal conductivity of the two electrodes is in a similar range for high porosities which is in line with the observations for uncalendered graphite electrodes with different coating thicknesses in Section 5.3. However, a deviation between the two electrodes becomes evident for porosities $\phi \lessapprox 0.4$. The thicker electrodes show significantly lower values here. This might be due to an underlying impact of the current collector which has a reduced influence with higher coating thickness. Furthermore, the binder migration might be more pronounced in the thicker samples. It is possible that its influence on the thermal conductivity only becomes apparent after calendering.

The mechanical changes happening during the calendering of graphite electrodes have been investigated by Billot et al. [202] and Scheffler et al. [78]. The results by Billot et al. do not show a clear u-shaped course of the adhesion strength between the coating and current collector over the porosity. Instead, for high calender temperatures of 125 °C a clearly increasing slope with decreasing porosity was found. For lower temperatures, which are more comparable to the 50 °C applied during the calendering in this work, the results by Billot et al. do not show a

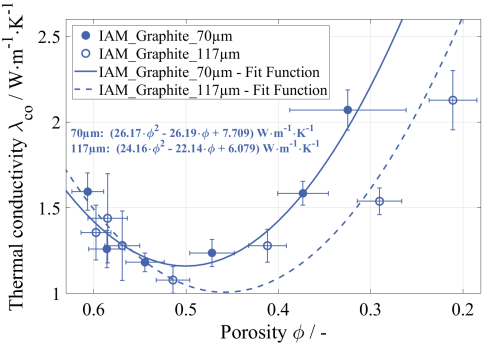

Figure 5.8: Thermal conductivity of the coating of varyingly strong calendered graphite electrodes with different starting thicknesses. Besides the experimental data, quadratic fit functions and the corresponding equations are given.

clear tendency. However, PVDF was used as binder by Billot et al., which might show a significantly different behavior than the CMC-SBR combination of the graphite electrodes in the present work. Scheffler et al. [78] used a CMC-SBR binder system with carbon black additive similar to the one in this work. Their measurements show a u-shaped course for the adhesion strength between coating and current collector. Similar to the cathodes, this supports the assumption that the effective thermal conductivity of the coating is impacted by the thermal contact resistance within the electrode stack.

The SEM images of the cross-section of the differently strong calendered samples in Figure 5.7 (b) give no indication of a deterioration and improvement of the connection at the interface. The most strongly calendered sample shows a slight gap between the coating and the current collector which can be explained by the strong shearing forces at high compression rates during calendering. This effect is particularly strong for graphite electrodes and might result in a partial delamination of the coating.

The thermal conductivity is the product of the thermal diffusivity and the volumetric heat capacity of the electrodes. To better understand the impact of both variables, it is reasonable to take a look at them separately as presented in the previous publication by Gandert et al. [36]. However, for this evaluation, the

thermal conductivity of the electrode stack must be used, since the electrode coating cannot be measured with the LFA on its own, and thus, no values for the thermal diffusivity of only the coating are available. Nevertheless, it still poses an interesting analysis for later discussion. The results for the NMC cathodes and graphite anodes are depicted in Figure 5.9. Hence, it can be followed that the increase in the thermal conductivity of the stack mainly stems from the increase in the volumetric heat capacity with decreasing porosity, while the decrease is solely due to the decrease in the thermal diffusivity.

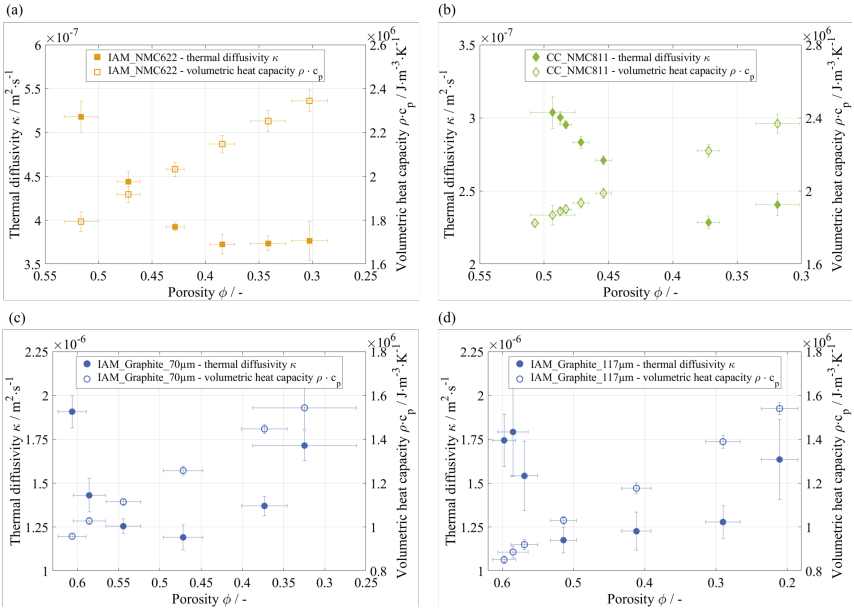

Figure 5.9: Effective thermal diffusivity and volumetric heat capacity of (a) the IAM_NMC622 cathode stacks, (b) the CC_NMC811 cathode stacks, (c) the IAM_Graphite_70µm anode stacks, and (d) the IAM_Graphite_117µm anode stacks in dependence on the porosity at a set temperature of 20 °C (adjusted from Gandert et al. [36], Creative Commons Attribution 4.0 License CC BY).

In addition to the comprehensive studies with the NMC and graphite electrodes, a first test of calendering was conducted with the TFT_HC-C_Cu electrodes

available from the variation of the drying rate. The results for different drying rates (0.75 $g \cdot m^{-2} \cdot s^{-1}$ and 6 $g \cdot m^{-2} \cdot s^{-1}$) are aggregated here, since the variation of the drying rate did not show a significant impact. As shown in Figure 5.10, the porosity could not be varied in a wide range, as a further increase of the force did not lead to a further compression of the coating. Mayer et al. [60] also showed that high line loads are needed for a significant compaction of HC electrodes. More than double the line load was necessary in comparison to NMC811 electrodes with a similar AM content to reach the same compaction rate [60].

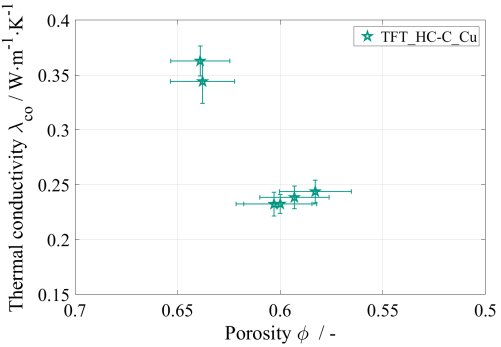

Figure 5.10: Thermal conductivity of the coating of HC electrodes calendered with different forces. The porosity could not be varied in a wide range here, as a further increase of the force did not lead to a further compression of the coating.

The results for two different calendering forces are shown here besides the uncalendered samples. Except for the calendered and uncalendered samples, no clustering occurs. Thus, even after calendering the drying rate does not seem to have a significant impact on the thermal conductivity for HC. Furthermore, in the case of HC, no variation can be found between the samples calendered with different forces.

However, a decrease in thermal conductivity can be observed for the first calendering step, which is in accordance with the other materials. Unfortunately, the investigations are insufficient to make further statements.

To allow for another investigation of the interconnection of the influences of the particle size, drying rate and degree of calendering, samples of TFT_LFP200 and TFT_LFP400 electrodes dried at 0.75 $g \cdot m^{-2} \cdot s^{-1}$ and 3 $g \cdot m^{-2} \cdot s^{-1}$ were subjected to calendering.

The results for the electrodes dried at 0.75 $g \cdot m^{-2} \cdot s^{-1}$ are depicted in Figure 5.11. They show a similar trend as that mentioned above with a decrease in the thermal conductivity at first and then an increase with decreasing porosity. Similar to the graphite electrodes, the enhancement is far more pronounced than the decline.

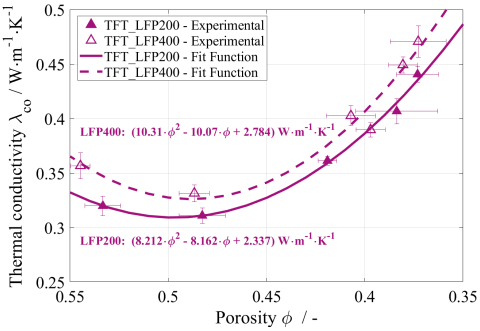

Figure 5.11: Thermal conductivity of the coating of LFP electrodes with different AM particle sizes x_{50} of 5.8 µm (LFP200) and 11.1 µm (LFP400), dried at a rate of 0.75 $g \cdot m^{-2} \cdot s^{-1}$ and calendered to different porosities. Besides the experimental data, quadratic fit functions and the corresponding equations are given.

As shown in Figure 5.12, the electrodes dried with the higher drying rate exhibit a higher scattering which is already observable for the uncalendered samples. The use of fit functions is not meaningful in this case and a differentiation between the LFP200 and LFP400 electrodes is difficult. Generally, a trend towards a higher thermal conductivity with decreasing porosity can be observed.

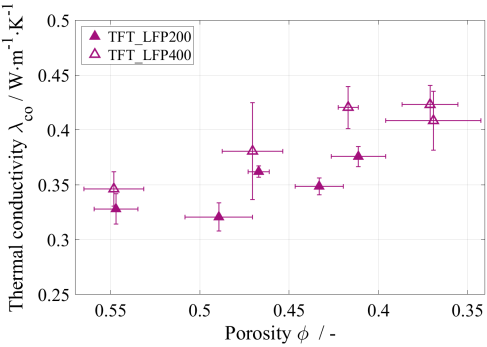

Figure 5.12: Thermal conductivity of the coating of LFP electrodes with different AM particle sizes x_{50} of 11.1 µm (LFP400) and 5.8 µm (LFP200), dried at a rate of 3 g·m^{-2}·s^{-1} and calendered to different porosities.

5.5.2 Comparison with Model-Based Thermal Conductivities

The analytical model introduced by Oehler et al. [32, 34, 113] was described in detail in Section 4.1. While it takes the properties of different active materials and the compositions of the electrodes into account, the particle size distribution is not considered in the model. This is why the same results are obtained for the TFT_LFP200 and TFT_LFP400 electrodes. The results from the model with helium as pore-filling fluid and the corresponding experimental data are given in Figure 5.13 for IAM_NMC622, CC_NMC811, IAM_Graphite and TFT_LFP. For the TFT_HC electrodes at a porosity of 0.6 the model predicts a thermal conductivity of approx. 0.6 W·m^{-1}·K^{-1} which is more than a factor 2 higher than the measured value. The compositions and material properties of the single components applied in the model can be found in Section 4.1.

In contradiction to the experimental results, the model shows a monotonous increase of the effective thermal conductivity with decreasing porosity. Except for the LFP, the model reveals higher values than the measurements for porosities $\phi < 0.5$ and the deviations increase and become significant with decreasing porosity. In this regard, it should be noted that a significantly lower AM thermal

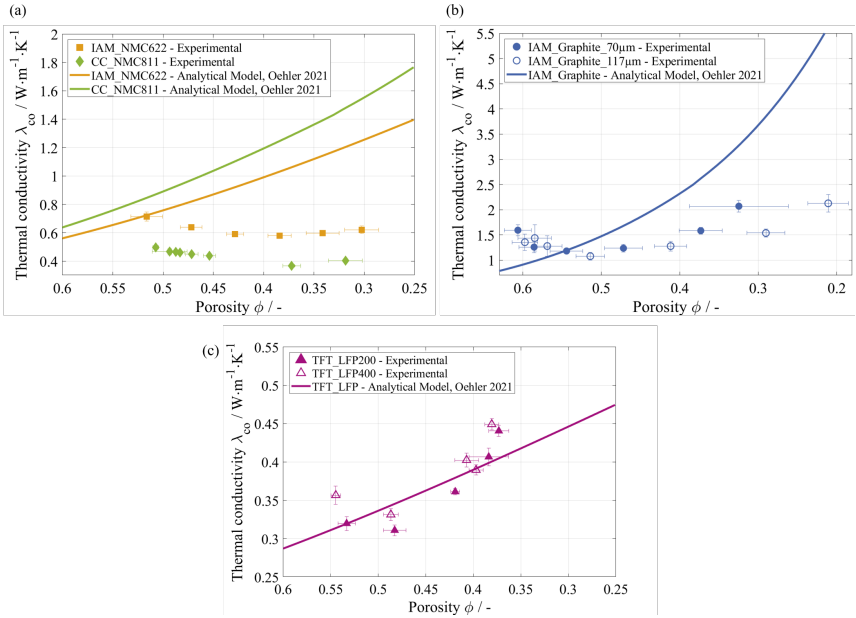

Figure 5.13: Experimental data and results of the analytical model by Oehler et al. [32, 34, 113] for the effective thermal conductivity of the coatings of (a) the NMC electrodes, (b) the graphite electrodes and (c) the LFP electrodes dried at 0.75 g·m^{-2}·s^{-1} as a function of the porosity ((a) and (b) adjusted from Gandert et al. [36, 220], Creative Commons Attribution 4.0 License CC BY).

conductivity was assumed for the LFP electrodes resulting in a similar range of values for modeled and experimental data. This raises the assumption that the AM and its high thermal conductivity in comparison to the BCB phase is too heavily weighted in the model.

It becomes apparent that the model predicts higher thermal conductivities for the CC_NMC811 electrodes in comparison to IAM_NMC622 electrodes, although the IAM_NMC622 electrodes showed higher values than the CC_NMC811 electrodes in the experimental results. This can be explained by the graphite additive within the IAM_NMC622 electrodes that presumably has a positive effect on the thermal conductivity. However, as discussed in Section 4.1, the present state of

the model does not allow a reasonable consideration of the large additive particles with high bulk thermal conductivity.

The generally high deviations between model and experimental data are also observable in the work by Oehler [34]. The model showed up to 30 % higher values for the anodes with an assumed thermal conductivity of the AM of 139 $W \cdot m^{-1} \cdot K^{-1}$ based on graphite. For the cathodes the model showed up to 95 % higher values with an assumed thermal conductivity of the AM of 4.3 $W \cdot m^{-1} \cdot K^{-1}$ based on NMC. Thus, a significantly larger deviation was found for the cathodes. This discrepancy between the model and the experimental data might be explained by the consideration of the binder phase. In the calculations of the data shown in Figure 5.13, the inner porosity of the BCB phase has not been considered, as its determination would have gone beyond the scope of this work. However, SEM images like the one given in Figure 5.7 and 5.14 indicate that such inner porosity might be significant for the investigated electrodes and can be an explanation of the observed deviations between measurement and model prediction. This is expected to be especially true for the PVDF-based BCB phase of the NMC cathodes. Particularly for measurements conducted in a gas phase, the inner porosity of the BCB phase might result in a considerable reduction of the thermal conductivity.

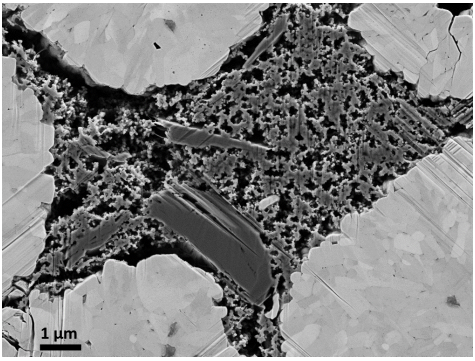

Figure 5.14: SEM image of the BCB phase in the IAM_NMC622_p6 cathode (reproduced from Gandert et al. [220], Creative Commons Attribution 4.0 License CC BY).

An additional factor to consider is the thermal conductivity according to Knudsen or Smoluchowski. As already mentioned in Section 5.1, the thermal conductivity of the gas within the discontinuum of the small pores might be significantly reduced in comparison to the continuum value used in the model [34, 240, 241]. An investigation of this effect was conducted by Oehler [34] (Appendix I) assuming a reduction of the thermal conductivity of the helium from 0.15 $W \cdot m^{-1} \cdot K^{-1}$ to 0.5 $W \cdot m^{-1} \cdot K^{-1}$. According to the data presented by Oehler [34], this effect can lead to a reduction of the calculated effective thermal conductivity of the electrode coating by up to 20 %.

Another model to consider for a comparison with the experimental data is the one by Sangrós et al. [49] for graphite anodes. The calculations predict a monotonous increase of the thermal conductivity with decreasing porosity as was shown in Figure 2.24. This effect is expected to be increasingly strong with elevated particle size. However, the BCB phase is neglected completely in the model. Furthermore, the graphite particles are described by spheres, although flat and uneven flake-like shapes are more realistic for this anode active material [146]. A direct comparison between the data obtained in the present work and the results by Sangrós et al. is not reasonable. A different composition was used in the mentioned study and an implementation of the model and simulation with the electrode compositions used in the present study is out of the scope of this work.

As a result, both models describe a monotonously increasing slope with decreasing porosity. While the model by Oehler [34] seems to overestimate the thermal conductivity, the model by Sangrós et al. [49] leads to lower values than the experiments in the considered porosity range conducted in the present study. For both models, the porosity is the main influencing factor. Changes in the microstructure such as the breakage or build up of new connections occurring during the process of calendering [197] were not considered in the calculation underlying the data in Figure 5.13. However, the models reflect the expectations that the effective thermal conductivity must increase with decreasing porosity and thus increasing volume fraction of the active material, since the active material has a significantly higher thermal conductivity than the fluid phase. The exact changes brought to the microstructure by calendering could not be taken into

account here, as they require new parameterizations or extensions of the models that are outside the scope of this work.

5.5.3 Applicability of the LFA and GHP Method

The content of this section is based on investigations conducted at NTNU. In addition to the previously used LFA, the thermal conductivity of the IAM_NMC622 and IAM_Graphite_70µm electrodes were measured with the GHP method. The findings were published in a joint paper [93].

In the following, firstly, the results obtained with the LFA and GHP are compared and their disparities are discussed. Secondly, various hypotheses are proposed that could explain the differences in the results and expectations for the true values are discussed.

The results for the coating thermal conductivity of the differently calendered IAM_NMC622 and IAM_Graphite_70µm electrodes for the different measurement methods are given in Figure 5.15. As shown in the literature, the purge gas applied during the measurement can have a significant impact on the obtained thermal conductivity for porous samples in a similar range of thermal conductivities [217, 247]. This is why the LFA measurements in both helium and nitrogen atmosphere are included in this comparison. Moreover, several authors showed that the pressure has a significant impact on the thermal conductivity resulting from the GHP measurements [41, 42, 44]. Therefore, the results of the GHP measurements at the lowest and highest applied pressure of 2 bar and 6 bar are given here.

Opposed to the u-shaped slope obtained with the LFA measurements, the GHP measurements of the IAM_NMC622 electrodes suggest a slight increase of the effective thermal conductivity of the coating with decreasing porosity. No decrease was found with the GHP method. The measurements at 6 bar yield a 0.05 $W \cdot m^{-1} \cdot K^{-1}$ to 0.1 $W \cdot m^{-1} \cdot K^{-1}$ higher thermal conductivity than the measurements at 2 bar. Under consideration of the uncertainty, the enhancement of

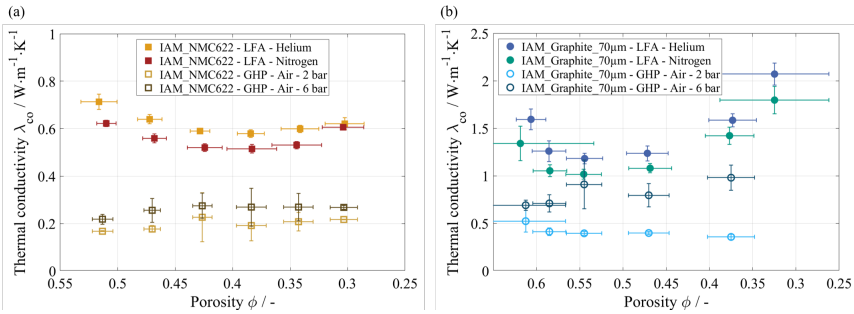

Figure 5.15: Comparison of the effective thermal conductivity of the electrode coating of (a) the differently strong calendered IAM_NMC622 cathodes and (b) the IAM_Graphite_70µm anodes obtained with the laser flash analysis (LFA) in helium and nitrogen atmosphere and the guarded hot plate method (GHP) in air at 2 bar and 6 bar. The LFA data were evaluated with the penetration model for porous samples in the NETZSCH software. The most strongly calendered graphite sheet could not be measured with the GHP method due to material scarcity. The data is plotted versus a decreasing porosity, which is equivalent to an increasing degree of calendering (adjusted from Gandert et al. [93], Creative Commons Attribution 4.0 License CC BY).

the thermal conductivity by the pressure increase is of a similar extent for all the differently calendered samples.

Using the nitrogen data for the LFA and the GHP data obtained at 2 bar for the comparison, the LFA measurements deliver values that are by a factor of 2.3 to 3.8 higher than that of the GHP measurements. This is in line with the expectations from the literature analysis in Section 2.1.4. However, the results of the two methods also show a different slope, particularly in the range of higher porosities between 0.4 and 0.55.

As comprehensively discussed above, the results of the LFA measurements also show a u-shaped course for the IAM_Graphite_70µm electrodes. The results measured in nitrogen are by a factor of 2.5 to 4.0 higher than the values obtained by the GHP at 2 bar. However, the GHP measurements of the IAM_Graphite_70µm electrodes show a picture different to that of the IAM_NMC622 electrodes. Here, the GHP measurements at 2 bar deliver fairly constant values. However, the pressure increase leads to a significant increase of the thermal conductivity of the IAM_Graphite_70µm coatings which is especially strong for the strongly

calendered electrodes. As a result, the thermal conductivity at 6 bar exhibits an increase with decreasing porosity.

The strong deviations between the results of the two methods give rise to the question which method's results are closer to the true value. The following paragraphs discuss the comparability of the results, potential error sources for both methods and how these are reflected in the obtained thermal conductivity values.

I. Thickness Measurements

It is noteworthy that different devices were used for the thickness measurement of the electrode samples and the measurements were conducted two years apart. As the thickness is an important determinant in both evaluation routes, deviations herein could also lead to differences in the thermal conductivity. However, the resulting thickness values of the samples obtained at KIT and NTNU showed no significant deviations for both the NMC622 and graphite electrodes (see Figure 5.16). Thus, a significant impact of the thickness measurements on the resulting thermal conductivity values is excluded.

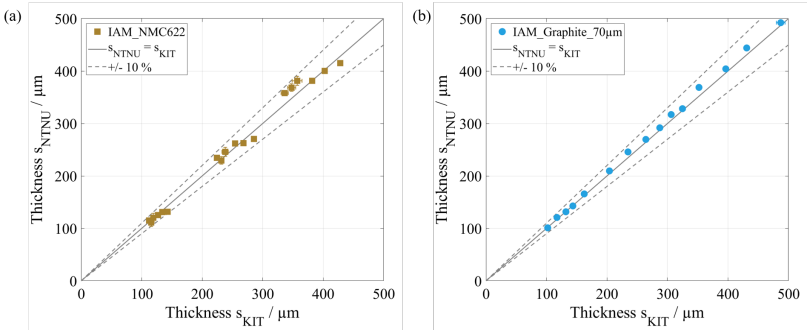

Figure 5.16: Comparison of the sample thickness of (a) the IAM_NMC622 cathode stacks and (b) the IAM_Graphite_70µm anode stacks measured with a micrometer for the LFA at KIT and with a micrometer within the GHP rig at NTNU for different layer numbers and porosities (adjusted from Gandert et al. [216], Creative Commons Attribution 4.0 License CC BY).

II. Fluid within the Pores

The helium generally used for the LFA measurements has a thermal conductivity of approx. 0.152 $W \cdot m^{-1} \cdot K^{-1}$ at 20 °C [235] in continuum and thereby provides a significantly better heat conduction than the air used for the GHP measurements with a thermal conductivity of approx. 0.026 $W \cdot m^{-1} \cdot K^{-1}$ at 20 °C [235]. However, nitrogen and air compare well in their thermal conductivity. Using nitrogen in the LFA measurements leads to notably lower thermal conductivity values and therefore should rather be used for a comparison of the two methods.

III. Different Evaluation Methods (LFA)

Most approaches for the evaluation of laser flash measurements assume solid, non-porous, homogeneous samples with isotropic transport properties as these feature the lowest complexity. The original model by Parker et al. [98] is based on adiabatic boundary conditions, meaning that no heat loss occurs in axial and radial direction. The function describing the dimensionless temperature rise at the backside of the sample for this most basic case is given in Equation (5.2) with the time t and sample thickness L [237]. x is the coordinate in axial direction and r the coordinate in radial direction.

$$T(x = L, r = 0, t) = 1 + 2 \sum_{i=1}^{\infty} (-1)^i e^{\frac{-i^2 \pi^2 \kappa t}{L^2}} \tag{5.2}$$

Especially for long durations until the maximum temperature is reached, it becomes very important to take the heat loss to the environment into account. Due to the low thickness of the electrode samples and the significantly shorter pulses in comparison to literature, heat loss is expected not to be particularly significant for the present investigations. However, the common approach by Cape and Lehmann [100] is said to also work well for taking into account the heat loss due to non-ideal sample geometries and the contact towards the sample holder. Both

are possible influencing factors in the present work and thus make an examination of the heat loss approach worthwhile.

As the standard models for the evaluation of laser flash measurements of solid samples are not suited for the application to porous materials, several authors [32, 37, 248] have recommended the model proposed by McMasters et al. [103] for the evaluation of battery electrodes instead. This approach assumes an uneven surface of the sample and takes the penetration of the laser into those pores into account. Thus, it is termed the "penetration model" in the following.

As a consequence, the assumption is made that not all of the radiation energy is absorbed at the surface of the sample, $x = 0$, but partially beyond the sample surface at $x > 0$. Thus, some of the heat is conducted through a shorter distance than the full sample thickness L. Assuming heat is absorbed according to Beer's law an exponential temperature profile is presumed for the initial time $t = 0$. The systematic derivation of the considered approach is given by McMasters et al. [103]. Generally, this approach results in a lower thermal diffusivity and thus a lower thermal conductivity in comparison to the standard model (Cape and Lehmann) for the same sample thickness.

The results of both, the standard heat loss model and the penetration model implemented in the Proteus LFA Analysis software (NETZSCH-Gerätebau GmbH, Germany), for the measurements carried out in nitrogen are depicted in Figure 5.17. According to NETZSCH the standard model is implemented according to Cape and Lehmann [100] and the penetration model is based on the derivations by McMasters et al. [103]. As expected, the penetration model delivers lower values for the thermal conductivity. Thus, it is possible that the evaluation approach for porous materials underestimates the actual thermal conductivity and that the true thermal conductivity of the material is even higher.

Since battery electrodes consist of at least two different layers – the coating and the current collector – and are thereby inhomogeneous and highly non-isotropic, they potentially exhibit challenges for all mentioned evaluation approaches. The comparison of the standard and penetration model for measurements conducted in helium is given in Figure 5.18. Herein, the penetration model leads to higher values

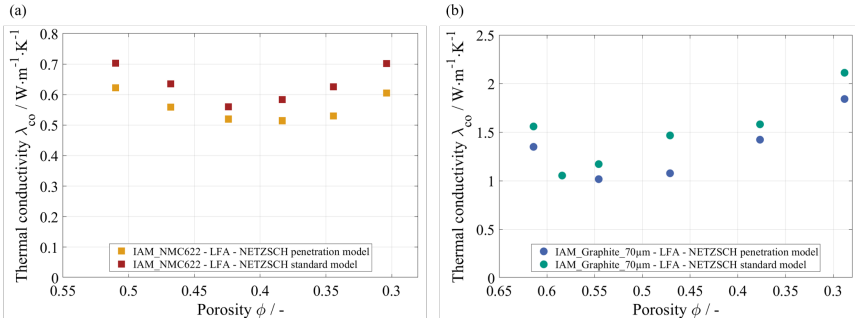

Figure 5.17: Effective thermal conductivity of the coating of (a) the IAM_NMC622 cathodes and (b) the IAM_Graphite_70µm anodes measured in nitrogen resulting from the evaluation with different models in the NETZSCH software. The value obtained with the penetration model for the IAM_Graphite_p2 electrode at a porosity of $\phi = 0.58$ is hidden behind the data point calculated with the standard model (adjusted from Gandert et al. [93], Creative Commons Attribution 4.0 License CC BY).

than the standard model for multiple samples – especially those of the graphite electrodes. This contradicts the expectations, and no clear trend can be found. This behavior might be explained in part by the relatively high thermal conductivity of helium, which possibly leads to an increase in heat loss to the environment. To what extent helium as applied gas is responsible for the inconsistencies stays unclear, as the source code for the fitting and calculation in the NETZSCH software is not accessible.

IV. Penetration Depth of the Light Pulse (LFA)

In the context of the light penetrating into the pores of the electrode samples, it is worthwhile to take a look at the SEM images of the cross sections of the electrodes (see Figure 5.19 (a) and (b)). These indicate that the penetration of the light pulse is reduced with increasing degree of calendering and thus the reduction of the porosity and surface roughness.

A quantitative comparison of the pore depth distribution of the differently calendered sheets is possible with the profilometer measurements of the surface

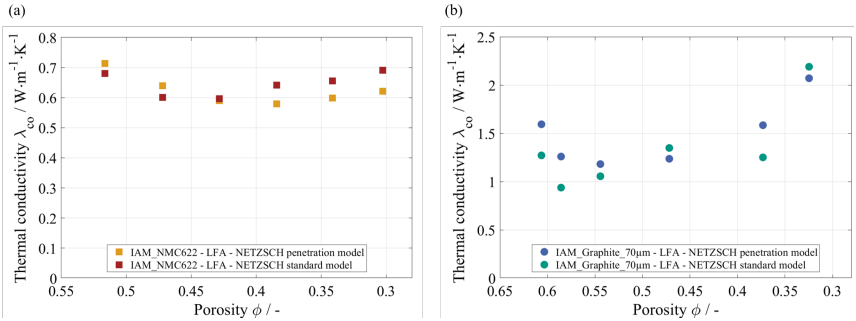

Figure 5.18: Effective thermal conductivity of the coating of (a) the IAM_NMC622 cathodes and (b) the IAM_Graphite_70µm anodes measured in helium resulting from the evaluation with different models in the NETZSCH software.

roughness as described in Section 3.9. The fitted distribution curves for the IAM_NMC622 and IAM_Graphite_70µm electrodes at the different degrees of calendering are given in Figure 5.19 (c) and (d). The data were fitted using the Kernel smoothing function in MATLAB® with a bandwidth of 500 nm.

In line with the expectations, the mean value of the pore depth distribution decreases with an increasing degree of calendering and thus a decreasing porosity. However, especially for the highly porous samples, the penetration depth might not be properly taken into account by the evaluation model. The penetration model by McMasters et al. [103] assumes that the porous material is effectively translucent which allows for Beer's law to be applied. If the translucence is due to the porous nature of an otherwise opaque material, the voids must be very small compared to the thickness of the sample in order for the material to be treated as a continuum. As can be seen in Figure 5.19, the size of the irregularities in the samples constitutes a large fraction of the material thickness and thereby undermines the validity of the continuum assumption. Although the solid portions of the material are quite opaque, the large relative scale of the irregularities within the coating and particularly at the surface, makes the applicability of the penetration model to evaluate LFA measurements of highly porous samples questionable. This could also mean that the depth of the light penetration is not properly considered by the penetration model which would lead

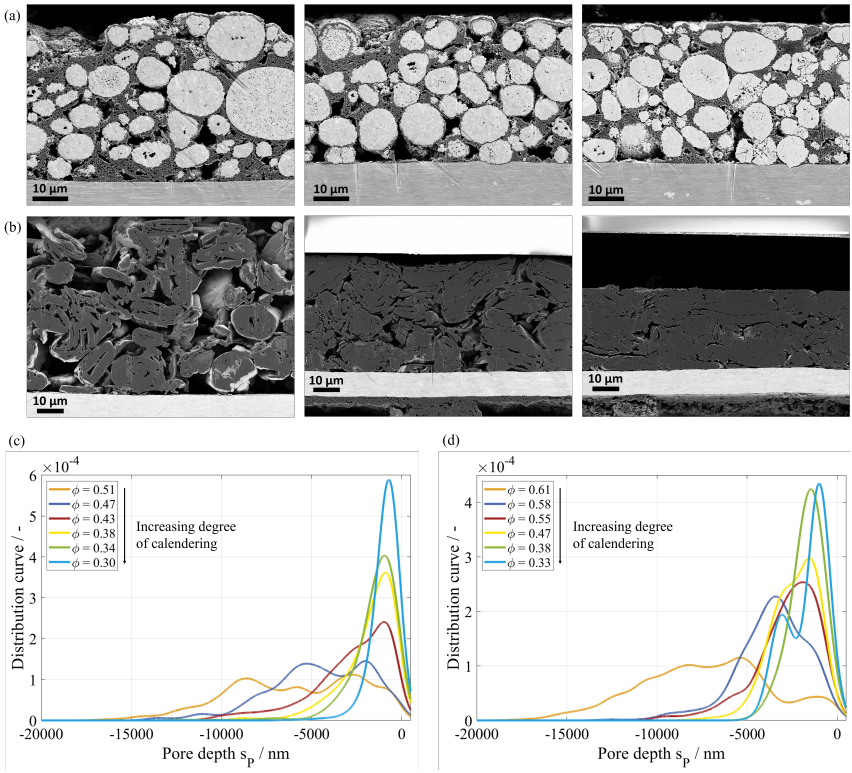

Figure 5.19: SEM images of the ion-milled cross sections of (a) the NMC622 electrodes at a porosity of 0.51, 0.38 and 0.30 and (b) the graphite electrodes at a porosity of 0.61, 0.48 and 0.33 and pore depth distributions of (c) the NMC622 electrodes and (d) the graphite electrodes (reproduced from Gandert et al. [93], Creative Commons Attribution 4.0 License CC BY).

to high errors, especially for highly porous, uncalendered samples, and might explain the differences in slope of the results of the LFA and GHP method.

To further analyze the importance of the light penetration, uncalendered graphite electrodes with coating thicknesses between 100 µm and 700 µm were measured

with the LFA. Thereby, the variation of the coating thickness presented in Section 5.3 was driven even further into a range of the coating thickness that is not realistic for the application in battery cells but constitutes an extreme case.

These investigations are based on the idea that the ratio of the penetration depth relative to the total thickness decreases as the coating thickness increases, assuming that the absolute penetration depth stays the same. This way, the impact of the light penetration on the resulting thermal conductivity should be reduced as well. Therefore, it is expected that the results asymptotically approach the true value of the thermal conductivity with increasing coating thickness. The results are depicted in Figure 5.20 (a).

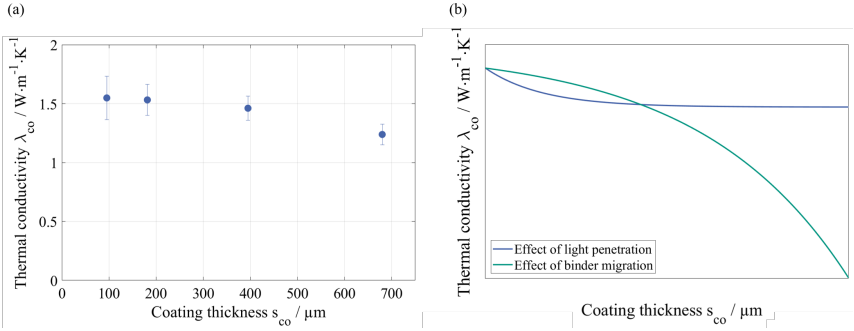

Figure 5.20: (a) Effective thermal conductivity of uncalendered graphite anode coatings with varied thickness measured with the LFA in helium and evaluated with the penetration model. (b) Expected slope of the effective thermal conductivity with varied thickness considering the effect of the light penetration and the effect of binder migration (reproduced from Gandert et al. [216], Creative Commons Attribution 4.0 License CC BY).

Against the expectations, a decrease with increasing slope is observed. It is assumed that a superposition of the effects of the binder migration during drying and the light penetration during the measurements might occur here. The expected qualitative course of the thermal conductivity for the separate effects is given in Figure 5.20 (b). Regarding the light penetration, a decrease of the thermal conductivity and subsequent approach of an asymptote is expected with increasing coating thickness.

The binder migration leads to an accumulation of the binder in the top layer and a depletion of binder in the bottom layer and thus results in a very inhomogeneous binder distribution. However, previous studies by Burheim et al. [97] with PTFE in fuel cell components suggest that the change in binder concentration does not have a significant impact of the thermal conductivity of the compound layer in the considered range. These results are expected to be transferable to battery electrodes since the investigated micro porous layers for fuel cells also contain a polymer matrix with a thermal conductivity comparable to PVDF and SBR, which encloses the much better conducting carbonaceous material. Instead of the binder distribution within the coating, the growing decline might be reasoned by the coating-current collector interface. Here, the binder concentration is successively reduced with an increasing degree of binder migration which results in a low adhesion strength between coating and current collector. The 700 µm samples even showed delamination during sample preparation. It is expected that the impaired mechanical contact entails thermal contact resistances and thus a drop in the effective thermal conductivity.

Against this background, the increasing slope of the experimental data implies a significant impact of the binder migration in the considered thickness range and a superimposition of the two effects is assumed. Therefore, the results allow no final statement about the impact of the penetration depth and its consideration in the evaluation model on the effective thermal conductivity.

In this context, it was also possible to remove the 400 µm and 700 µm thick coatings from the current collector and to measure them separately. The corresponding thermal conductivity values are shown in Figure 5.21. The results clearly demonstrate a higher thermal conductivity for the coatings measured without the current collector. This might indicate the importance of the thermal contact resistance and that it significantly reduces the effective thermal conductivity when measured with the current collector. However, a cause from the measurement method can not be excluded, since the single coating has a highly porous, rough surface on both sides. This might influence the IR signal in the measurement.

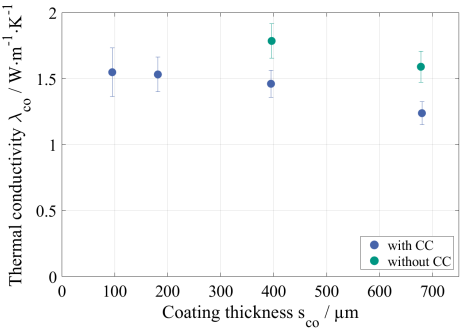

Figure 5.21: Comparison of the effective thermal conductivity of the coating layer of graphite anodes measured with and without current collector and calculated according to a series connection of the two layers.

V. Graphite Paint on the Current Collector (LFA)

For the LFA measurements, the metal side of the samples was coated with a thin layer of graphite spray of approx. 3 µm to 10 µm. With this layer an additional thermal resistance is added to the sample. The thickness of the graphite spray is neglected in the calculation of the coating thermal conductivity according to a series connection. Thus, it reduces the resulting thermal conductivity of the coating. This would suggest that the results obtained with the LFA are an underestimation and that the true thermal conductivity might even be higher. However the effect of the graphite spray is expected to be rather low and not the most significant in this analysis.

VI. Anisotropic Thermal Conductivity (LFA)

An investigation of the influence of radial heat losses on the thermal conductivity was conducted with the help of the FEM model presented in Section 4.2. The model considers the in-plane conduction within the sample and towards the current collector. The in-plane thermal conductivity of the two-layer electrode samples is orders of magnitude higher than the through-plane thermal conductivity due

to the good conduction path through the current collector. Generally, radial heat losses can be neglected for isotropic samples with $s << d$. However, due to the anisotropic character of the present samples, the radial conduction is expected to be much faster than the axial conduction and should thus be considered.

The coating thermal conductivity resulting from the different model geometries defined in Figure 4.2 is given in Table 5.2. The results suggest, that the graphite spray does have an impact with the set thermal conductivity of 0.2 $W \cdot m^{-1} \cdot K^{-1}$. However, the true thermal conductivity of the graphite spray is unknown and difficult to determine. More importantly, the results do not vary significantly between the different model geometries and thus suggest that the radial heat conduction does not have a substantial impact on the LFA measurements.

Table 5.2: Obtained thermal conductivity of the coating in $W \cdot m^{-1} \cdot K^{-1}$ for the most strongly calendered graphite anode sheet IAM_Graphite_70µm_p6 with different model geometries and boundary conditions. Either no graphite spray at all or a 3 µm thin layer was considered.

Boundary conditions	without graphite spray	with graphite spray
Reference case	1.810	1.565
18 mm disc	1.817	1.567
20 mm disc	1.817	1.567
18 mm disc with sample holder and 10 µm He contact resistance	1.822	1.570
18 mm disc with sample holder and without contact resistance	1.819	1.570
20 mm disc with sample holder and without contact resistance	1.822	1.571

VII. Gas Flow and Convective Heat Loss (LFA)

In their investigation of porous samples using the LFA, Lauerer and Lunev [217] demonstrated that a gas flow within the measurement chamber might result in higher thermal conductivity values. Due to the higher convective heat losses from the sample to the surrounding air, the maximum temperature is reached faster. In

the evaluation according to Equation 2.14 this leads to a higher thermal diffusivity and thus a higher thermal conductivity.

In the LFA 467 HyperFlash® (NETZSCH-Gerätebau GmbH, Germany) that was used in the present work, a cooling gas flow is applied for temperatures $T \leq 20\,°C$. The impact of this gas flow could be observed in the temperature-dependent measurements. Here, a step was found between 20 °C and 30 °C for the thermal diffusivity data as shown for the IAM_Graphite_70µm_p1 electrode in Figure A.6 in the Appendix. The step is improbable to originate only from the temperature dependency of the thermal transport properties, but is assumed to mainly stem from the deactivation of the gas flow. It is thus assumed that the thermal conductivity values featured in this work and measured at 20 °C would be up to 10 % lower as specified by Lauerer and Lunev [217], if the gas in the system was not under forced convection. With the results obtained in the present work, the effect of the forced convection is expected to be even lower.

The convective heat losses might also be partly responsible for the differences between the measurements in helium and nitrogen. Though the use of helium causes a higher thermal conductivity within the pores, which increases the thermal conductivity of the coating, the higher thermal conductivity of helium in comparison to nitrogen also leads to enhanced convection. The latter might be more substantial for the increase in the thermal conductivity. If this is the case, the effect should also be seen for solid, nonporous materials.

VIII. Internal Thermal Contact Resistances (GHP)

Within the GHP rig, internal thermal contact resistances might exist between the stacked layers of the sample in addition to the resistance $R_{\text{Al-sample}}$ between the sample and the apparatus. These resistances were neglected in the evaluation. This proceeding is necessary to quantify the effective thermal conductivity. Burheim et al. [39, 97] also investigated the relevance of these resistances for the measurement of micro-porous layers used in fuel cells and battery electrodes. They compared the resulting thermal conductivity for stacked layers and single

layers with increased thickness and found that the internal resistances are negligible. However, these previous studies used samples with much higher thicknesses than in the present work, which is why a more detailed analysis will be conducted here.

In the present work, an enhancement of the effective thermal conductivity with an increased pressure is evident. One idea is that this might be due to the compression and the consequent thickness reduction. However, the thickness was measured during the compression within the rig. A higher resulting thermal conductivity due to the reference of the absolute conduction to a smaller thickness can thus be excluded. Moreover, it was shown, that the thickness change within the rig due to compression is rather small. The graphite electrodes were used for this analysis as they are generally softer than the NMC622 electrodes and thus a stronger deformation is expected. For one thing, the stack thicknesses measured before and during the compression in the rig were compared. The results show that even at the highest pressure of 6 bar the thickness reduction constitutes less than 5 % (see Figure A.8 in the Appendix). Additionally, the thickness of the stacks before and after the GHP measurements were put into relation. Considering the uncertainty of the results, they showed less than 1 % plastic deformation (see Figure A.9 in the Appendix).

Therefore, it is concluded that the enhancement of thermal conductivity due to an increase in pressure is, at most, only slightly affected by changes in thickness during compression. Instead, the increase in the thermal conductivity is associated with a better contact, which, contrary to the above assumption, strengthens the idea that sample-sample (s-s) contact resistances have a significant influence on the measured thermal conductivity. The importance of these resistances is expected to depend on a number of influencing factors including the thickness of the coating, its porosity, the pressure applied, the stacking method defining the orientation within the rig, the AM, the binder content and potentially the elastic vs. plastic behavior of the binder used in the electrodes. Understanding how these influencing factors affect the internal thermal contact resistances, and under which conditions they are negligible, is of great interest.

To verify that significant s-s contact resistances exist within the rig, electrodes with different coating thicknesses were examined. Due to the material availability at NTNU, NMC111 was used as AM here. The available electrodes showed thicknesses between approx. 15 µm and 60 µm. The porosities lie in a range of 0.35 to 0.6. The electrodes were dried at a plate temperature of 60 °C. Due to the relatively low drying temperature and comparably small coating thickness, the impact of binder migration is assumed to be minor [64].

For the GHP measurements, two different stacking approaches were applied. For one thing, stacks of two, four and six electrodes were measured equivalent to the measurements carried out with the IAM_NMC622 and IAM_Graphite_70µm samples. Thus, in this case the coatings were facing each other which was termed face to face stacking. Secondly, stacks of one to five electrodes all facing in the same direction were investigated. This configuration was termed face to back stacking.

The thermal conductivity values resulting from the different stacking methods are given in Figure 5.22 (a) with respect to the coating thickness. They show a trend towards an increasing thermal conductivity with increasing coating thickness and seem to approach a constant value. It is assumed that the increase in the thermal conductivity does not actually originate from changes in the coating itself but rather demonstrates the lowered impact of the s-s contact resistances. For thin coatings, the proportion of the s-s contact resistances of the total thermal resistance is higher. Thus, in this case the internal contact resistances significantly reduce the effective thermal conductivity.

Since the samples showed some differences in their porosity, an additional depiction was chosen that exhibits the thermal conductivity of the coating with respect to the solid thickness $(1 - \phi) \cdot s_{\mathrm{co}}$. This relation is given in Figure 5.22 (b). The results show the same increasing and then flattening trend. The measurements at 5 bar showed slightly higher absolute values, but the same qualitative trends (see Figure A.10 in the Appendix). Thus, it is concluded that the stacking method does not have a considerable effect on the resulting thermal conductivity for pressures up to 5 bar.

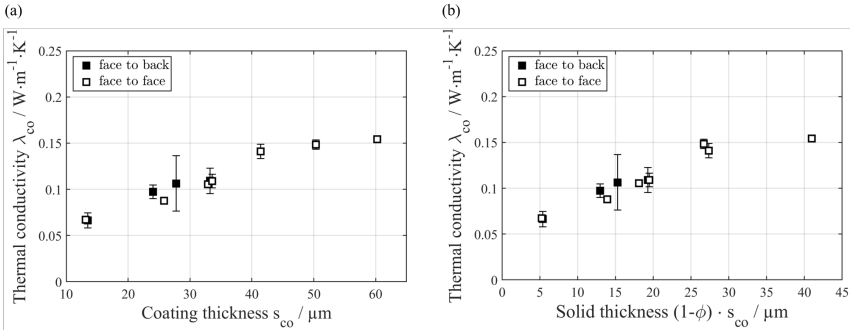

Figure 5.22: Effective thermal conductivity of the face to face and face to back stacks for NMC111 electrodes with varying coating thicknesses, shown with double standard deviations. The data is either referred to (a) the thickness of a single coating layer or (b) to the effective thickness of only the solid material. The measurements were conducted at 2.5 bar (adjusted from Gandert et al. [216], Creative Commons Attribution 4.0 License CC BY).

These findings are in line with the observations by Burheim et al. [249]. Their investigations of porous transport layers (PTLs) of fuel cells showed a trend towards higher effective thermal conductivities with an increased thickness of the porous layer as well. Moreover, an increased pressure also resulted in a considerable enhancement of the thermal conductivity which – given the current state of knowledge – is attributable to a reduction of the s-s contact resistances.

Additionally, Burheim et al. [249] investigated the impact of different PTFE contents. A higher binder content is generally expected to result in a reduction of the effective thermal conductivity of the porous layer, as the binder has a lower thermal conductivity than the other components. Burheim et al. believed the binder to impede the contact between graphite fiber to graphite fiber in the PTL [249]. Here this translates to restricted AM particle-particle contacts as the amount of binder is increased in the electrode coating. However, the PTLs with a higher binder content showed a reduced dependency on the pressure. This strengthens the assumption that the impact of the s-s contact resistances is less significant, if the thermal conductivity of the porous layer itself is lower and thus the total resistance of the sample stack is higher. To elaborate, when

weighing the contribution from the thermal resistance of the coating and the s-s contact resistance to the measured total resistance, both, the sample thermal conductivity, λ_{sample}, and the sample thickness, s_{sample} must be considered. This is because the sample thermal resistance is a combination of the two, expressed as $R_{\text{sample}} = s_{\text{sample}}/\lambda_{\text{sample}}$. This means that for thick samples and samples with low thermal conductivity, the s-s thermal contact resistance is of negligible importance and thus will be excluded in the analysis. On the contrary, when the sample's thickness is below a certain value or its thermal conductivity exceeds a certain value, at some point the s-s contact resistances must be accounted for. However, the point at which this becomes relevant depends heavily on the material.

Examining the data in Figure 5.15, it is evident that the effect of the pressure variation differs between the IAM_NMC622 and IAM_Graphite_70µm samples. For the IAM_NMC622 electrodes, the enhancement of the thermal conductivity is almost constant for all investigated degrees of calendering. For the IAM_Graphite_70µm electrodes on the other hand, the positive impact of the pressure on the thermal conductivity increases with an increasing degree of calendering. This difference might be explained by the very unequal characteristics of the two AMs. NMC are rigid, almost spherical particles, while graphite particles are soft and flaky and change their shape during calendering.

Moreover, different binder systems were applied (see Table 3.1). While the IAM_NMC622 electrodes are based on PVDF, a combination of CMC and SBR was used for the IAM_Graphite_70µm electrodes. This makes the anode material more prone to elastic behavior, which is a possible explanation of the stronger enhancement of the thermal conductivity of the anodes in comparison to the cathodes with increasing pressure. The elasticity allows a stronger flattening of the electrode surface during compression and thereby reduces the contact resistances between the stacked electrodes.

In addition, graphite electrodes generally have a much higher effective thermal conductivity than NMC electrodes. Following the reasoning above, the adverse impact of the s-s contact resistances is thus more severe for the graphite electrodes and the reduction of these resistances by a pressure increase is more pronounced.

Moreover, the effect of the pressure increase is enhanced with an increasing degree of calendering for the IAM_Graphite_70µm electrodes. This can also be explained by the enhanced thermal conductivity with increasing degree of calendering. The higher the thermal conductivity of the material itself, the higher is the reductive impact of the internal contact resistances.

Thus, it can be concluded that the thermal conductivity values of the graphite electrodes at 2 bar are strongly defined by the internal contact resistances, while the values at higher pressures (6 bar) are less influenced by the internal contact resistances and are thereby closer to the true value.

This raises the question of how and to what extent the results of Figure 5.22 can be transferred to the measurements of the IAM_NMC622 cathodes or even the IAM_Graphite_70µm anodes shown above. The IAM_NMC622 electrodes feature a lower binder content of 3 wt.% PVDF instead of 5 wt.%. It can be concluded from this that the thermal conductivity of the IAM_NMC622 coatings is higher than that of the NMC111 coatings and thus the thermal contact resistances are more important for the former. In other words, since the IAM_NMC622 electrodes exhibit only approx. half the amount of binder of the NMC111 electrodes and based on the results found by Burheim et al. [249], it is assumed that the critical thickness, above which the s-s contact resistances become relevant, shifts to higher values. Therefore, it is very likely that the NMC622 coatings have not exceeded the critical thickness required to neglect the s-s thermal contact resistance, and hence the true thermal conductivity of the electrodes in Figure 5.15 is higher than the reported values. Since the IAM_Graphite_70µm coatings have an even higher thermal conductivity, the thermal resistance is most certainly relevant in the regarded thickness range.

The literature data considered in Figure 2.10 include commercial electrodes with thicknesses of at least 50 µm [39, 41–44]. For the cathodes, the thermal contact resistance is expected to be negligible in this thickness range. However, the graphite electrodes also showed a strong increase of the thermal conductivity with increasing pressure in the literature (see Figure 2.12).

Another interesting, theoretical analysis of the s-s contact resistances can be conducted by assuming the thermal conductivity values measured with the LFA in nitrogen to be the true values. In this case the lowering of the GHP values in comparison to the LFA values only stems from the internal contact resistances. Then the s-s contact resistances for the measurements with a number of layers n_{layers} of two, four and six – here defined as the resistance between two coatings in the face to face stacking approach – can be calculated according to Equation 5.3.

$$R_{\text{s-s}} = \frac{R_{\text{total}} - 2 \cdot R_{\text{Al-sample}} - \frac{s_{\text{sample}}}{\lambda_{\text{stack,LFA}}}}{n_{\text{layers}}/2} \tag{5.3}$$

The thermal contact resistances predicted with Equation 5.3 for the differently calendered sheets are given in Figure 5.23 as a function of the porosity. The resulting values are on average 1.26 times the contact resistance between sample and apparatus $R_{\text{Al-sample}}$ for the IAM_Graphite_70µm electrodes and 1.95 times $R_{\text{Al-sample}}$ for the IAM_NMC622 electrodes. Thus, they are in a realistic order of magnitude. The lower s-s contact resistances of the IAM_Graphite_70µm electrodes might be reasoned by their significantly softer and more elastic character in comparison to the IAM_NMC622 electrodes. Therefore, they might be deformed during pressure application leading to a better contact.

Interim Conclusion

To briefly summarize the investigations of the LFA and GHP method, it can be said that both methods have limitations. For the considered graphite and NMC622 samples, the LFA method is expected to be well-suited for electrodes with low porosity. For uncalendered electrodes with high porosities, the light pulse might penetrate far into the porous material. In those cases, the penetration depth might not be appropriately accounted for by the evaluation model.

The GHP measurements conducted on graphite and NMC622 samples in this work suggest that it is more suitable for thicker electrode samples. The critical thickness is expected to vary with the thermal conductivity of the electrode. For

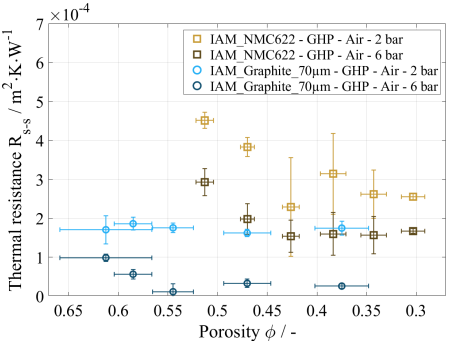

Figure 5.23: Internal thermal contact resistances between the electrode coatings within the GHP measurement rig. The values were calculated with the assumption that the thermal conductivity obtained with the LFA is correct (adjusted from Gandert et al. [216], Creative Commons Attribution 4.0 License CC BY).

lower thicknesses, the internal thermal contact resistances between the stacked layers in the rig become relevant and considerably reduce the resulting effective thermal conductivity.

Regarding the literature data in Figure 2.12 measured with the GHP method, these findings underline the hypothesis that the pressure increase does not really enhance the thermal conductivity of the coating itself but rather leads to a reduced thermal contact resistance.

Moreover, the results indicate that the LFA measurements of uncalendered electrodes are most prone to errors due to their high porosity. The samples in all previous chapters were taken from highly porous electrodes and were, moreover, all measured in helium. It is assumed that the thermal conductivity is overestimated. Thus, the absolute values should be considered with caution. The relative comparison of the results for the uncalendered samples among each other, however, should not be considerably interfered by this.

For the differently calendered electrodes that were not measured with both methods – IAM_Graphite_117µm, CC_NMC811, TFT_HC-C_Cu and TFT_LFP – this implies that the decrease in the thermal conductivity from uncalendered to slightly calendered samples should be considered with caution. Although there may be a

connection to the quality of the contact between coating and current collector, it is also possible that the decline is exclusively due to the consideration of the light penetration in the evaluation of the measurements.

5.5.4 Impact of the Electrolyte and Transfer to the Cell Level

LFA measurements of battery electrodes are mostly conducted within a gaseous phase. However, it was shown in several studies that the better conducting electrolyte solvent, which also fills the pores during the operation of the cells, entails much higher thermal conductivity values [7, 39, 41–43]. The evaluations in Figure 2.13 suggest a thermal conductivity of the soaked electrodes that is by a factor of 2 to 4 higher than that of the dry electrodes. As the thermal transport properties during the operation of the cells are of considerable importance for the simulation and modeling of the temperature distribution within the cells, an estimation of the values for electrolyte-soaked electrodes based on the results obtained in the present work poses an interesting addition.

The thermal conductivity of the electrolyte solvent with 0.18 $\mathrm{W{\cdot}m^{-1}{\cdot}K^{-1}}$ [18] was often said to be similar to that of helium [34, 248], which has a continuum thermal conductivity of 0.152 $\mathrm{W{\cdot}m^{-1}{\cdot}K^{-1}}$ at 20 °C [235]. However, it is plausible that the thermal conductivity of the gas might be impaired within the small pores of the electrodes due to the so-called Knudsen or Smoluchowski effect [36, 113]. Moreover, the higher thermal conductivity of the soaked electrodes in the GHP measurements might in part originate from reduced thermal contact resistances between the coatings as the large voids at the interface are filled up with a significantly better conducting fluid. Thus, the factor of 2 to 4 is only valid for liquid electrolyte in the GHP measurements and not for gaseous helium since they behave differently.

The true impact of the deviations in the electrodes' thermal transport properties appears on cell level. That is why a comparison of the resulting in-plane and through-plane thermal conductivities of the cell stack for the LFA and GHP

method is conducted. This estimation was done based on a cell stack with 20 double-sided coated cathodes and 21 double-sided coated anodes for the uncalendered electrodes (p1) and the most strongly calendered electrodes that could both be measured with GHP (p5). The separator was assumed to have a thickness of 25 µm. The thermal conductivity of copper and aluminum was set to 400 $W \cdot m^{-1} \cdot K^{-1}$ and 236 $W \cdot m^{-1} \cdot K^{-1}$, respectively. The thermal conductivity of the separator was set to 0.203 $W \cdot m^{-1} \cdot K^{-1}$ [18] for both the dry and soaked cases. For the dry electrodes, the nitrogen or air data was used, respectively. An estimation of the thermal conductivity of the soaked electrodes was conducted by multiplying the GHP values by factor 3 as a mean value of the analysis in Figure 2.13 in Section 2.1.4. The effective thermal conductivities resulting for the cell stack are given in Table 5.3.

For the in-plane thermal conductivity, no significant differences (approx. 2 %) were found between the two methods. This may be explained by the predominance of the current collector foil in this consideration. The increase in the metal volume fraction during calendering leads to an increase in the in-plane conductivity from p1 to p5.

The through-plane thermal conductivity shows significantly larger deviations by approx. a factor of 2 between LFA and GHP. This is reasonable since the materials with low thermal conductivities dominate the calculation of the through-plane thermal conductivity. Furthermore, it becomes apparent that the LFA values for dry electrodes are more comparable to the GHP values for soaked electrodes.

Several primary and meta-studies [22, 44, 111, 250, 251] reported in-plane thermal conductivities in the range of 21 to 40 $W \cdot m^{-1} \cdot K^{-1}$ and through-plane thermal conductivities of 0.15 to 1.8 $W \cdot m^{-1} \cdot K^{-1}$ for soaked cell stacks. Thus, the estimated thermal conductivity values for a soaked cell lie within a range comparable to other reported values.

With respect to the calendering step, from a thermal perspective two different optimizations are possible as the calendering step does not only influence the thermal conductivity but also the thickness of the electrodes.

Table 5.3: In-plane and through-plane thermal conductivity on cell level in $W \cdot m^{-1} \cdot K^{-1}$ for the combination of both p1 electrodes and both p5 electrodes, respectively. Furthermore, it was varied between the values obtained by LFA in helium (He), LFA in nitrogen (N_2), GHP at 6 bar in air and estimated values for the soaked electrodes by multiplying the GHP values by factor 3.

	LFA He p1	LFA He p5	LFA N_2 p1	LFA N_2 p5	GHP p1	GHP p5	soaked p1	soaked p5
In-plane thermal conductivity	26	34	25	34	25	34	26	35
Through-plane thermal conductivity	0.67	0.55	0.62	0.52	0.35	0.38	0.6	0.5

The first one is the optimization regarding power peaks. In this case of optimization, the generated heat cannot be conducted out of the battery cell quickly enough and primarily leads to a temperature rise within the cell. The extent of this temperature rise is influenced by the internal electrical resistance of the cells. A detailed analysis of the influence of the calendering process on the internal electrical resistance was out of the scope of this work. However, it is expected that too extensive calendering results in higher resistances and, thus, a more intensive heat generation. Lower degrees of calendering are also preferred with respect to the heat capacity as thicker electrodes – in consideration of the electrolyte – have a higher absolute heat capacity. As a result, the cell undergoes a lower temperature increase with the same heat input. This is in line with the thermal optimum.

The second optimization regards the steady state heat conduction. For this, it is assumed that all of the generated heat is conducted out of the cell so that the temperature within the cell stays constant. To keep the temperature gradient within the cell ideally low, the effective thermal conductivity should be as high as possible and the electrode thickness as low as possible. On an electrode level the optimum would, thus, be the most strongly calendered electrode. Considering the cell data in Table 5.3, it becomes evident that the through-plane thermal conductivity of the cell is lower for the most strongly calendered case (p5) in comparison to the uncalendered case (p1) due to the larger influence of the poorly conducting separator. However, it should be considered, that calendering also results in a much lower thickness of the electrodes, which works in favor of lower thermal gradients.

For the second case of optimization the thermal optimum contradicts the electrical optimum. Although a high degree of calendering results in a low porosity and is thus advantageous for a high energy density and electrical conductivity of the electrodes, the ionic conduction is highly restricted and becomes the limiting factor. As a consequence, the electrical optimum of the porosity lies in a medium range of the porosity between approx. 0.3 and 0.4 depending on the application.

Thus, there are cases in which the thermal and electrical optimums do not align and a compromise needs to be found.

5.5.5 Electrical Resistance Measurements

The composite volume resistivity ρ_{el} of the IAM_NMC622 electrodes and the IAM_Graphite_70µm electrodes was measured. For a better comparison with the thermal conductivity it was converted into the specific electrical conductivity ($\sigma_{el} = 1/\rho_{el}$). The specific electrical conductivity as a function of the porosity is depicted in Figure 5.24. For the IAM_NMC622 electrodes, no distinctive conclusion can be drawn, as the relative uncertainties are very high and no significant changes in the electrical conductivity can be found. The samples from the IAM_Graphite_70µm electrodes, in contrast, show lower relative uncertainties due to their much higher absolute values. Thus, a significant increase of the specific electrical conductivity with decreasing porosity could be found here. The behavior observed for the graphite electrodes matches the findings in the literature [61, 82, 191].

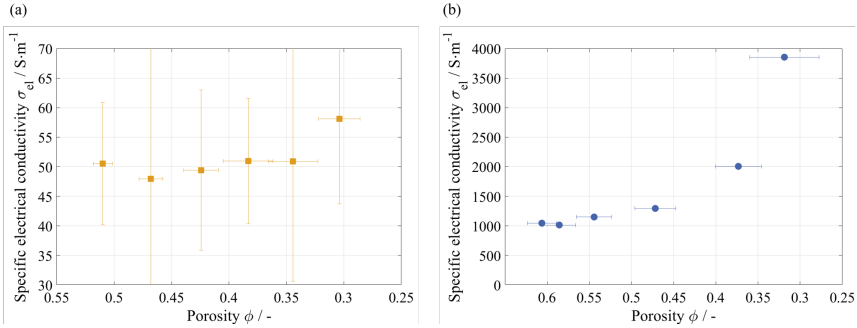

Figure 5.24: Specific electrical conductivity of (a) the differently strong calendered IAM_NMC622 electrodes and (b) the IAM_Graphite_70µm electrodes with respect to the porosity.

Considering the decrease of the thermal conductivity between $\phi = 0.62$ and $\phi = 0.54$ for the values measured with the LFA to be most certainly reasoned by the measuring and evaluation method, the electrical and thermal properties show a similar qualitative behavior in this context.

A quantitative comparison is made possible by the application of the Wiedemann Franz Law. This allows the conversion of the electrical conductivity to the thermal conductivity for electrically conducting materials and is primarily applied for metals. In the present context it was only applied for the graphite electrodes as graphite constitutes a highly conducting material. According to the Wiedemann Franz Law, the thermal conductivity can be calculated following $\lambda = \sigma \cdot L \cdot T$ with the Lorenz number L and the temperature T in K [252–254].

A comparison of the thermal conductivity of the graphite electrodes measured with the LFA in helium and the values calculated from the electrical conductivity with $T = 292$ K and $L = 2.33 \cdot 10^{-8}$ W·Ω·K^2 in accordance with Ashcroft et al. [253] and Kittel [254] is given in Figure 5.25.

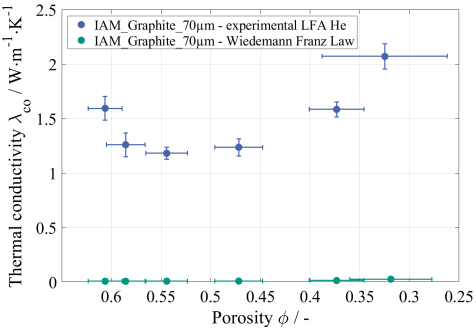

Figure 5.25: Comparison of the thermal conductivity of the IAM_Graphite_70µm electrode coatings obtained by LFA measurements in helium and calculated from the data of the specific electrical conductivity according to the Wiedemann Franz Law.

It is obvious that the Wiedemann Franz analogy delivers considerably lower thermal conductivity values than those measured directly with a factor of 79 to 226 between the two values. Thereby, it significantly underestimates the thermal transport in the electrodes and should, thus, not be applied for this comparison. This observation can be reasoned by the binder and carbon black present in the electrodes in addition to the graphite. Opposed to well conducting pure graphite, the conduction pathways are interrupted multiple times in case of the electrodes.

This can be mainly explained by the binder, which can be expected to insulate electrically, however, still has a reasonable thermal conductivity.

As a consequence, transferring findings regarding the thermal properties to the electrical properties and vice versa should be avoided.

5.6 Dry Manufacturing

Three different types of dry-manufactured IAM_NMC622 electrodes were investigated in this work: free-standing electrodes, laminated free-standing electrodes and directly calendered electrodes. Details on the different processing approaches can be found in the Sections 2.2.7 and 3.1.

As the free-standing electrodes do not have a current collector layer for their stabilization, their mechanical integrity is impaired. Some of these samples showed visible cracks during the sample preparation for the LFA measurements. To mark the values obtained for the fractured samples, the effective thermal conductivity of all the single samples of the dry-manufactured electrodes is depicted in Figure 5.26 instead of the mean values. Here, the effective thermal conductivity of the coating – or the whole sample in case of the free-standing electrodes – is compared to the results of the differently strong calendered wet-processed electrodes.

The directly calendered electrodes continue the course of the wet-processed samples very well. As the former show a significantly lower porosity, a direct comparison is not possible.

The free-standing and the laminated electrodes exhibit a porosity similar to the lower porosity range of the differently strong calendered, wet-processed samples. The free-standing electrodes show a tendency towards a higher effective thermal conductivity in comparison to the laminated electrodes, although they are of similar porosity. This behavior resembles the observations in Section 5.5.3 where the graphite coatings detached from the current collector foil also showed a higher thermal conductivity in comparison to the measurements with the current

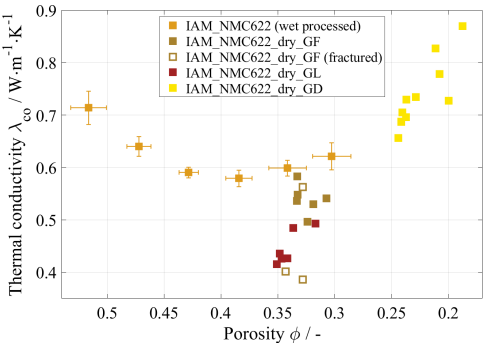

Figure 5.26: Effective thermal conductivity of the dry-manufactured NMC622 electrodes in comparison to the wet-processed electrodes with the same composition at different degrees of calendering measured in helium.

collector foil. As discussed above, it is still unclear, if those differences come from the thermal contact resistance between the two layers or potential effects of the measurement and evaluation method when it comes to porous samples, that are even more dominant for two-sided porous samples.

Therefore, although the same composition was used for both processing routes, a comparison of the samples is difficult due to the formation of a strongly differing microstructure. The wet-processed electrodes exhibit a very inhomogeneous binder distribution with areas almost free of additives and areas densely packed with the BCB phase. In the dry-manufactured electrodes on the other hand, the PVDF builds fine fibrils. Moreover, the dry-manufactured electrodes were coated onto a precoated aluminum foil.

5.7 Summary of the Separate Investigations

The results discussed in this chapter show that the mechanical stress applied during mixing and the rate of drying do not have a significant influence on the thermal conductivity of the electrode coating in the range of parameter variation considered here.

The dry film thickness of the LFP electrodes set during the wet coating process was shown to have a slight negative impact on the thermal conductivity in the investigated range of up to 170 µm dry coating thickness. For the graphite electrodes, the impact on the thermal conductivity is only visible for very high values of the coating thickness. Here, a significant decrease in the thermal conductivity of the coating could be found at a coating thickness of 700 µm. This behavior is reasoned by the binder migration that provokes a low binder content and thus an impaired contact at the interface between the coating and the current collector. The effect of binder migration is increasingly strong with increasing coating thickness. However, thicknesses of more than approx. 250 µm – even in the uncalendered state – are not realistically applicable in real battery cells.

An increase of the particle size of the active material was shown to have a positive impact on the thermal conductivity of the coating. This is explained by the smaller number of particle-particle contacts in the case of larger particles. The particle-particle contacts constitute additional resistances due to the small contact area and the low thermal conductivity of the BCB phase that fills the gap. This effect was found for both, LFP and HC electrodes.

The process step with the strongest impact on the thermal transport properties was found to be the calendering step. Thus, it was most extensively studied in this work. First results measured with the LFA show a u-shaped course of the coating thermal conductivity with respect to a decreasing porosity. The general behavior was similar for all active materials investigated, however, the emphasis varied. The LFP and graphite electrodes showed a much stronger increase on the thermal conductivity than the NMC electrodes.

In addition, the GHP method was applied to the NMC622 and graphite electrodes with different degrees of calendering. Thorough investigations of both methods led to the assumption that the decrease of the thermal conductivity from the uncalendered to slightly calendered samples might stem from a flaw in the LFA measurement and evaluation of highly porous samples. Especially the results obtained for the electrodes in the upper porosity range and with helium as measurement gas should be treated with caution.

The GHP method, however, has its challenges as well. For low electrode thicknesses and high thermal conductivities of the electrodes themselves, significant contact resistances exist between the stacked layers within the rig. This leads to lower thermal conductivity values resulting from the measurement. The application of higher pressures lowers these resistances yielding more realistic thermal conductivity values.

A comparison of the thermal conductivity of the coating with its specific electrical conductivity reveals similarities in the porosity dependence of the thermal and electrical transport properties.

Moreover, different dry-manufactured NMC electrodes were investigated and compared to the wet-processed, calendered electrodes. The extrapolated course of the wet-processed electrodes to even lower porosities is herein represented very well by the directly calendered electrodes. The free-standing and laminated electrodes, however, showed a significantly lower thermal conductivity than the wet-processed electrodes with the same porosity. The dry manufacturing leads to the formation of a very different structure of the binder phase compared to the wet-processed electrodes and thereby entails a different form of heat conduction pathways.

Lastly, it is interesting to compare the thermal conductivity of the electrode coatings with different active materials. Therefore, the results of the differently calendered electrodes of all the different AMs are given in Figure 5.27.

It is evident that the graphite coatings exhibit both, the highest absolute values and the strongest increase in thermal conductivity by calendering. The high effective thermal conductivity of the coating is not only due to the high thermal conductivity of graphite, but might also in part stem from the high AM content and the consequently low amount of insulating binder within the coating. Furthermore, the rather soft graphite particles allow plastic deformation during calendering, which results in larger contact areas between the particles and toward the interface, which also entails a higher effective thermal conductivity.

The NMC622 coatings exhibit a higher thermal conductivity than the NMC811 coatings, which is attributed to the graphite additives applied in the former. The

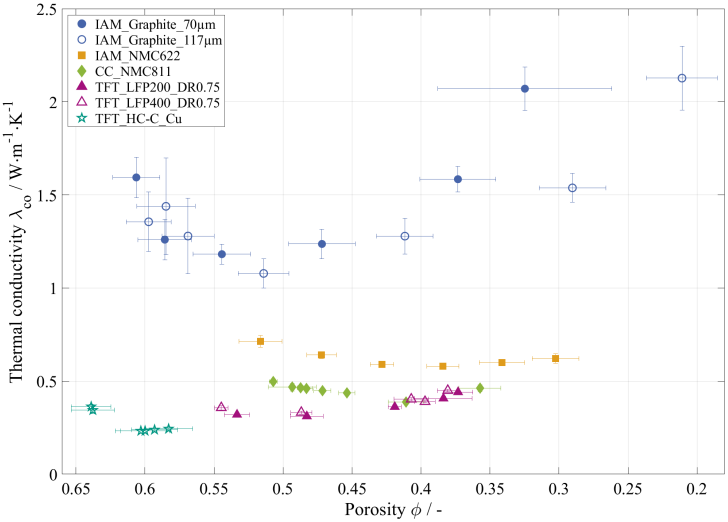

Figure 5.27: Thermal conductivity of the coating of the differently calendered electrodes of all the investigated AMs. For LFP only the electrodes produced with a drying rate of 0.75 g·m^{-2}·s^{-1}.

NMC811 and LFP coatings exhibit a similar effective thermal conductivity. In comparison to the influence of the choice on the active material, the impact of the particle size of the LFP is rather small.

Moreover, it is evident that the anodes, made of graphite and HC, show a significantly higher porosity after drying and thus in the uncalendered state than all the investigated cathodes.

6 Conclusion

This work presents a thorough investigation of the interconnection between the production steps and their respective set parameters and the thermal transport properties of the produced electrodes. Numerous studies in the literature have shown significant impacts of the process parameters used for electrode production on the mechanical and electrical properties of the electrodes as well as their microstructure. Investigations connecting the thermal properties with the production route are yet very scarce. However, the influence of the production parameters on the thermal transport properties is expected to be considerable. Thus, the topic of this work addresses a large research gap that was formulated in a number of research questions. These research questions were dealt with in this work and the key findings are summarized below.

How do the different production parameters influence the thermal transport in battery electrodes?

In this context, the potential influences of the wet mixing, coating, drying, calendering and dry manufacturing steps as well as the active material type and its mean particle size were investigated.

The parameter variation during wet mixing was performed by using extruders with different screw geometries, rotation speeds, and mass flows. The results, however, do not show a significant impact of these variables on the thermal conductivity of the dried but uncalendered electrodes.

Regarding a variation of the coating thickness, the severity of the observed effect varies for the different active materials and maximum coating thicknesses.

For the HC electrodes, no significant influence of the coating thickness on the thermal transport properties is found. LFP electrodes with coating thicknesses of up to 170 µm show a slight decrease in thermal conductivity with increasing thickness. Graphite electrodes show the same trend, however, much higher coating thicknesses were used here to obtain a significant influence. The decrease in the thermal conductivity is possibly explained by the impaired contact between coating and current collector that is caused by the binder migration during drying, a process which is particularly strong for high coating thicknesses.

With the thorough analysis using both the LFA and the GHP method, stronger calendering and thus a reduction of the porosity is assumed to lead to an increase of the thermal conductivity. In the present study, the enhancement was particularly strong for the graphite electrodes, due to their low binder content and the good deformability of the AM particles.

The particle size of the AM was shown to have an impact on the thermal conductivity of the thereof produced electrodes for both HC and LFP as active materials. In both cases, a tendency towards a higher thermal conductivity of the coating with larger particle size is evident. This meets the expectations and can be explained by the lower number of particle-particle contacts along the paths for heat conduction in the case of larger AM particles.

Do production steps aimed at achieving optimal capacity and electrical transport properties also lead to optimal thermal transport properties?

The process settings during mixing, coating and drying did not show a significant impact on the thermal transport properties of the electrodes and can thus be optimized solely from an electrical perspective. However, the optimization of the particle size and its distribution as well as the degree of calendering applied constitute a conflict of objectives between the electrical and thermal optimum.

Regarding the particle size, from a thermal perspective larger particles are preferred as they result in a higher effective thermal conductivity of the electrodes due

to the lower number of gaps in the conduction path. From an electrical perspective, however, an optimum of electrical conduction, ionic conduction in the liquid phase and ionic conduction within the particles needs to be found. Moreover, the width of the particle size distribution can be varied. While a wider distribution has a positive impact on the energy density, it can limit the ion diffusion and thus the maximum power applicable to the electrodes and battery cells.

With respect to the calendering step, the thermal behavior can be optimized either for the application of power peaks or for a stationary state. Power peaks lead to a substantial temperature rise within the cell, while all the generated heat is conducted to the outside in the stationary consideration and thus the temperature stays constant.

For the application of power peaks, thick, only slightly calendered electrodes with a lower internal resistance and a higher absolute heat capacity – including the electrolyte – are preferred. This is in line with the electrical optimum for this case.

For the stationary case, the effective thermal conductivity of the electrodes should be as high as possible to keep the thermal gradients within the battery cells as low as possible. The most strongly calendered electrodes would thus be preferred. However, this contradicts the electrical optimum. Even though a low porosity obtained through a high degree of calendering – similar to a wide particle size distribution – leads to an enhanced energy density and electrical conductivity of the electrodes, it considerably limits ion diffusion. Thus, from an electrical perspective, a mean porosity is preferable in this case.

As a consequence, there are some cases in which the electrical and thermal optimums do not coincide, and a compromise needs to be found according to the application.

What are important effects to be considered when determining the thermal transport properties using LFA and GHP?

Differently calendered electrodes – as samples with the strongest variation in their thermal conductivity – were measured with both the LFA and GHP method in this work. The results of the effective thermal conductivity differed greatly with significantly higher values for the laser flash method and a deviating slope when plotted against the porosity.

An in-depth analysis of potential error sources of both methods has been conducted. The following were identified as the most severe sources of error.

For porous samples in the LFA, the light pulse irradiating the sample penetrates into the pores. The higher the porosity of the sample is, the higher are the inhomogeneities and the surface roughness. For very high porosities the penetration depth of the light pulse might not be taken into account properly by the evaluation model within the LFA software and the thermal diffusivity and thus the thermal conductivity of the material might be overestimated. Thus, the decrease of the thermal conductivity from uncalendered to slightly calendered samples might be a flaw of the measurement method and does not necessarily present the real porosity-dependence of the thermal conductivity.

For the measurement of electrodes with the GHP method, the existence of significant thermal contact resistances between the stacked layers could be proven. These are expected to be especially relevant for low coating thicknesses and high thermal conductivities of the coatings. The exact critical value varies for the different electrodes depending on the composition and microstructure. Moreover, it was shown that the importance of the internal contact resistances can be reduced by increasing the pressure applied to the stacked samples. Increasing the pressure leads to a significant increase of the determined value of the effective thermal conductivity which is particularly strong for the graphite electrodes due to the higher thermal conductivity of the material and the more elastic behavior of the binder. The application of a pressure of at least 6 bar is recommended.

Outlook

This work provides the basis for future investigations and the implementation of further analysis methods.

Several approaches similar to the LFA were proposed for in-line measurements during electrode production. These are helpful for both, the detection of irregularities and the analysis of the overall properties of the coating. The present work, for one thing, provides information on the impact of the different production steps on the thermal transport properties and thereby an important foundation for their monitoring in the future. Secondly, the comparison of the LFA and GHP shows the limitations of the application of radiation based methods for porous samples. It is, however conceivable to apply such a system for the quality control of the electrodes in a calendered state and thereby detect discrepancies in the thickness or porosity of the electrode.

All experimental investigations in this work consider the through-plane thermal conductivity of electrode coatings. For the transfer to cell level and the calculation of the in-plane thermal conductivity it is generally assumed that the thermal conductivity of the electrode coating itself is isotropic. However, especially for soft active materials like graphite, the calendering step might lead to a reorientation and even deformation of the AM particles. It is thus questionable, if the assumption of isotropic transport properties is still valid for calendered electrodes and therefore provides a starting point for further investigations. These should, however, be conducted without the current collector, due to its high thermal conductivity, which – in combination with the uncertainty of the thickness measurements – poses a great error source in the evaluation.

Bibliography

[1] Matthias Fleckenstein, Oliver Bohlen, Michael A. Roscher, and Bernard Bäker. Current density and state of charge inhomogeneities in Li-ion battery cells with LiFePO4 as cathode material due to temperature gradients. *J. Power Sources*, 196(10):4769–4778, January 2011. ISSN 0378-7753. doi: 10.1016/j.jpowsour.2011.01.043.

[2] Yannic Troxler, Billy Wu, Monica Marinescu, Vladimir Yufit, Yatish Patel, Andrew J. Marquis, Nigel P. Brandon, and Gregory J. Offer. The effect of thermal gradients on the performance of lithium-ion batteries. *J. Power Sources*, 247:1018–1025, January 2014. ISSN 0378-7753. doi: 10.1016/j.jpowsour.2013.06.084.

[3] Ian A. Hunt, Yan Zhao, Yatish Patel, and J. Offer. Surface Cooling Causes Accelerated Degradation Compared to Tab Cooling for Lithium-Ion Pouch Cells. *J. Electrochem. Soc.*, 163(9):1846–1852, January 2016. ISSN 0378-7753. doi: 10.1149/2.0361609jes.

[4] Daniel Werner, Sabine Paarmann, Achim Wiebelt, and Thomas Wetzel. Inhomogeneous Temperature Distribution Affecting the Cyclic Aging of Li-Ion Cells. Part I: Experimental Investigation. *Batteries (Basel, Switz.)*, 6(1):13, January 2020. doi: 10.3390/batteries6010013.

[5] Daniel Werner, Sabine Paarmann, Achim Wiebelt, and Thomas Wetzel. Inhomogeneous Temperature Distribution Affecting the Cyclic Aging of Li-Ion Cells. Part II: Analysis and Correlation. *Batteries (Basel, Switz.)*, 6 (1):12, January 2020. doi: 10.3390/batteries6010012.

[6] Sabine Paarmann, Lisa Cloos, Jakob Technau, and Thomas Wetzel. Measurement of the Temperature Influence on the Current Distribution in Lithium-Ion Batteries. *Energy Technol.*, 158:2000862, January 2021. ISSN 21944288. doi: 10.1002/ente.202000862.

[7] Lena Spitthoff, Markus Solberg Wahl, Jacob Joseph Lamb, Paul Robert Shearing, Preben J. S. Vie, and Odne Stokke Burheim. On the Relations between Lithium-Ion Battery Reaction Entropy, Surface Temperatures and Degradation. *Batteries (Basel, Switz.)*, 9(5):249, January 2023. doi: 10.3390/batteries9050249.

[8] Lisa Cloos, Oliver Queisser, Ahmed Chahbaz, Sabine Paarmann, Dirk Uwe Sauer, and Thomas Wetzel. Thermal Transients to Accelerate Cyclic Aging of Lithium-Ion Batteries. *Batteries & Supercaps*, page e202300445, December 2023. ISSN 2566-6223, 2566-6223. doi: 10.1002/batt.202300445.

[9] L. Cloos, J. Langer, M. Schiffler, A. Weber, and Th. Wetzel. Challenges of Predicting Temperature Dependent Capacity Loss Using the Example of NMC-LMO Lithium-Ion Battery Cells. *J. Electrochem. Soc.*, 171(4): 040538, April 2024. ISSN 0013-4651, 1945-7111. doi: 10.1149/1945-7111/ad3ec3.

[10] Yujie Wang, Jiaqiang Tian, Zhendong Sun, Li Wang, Ruilong Xu, Mince Li, and Zonghai Chen. A comprehensive review of battery modeling and state estimation approaches for advanced battery management systems. *Renewable and Sustainable Energy Reviews*, 131:110015, October 2020. ISSN 13640321. doi: 10.1016/j.rser.2020.110015.

[11] S. Tamilselvi, S. Gunasundari, N. Karuppiah, Abdul Razak Rk, S. Madhusudan, Vikas Madhav Nagarajan, T. Sathish, Mohammed Zubair M. Shamim, C. Ahamed Saleel, and Asif Afzal. A Review on Battery Modelling Techniques. *Sustainability*, 13(18):10042, September 2021. ISSN 2071-1050. doi: 10.3390/su131810042.

[12] R. Ranjith Kumar, C. Bharatiraja, K. Udhayakumar, S. Devakirubakaran, K. Sathiya Sekar, and Lucian Mihet-Popa. Advances in Batteries, Battery

Modeling, Battery Management System, Battery Thermal Management, SOC, SOH, and Charge/Discharge Characteristics in EV Applications. *IEEE Access*, 11:105761–105809, 2023. ISSN 2169-3536. doi: 10.1109/ACCESS.2023.3318121.

[13] Arno Arzberger, Matthias Hellenbrand, and Dirk Uwe Sauer. The change of thermal conductivity of Lithium-Ion pouch cells with operating point and what this means for battery thermal management. In *Advanced Automotive Battery Confernce, AABTAM Symposium - Advanced Automotive Battery Technology, Application and Market, AABC and AABTAM*. Atlanta, Georgia, January 2014.

[14] Hossein Maleki, Hsin Wang, Wally Porter, and Jerry Hallmark. Li-Ion polymer cells thermal property changes as a function of cycle-life. *J. Power Sources*, 263:223–230, January 2014. ISSN 0378-7753. doi: 10.1016/j.jpowsour.2014.04.033.

[15] Stephen J. Bazinski and Xia Wang. Experimental study on the influence of temperature and state-of-charge on the thermophysical properties of an LFP pouch cell. *J. Power Sources*, 293:283–291, January 2015. ISSN 0378-7753. doi: 10.1016/j.jpowsour.2015.05.084.

[16] Aalok Gaitonde, Amulya Nimmagadda, and Amy Marconnet. Experimental Characterization of Thermal Conductance across the Separator-Shell Interface in Dry Cylindrical Lithium Ion Batteries. In Paul Wesling, editor, *Proceedings of the Sixteenth InterSociety Conference on Thermal and Thermomechanical Phenomena in Electronic Systems, ITherm 2017: May 30-June 2, 2017, Orlando (Lake Buena Vista), FL, USA*. IEEE, Piscataway, NJ, January 2017. ISBN 978-1-5090-2995-2.

[17] Aalok Gaitonde, Amulya Nimmagadda, and Amy Marconnet. Measurement of interfacial thermal conductance in Lithium ion batteries. *J. Power Sources*, 343(3):431–436, January 2017. ISSN 0378-7753. doi: 10.1016/j.jpowsour.2017.01.019.

[18] Daniel Werner, André Loges, Dominic J. Becker, and Thomas Wetzel. Thermal conductivity of Li-ion batteries and their electrode configurations – A novel combination of modelling and experimental approach. *J. Power Sources*, 364(6):72–83, January 2017. ISSN 0378-7753. doi: 10.1016/j.jpowsour.2017.07.105.

[19] Marco Steinhardt, Elisabeth Irene Gillich, Maximilian Stiegler, and Andreas Jossen. Thermal conductivity inside prismatic lithium-ion cells with dependencies on temperature and external compression pressure. *J. Energy Storage*, 32(7):101680, January 2020. ISSN 2352152X. doi: 10.1016/j.est.2020.101680.

[20] Marco Steinhardt, Elisabeth Irene Gillich, Alexander Rheinfeld, Ludwig Kraft, Markus Spielbauer, Oliver Bohlen, and Andreas Jossen. Low-effort determination of heat capacity and thermal conductivity for cylindrical 18650 and 21700 lithium-ion cells. *J. Energy Storage*, 42(7):103065, January 2021. ISSN 2352152X. doi: 10.1016/j.est.2021.103065.

[21] Georgi Kovachev, Andrea Astner, Gregor Gstrein, Luigi Aiello, Johann Hemmer, Wolfgang Sinz, and Christian Ellersdorfer. Thermal Conductivity in Aged Li-Ion Cells under Various Compression Conditions and State-of-Charge. *Batteries (Basel, Switz.)*, 7(3):42, January 2021. doi: 10.3390/batteries7030042.

[22] Luca Tendera, Dominik Wycisk, Carlos Gonzalez, Gerrit Karl Mertin, Hendrik Pegel, and Kai Peter Birke. Effects of geometric, structural and operational parameters on the thermal conductivity of lithium-ion cells. *J. Electrochem. Soc.*, 549(10):232120, January 2022. ISSN 0378-7753. doi: 10.1016/j.jpowsour.2022.232120.

[23] Matthias Faber, Oliver Buitkamp, Simon Ritz, Martin Börner, Jonathan Berger, Julian Friedrich, Arno Arzberger, and Dirk Uwe Sauer. A method to determine the specific heat capacity of lithium-ion battery cells using thermal insulation. *J. Power Sources*, 583(4):233499, January 2023. ISSN 0378-7753. doi: 10.1016/j.jpowsour.2023.233499. Num Pages: 12.

[24] Arno Kwade, Wolfgang Haselrieder, Ruben Leithoff, Armin Modlinger, Franz Dietrich, and Klaus Droeder. Current status and challenges for automotive battery production technologies. *Nat Energy*, 3(4):290–300, January 2018. doi: 10.1038/s41560-018-0130-3.

[25] Florian Degen and Oliver Krätzig. Future in Battery Production: An Extensive Benchmarking of Novel Production Technologies as Guidance for Decision Making in Engineering. *IEEE Trans. Eng. Manage.*, 71: 1038–1056, 2024. ISSN 0018-9391, 1558-0040. doi: 10.1109/TEM.2022.3144882.

[26] Hossein Maleki, J.Robert Selman, R.B Dinwiddie, and H. Wang. High thermal conductivity negative electrode material for lithium-ion batteries. *J. Electrochem. Soc.*, 94(1):26–35, January 2001. ISSN 0378-7753. doi: 10.1016/S0378-7753(00)00661-3.

[27] Shrikant C. Nagpure, Ralph Dinwiddie, S. S. Babu, Giorgio Rizzoni, Bharat Bhushan, and Tim Frech. Thermal diffusivity study of aged Li-ion batteries using flash method. *J. Power Sources*, 195(3):872–876, January 2010. ISSN 0378-7753. doi: 10.1016/j.jpowsour.2009.08.025.

[28] Bonil Koo, Pradyumna Goli, Anirudha V. Sumant, Paula Cecilia dos Santos Claro, Tijana Rajh, Christopher S. Johnson, Alexander A. Balandin, and Elena V. Shevchenko. Toward lithium ion batteries with enhanced thermal conductivity. *ACS Nano*, 8(7):7202–7, January 2014. doi: 10.1021/nn502212b.

[29] Pamina Bohn, Gerd Liebig, Lidiya Komsiyska, and Gunther Wittstock. Temperature propagation in prismatic lithium-ion-cells after short term thermal stress. *J. Power Sources*, 313:30–36, January 2016. ISSN 0378-7753. doi: 10.1016/j.jpowsour.2016.02.055.

[30] Petronela Gotcu and Hans J. Seifert. Thermophysical properties of LiCoO-LiMnO blended electrode materials for Li-ion batteries. *Phys. Chem. Chem. Phys.*, 18(15):10550–62, January 2016. doi: 10.1039/c6cp00887a.

[31] Petronela Gotcu, Wilhelm Pfleging, Peter Smyrek, and Hans J. Seifert. Thermal behaviour of LixMeO2 (Me = Co or Ni + Mn + Co) cathode materials. *Phys. Chem. Chem. Phys.*, 19(19):11920–11930, January 2017. doi: 10.1039/c7cp00513j.

[32] Dieter Oehler, Philipp Seegert, and Thomas Wetzel. Modeling the Thermal Conductivity of Porous Electrodes of Li-Ion Batteries as a Function of Microstructure Parameters. *Energy Technol.*, 58:2000574, January 2020. ISSN 21944288. doi: 10.1002/ente.202000574.

[33] Gerd Liebig, Ulf Kirstein, Stefan Geißendörfer, Frank Schuldt, and Carsten Agert. The Impact of Environmental Factors on the Thermal Characteristic of a Lithium–ion Battery. *Batteries (Basel, Switz.)*, 6(1):3, January 2020. doi: 10.3390/batteries6010003.

[34] Dieter Oehler. *Bestimmung der thermischen Transporteigenschaften poröser Elektroden von Lithium-Ionen Batterien.* Ph.D. Thesis, Karlsruhe Institute of Technology (KIT), Karlsruhe, January 2021.

[35] Markus Koller, Johanna Unterkofler, Gregor Glanz, Daniel Lager, Alexander Bergmann, and Hartmut Popp. Radial Thermal Conductivity Measurements of Cylindrical Lithium-Ion Batteries—An Uncertainty Study of the Pipe Method. *Batteries (Basel, Switz.)*, 8(2):16, January 2022. doi: 10.3390/batteries8020016.

[36] Julia C. Gandert, Marcus Müller, Sabine Paarmann, Oliver Queisser, and Thomas Wetzel. Effective Thermal Conductivity of Lithium-Ion Battery Electrodes in Dependence on the Degree of Calendering. *Energy Technol.*, 158:2000862, January 2023. ISSN 21944288. doi: 10.1002/ente.202300259.

[37] Amy Marconnet, Sabrina Herberger, Sabine Paarmann, Philipp Seegert, and Thomas Wetzel. Impact of aging on the thermophysical properties of lithium-ion battery electrodes. *J. Power Sources*, 603:234367, May 2024. ISSN 03787753. doi: 10.1016/j.jpowsour.2024.234367.

[38] Li Song and James W. Evans. Measurements of the Thermal Conductivity of Lithium Polymer Battery Composite Cathodes. *J. Electrochem. Soc.*, 146 (3):869–871, January 1999. ISSN 0378-7753. doi: 10.1149/1.1391694.

[39] Odne S. Burheim, Morten A. Onsrud, Jon G. Pharoah, Fride Vullum-Bruer, and Preben J. S. Vie. Thermal Conductivity, Heat Sources and Temperature Profiles of Li-Ion Batteries. *ECS Trans.*, 58(48):145–171, January 2014. ISSN 1938-5862. doi: 10.1149/05848.0145ecst.

[40] Satyam Panchal, Scott Mathewson, Roydon Fraser, Richard Culham, and Michael Fowler. Experimental Measurements of Thermal Characteristics of LiFePO 4 Battery. SAE Technical Paper Series. SAE International400 Commonwealth Drive, Warrendale, PA, United States, January 2015. doi: 10.4271/2015-01-1189.

[41] Frank Richter, Signe Kjelstrup, Preben J.S. Vie, and Odne S. Burheim. Thermal conductivity and internal temperature profiles of Li-ion secondary batteries. *J. Power Sources*, 359:592–600, January 2017. ISSN 0378-7753. doi: 10.1016/j.jpowsour.2017.05.045.

[42] Frank Richter, Preben J.S. Vie, Signe Kjelstrup, and Odne Stokke Burheim. Measurements of ageing and thermal conductivity in a secondary NMC-hard carbon Li-ion battery and the impact on internal temperature profiles. *Electrochim. Acta*, 250(19):228–237, January 2017. ISSN 00134686. doi: 10.1016/j.electacta.2017.07.173.

[43] Sean D. Lubner, Sumanjeet Kaur, Yanbao Fu, Vince Battaglia, and Ravi S. Prasher. Identification and characterization of the dominant thermal resistance in lithium-ion batteries using operando 3-omega sensors. *J. Appl. Phys. (Melville, NY, U. S.)*, 127(10):105104, January 2020. ISSN 0021-8979. doi: 10.1063/1.5134459.

[44] Lena Spitthoff, Markus Solberg Wahl, Preben J.S. Vie, and Odne Stokke Burheim. Thermal transport in lithium-ion batteries: The effect of degradation. *J. Power Sources*, 577(April 2016):233149, January 2023. ISSN 0378-7753. doi: 10.1016/j.jpowsour.2023.233149.

[45] Kai Peter Birke. *Modern battery engineering: A comprehensive introduction*. January 2019. ISBN 978-981-327-215-6.

[46] Reiner Korthauer, editor. *Lithium-Ion Batteries: Basics and Applications*. Springer Berlin Heidelberg, Berlin, Heidelberg, 2018. ISBN 978-3-662-53069-6 978-3-662-53071-9.

[47] Silje Nornes Bryntesen, Anders Hammer Strømman, Ignat Tolstorebrov, Paul R. Shearing, Jacob J. Lamb, and Odne Stokke Burheim. Opportunities for the State-of-the-Art Production of LIB Electrodes—A Review. *Energies*, 14(5):1406, January 2021. doi: 10.3390/en14051406.

[48] R. Gonçalves, S. Lanceros-Méndez, and C. M. Costa. Electrode fabrication process and its influence in lithium-ion battery performance: State of the art and future trends. *Electrochemistry Communications*, 135(5):107210, January 2022. ISSN 13882481. doi: 10.1016/j.elecom.2022.107210.

[49] Clara Sangrós, Carsten Schilde, and Arno Kwade. Effect of Microstructure on Thermal Conduction within Lithium-Ion Battery Electrodes using Discrete Element Method Simulations. *Energy Technol.*, 4(12):1611–1619, January 2016. ISSN 21944288. doi: 10.1002/ente.201600144.

[50] Linus Froboese, Paul Titscher, Bastian Westphal, Wolfgang Haselrieder, and Arno Kwade. Mercury intrusion for ion- and conversion-based battery electrodes – Structure and diffusion coefficient determination. *Mater. Charact.*, 133(11):102–111, January 2017. ISSN 1044-5803. doi: 10.1016/j.matchar.2017.09.002.

[51] I. N. McCave, R. J. Bryant, H. F. Cook, and C. A. Coughanowr. Evaluation of a laser-diffraction-size analyzer for use with natural sediments. *Journal of Sedimentary Research*, 56(4):561–564, July 1986. ISSN 1527-1404. doi: 10.1306/212F89CC-2B24-11D7-8648000102C1865D.

[52] Gerben B. J. De Boer, Cornelis De Weerd, Dirk Thoenes, and Hendrik W. J. Goossens. Laser Diffraction Spectrometry: Fraunhofer Diffraction Versus Mie Scattering. *Part & Part Syst Charact*, 4(1-4):14–19, January 1987. ISSN 0934-0866, 1521-4117. doi: 10.1002/ppsc.19870040104.

[53] X.-S. Cai and N.-N. Wang. Determination of particle size distribution using the light extinction method. *Advanced Powder Technology*, 3(3):153–161, 1992. ISSN 09218831. doi: 10.1016/S0921-8831(08)60667-6.

[54] Juan Fernando Meza Gonzalez, Hermann Nirschl, and Frank Rhein. Continuous Anode Slurry Production in Twin-Screw Extruders: Effects of the Process Setup on the Dispersion. *Batteries*, 10(5):145, April 2024. ISSN 2313-0105. doi: 10.3390/batteries10050145.

[55] Edward W. Washburn. Note on a Method of Determining the Distribution of Pore Sizes in a Porous Material. *Proc. Natl. Acad. Sci. U.S.A.*, 7(4):115–116, April 1921. ISSN 0027-8424, 1091-6490. doi: 10.1073/pnas.7.4.115.

[56] Jhonatan Jair Arismendi Florez, Jean Vicente Ferrari, and Carina Ulsen. Study of the contact angle and roughness effects on mercury intrusion porosimetry (MIP) analysis in natural/real carbonate rocks using massive pure minerals and synthetic carbonate rocks. *Journal of Materials Research and Technology*, 32:286–317, September 2024. ISSN 22387854. doi: 10.1016/j.jmrt.2024.07.177. URL `https://linkinghub.elsevier.com/retrieve/pii/S2238785424017307`.

[57] S. Radloff, L.S. Kremer, A. Hoffmann, and M. Wohlfahrt-Mehrens. Characterization of structured ultra-thick LiNi0.6Co0.2Mn0.2O2 lithium-ion battery electrodes by mercury intrusion porosimetry. *Materials Today Communications*, 28:102549, September 2021. ISSN 23524928. doi: 10.1016/j.mtcomm.2021.102549.

[58] Joseph I. Goldstein, Dale E. Newbury, Joseph R. Michael, Nicholas W.M. Ritchie, John Henry J. Scott, and David C. Joy. *Scanning Electron Microscopy and X-Ray Microanalysis*. Springer New York, New York, NY, 2018. ISBN 978-1-4939-6674-5 978-1-4939-6676-9. doi: 10.1007/978-1-4939-6676-9.

[59] Silje Nornes Bryntesen, Armin Kahrom, Jacob Joseph Lamb, Ignat Tolstorebrov, and Odne Stokke Burheim. Experimental Analysis of Drying Kinetics and Quality Aspects of Convection-Dried Cathodes at Laboratory Scale. *Batteries (Basel, Switz.)*, 9(2):96, January 2023. doi: 10.3390/batteries9020096.

[60] Dominik Mayer, Ann-Kathrin Wurba, Benjamin Bold, Jonathan Bernecker, Anna Smith, and Jürgen Fleischer. Investigation of the Mechanical Behavior of Electrodes after Calendering and Its Influence on Singulation and Cell Performance. *Processes*, 9(11):2009, January 2021. doi: 10.3390/pr9112009.

[61] Werner Bauer, Dorit Nötzel, Valentin Wenzel, and Hermann Nirschl. Influence of dry mixing and distribution of conductive additives in cathodes for lithium ion batteries. *J. Power Sources*, 288(12):359–367, January 2015. ISSN 0378-7753. doi: 10.1016/j.jpowsour.2015.04.081.

[62] A. J. Garratt-Reed and D. C. Bell. *Energy-dispersive X-ray analysis in the electron microscope*. BIOS, Oxford, UK, 2005. ISBN 978-1-85996-109-4 978-0-203-48342-8.

[63] Marcus Müller, Lukas Pfaffmann, Stefan Jaiser, Michael Baunach, Vanessa Trouillet, Frieder Scheiba, Philip Scharfer, Wilhelm Schabel, and Werner Bauer. Investigation of binder distribution in graphite anodes for lithium-ion batteries. *J. Power Sources*, 340:1–5, January 2017. ISSN 0378-7753. doi: 10.1016/j.jpowsour.2016.11.051.

[64] Bastian G. Westphal and Arno Kwade. Critical electrode properties and drying conditions causing component segregation in graphitic anodes for lithium-ion batteries. *Journal of Energy Storage*, 18:509–517, January 2018. ISSN 2352152X. doi: 10.1016/j.est.2018.06.009.

[65] Ali Davoodabadi, Jianlin Li, Yongfeng Liang, Robert Wang, Hui Zhou, David L. Wood, Timothy J. Singler, and Congrui Jin. Characterization of Surface Free Energy of Composite Electrodes for Lithium-Ion Batteries.

J. Electrochem. Soc., 165(11):A2493–A2501, 2018. ISSN 0013-4651, 1945-7111. doi: 10.1149/2.0341811jes.

[66] Wolfgang Haselrieder, Bastian Westphal, Henrike Bockholt, Alexander Diener, Steffi Höft, and Arno Kwade. Measuring the coating adhesion strength of electrodes for lithium-ion batteries. *Int. J. Adhes. Adhes.*, 60:1–8, January 2015. ISSN 0143-7496. doi: 10.1016/j.ijadhadh.2015.03.002.

[67] Libao Chen, Xiaohua Xie, Jingying Xie, Ke Wang, and Jun Yang. Binder effect on cycling performance of silicon/carbon composite anodes for lithium ion batteries. *J Appl Electrochem*, 36(10):1099–1104, October 2006. ISSN 0021-891X, 1572-8838. doi: 10.1007/s10800-006-9191-2.

[68] Jing Li, L. Christensen, M. N. Obrovac, K. C. Hewitt, and J. R. Dahn. Effect of Heat Treatment on Si Electrodes Using Polyvinylidene Fluoride Binder. *J. Electrochem. Soc.*, 155(3):A234, 2008. ISSN 00134651. doi: 10.1149/1.2830545.

[69] Hye-Kyoung Park, Byung-Seon Kong, and Eun-Suok Oh. Effect of high adhesive polyvinyl alcohol binder on the anodes of lithium ion batteries. *Electrochemistry Communications*, 13(10):1051–1053, October 2011. ISSN 13882481. doi: 10.1016/j.elecom.2011.06.034.

[70] Bongki Son, Myung-Hyun Ryou, Jaecheol Choi, Taejoo Lee, Hyung Kyun Yu, Jong Hun Kim, and Yong Min Lee. Measurement and Analysis of Adhesion Property of Lithium-Ion Battery Electrodes with SAICAS. *ACS Appl. Mater. Interfaces*, 6(1):526–531, January 2014. ISSN 1944-8244, 1944-8252. doi: 10.1021/am404580f.

[71] Julian Klemens, Luca Schneider, Eike Christian Herbst, Nicole Bohn, Marcus Müller, Werner Bauer, Philip Scharfer, and Wilhelm Schabel. Drying of NCM Cathode Electrodes with Porous, Nanostructured Particles Versus Compact Solid Particles: Comparative Study of Binder Migration as a Function of Drying Conditions. *Energy Technol.*, 10(4):2100985, January 2022. ISSN 21944288. doi: 10.1002/ente.202100985.

[72] Julian Klemens, David Burger, Luca Schneider, Sandro Spiegel, Marcus Müller, Nicole Bohn, Werner Bauer, Helmut Ehrenberg, Philip Scharfer, and Wilhelm Schabel. Drying of Compact and Porous NCM Cathode Electrodes in Different Multilayer Architectures: Influence of Layer Configuration and Drying Rate on Electrode Properties. *Energy Technol.*, 11: 2300267, January 2023. ISSN 21944288. doi: 10.1002/ente.202300267.

[73] Julian Klemens, Luca Schneider, David Burger, Nadine Zimmerer, Marcus Müller, Werner Bauer, Helmut Ehrenberg, Philip Scharfer, and Wilhelm Schabel. Process and Drying Behavior Toward Higher Drying Rates of Hard Carbon Anodes for Sodium-Ion Batteries with Different Particle Sizes: An Experimental Study in Comparison to Graphite for Lithium-Ion-Batteries. *Energy Technol.*, 57:102, January 2023. ISSN 21944288. doi: 10.1002/ente.202300338.

[74] Julian Klemens, Ann-Kathrin Wurba, David Burger, Marcus Müller, Werner Bauer, Sebastian Büchele, Olatz Leonet, J. Alberto Blázquez, Iker Boyano, Elixabete Ayerbe, Helmut Ehrenberg, Jürgen Fleischer, Anna Smith, Philip Scharfer, and Wilhelm Schabel. Challenges and Opportunities for Large-Scale Electrode Processing for Sodium-Ion and Lithium-Ion Battery. *Batteries Supercaps*, 447:10, January 2023. ISSN 2566-6223. doi: 10.1002/batt.202300291.

[75] Kubra Uzun, Bhamiti Sharma, Bradley R. Frieberg, Ming Wang, Jiazhi Hu, Anita Li, Xiaosong Huang, and Yang-Tse Cheng. Investigating the Structure and Performance of Electrodes Made by Dry and Wet Slurry Processes. *J. Electrochem. Soc.*, 171(2):020516, February 2024. ISSN 0013-4651, 1945-7111. doi: 10.1149/1945-7111/ad242d.

[76] R. Bartali, V. Micheli, G. Gottardi, A. Vaccari, and N. Laidani. Nanoindentation: Unload-to-load work ratio analysis in amorphous carbon films for mechanical properties. *Surface and Coatings Technology*, 204(12-13): 2073–2076, March 2010. ISSN 02578972. doi: 10.1016/j.surfcoat.2009.11.002.

[77] Hai Yen Tran, Giorgia Greco, Corina Täubert, Margret Wohlfahrt-Mehrens, Wolfgang Haselrieder, and Arno Kwade. Influence of electrode preparation on the electrochemical performance of LiNi0.8Co0.15Al0.05O2 composite electrodes for lithium-ion batteries. *J. Power Sources*, 210(2):276–285, January 2012. ISSN 0378-7753. doi: 10.1016/j.jpowsour.2012.03.017.

[78] Sören Scheffler, René Jagau, Nele Müller, Alexander Diener, and Arno Kwade. Calendering of Silicon-Containing Electrodes and Their Influence on the Mechanical and Electrochemical Properties. *Batteries (Basel, Switz.)*, 8(5):46, January 2022. doi: 10.3390/batteries8050046.

[79] Bastian Westphal, Henrike Bockholt, T. Günther, W. Haselrieder, and Arno Kwade. Influence of Convective Drying Parameters on Electrode Performance and Physical Electrode Properties. *ECS Trans.*, 64(22):57–68, January 2015. ISSN 1938-5862. doi: 10.1149/06422.0057ecst.

[80] Henrike Bockholt, Wolfgang Haselrieder, and Arno Kwade. Intensive powder mixing for dry dispersing of carbon black and its relevance for lithium-ion battery cathodes. *Powder Technol.*, 297:266–274, January 2016. ISSN 0032-5910. doi: 10.1016/j.powtec.2016.04.011.

[81] Marcus Müller, Luca Schneider, Nicole Bohn, Joachim R. Binder, and Werner Bauer. Effect of Nanostructured and Open-Porous Particle Morphology on Electrode Processing and Electrochemical Performance of Li-Ion Batteries. *ACS Appl. Energy Mater.*, 4(2):1993–2003, January 2021. ISSN 2574-0962. doi: 10.1021/acsaem.0c03187.

[82] Clara Sangrós Giménez, Carsten Schilde, Linus Froböse, Stoyan Ivanov, and Arno Kwade. Mechanical, Electrical, and Ionic Behavior of Lithium-Ion Battery Electrodes via Discrete Element Method Simulations. *Energy Technol.*, 8(2):1900180, January 2020. ISSN 21944288. doi: 10.1002/ente.201900180.

[83] Jana Kumberg, Werner Bauer, Joyce Schmatz, Ralf Diehm, Max Tönsmann, Marcus Müller, Kevin Ly, Philip Scharfer, and Wilhelm Schabel.

Reduced Drying Time of Anodes for Lithium-Ion Batteries through Simultaneous Multilayer Coating. *Energy Technol.*, 9(10):421, January 2021. ISSN 21944288. doi: 10.1002/ente.202100367.

[84] Luca Schneider, Julian Klemens, Eike Christian Herbst, Marcus Müller, Philip Scharfer, Wilhelm Schabel, Werner Bauer, and Helmut Ehrenberg. Transport Properties in Electrodes for Lithium-Ion Batteries: Comparison of Compact versus Porous NCM Particles. *J. Electrochem. Soc.*, 169(10): 100553, October 2022. ISSN 0013-4651, 1945-7111. doi: 10.1149/1945-7111/ac9c37.

[85] David Burger, Noah Keim, Junaid Shabbir, Yuhao Gao, Marcus Müller, Werner Bauer, Alexander Hoffmann, Philip Scharfer, and Wilhelm Schabel. Simultaneous Primer Coating for Fast Drying of Battery Electrodes. *Energy Tech*, page 2401668, November 2024. ISSN 2194-4288, 2194-4296. doi: 10.1002/ente.202401668.

[86] Burster Präzisionsmesstechnik GmbH & Co KG. Bedienungsan-leitung RESISTOMAT® 2329. Available online at: https://www.burster.de/fileadmin/user_upload/redaktion/Documents/Products/Manuals/Section_2/BA_2329_DE.pdf, last accessed on March 31, 2025.

[87] Andreas Stadler. *Photonik der Solarzellen: Innovative Messverfahren für moderne Solarzellen*. SpringerLink Bücher. Springer Vieweg, Wiesbaden, 2. aufl. 2017 edition, 2017. ISBN 978-3-658-18964-8. doi: 10.1007/978-3-658-18965-5.

[88] Hioki E. E. Corporation. Electrode Resistance Measurement System RM2610. Available online at: https://www.hioki.com/euro-en/download/33105, last accessed on March 31, 2025.

[89] Nicholas Loeffler, Guk.-T. Kim, Stefano Passerini, Cesar Gutierrez, Iosu Cendoya, Iratxe DeMeatza, Fabrizio Alessandrini, and Giovanni B. Appetecchi. Performance and Ageing Robustness of Graphite/NMC Pouch Prototypes Manufactured through Eco-Friendly Materials and Processes.

ChemSusChem, 10(18):3581–3587, September 2017. ISSN 1864-5631, 1864-564X. doi: 10.1002/cssc.201701087.

[90] Henrike Bockholt, Maira Indrikova, Andreas Netz, Frederik Golks, and Arno Kwade. The interaction of consecutive process steps in the manufacturing of lithium-ion battery electrodes with regard to structural and electrochemical properties. *J. Power Sources*, 325(4):140–151, January 2016. ISSN 0378-7753. doi: 10.1016/j.jpowsour.2016.05.127.

[91] Carina A. Heck, Fabienne Huttner, Julian K. Mayer, Olga Fromm, Markus Börner, Thilo Heckmann, Philip Scharfer, Wilhelm Schabel, Martin Winter, and Arno Kwade. Production of Nickel-Rich Cathodes for Lithium-Ion Batteries from Lab to Pilot Scale under Investigation of the Process Atmosphere. *Energy Technol.*, 11(5):69, January 2023. ISSN 21944288. doi: 10.1002/ente.202200945.

[92] Andreas Gyulai, Werner Bauer, and Helmut Ehrenberg. Dry Electrode Manufacturing in a Calender: The Role of Powder Premixing for Electrode Quality and Electrochemical Performance. *ACS Appl. Energy Mater.*, 6 (10):5122–5134, January 2023. ISSN 2574-0962. doi: 10.1021/acsaem .2c03755.

[93] Julia C. Gandert, Marcus Müller, Simon B. B. Solberg, Robert L McMasters, Thomas Wetzel, and Odne S. Burheim. Challenges of the Measurement of the Effective Thermal Conductivity of Battery Electrodes with Laser Flash Analysis and Guarded Hot Plate Method. *Energy Technol.*, 2025.

[94] Robert R. Zarr. A History of Testing Heat Insulators at the National Institute of Standards and Technology. *ASHRAE Trans.*, 107 (2), January 2001. Available online at: https://tsapps.nist.gov/publication/get_pdf.cfm?pub_id=860832, last accessed September 09, 2025.

[95] Robert R. Zarr. The Testing of Thermal Insulators. *A Century of Excellence in Measurements, Standards, and Technology: A Chronicle of Selected NBS/NIST Publications*, 2001. Available online

at: https://nvlpubs.nist.gov/nistpubs/sp958-lide/010-013.pdf, last accessed September 08, 2025.

[96] Odne Burheim, Preben J. S. Vie, Jon G. Pharoah, and Signe Kjelstrup. Ex situ measurements of through-plane thermal conductivities in a polymer electrolyte fuel cell. *J. Power Sources*, 195(1):249–256, January 2010. ISSN 0378-7753. doi: 10.1016/j.jpowsour.2009.06.077.

[97] Odne S. Burheim, Huaneng Su, Sivakumar Pasupathi, Jon G. Pharoah, and Bruno G. Pollet. Thermal conductivity and temperature profiles of the micro porous layers used for the polymer electrolyte membrane fuel cell. *International Journal of Hydrogen Energy*, 38(20):8437–8447, July 2013. ISSN 03603199. doi: 10.1016/j.ijhydene.2013.04.140.

[98] W. J. Parker, R. J. Jenkins, C. P. Butler, and G. L. Abbott. Flash Method of Determining Thermal Diffusivity, Heat Capacity, and Thermal Conductivity. *J. Appl. Phys. (Melville, NY, U. S.)*, 32(9):1679–1684, January 1961. ISSN 0021-8979. doi: 10.1063/1.1728417. Num Pages: 7.

[99] Robert D. Cowan. Pulse Method of Measuring Thermal Diffusivity at High Temperatures. *J. Appl. Phys. (Melville, NY, U. S.)*, 34(4):926–927, January 1963. ISSN 0021-8979. doi: 10.1063/1.1729564. Num Pages: 3.

[100] J. A. Cape and G. W. Lehman. Temperature and Finite Pulse-Time Effects in the Flash Method for Measuring Thermal Diffusivity. *J. Appl. Phys.*, 34 (7):1909–1913, July 1963. ISSN 0021-8979, 1089-7550. doi: 10.1063/1.1729711.

[101] László Dusza. Combined solution of the simultaneous heat loss and finite pulse corrections with the laser flash method. *High Temp.-High Press.*, 27/28(5):467–473, 1995. ISSN 0018-1544, 1472-3441. doi: 10.1068/htrt26.

[102] Jürgen Blumm, Jack Henderson, Ove Nilsson, and Jochen Fricke. Laser flash measurement of the phononic thermal diffusivity of glasses in the presence of ballistic radiative transfer. *High Temp.-High Press.*, 29(5): 555–560, 1997. ISSN 0018-1544, 1472-3441. doi: 10.1068/htec141.

[103] Robert L. McMasters, James Vere Beck, Ralph B. Dinwiddie, and Hsin Wang. Accounting for Penetration of Laser Heating in Flash Thermal Diffusivity Experiments. *J. Heat Transfer*, 121(1):15–21, January 1999. ISSN 0022-1481. doi: 10.1115/1.2825929. Num Pages: 7.

[104] DSC Differential Scanning Calorimeter - Q Series Getting Started Guide, January 2007. Available online at: https://www.nmt.edu/ academics/mtls/-faculty/mccoy/docs/dsc/ta_mdsc_manual2007.pdf, last accessed on April 14, 2025.

[105] NETZSCH-Gerätebau GmbH. Functional principle of a heat-flux DSC. Available online at: https://analyzing-testing.netzsch.com/de/landingpages/funktionsprinzip-einer-waermestrom-dsc, last accessed on April 14, 2025.

[106] Günther Höhne, Wolfgang Hemminger, Hans-Jürgen Flammersheim, Wolfgang Hemminger, and H.-J. Flammersheim. *Differential Scanning Calorimetry*. Springer Berlin, Berlin, 2., nd rev. a. enlarged ed. softcover version of original hardcover edition 2003 edition, 2010. ISBN 978-3-642-05593-5.

[107] Alfred Fahr. *Voigt's pharmaceutical technology*. Wiley, Hoboken, NJ, 2018. ISBN 978-1-118-97243-4 978-1-118-97244-1.

[108] Seymour Lowell, editor. *Characterization of porous solids and powders: surface area, pore size and density*. Number 16 in Particle technology series. Springer, Dordrecht, 4. ed., 1. reprint with some corr edition, 2006. ISBN 978-1-4020-2302-6.

[109] Jianbo Zhang, Bin Wu, Zhe Li, and Jun Huang. Simultaneous estimation of thermal parameters for large-format laminated lithium-ion batteries. *J. Power Sources*, 259:106–116, January 2014. ISSN 0378-7753. doi: 10.1016/j.jpowsour.2014.02.079.

[110] André Loges, Sabrina Herberger, Daniel Werner, and Thomas Wetzel. Thermal characterization of Li-ion cell electrodes by photothermal deflection spectroscopy. *J. Power Sources*, 325:104–115, January 2016. ISSN 0378-7753. doi: 10.1016/j.jpowsour.2016.05.082.

[111] Marco Steinhardt, Jorge V. Barreras, Haijun Ruan, Billy Wu, Gregory J. Offer, and Andreas Jossen. Meta-analysis of experimental results for heat capacity and thermal conductivity in lithium-ion batteries: A critical review. *J. Power Sources*, 522:230829, January 2022. ISSN 0378-7753. doi: 10.1016/j.jpowsour.2021.230829.

[112] Hossein Maleki, Said Al Hallaj, J. Robert Selman, Ralph B. Dinwiddie, and H. Wang. Thermal Properties of Lithium-Ion Battery and Components // Thermal Properties of Lithium-Ion Battery and Components. *J. Electrochem. Soc.*, 146(3):947–954, January 1999. ISSN 0378-7753. doi: 10.1149/1.1391704.

[113] Dieter Oehler, Jonas Bender, Philipp Seegert, and Thomas Wetzel. Investigation of the Effective Thermal Conductivity of Cell Stacks of Li-Ion Batteries. *Energy Technol.*, 336:2000722, January 2020. ISSN 21944288. doi: 10.1002/ente.202000722.

[114] Todd M. Bandhauer, Srinivas Garimella, and Thomas F. Fuller. A Critical Review of Thermal Issues in Lithium-Ion Batteries. *J. Electrochem. Soc.*, 158(3):1, January 2011. ISSN 0378-7753. doi: 10.1149/1.3515880.

[115] Mathis Wissler. Graphite and carbon powders for electrochemical applications. *J. Power Sources*, 156(2):142–150, January 2006. ISSN 0378-7753. doi: 10.1016/j.jpowsour.2006.02.064.

[116] Laura Gottschalk, Jannes Müller, Alexander Schoo, Ernesto Baasch, and Arno Kwade. Spherical Graphite Anodes: Influence of Particle Size Distribution and Multilayer Structuring in Lithium-Ion Battery Cells. *Batteries*, 10(2):40, January 2024. ISSN 2313-0105. doi: 10.3390/batteries10020040.

[117] L. Y. Beaulieu, K. W. Eberman, R. L. Turner, L. J. Krause, and J. R. Dahn. Colossal Reversible Volume Changes in Lithium Alloys. *Electrochem. Solid-State Lett.*, 4(9):A137, 2001. ISSN 10990062. doi: 10.1149/1.1388178.

[118] L. Y. Beaulieu, T. D. Hatchard, A. Bonakdarpour, M. D. Fleischauer, and J. R. Dahn. Reaction of Li with Alloy Thin Films Studied by In Situ AFM. *J. Electrochem. Soc.*, 150(11):A1457, 2003. ISSN 00134651. doi: 10.1149/1.1613668.

[119] Xiao Hua Liu, Li Zhong, Shan Huang, Scott X. Mao, Ting Zhu, and Jian Yu Huang. Size-Dependent Fracture of Silicon Nanoparticles During Lithiation. *ACS Nano*, 6(2):1522–1531, February 2012. ISSN 1936-0851, 1936-086X. doi: 10.1021/nn204476h.

[120] Matthew B. Pinson and Martin Z. Bazant. Theory of SEI Formation in Rechargeable Batteries: Capacity Fade, Accelerated Aging and Lifetime Prediction. *J. Electrochem. Soc.*, 160(2):A243–A250, 2013. ISSN 0013-4651, 1945-7111. doi: 10.1149/2.044302jes.

[121] John Christensen, Venkat Srinivasan, and John Newman. Optimization of Lithium Titanate Electrodes for High-Power Cells. *J. Electrochem. Soc.*, 153(3):A560, 2006. ISSN 00134651. doi: 10.1149/1.2172535.

[122] Edward Buiel and J R Dahn. Li-insertion in hard carbon anode materials for Li-ion batteries. *Electrochimica Acta*, 1999. doi: 10.1016/S0013-4686(99)00198-X.

[123] Kuan-Hung Chen, Vishwas Goel, Min Ji Namkoong, Markus Wied, Simon Müller, Vanessa Wood, Jeff Sakamoto, Katsuyo Thornton, and Neil P. Dasgupta. Enabling 6C Fast Charging of Li-Ion Batteries with Graphite Hard Carbon Hybrid Anodes.pdf. *Adv. Energy Mater.*, 11(5):2003336, December 2020. doi: 10.1002/aenm.202003336.

[124] Harald Ulrik Sverdrup, Kristin Vala Ragnarsdottir, and Deniz Koca. Integrated Modelling of the Global Cobalt Extraction, Supply, Price and

Depletion of Extractable Resources Using the WORLD6 Model. *Biophys Econ Resour Qual*, 2(1):6649, January 2017. ISSN 2366-0112. doi: 10.1007/s41247-017-0017-0.

[125] Gondia Sokhna Seck, Emmanuel Hache, and Charlène Barnet. Potential bottleneck in the energy transition: The case of cobalt in an accelerating electro-mobility world. *Resources Policy*, 75(128):102516, January 2022. ISSN 03014207. doi: 10.1016/j.resourpol.2021.102516.

[126] Naoki Nitta, Feixiang Wu, Jung Tae Lee, and Gleb Yushin. Li-ion battery materials: present and future. *Materials Today*, 18(5):252–264, June 2015. ISSN 13697021. doi: 10.1016/j.mattod.2014.10.040.

[127] Alex Hebert and Eric McCalla. The role of metal substitutions in the development of Li batteries, part I: cathodes. 2021. doi: 10.1039/d1ma00081k.

[128] E. Petavratzi, P. Josso, and British Geological Survey. Global material flows of lithium for the lithium-ion and lithium iron phosphate battery market. Technical report, Nottingham, UK, January 2021. URL `https://nora.nerc.ac.uk/id/eprint/531362/`.

[129] M. Stanley Whittingham and Jie Xiao. Fifty years of lithium-ion batteries and what is next? *MRS Bulletin*, 192:1126, January 2023. ISSN 0883-7694. doi: 10.1557/s43577-023-00627-z.

[130] Nanny Strzelczyk, Laura Gottschalk, Jannes Müller, and Arno Kwade. The Influence of Calendering on the Fast Charging Performance and Lithium Plating of Hard Carbon Blend Anodes. *Energy Technol.*, 11(5):135, January 2023. ISSN 21944288. doi: 10.1002/ente.202200865.

[131] Chia-Chen Li, Jyh-Tsung Lee, Yi-Ling Tung, and Chang-Rung Yang. Effects of pH on the dispersion and cell performance of LiCoO2 cathodes based on the aqueous process. *J Mater Sci*, 42(14):5773–5777, January 2007. ISSN 0022-2461. doi: 10.1007/s10853-006-1172-7.

[132] Shu-Lei Chou, Yuede Pan, Jia-Zhao Wang, Hua-Kun Liu, and Shi-Xue Dou. Small things make a big difference: binder effects on the performance of Li and Na batteries. *Phys. Chem. Chem. Phys.*, 16(38):20347–59, January 2014. doi: 10.1039/c4cp02475c.

[133] Italo Doberdò, Nicholas Löffler, Nina Laszczynski, Dario Cericola, Nerino Penazzi, Silvia Bodoardo, Guk-Tae Kim, and Stefano Passerini. Enabling aqueous binders for lithium battery cathodes – Carbon coating of aluminum current collector. *Journal of Power Sources*, 248:1000–1006, February 2014. ISSN 03787753. doi: 10.1016/j.jpowsour.2013.10.039.

[134] Michaela Memm, Alice Hoffmann, and Margret Wohlfahrt-Mehrens. Water-based LiNi1/3Mn1/3Co1/3O2-cathodes with good electrochemical performance by use of additives. *Electrochimica Acta*, 260:664–673, January 2018. ISSN 00134686. doi: 10.1016/j.electacta.2017.12.014.

[135] Werner Bauer, Fatih A. Çetinel, Marcus Müller, and Ulrike Kaufmann. Effects of pH control by acid addition at the aqueous processing of cathodes for lithium ion batteries. *Electrochimica Acta*, 317:112–119, January 2019. ISSN 00134686. doi: 10.1016/j.electacta.2019.05.141.

[136] A. Gören, C.M. Costa, M.M. Silva, and S. Lanceros-Méndez. State of the art and open questions on cathode preparation based on carbon coated lithium iron phosphate. *Composites Part B: Engineering*, 83:333–345, December 2015. ISSN 13598368. doi: 10.1016/j.compositesb.2015.08.064.

[137] Michael E. Spahr. Carbon-Conductive Additives for Lithium-Ion Batteries. In Masaki Yoshio, Ralph J. Brodd, and Akiya Kozawa, editors, *Lithium-Ion Batteries*, pages 1–38. Springer New York, New York, NY, January 2009. ISBN 978-0-387-34444-7. doi: 10.1007/978-0-387-34445-4_5.

[138] Jin K. Hong, Jong H. Lee, and Seung M. Oh. Effect of carbon additive on electrochemical performance of LiCoO2 composite cathodes. *J. Electrochem. Soc.*, 111(1):90–96, January 2002. ISSN 0378-7753. doi: 10.1016/S0378-7753(02)00264-1.

[139] Marina Despotopoulou and Michael T. Burchill. Coatings for electrochemical applications. *Progress in Organic Coatings*, 45(2-3):119–126, January 2002. ISSN 03009440. doi: 10.1016/S0300-9440(02)00105-4.

[140] Chris Meyer, Matthias Weyhe, Wolfgang Haselrieder, and Arno Kwade. Heated Calendering of Cathodes for Lithium-Ion Batteries with Varied Carbon Black and Binder Contents. *Energy Technol.*, 8(2):1900175, January 2020. ISSN 21944288. doi: 10.1002/ente.201900175.

[141] G. Liu, H. Zheng, S. Kim, Y. Deng, A. M. Minor, X. Song, and V. S. Battaglia. Effects of Various Conductive Additive and Polymeric Binder Contents on the Performance of a Lithium-Ion Composite Cathode. *J. Electrochem. Soc.*, 155(12):887, January 2008. ISSN 0378-7753. doi: 10.1149/1.2976031.

[142] Alexander Diener, Stoyan Ivanov, Wolfgang Haselrieder, and Arno Kwade. Evaluation of Deformation Behavior and Fast Elastic Recovery of Lithium-Ion Battery Cathodes via Direct Roll-Gap Detection During Calendering. *Energy Tech*, 10(4):2101033, April 2022. ISSN 2194-4288, 2194-4296. doi: 10.1002/ente.202101033.

[143] Dominic Bresser, Daniel Buchholz, Arianna Moretti, Alberto Varzi, and Stefano Passerini. Alternative binders for sustainable electrochemical energy storage – the transition to aqueous electrode processing and bio-derived polymers. *Energy Environ. Sci.*, 11(11):3096–3127, January 2018. ISSN 1754-5692. doi: 10.1039/C8EE00640G.

[144] Fabian Jeschull, Matthew J. Lacey, and Daniel Brandell. Functional binders as graphite exfoliation suppressants in aggressive electrolytes for lithium-ion batteries. *Electrochimica Acta*, 175:141–150, September 2015. ISSN 00134686. doi: 10.1016/j.electacta.2015.03.072.

[145] Moses Ender, Jochen Joos, André Weber, and Ellen Ivers-Tiffée. Anode microstructures from high-energy and high-power lithium-ion cylindrical cells obtained by X-ray nano-tomography. *J. Power Sources*, 269:912–919, January 2014. ISSN 0378-7753. doi: 10.1016/j.jpowsour.2014.07.070.

[146] Chris Meyer, Henrike Bockholt, Wolfgang Haselrieder, and Arno Kwade. Characterization of the calendering process for compaction of electrodes for lithium-ion batteries. *J. Mater. Process. Technol.*, 249(15):172–178, January 2017. ISSN 0924-0136. doi: 10.1016/j.jmatprotec.2017.05.031.

[147] Xuekun Lu, Sohrab R. Daemi, Antonio Bertei, Matthew D.R. Kok, Kieran B. O'Regan, Lara Rasha, Juyeon Park, Gareth Hinds, Emma Kendrick, Dan J.L. Brett, and Paul R. Shearing. Microstructural Evolution of Battery Electrodes During Calendering. *Joule*, 4(12):2746–2768, January 2020. ISSN 25424351. doi: 10.1016/j.joule.2020.10.010.

[148] Henrike Bockholt, Wolfgang Haselrieder, and Arno Kwade. Intensive Dry and Wet Mixing Influencing the Structural and Electrochemical Properties of Secondary Lithium-Ion Battery Cathodes. *ECS Trans.*, 50(26):25–35, January 2013. ISSN 1938-5862. doi: 10.1149/05026.0025ecst.

[149] Bastian Georg Westphal, Nils Mainusch, Chris Meyer, Wolfgang Haselrieder, Maira Indrikova, Paul Titscher, Henrike Bockholt, Wolfgang Viöl, and Arno Kwade. Influence of high intensive dry mixing and calendering on relative electrode resistivity determined via an advanced two point approach. *Journal of Energy Storage*, 11:76–85, January 2017. ISSN 2352152X. doi: 10.1016/j.est.2017.02.001.

[150] Brandon Ludwig, Jin Liu, I-Meng Chen, Yangtao Liu, Wan Shou, Yan Wang, and Heng Pan. Understanding Interfacial-Energy-Driven Dry Powder Mixing for Solvent-Free Additive Manufacturing of Li-Ion Battery Electrodes. *Adv. Mater. Interfaces*, 4(21):1700570, January 2017. ISSN 2196-7350. doi: 10.1002/admi.201700570.

[151] Yang Lu, Chen-Zi Zhao, Hong Yuan, Jiang-Kui Hu, Jia-Qi Huang, and Qiang Zhang. Dry electrode technology, the rising star in solid-state battery industrialization. *Matter*, 5(3):876–898, March 2022. ISSN 25902385. doi: 10.1016/j.matt.2022.01.011.

[152] Julian Kristoffer Mayer, Laura Almar, Ermek Asylbekov, Wolfgang Haselrieder, Arno Kwade, André Weber, and Hermann Nirschl. Influence of the

Carbon Black Dispersing Process on the Microstructure and Performance of Li-Ion Battery Cathodes. *Energy Technol.*, 8(2):1900161, January 2020. ISSN 21944288. doi: 10.1002/ente.201900161.

[153] Jianlin Li, James Fleetwood, W. Blake Hawley, and William Kays. From Materials to Cell: State-of-the-Art and Prospective Technologies for Lithium-Ion Battery Electrode Processing. *Chem Rev*, 122(1):903–956, January 2022. ISSN 0009-2665. doi: 10.1021/acs.chemrev.1c00565.

[154] Henning Dreger, Henrike Bockholt, Wolfgang Haselrieder, and Arno Kwade. Discontinuous and Continuous Processing of Low-Solvent Battery Slurries for Lithium Nickel Cobalt Manganese Oxide Electrodes. *Journal of Elec Materi*, 44(11):4434–4443, November 2015. ISSN 0361-5235, 1543-186X. doi: 10.1007/s11664-015-3981-4. URL `http://link.springer.com/10.1007/s11664-015-3981-4`.

[155] Matthias Haarmann, Wolfgang Haselrieder, and Arno Kwade. Extrusion-Based Processing of Cathodes: Influence of Solid Content on Suspension and Electrode Properties. *Energy Technol.*, 8(2):133, January 2020. ISSN 21944288. doi: 10.1002/ente.201801169.

[156] Jan-Hinnerk Schünemann, Henning Dreger, Henrike Bockholt, and Arno Kwade. Smart Electrode Processing for Battery Cost Reduction. *ECS Trans.*, 73(1):153–159, August 2016. ISSN 1938-5862, 1938-6737. doi: 10.1149/07301.0153ecst.

[157] J. Seeba, S. Reuber, C. Heubner, A. Müller-Köhn, M. Wolter, and A. Michaelis. Extrusion-based fabrication of electrodes for high-energy Li-ion batteries. *Chemical Engineering Journal*, 402(4):125551, January 2020. ISSN 13858947. doi: 10.1016/j.cej.2020.125551.

[158] Matthias Haarmann, Desiree Grießl, and Arno Kwade. Continuous Processing of Cathode Slurry by Extrusion for Lithium-Ion Batteries. *Energy Technol.*, 9(10):317, January 2021. ISSN 21944288. doi: 10.1002/ente.202100250.

[159] Juan Fernando Meza Gonzalez, Annika Völp, Hermann Nirschl, and Frank Rhein. A Scale-Up Study on the Continuous Production of Battery Slurry in Twin-Screw-Extruders based on Flow Behavior and Material Dispersion. *Energy Technol.*, 2026. doi: 10.1002/ente.202501872.

[160] Boris Bitsch, Jens Dittmann, Marcel Schmitt, Philip Scharfer, Wilhelm Schabel, and Norbert Willenbacher. A novel slurry concept for the fabrication of lithium-ion battery electrodes with beneficial properties. *Journal of Power Sources*, 265:81–90, November 2014. ISSN 03787753. doi: 10.1016/j.jpowsour.2014.04.115.

[161] Robert Dominko, Miran Gaberscek, Jernej Drofenik, Marjan Bele, Stane Pejovnik, and Janko Jamnik. The role of carbon black distribution in cathodes for Li ion batteries. *Journal of Power Sources*, 119-121:770–773, June 2003. ISSN 03787753. doi: 10.1016/S0378-7753(03)00250-7.

[162] Michael J. Lain, James Brandon, and Emma Kendrick. Design Strategies for High Power vs. High Energy Lithium Ion Cells. *Batteries (Basel, Switz.)*, 5(4):64, January 2019. doi: 10.3390/batteries5040064.

[163] Chris Meyer, Malte Kosfeld, Wolfgang Haselrieder, and Arno Kwade. Process modeling of the electrode calendering of lithium-ion batteries regarding variation of cathode active materials and mass loadings. *J. Energy Storage*, 18(454–455):371–379, January 2018. ISSN 2352152X. doi: 10.1016/j.est.2018.05.018.

[164] Jana Kumberg, Michael Baunach, Jochen C. Eser, Andreas Altvater, Philip Scharfer, and Wilhelm Schabel. Influence of Layer Thickness on the Drying of Lithium-Ion Battery Electrodes—Simulation and Experimental Validation. *Energy Technol.*, 9(5):2100013, January 2021. ISSN 21944288. doi: 10.1002/ente.202100013.

[165] Nicolas Billot, Moritz Beyer, Nico Koch, Christian Ihle, and Gunther Reinhart. Development of an adhesion model for graphite-based lithium-ion battery anodes. *J. Manuf. Syst.*, 58(93):131–142, January 2021. ISSN 0278-6125. doi: 10.1016/j.jmsy.2020.10.016.

[166] Nobuhiro Ogihara, Yuichi Itou, Tsuyoshi Sasaki, and Yoji Takeuchi. Impedance Spectroscopy Characterization of Porous Electrodes under Different Electrode Thickness Using a Symmetric Cell for High-Performance Lithium-Ion Batteries. *J. Phys. Chem. C*, 119(9):4612–4619, January 2015. ISSN 1932-7447. doi: 10.1021/jp512564f.

[167] Honghe Zheng, Jing Li, Xiangyun Song, Gao Liu, and Vincent S. Battaglia. A comprehensive understanding of electrode thickness effects on the electrochemical performances of Li-ion battery cathodes. *Electrochimica Acta*, 71(1):258–265, January 2012. ISSN 00134686. doi: 10.1016/j.electacta.2012.03.161.

[168] Madhav Singh, Jörg Kaiser, and Horst Hahn. Thick Electrodes for High Energy Lithium Ion Batteries. *J. Electrochem. Soc.*, 162(7):1196–1201, January 2015. ISSN 0378-7753. doi: 10.1149/2.0401507jes.

[169] Zhijia Du, D. L. Wood, C. Daniel, S. Kalnaus, and Jianlin Li. Understanding limiting factors in thick electrode performance as applied to high energy density Li-ion batteries. *J Appl Electrochem*, 47(3):405–415, January 2017. ISSN 0021-891X. doi: 10.1007/s10800-017-1047-4.

[170] Kelsey Rollag, Daniel Juarez-Robles, Zhijia Du, David L. Wood, and Partha P. Mukherjee. Drying Temperature and Capillarity-Driven Crack Formation in Aqueous Processing of Li-Ion Battery Electrodes. *ACS Appl. Energy Mater.*, 2(6):4464–4476, January 2019. ISSN 2574-0962. doi: 10.1021/acsaem.9b00704.

[171] Stefan Jaiser, Marcus Müller, Michael Baunach, Werner Bauer, Philip Scharfer, and Wilhelm Schabel. Investigation of film solidification and binder migration during drying of Li-Ion battery anodes. *J. Power Sources*, 318(5):210–219, January 2016. ISSN 0378-7753. doi: 10.1016/j.jpowsour.2016.04.018.

[172] M. Baunach, S. Jaiser, S. Schmelzle, H. Nirschl, P. Scharfer, and W. Schabel. Delamination behavior of lithium-ion battery anodes: Influence of drying temperature during electrode processing. *Drying Technol.*, 34(4):

462–473, January 2016. ISSN 0737-3937. doi: 10.1080/07373937.2015.1060497.

[173] F. Font, B. Protas, G. Richardson, and J. M. Foster. Binder migration during drying of lithium-ion battery electrodes: Modelling and comparison to experiment. *J. Electrochem. Soc.*, 393(3):177–185, January 2018. ISSN 0378-7753. doi: 10.1016/j.jpowsour.2018.04.097. Num Pages: 10.

[174] Andreas Altvater, Thilo Heckmann, Jochen Christoph Eser, Sandro Spiegel, Philip Scharfer, and Wilhelm Schabel. (Near-) Infrared Drying of Lithium-Ion Battery Electrodes: Influence of Energy Input on Process Speed and Electrode Adhesion. *Energy Tech*, 11(5):2200785, May 2023. ISSN 2194-4288, 2194-4296. doi: 10.1002/ente.202200785.

[175] Christian Vedder, Dominik Hawelka, Mareike Wolter, Diana Leiva, Jochen Stollenwerk, and Konrad Wissenbach. Laser-based drying of battery electrode layers. In *International Congress on Applications of Lasers & Electro-Optics*, page N501, San Diego, California, USA, 2016. Laser Institute of America. ISBN 978-1-940168-17-3. doi: 10.2351/1.5118636.

[176] Bastian Westphal. *Prozessinduzierter und erzwungener Strukturaufbau in der Elektrodenbeschichtung von Lithium-Ionen Batterien*. PhD thesis, Braunschweig, January 2018.

[177] Hideki Hagiwara, Wieslaw J. Suszynski, and Lorraine F. Francis. A Raman spectroscopic method to find binder distribution in electrodes during drying. *J Coat Technol Res*, 11(1):11–17, January 2014. ISSN 1547-0091. doi: 10.1007/s11998-013-9509-z.

[178] Chris Meyer. *Prozessmodellierung der Kalandrierung von Lithium-Ionen-Batterie-Elektroden*. PhD thesis, Braunschweig, January 2019. Edition: 1. Auflage ISBN: 978-3-96548-043-8 Series: iPAT-Schriftenreihe Volume: Bd. 32.

[179] Jana Kumberg, Marcus Müller, Ralf Diehm, Sandro Spiegel, Christian Wachsmann, Werner Bauer, Philip Scharfer, and Wilhelm Schabel. Drying

of Lithium-Ion Battery Anodes for Use in High-Energy Cells: Influence of Electrode Thickness on Drying Time, Adhesion, and Crack Formation. *Energy Technol.*, 7(11):20171, January 2019. ISSN 21944288. doi: 10.1002/ente.201900722.

[180] G. A. B. Matthews, S. Wheeler, J. Ramírez-González, and P. S. Grant. Solvent-free NMC electrodes for Li-ion batteries: unravelling the microstructure and formation of the PTFE nano-fibril network. *Front. Energy Res.*, 11:1336344, January 2024. ISSN 2296-598X. doi: 10.3389/fenrg.2023.1336344.

[181] David Burger, Noah Keim, Junaid Shabbir, Yuhao Gao, Marcus Müller, Werner Bauer, Alexander Hoffmann, Philip Scharfer, and Wilhelm Schabel. Supplementary Information to the Article "Simultaneous Primer Coating for Fast Drying of Battery Electrodes". *Energy Tech*, page 2401668, November 2024. ISSN 2194-4288, 2194-4296. doi: 10.1002/ente.202401668.

[182] Mojdeh Nikpour, Baichuan Liu, Paul Minson, Zachary Hillman, Brian Mazzeo, and Dean Wheeler. Li-ion Electrode Microstructure Evolution during Drying and Calendering. *Batteries (Basel, Switz.)*, 8(9):107, January 2022. doi: 10.3390/batteries8090107.

[183] Wolfgang Haselrieder, Stoyan Ivanov, Daniel Klaus Christen, Henrike Bockholt, and Arno Kwade. Impact of the Calendering Process on the Interfacial Structure and the Related Electrochemical Performance of Secondary Lithium-Ion Batteries. *ECS Trans.*, 50(26):59–70, January 2013. ISSN 1938-5862. doi: 10.1149/05026.0059ecst.

[184] Till Günther, David Schreiner, Ajinkya Metkar, Chris Meyer, Arno Kwade, and Gunther Reinhart. Classification of Calendering-Induced Electrode Defects and Their Influence on Subsequent Processes of Lithium-Ion Battery Production. *Energy Technol.*, 8(2):1900026, January 2020. ISSN 21944288. doi: 10.1002/ente.201900026.

[185] Benjamin Delattre, Ruhul Amin, Jonathan Sander, Joël Coninck, Antoni P. Tomsia, and Yet-Ming Chiang. Impact of Pore Tortuosity on Electrode Kinetics in Lithium Battery Electrodes: Study in Directionally Freeze-Cast LiNi 0.8 Co 0.15 Al 0.05 O 2 (NCA). *J. Electrochem. Soc.*, 165(2): 388–395, January 2018. ISSN 0378-7753. doi: 10.1149/2.1321802jes.

[186] Linus Froboese, Jan Felix van der Sichel, Thomas Loellhoeffel, Laura Helmers, and Arno Kwade. Effect of Microstructure on the Ionic Conductivity of an All Solid-State Battery Electrode. *J. Electrochem. Soc.*, 166(2): 318–328, January 2019. ISSN 0378-7753. doi: 10.1149/2.0601902jes.

[187] Fabienne Huttner, Alexander Diener, Thilo Heckmann, Jochen C. Eser, Tugay Abali, Julian K. Mayer, Philip Scharfer, Wilhelm Schabel, and Arno Kwade. Increased Moisture Uptake of NCM622 Cathodes after Calendering due to Particle Breakage. *J. Electrochem. Soc.*, 168(9):090539, January 2021. ISSN 0378-7753. doi: 10.1149/1945-7111/ac24bb.

[188] Mona Faraji Niri, Geanina Apachitei, Michael Lain, Mark Copley, and James Marco. The Impact of Calendering Process Variables on the Impedance and Capacity Fade of Lithium-Ion Cells: An Explainable Machine Learning Approach. *Energy Technol.*, 10(12):71, January 2022. ISSN 21944288. doi: 10.1002/ente.202200893.

[189] Mark Lippke, Jakob Meister, Carsten Schilde, and Arno Kwade. Preheating of Lithium-Ion Battery Electrodes as Basis for Heated Calendering—A Numerical Approach. *Processes*, 10(8):1667, January 2022. doi: 10.3390/pr10081667.

[190] C. Fongy, A.-C. Gaillot, S. Jouanneau, D. Guyomard, and B. Lestriez. Ionic vs Electronic Power Limitations and Analysis of the Fraction of Wired Grains in LiFePO[sub 4] Composite Electrodes. *J. Electrochem. Soc.*, 157 (7):885, January 2010. ISSN 0378-7753. doi: 10.1149/1.3432559.

[191] C.-W. Wang, Y.-B. Yi, A. M. Sastry, J. Shim, and K. A. Striebel. Particle Compression and Conductivity in Li-Ion Anodes with Graphite Additives.

J. Electrochem. Soc., 151(9):1489, January 2004. ISSN 0378-7753. doi: 10.1149/1.1783909.

[192] Arnaud Du Baret de Limé, Tobias Lein, Sebastian Maletti, Karoline Schmal, Sebastian Reuber, Christian Heubner, and Alexander Michaelis. Impact of Electrode Defects on Battery Cell Performance: A Review. *Batteries Supercaps*, 5(10), January 2022. ISSN 2566-6223. doi: 10.1002/batt.202200239.

[193] Benjamin Bold and Jürgen Fleischer. Kalandrieren von Elektroden für Li-Ionen-Batterien: Wechselwirkungen zwischen Anlagen- und Materialparametern. *ZWF*, 113(9):571–575, January 2018. doi: 10.3139/104.111968. Num Pages: 5 Publisher: Carl Hanser Verlag, München.

[194] Ann-Kathrin Wurba, Lennart Altmann, and Jürgen Fleischer. Analysis of longitudinal wrinkle formation during calendering of NMC811 cathodes under variation of different process parameters. *Prod. Eng. Res. Devel.*, January 2024. ISSN 0944-6524, 1863-7353. doi: 10.1007/s11740-023-01258-8.

[195] Christiane Schilcher, Chris Meyer, and Arno Kwade. Structural and Electrochemical Properties of Calendered Lithium Manganese Oxide Cathodes. *Energy Technol.*, 4(12):1604–1610, January 2016. ISSN 21944288. doi: 10.1002/ente.201600130.

[196] David Schreiner, Maximilian Oguntke, Till Günther, and Gunther Reinhart. Modelling of the Calendering Process of NMC-622 Cathodes in Battery Production Analyzing Machine/Material–Process–Structure Correlations. *Energy Technol.*, 7(11):1900840, January 2019. ISSN 21944288. doi: 10.1002/ente.201900840.

[197] Wolfgang Haselrieder. *Kalandrierung zur gezielten Einstellung der Batterieelektroden-Performance*. PhD thesis, Braunschweig, January 2017. Edition: 1. Auflage ISBN: 978-3-86844-942-6 Series: iPAT-Schriftenreihe Volume: Bd. 25.

[198] Andrew van Bommel and Ranjith Divigalpitiya. Effect of Calendering LiFePO4 Electrodes. *J. Electrochem. Soc.*, 159(11):1791–1795, January 2012. ISSN 0378-7753. doi: 10.1149/2.029211jes.

[199] Denny Schmidt, Marc Kamlah, and Volker Knoblauch. Highly densified NCM-cathodes for high energy Li-ion batteries: Microstructural evolution during densification and its influence on the performance of the electrodes. *Journal of Energy Storage*, 17(26):213–223, January 2018. ISSN 2352152X. doi: 10.1016/j.est.2018.03.002.

[200] Petr Novák, Werner Scheifele, Martin Winter, and Otto Haas. Graphite electrodes with tailored porosity for rechargeable ion-transfer batteries. *J. Electrochem. Soc.*, 68(2):267–270, January 1997. ISSN 0378-7753. doi: 10.1016/S0378-7753(96)02561-X.

[201] Ali Davoodabadi, Jianlin Li, Hui Zhou, David L. Wood, Timothy J. Singler, and Congrui Jin. Effect of calendering and temperature on electrolyte wetting in lithium-ion battery electrodes. *J. Energy Storage*, 26(11):101034, January 2019. ISSN 2352152X. doi: 10.1016/j.est.2019.101034.

[202] Nicolas Billot, Till Günther, David Schreiner, Ralf Stahl, Jakob Kranner, Moritz Beyer, and Gunther Reinhart. Investigation of the Adhesion Strength along the Electrode Manufacturing Process for Improved Lithium-Ion Anodes. *Energy Technol.*, 8(2):1801136, January 2020. ISSN 21944288. doi: 10.1002/ente.201801136.

[203] J.S Gnanaraj, Yaron S. Cohen, M.D Levi, and D. Aurbach. The effect of pressure on the electroanalytical response of graphite anodes and LiCoO2 cathodes for Li-ion batteries. *J. Electroanal. Chem. Interfacial Electrochem.*, 516(1-2):89–102, January 2001. ISSN 0022-0728. doi: 10.1016/S0022-0728(01)00663-5.

[204] Thomas Marks, Simon Trussler, A. J. Smith, Deijun Xiong, and J. R. Dahn. A Guide to Li-Ion Coin-Cell Electrode Making for Academic Researchers. *J. Electrochem. Soc.*, 158(1):51, January 2011. ISSN 0378-7753. doi: 10.1149/1.3515072.

[205] Williams Agyei Appiah, Joonam Park, Seonghyun Song, Seoungwoo Byun, Myung-Hyun Ryou, and Yong Min Lee. Design optimization of LiNi0.6Co0.2Mn0.2O2/graphite lithium-ion cells based on simulation and experimental data. *J. Power Sources*, 319:147–158, January 2016. ISSN 0378-7753. doi: 10.1016/j.jpowsour.2016.04.052.

[206] Chris Yuan, Yelin Deng, Tonghui Li, and Fan Yang. Manufacturing energy analysis of lithium ion battery pack for electric vehicles. *CIRP Annals*, 66 (1):53–56, 2017. ISSN 00078506. doi: 10.1016/j.cirp.2017.04.109.

[207] Karl-Heinz Pettinger and Winny Dong. When Does the Operation of a Battery Become Environmentally Positive? *Journal of The Electrochemical Society*, 164(1):A6274, 2017.

[208] David L. Wood, Jeffrey D. Quass, Jianlin Li, Shabbir Ahmed, David Ventola, and Claus Daniel. Technical and economic analysis of solvent-based lithium-ion electrode drying with water and NMP. *Drying Technology*, 36 (2):234–244, January 2018. ISSN 0737-3937. doi: 10.1080/07373937.2017.1319855.

[209] Marcella Horst, Franziska Beverborg, Lukas Bahlmann, Svenja Schreiber, Julius Gerk, Peter Michalowski, and Arno Kwade. Effect of active material morphology on PTFE-fibrillation, powder characteristics and electrode properties in dry electrode coating processes. *Powder Technology*, 451: 120451, February 2025. ISSN 00325910. doi: 10.1016/j.powtec.2024.120451.

[210] Patrick S Grant, David Greenwood, Kunal Pardikar, Rachel Smith, Thomas Entwistle, Laurence A. Middlemiss, Glen Murray, Serena A. Cussen, M. J. Lain, M. J. Capener, M. Copley, Carl D. Reynolds, Sam D. Hare, Mark J. H. Simmons, Emma Kendrick, Stanislaw P. Zankowski, Samuel Wheeler, Pengcheng Zhu, Peter R. Slater, Ye Shui Zhang, Andrew R. T. Morrison, Will Dawson, Juntao Li, Paul R. Shearing, Dan J. L. Brett, Guillaume Matthews, Ruihuan Ge, Ross Drummond, Eloise C. Tredenick, Chuan Cheng, Stephen R. Duncan, Adam M. Boyce, Mona Faraji-Niri, James

Marco, Luis A. Roman-Ramirez, Charlotte Harper, Paul Blackmore, Tim Shelley, Ahmad Mohsseni, and Denis J. Cumming. Roadmap on Li-ion battery manufacturing research. *J. Phys. Energy*, 4(4):042006, October 2022. ISSN 2515-7655. doi: 10.1088/2515-7655/ac8e30.

[211] IBU tec advanced materials AG. IBU-tec - Lithium-Eisenphosphat - IBUvolt(R) LFP. Available online at: https://www.ibu-tec.de/produkte/lithium-eisenphosphat-lfp/, last accessed on February 21, 2023.

[212] Andreas Gyulai. *Dry Manufacturing of Lithium-ion Battery Cathodes by Direct Powder Compaction in a Two-roll Calender*. PhD thesis, Karlsruher Institut für Technologie (KIT), Karlsruhe, 2024.

[213] Luca Graf. *Experimentelle Bestimmung der Wärmeleitfähigkeit von Batterieelektroden und ihrer Porositätsabhängigkeit*. Bachelor's thesis, Hochschule Offenburg, Offenburg, 2022.

[214] Adrian Reyes Mayorga. *Untersuchung der Wärmeleitfähigkeit poröser Batterieelektroden in Abhängigkeit vom Kalandrierungsgrad*. Bachelor's thesis, Karlsruhe Institute of Technology (KIT), Karlsruhe, 2022.

[215] Yasmin Grübbel. *Untersuchung des Einflusses der Formulierung und der Trocknungsparameter auf die Wärmeleitfähigkeit poröser Batterieelektroden*. Bachelor's thesis, Karlsruhe Institute of Technology (KIT), Karlsruhe, 2024.

[216] Julia C. Gandert, Marcus Müller, Simon B. B. Solberg, Robert L McMasters, Thomas Wetzel, and Odne S. Burheim. Supplementray Information for the Article: "Challenges of the Measurement of the Effective Thermal Conductivity of Battery Electrodes with Laser Flash Analysis and Guarded Hot Plate Method". *Energy Technol.*, 2025. doi: 10.1002/ente.202501125.

[217] Alexander Lauerer and Artem Lunev. Experimental evidence of gas-mediated heat transfer in porous solids measured by the flash method. *International Journal of Thermal Sciences*, 184:107948, February 2023. ISSN 12900729. doi: 10.1016/j.ijthermalsci.2022.107948.

[218] Mahr GmbH. Integrated Wireless Familien - MarCal, Micromar, MarCator, 2020. Available online at: https://metrology.mahr.com/en-int/products/article/4157100-digitale-buegelmessschraube-micromar-40-ewri, last accessed on January 22, 2025.

[219] Mitutoyo Corporation. ID-H0530/0560 - Digimatic Indicator, User's Manual No. 99MAH016B6 SERIES No. 543. Available online at: https://shop.mitutoyo.eu/media/mitutoyoData/DO/base/99MAH016B6_en.pdf, last accessed on January 22, 2025.

[220] Julia C. Gandert, Marcus Müller, Sabine Paarmann, Oliver Queisser, and Thomas Wetzel. Supplementary information for the arcticle "Effective Thermal Conductivity of Lithium-Ion Battery Electrodes in Dependence on the Degree of Calendering". *Energy Tech*, 11(8):2300259, August 2023. ISSN 2194-4288, 2194-4296. doi: 10.1002/ente.202300259.

[221] Documentation of the Proteus LFA Analysis Software - Penetration Model.

[222] P. Zehner and E. U. Schlünder. Wärmeleitfähigkeit von Schüttungen bei mäßigen Temperaturen. *Chemie Ingenieur Technik*, 42(14):933–941, July 1970. ISSN 0009-286X, 1522-2640. doi: 10.1002/cite.330421408.

[223] P. Zehner and E. U. Schlünder. Einfluß der Wärmestrahlung und des Druckes auf den Wärmetransport in nicht durchströmten Schüttungen. *Chemie Ingenieur Technik*, 44(23):1303–1308, December 1972. ISSN 0009-286X, 1522-2640. doi: 10.1002/cite.330442305.

[224] Peter Zehner and Ernst Ulrich Schlünder. Die effektive Wärmeleitfähigkeit durchströmter Kugelschüttungen bei mäßigen und hohen Temperaturen. *Chemie Ingenieur Technik*, 45(5):272–276, March 1973. ISSN 0009-286X, 1522-2640. doi: 10.1002/cite.330450509.

[225] Robert A. Buerschaper. Thermal and Electrical Conductivity of Graphite and Carbon at Low Temperatures. *J. Appl. Phys. (Melville, NY, U. S.)*, 15 (5):452–454, January 1944. ISSN 0021-8979. doi: 10.1063/1.1707454.

[226] C. Y. Ho, R. W. Powell, and P. E. Liley. Thermal Conductivity of the Elements. *J. Phys. Chem. Ref. Data*, 1(2):279–421, January 1972. ISSN 0047-2689. doi: 10.1063/1.3253100.

[227] Sandra Rodrigues, Manuela Marques, Isabel Suárez-Ruiz, Ignacio Camean, Deolinda Flores, and Barbara Kwiecinska. Microstructural investigations of natural and synthetic graphites and semi-graphites. *International Journal of Coal Geology*, 111:67–79, May 2013. ISSN 01665162. doi: 10.1016/j.coal.2012.06.013.

[228] Eric Jianfeng Cheng, Kicheol Hong, Nathan John Taylor, Heeman Choe, Jeff Wolfenstine, and Jeff Sakamoto. Mechanical and physical properties of LiNi 0.33 Mn 0.33 Co 0.33 O 2 (NMC). *J. Eur. Ceram. Soc.*, 37(9): 3213–3217, January 2017. ISSN 0955-2219. doi: 10.1016/j.jeurceramsoc.2017.03.048.

[229] Jagjit Nanda, Surendra K. Martha, Wallace D. Porter, Hsin Wang, Nancy J. Dudney, Maxwell D. Radin, and Donald J. Siegel. Thermophysical properties of LiFePO4 cathodes with carbonized pitch coatings and organic binders: Experiments and first-principles modeling. *J. Power Sources*, 251:8–13, January 2014. ISSN 0378-7753. doi: 10.1016/j.jpowsour.2013.11.022.

[230] A. Smontara, K. Biljaković, D. Starešinić, D. Pajić, M. E. Kozlov, M. Hirabayashi, M. Tokumoto, and H. Ihara. Thermal conductivity of hard carbon prepared from C60 fulleren. *Physica B: Condensed Matter*, 219-220:160–162, January 1996. ISSN 09214526. doi: 10.1016/0921-4526(95)00682-6.

[231] Solef PVDF for Li-Ion Batteries. Available online at: https://content.syensqo.com/solef-pvdf-typical-properties, last accessed May 09, 2025.

[232] James E. Mark, editor. *Physical properties of polymers handbook*. Springer, New York, 2nd ed edition, 2006. ISBN 978-0-387-31235-4.

[233] T. Bhowmick and S. Pattanayak. Thermal conductivity, heat capacity and diffusivity of rubbers from 60 to 300 K. *Cryogenics*, 30(2):116–121, February 1990. ISSN 00112275. doi: 10.1016/0011-2275(90)90256-C.

[234] Jawad K. Oleiwi, Mohammed S. Hamza, and Nassier A. Nassir. A Study of The Effect of Carbon Black Powder on The Physical Properties of SBR/NR Blends Used In Passenger Tire Treads. *Eng. & Tech. Journal*, 29(5), 2011. Available online at: https://iasj.rdd.edu.iq/journals/uploads/2025/03/18/6b2980a6fa722c9c1e56cb5d33367cd6.pdf, last accessed on September 09, 2025.

[235] Michael Kleiber, Ralph Joh, and Roland Span. D3 Properties of Pure Fluid Substances. In *VDI Heat Atlas*, pages 301–418. Springer Berlin Heidelberg, Berlin, Heidelberg, January 2010. doi: 10.1007/978-3-540-77877-6_18.

[236] R. L. Hamilton and O. K. Crosser. Thermal Conductivity of Heterogeneous Two-Component Systems. *Ind. Eng. Chem. Fund.*, 1(3):187–191, January 1962. ISSN 0196-4313. doi: 10.1021/i160003a005.

[237] Alexandra Philipp, Jonas F. Eichinger, Roland C. Aydin, Argyrios Georgiadis, Christian J. Cyron, and Markus Retsch. The accuracy of laser flash analysis explored by finite element method and numerical fitting. *Heat Mass Transfer*, 56(3):811–823, March 2020. ISSN 0947-7411, 1432-1181. doi: 10.1007/s00231-019-02742-7.

[238] Alexandra Philipp, Jonas F. Eichinger, Roland C. Aydin, Argyrios Georgiadis, Christian J. Cyron, and Markus Retsch. Computational Framework for the Evalution of the LFA Measurement - Supplementary Material (ESM 2) to the Article "The accuracy of laser flash analysis explored by finite element method and numerical fitting". *Heat Mass Transfer*, 56(3):811–823, March 2020. ISSN 0947-7411, 1432-1181. doi: 10.1007/s00231-019-02742-7.

[239] JCGM. Guide to the expression of uncertainty in measurement - JCGM 100:2008 (GUM 1995 with minor corrections - Evaluation of measurement data.

[240] Ernst-Ulrich Schlünder and Evangelos Tsotsas. *Wärmeübertragung in Festbetten, durchmischten Schüttgütern und Wirbelschichten: 33 Tabellen*. Lehrbuchreihe Chemieingenieurwesen/Verfahrenstechnik. Thieme, Stuttgart New York, 1988. ISBN 978-3-13-713001-7.

[241] Sebastian Sonnick, Lars Erlbeck, Manuel Meier, Hermann Nirschl, and Matthias Rädle. Methodical selection of thermal conductivity models for porous silica-based media with variation of gas type and pressure. *Int. J. Heat Mass Transfer*, 187(11):122519, January 2022. ISSN 0017-9310. doi: 10.1016/j.ijheatmasstransfer.2022.122519.

[242] IBU tec advanced materials AG. IBUvolt® LFP200 Datenblatt, February 2024. Available online at: https://www.ibu-tec.de/fileadmin/user_upload/Download_PDF/IBUvolt_PDFs/IBUvolt_LFP200.pdf, last accessed on September 08, 2025.

[243] IBU tec advanced materials AG. IBUvolt® LFP400 Datenblatt, February 2024. Available online at: https://www.ibu-tec.de/fileadmin/user_upload/Download_PDF/IBUvolt_PDFs/IBUvolt_LFP400.pdf, last accessed on September 08, 2025.

[244] Juan Fernando Meza Gonzalez. *Prozessauslegung und Digitalisierung der kontinuierlichen Herstellung von Batteriepasten in Doppelschneckenextrudern*. PhD thesis, Karlsruhe Institute of Technology (KIT), Karlsruhe, 2026 (submitted).

[245] Henrike Bockholt. *Formulierungstechniken für eigenschaftsoptimierte Lithiumionenbatterieelektroden*, volume Bd. 21 of *iPAT-Schriftenreihe*. 1. auflage edition, January 2016. ISBN 978-3-86844-843-6.

[246] Junpeng Zhang, Huagui Huang, and Jingna Sun. Investigation on mechanical and microstructural evolution of lithium-ion battery electrodes during the calendering process // Investigation on mechanical and microstructural evolution of lithium-ion battery electrode during the calendering process. *Powder Technol.*, 409(4):117828, January 2022. ISSN 0032-5910. doi: 10.1016/j.powtec.2022.117828.

[247] Robert Bock, Bjørnar Hamre, Morten Andreas Onsrud, Håvard Karoliussen, Frode Seland, and Odne Stokke Burheim. The Influence of Argon, Air and Hydrogen Gas on Thermal Conductivity of Gas Diffusion Layers and Temperature Gradients in PEMFCS. *ECS Trans.*, 92(8):223–245, July 2019. ISSN 1938-6737, 1938-5862. doi: 10.1149/09208.0223ecst.

[248] Adrian Schmidt, Dieter Oehler, André Weber, Thomas Wetzel, and Ellen Ivers-Tiffée. A multi scale multi domain model for large format lithium-ion batteries. *Electrochim. Acta*, 393:139046, January 2021. ISSN 00134686. doi: 10.1016/j.electacta.2021.139046.

[249] Odne S. Burheim, Jon G. Pharoah, Hannah Lampert, Preben J. S. Vie, and Signe Kjelstrup. Through-Plane Thermal Conductivity of PEMFC Porous Transport Layers. *Journal of Fuel Cell Science and Technology*, 8 (2):021013, April 2011. ISSN 1550-624X, 1551-6989. doi: 10.1115/1.4002403.

[250] Jie Lin, Howie N. Chu, Charles W. Monroe, and David A. Howey. Anisotropic Thermal Characterisation of Large-Format Lithium-Ion Pouch Cells. *Batteries Supercaps*, 5(5):16, January 2022. ISSN 2566-6223. doi: 10.1002/batt.202100401.

[251] Jie Lin, Howie N. Chu, David A. Howey, and Charles W. Monroe. Multiscale coupling of surface temperature with solid diffusion in large lithium-ion pouch cells. *Comms. Eng.*, 1(1):107, January 2022. doi: 10.1038/s44172-022-00005-8.

[252] R. Franz and G. Wiedemann. Ueber die Wärme-Leitungsfähigkeit der Metalle. *Annalen der Physik*, 165(8):497–531, January 1853. ISSN 0003-3804, 1521-3889. doi: 10.1002/andp.18531650802.

[253] Neil W. Ashcroft and N. David Mermin. *Solid state physics*. Saunders College Publ. [u.a.], Fort Worth, internat. ed., 21. print edition, 1995. ISBN 978-0-03-049346-1 978-0-03-083993-1.

[254] Charles Kittel. *Introduction to solid state physics*. Wiley, Hoboken, NJ, 8. ed., [repr.] edition, 2005. ISBN 978-0-471-41526-8.

[255] Linus Janning. Untersuchung der Mikrostrukturausbildung und der Porenentleerung in Abhängigkeit von Slurry-Eigenschaften und Trocknungsbedingungen. Master's thesis, Karlsruhe Institute of Technology (KIT), Karlsruhe, August 2023.

[256] Julian Klemens, Luca Schneider, David Burger, Nadine Zimmerer, Marcus Müller, Werner Bauer, Helmut Ehrenberg, Philip Scharfer, and Wilhelm Schabel. Supplementary Information to the Article "Process and Drying Behavior Toward Higher Drying Rates of Hard Carbon Anodes for Sodium-Ion Batteries with Different Particle Sizes: An Experimental Study in Comparison to Graphite for Lithium-Ion-Batteries". *Energy Technol.*, 11(8): 2200785, January 2023. ISSN 21944288. doi: 10.1002/ente.202300338.

List of Publications

Journal Articles

1. **J. C. Gandert**, M. Müller, S. B. B. Solberg, R. L. McMasters, T. Wetzel, O. Burheim: Challenges of the Measurement of the Effective Thermal Conductivity of Battery Electrodes with Laser Flash Analysis and Guarded Hot Plate Method, *Energy Technol.* **2025**, DOI: 10.1002/ente.202501125

2. **J. C. Gandert**, R. Mühlpfort, P. Müller-Welt, D. Schall, A. Schmidt, S. Schuhmann, P. Seegert, N. Weber, Y. Zeng, T. Wetzel, S. Paarmann: Methodology for the Holistic Design of Format-Flexible Lithium-Ion Battery Systems, *Int. J. Energy Res.* **2024**, DOI: 10.1155/2024/2125023

3. **J. C. Gandert**, M. Müller, S. Paarmann, O. Queisser, T. Wetzel: Effective Thermal Conductivity of Lithium-Ion Battery Electrodes in Dependence on the Degree of Calendering, *Energy Technol.* **2023**, DOI: 10.1002/ente.202300259

Proceedings

1. **J. Gandert**, M. Müller, T. Wetzel: How the Effective Thermal Conductivity of Lithium-Ion Cell Electrodes Is Impacted By the Compression during Calendering, *ECS Meeting Abstracts*, October 08-12, **2023**, Gothenburg, Sweden. DOI: 10.1149/MA2023-027964mtgabs

2. J. Ruhland, T. Storz, F. Kößler, A. Ebel, J. Sawodny, J. Hillenbrand, P. Gönnheimer, L. Overbeck, G. Lanza, M. Hagen, J. Tübke, **J. Gandert**, S. Paarmann, T. Wetzel, J. Mohacsi, A. Altvater, S. Spiegel, J. Klemens, P. Scharfer, W. Schabel, K. Nowoseltschenko, P. Müller-Welt, K. Bause, A. Albers, D. Schall, T. Grün, M. Hiller, A. Schmidt, A. Weber, L. de Biasi, H. Ehrenberg, J. Fleischer: Development of a Parallel Product-Production Co-design for an Agile Battery Cell Production System. In: Andersen A.-L. et al. (eds) *Towards Sustainable Customization: Bridging Smart Products and Manufacturing Systems. CARV 2021, MCPC 2021. Lecture Notes in Mechanical Engineering*. Springer, Cham, November 01-02, **2021**, Aalborg, Denmark. DOI: 10.1007/978-3-030-90700-6_10

3. J. Hofele, **J. Gandert**, G. Link, J. Jelonnek: Modelling the thermal run-away during the stabilization phase of the carbon fiber production using microwave heating. In: *AMPERE 2021: 18th International Conference on Microwave and High-Frequency Applications*: September 13-16, **2021**, Gothenburg, Sweden. DOI: 10.5445/IR/1000141193

Conference Contributions

1. **J. Gandert**, M. Müller, S. Solberg, Th. Wetzel, O. Burheim: Challenges in Thermal Conductivity Measurements of Porous Multi-Layer Samples, *Jahrestreffen der DECHEMA/VDI-Fachgruppe Wärme- und Stoffübertragung*, Stuttgart, Germany, March 10-12, **2025** (Poster)

2. **J. Gandert**, M. Müller, Th. Wetzel, O. Burheim: Comparison of Measurement Techniques for the Determination of the Effective Thermal Conductivity of Battery Electrodes, *International Battery Production Conference*, Braunschweig, Germany, November 27-29, **2024** (Poster)

3. **J. Gandert**, M. Müller, J. Klemens, P. Scharfer, W. Schabel, T. Wetzel: Influence of Lithium-Ion Electrode Production Steps on the Effective Thermal Conductivity, *International Battery Production Conference*, Braunschweig, Germany, November 07-09, **2023** (Poster)

4. **J. Gandert**, M. Müller, T. Wetzel: How the Effective Thermal Conductivity of Lithium-Ion Cell Electrodes is Impacted by the Compression during Calendering, *244th ECS Meeting*, Gothenburg, Sweden, October 08-12, **2023** (Poster)

5. **J. Gandert**, M. Müller, T. Wetzel: How Calendering Impacts the Effective Thermal Conductivity of Lithium-Ion Battery Electrodes, *Advanced Battery Power Conference*, Aachen, Germany, April 27-28, **2023** (Poster)

6. **J. Gandert**, Q. Queisser, H. Reppich T. Wetzel: Impact of Thermal Material Properties on the Temperature Distribution within a Lithium-Ion Pouch Cell, *Advanced Battery Power Conference*, Münster, Germany, March 29-30, **2022** (Poster)

7. **J. Gandert**, T. Grün, P. Müller-Welt, K. Nowoseltschenko, S. Paarmann, D. Schall, A. Schmidt, T. Wetzel: Holistic Design of Flexible Lithium-ion Pouch Cells – Project AgiloBat, *Advanced Battery Power Conference*, Online, April 28-29, **2021** (Poster)

List of Supervised Theses

1. Yasmin Grübbel: “Untersuchung des Einflusses der Formulierung und der Trocknungsparameter auf die Wärmeleitfähigkeit poröser Batterieelektroden”, Bachelor thesis, 2024.

2. Martin Böhm: “Experimentelle Untersuchung der effektiven Wärmeleitfähigkeit von Separatoren”, Bachelor thesis, 2023.

3. Simon Pelzer: “Optimierung des inneren Aufbaus von Lithium-Ionen Pouchzellen unter Berücksichtigung der Leistungsfähigkeit und des thermischen Verhaltens”, Bachelor thesis, 2022.

4. Adrian Reyes Mayorga: “Untersuchung der Wärmeleitfähigkeit poröser Batterieelektroden in Abhängigkeit vom Kalandrierungsgrad”, Bachelor thesis, 2022.

5. Luca Graf: “Experimentelle Bestimmung der Wärmeleitfähigkeit von Elektroden und deren Porositätsabhängigkeit”, Bachelor thesis, 2022.

6. Moritz Link: “Thermische Modellierung zur Auslegung eines Kühlsystems für Lithium-Ionen Pouchzellen”, Master thesis, 2022.

7. Maximilian Birkle: “Untersuchung und Optimierung der thermischen Transporteigenschaften einer Lithium-Ionen Pouchzelle unter Berücksichtigung der Zellkapazität”, Bachelor thesis, 2022.

8. Saskia Müller: “Numerische Untersuchung des Wärmeübergangs bei der einphasigen, laminaren Durchströmung rechteckiger Kanäle”, Bachelor thesis, 2022.

9. Helene Reppich: “Untersuchung des Einflusses thermischer Stoffeigenschaften und Randbedingungen auf die Temperaturverteilung in einer Lithium-Ionen Pouchzelle”, Bachelor thesis, 2021.

10. David Seifert: “Analytische Untersuchung zur Auslegung eines Kühlsystems für Lithium-Ionen Batterien”, Bachelor thesis, 2021.

A Appendix

A.1 Additional Data

Table A.1: Thermal conductivity data of dry electrodes in $W \cdot m^{-1} \cdot K^{-1}$ measured with the LFA.

Active material	Notes	Thermal conductivity	Reference
LCO	at 2.45 V	2.33	Maleki et al. [112]
Graphite		0.32	Maleki et al. [26]
LCO		0.66	Gotcu et al. [30]
LCO		0.33	Gotcu et al. [31]
NMC		0.38	Gotcu et al. [31]
Graphite		1.45	Liebig et al. [33]
NMC		0.66	Liebig et al. [33]
Graphite		2.46	Oehler et al. [32, 34, 113]
Graphite		2.74	Oehler et al. [32, 34, 113]
Graphite		2.25	Oehler [34]
Graphite		2.25	Oehler [34]
Graphite		1.69	Oehler [34]

Table A.2: Thermal conductivity data of dry electrodes in $W \cdot m^{-1} \cdot K^{-1}$ measured with the GHP.

Active material	Notes	Thermal conductivity	Reference
Graphite / Carbon	dry, 9.3 bar	0.30	Burheim et al. [39]
	wet, 9.3 bar	0.89	Burheim et al. [39]
LCO	dry, 9.3 bar	0.36	Burheim et al. [39]
	wet, 9.3 bar	1.1	Burheim et al. [39]
Graphite	XALT, dry	0.32	Richter et al. [41]
	XALT, wet	0.89	Richter et al. [41]
NMC	XALT, dry	0.30	Richter et al. [41]
	XALT, wet	0.82	Richter et al. [41]
LFP	MTI, dry	0.13	Richter et al. [41]
	MTI, wet	0.32	Richter et al. [41]
LCO	Hohsen,dry	0.17	Richter et al. [41]
	Hohsen, wet	1.03	Richter et al. [41]
Graphite	Hohsen, dry	0.26	Richter et al. [41]
	Hohsen, wet	1.11	Richter et al. [41]
NMC	dry	0.14	Richter et al. [42]
	wet	0.54	Richter et al. [42]
Hard carbon	dry	0.31	Richter et al. [42]
	wet	0.66	Richter et al. [42]
Graphite	64 Ah, dry	0.902	Spitthoff et al. [44]
	64 Ah, wet	1.93	Spitthoff et al. [44]
NMC	64 Ah, dry	0.448	Spitthoff et al. [44]
	64 Ah, wet	0.717	Spitthoff et al. [44]
Graphite	6.55 Ah, dry	0.50	Spitthoff et al. [44]

Table A.2 – continued from previous page

Active material	Notes	Thermal conductivity	Reference
	6.55 Ah, wet	1.04	Spitthoff et al. [44]
LCO	6.55 Ah, dry	0.397	Spitthoff et al. [44]
	6.55 Ah, wet	1.339	Spitthoff et al. [44]
Graphite	10 Ah, dry	0.379	Spitthoff et al. [44]
NMC	10 Ah, dry	0.292	Spitthoff et al. [44]
Graphite	dry	1.05	Lubner et al. [43]
	wet	1.44	Lubner et al. [43]
NMC	dry	0.55	Lubner et al. [43]
	wet	0.83	Lubner et al. [43]

Table A.3: Thermal conductivity data of dry electrodes in $W \cdot m^{-1} \cdot K^{-1}$ measured with additional methods. All data were obtained from the graphs by Loges et al. [110].

Active material	Notes	Thermal conductivity	Reference
Graphite	Cell A	2.08	Loges et al. [110]
LCO	Cell A	1.47	Loges et al. [110]
Graphite	Cell B	2.68	Loges et al. [110]
LCO	Cell B	0.86	Loges et al. [110]
Graphite	Cell C	3.17	Loges et al. [110]
NMC	Cell C	0.17	Loges et al. [110]

Table A.4: Thermal conductivity data in $W \cdot m^{-1} \cdot K^{-1}$ measured with the GHP for varied pressure by Richter et al. [41, 42].

Active material	Notes	2.3 bar	4.6 bar	6.9 bar	9.2 bar	11.5 bar	Reference
Graphite	XALT, dry	0.32	0.39	0.47	0.54	0.61	Richter et al. [41]
	XALT, wet	0.89	1.03	1.16	1.24	1.37	Richter et al. [41]
NMC	XALT, dry	0.3	0.35	0.37	0.38	0.39	Richter et al. [41]
	XALT, wet	0.82	0.84	0.87	0.89	0.9	Richter et al. [41]
LFP	MTI, dry	0.13	0.14	0.14	0.15	0.15	Richter et al. [41]
	MTI, wet	0.32	0.32	0.34	0.36	0.36	Richter et al. [41]
Graphite	Hohsen, dry	0.26	0.32	0.40	0.46	0.52	Richter et al. [41]
	Hohsen, wet	1.11	1.15	1.35	1.43	1.38	Richter et al. [41]
LCO	Hohsen, dry	0.17	0.19	0.22	0.24	0.26	Richter et al. [41]
	Hohsen, wet	1.03	1.16	1.28	1.48	1.48	Richter et al. [41]
Hard Carbon	dry	0.31	0.35	0.38	0.39	0.40	Richter et al. [42]
	wet	0.66	0.67	0.69	0.70	0.71	Richter et al. [42]
NMC	dry	0.14	0.15	0.15	0.17	0.17	Richter et al. [42]
	wet	0.54	0.54	0.55	0.56	0.56	Richter et al. [42]

Table A.5: Thermal conductivity data in $W \cdot m^{-1} \cdot K^{-1}$ measured with the GHP for varied pressure by Spitthoff et al. [44].

Active material	Notes	2 bar	2.9 bar	3.9 bar	4.9 bar	5.8 bar	6 bar	Reference
Graphite	64 Ah, dry	0.902	0.96	1.02	1.08	1.14	1.17	Spitthoff et al. [44]
	64 Ah, wet	1.93	1.92	1.98	2.01	2.08	2.10	Spitthoff et al. [44]
NMC	64 Ah, dry	0.448	0.455	0.476	0.491	0.504	0.513	Spitthoff et al. [44]
	64 Ah, wet	0.717	0.703	0.713	0.711	0.728	0.728	Spitthoff et al. [44]
Graphite	6.55 Ah, dry	0.50	0.59	0.67	0.74	0.79	0.80	Spitthoff et al. [44]
	6.55 AH, wet	1.04	1.05	1.087	1.168	1.22	1.22	Spitthoff et al. [44]
LCO	6.55 Ah, dry	0.397	0.416	0.426	0.442	0.467	0.464	Spitthoff et al. [44]
	6.55 Ah, wet	1.339	1.39	1.497	1.56	1.61	1.615	Spitthoff et al. [44]
Graphite	10 Ah, dry	0.379	0.424	0.466	0.50	0.527	0.528	Spitthoff et al. [44]
NMC	10 Ah, dry	0.292	0.30	0.31	0.31	0.31	0.31	Spitthoff et al. [44]

Table A.6: List of all electrode sheets measured in the context of this thesis. Identifier of the electrode sheets with the corresponding coating thickness, current collector thickness, porosity and thermal conductivity obtained with the laser flash analysis in helium and nitrogen at 20 °C. Uncertainties according to GUM A with a coverage factor of $k = 2$. Due to a lack of available data for the uncertainty analysis, double standard deviations are given for the dry manufactured samples.

Identifier	s_{co} / µm	s_{cc} / µm	ϕ / -	$\lambda_{co,He}$ / $\mathbf{W \cdot m^{-1} \cdot K^{-1}}$	λ_{co,N_2} / $\mathbf{W \cdot m^{-1} \cdot K^{-1}}$
MVM_Graphite_TSE11_n300_m0.4	79.8 ± 1.1	11.6 ± 0.3	0.605 ± 0.020	1.467 ± 0.070	
MVM_Graphite_TSE11_n300_m0.8	81.0 ± 1.5	11.6 ± 0.3	0.612 ± 0.019	1.394 ± 0.153	
MVM_Graphite_TSE11_n600_m0.4	78.2 ± 1.3	11.6 ± 0.3	0.596 ± 0.018	1.528 ± 0.035	
MVM_Graphite_TSE11_n600_m0.8	77.1 ± 0.8	11.6 ± 0.3	0.609 ± 0.018	1.478 ± 0.050	
MVM_Graphite_TSE11_n900_m0.4	76.2 ± 1.5	11.6 ± 0.3	0.594 ± 0.019	1.525 ± 0.055	
MVM_Graphite_TSE11_n900_m0.8	76.5 ± 0.9	11.6 ± 0.3	0.598 ± 0.018	1.519 ± 0.036	
MVM_Graphite_TSE16_n300_m1.2	75.8 ± 0.9	11.6 ± 0.3	0.618 ± 0.020	1.302 ± 0.179	
MVM_Graphite_TSE16_n300_m2.4	76.2 ± 4.2	11.6 ± 0.3	0.663 ± 0.039	1.537 ± 0.263	
MVM_Graphite_TSE16_n600_m1.2	71.3 ± 0.9	11.6 ± 0.3	0.609 ± 0.018	1.154 ± 0.178	
MVM_Graphite_TSE16_n600_m2.4	74.6 ± 1.3	11.6 ± 0.3	0.618 ± 0.021	1.314 ± 0.116	
MVM_Graphite_TSE16_n900_m1.2	70.0 ± 0.4	11.6 ± 0.3	0.596 ± 0.018	1.194 ± 0.121	
MVM_Graphite_TSE16_n900_m2.4	75.0 ± 1.3	11.6 ± 0.3	0.613 ± 0.019	1.165 ± 0.157	
MVM_Graphite_TSE18_n300_m2	65.0 ± 2.0	11.6 ± 0.3	0.640 ± 0.028	1.578 ± 0.049	
MVM_Graphite_TSE18_n300_m4	73.5 ± 3.6	11.6 ± 0.3	0.631 ± 0.036	1.504 ± 0.048	
MVM_Graphite_TSE18_n600_m2	65.4 ± 1.9	11.6 ± 0.3	0.621 ± 0.025	1.685 ± 0.042	
MVM_Graphite_TSE18_n600_m4	72.6 ± 1.7	11.6 ± 0.3	0.616 ± 0.023	1.550 ± 0.050	
MVM_Graphite_TSE18_n900_m2	63.9 ± 1.7	11.6 ± 0.3	0.627 ± 0.026	1.524 ± 0.122	
MVM_Graphite_TSE18_n900_m4	65.9 ± 1.6	11.6 ± 0.3	0.627 ± 0.024	1.548 ± 0.051	
MVM_Graphite_TSE24_n300_m4	69.6 ± 1.9	11.6 ± 0.3	0.679 ± 0.031	1.634 ± 0.250	

Table A.6 – continued from previous page

Identifier	s_{co} / µm	s_{cc} / µm	ϕ / -	$\lambda_{co,He}$ / W·m^{-1}·K^{-1}	λ_{co,N_2} / W·m^{-1}·K^{-1}
MVM_Graphite_TSE24_n300_m8	85.8 ± 3.3	11.6 ± 0.3	0.638 ± 0.035	1.604 ± 0.087	
MVM_Graphite_TSE24_n600_m4	80.1 ± 1.9	11.6 ± 0.3	0.597 ± 0.022	1.454 ± 0.060	
MVM_Graphite_TSE24_n600_m8	87.0 ± 3.7	11.6 ± 0.3	0.606 ± 0.028	1.482 ± 0.078	
MVM_Graphite_TSE24_n900_m4	81.9 ± 1.1	11.6 ± 0.3	0.583 ± 0.017	1.497 ± 0.105	
MVM_Graphite_TSE24_n900_m8	88.2 ± 3.6	11.6 ± 0.3	0.593 ± 0.030	1.508 ± 0.043	
TFT_Graphite_37µm_DR0.75	36.6 ± 1.4	9.0 ± 1.4	0.491 ± 0.142	0.971 ± 0.223	
TFT_Graphite_67µm_DR0.75	66.2 ± 1.8	9.0 ± 1.4	0.511 ± 0.082	0.898 ± 0.171	
TFT_Graphite_67µm_DR1.5	66.7 ± 1.4	9.0 ± 1.4	0.511 ± 0.079	0.997 ± 0.169	
TFT_Graphite_67µm_DR3	69.2 ± 1.4	9.0 ± 1.4	0.511 ± 0.076	1.0415 ± 0.162	
TFT_Graphite_96µm_DR0.75	95.8 ± 1.5	9.0 ± 1.4	0.519 ± 0.055	1.177 ± 0.151	
TFT_Graphite_95µm_DR0.75	95.3 ± 1.5	9.0 ± 1.4	0.545 ± 0.056	1.548 ± 0.185	
TFT_Graphite_181µm_DR0.75	181.4 ± 1.5	9.0 ± 1.4	0.548 ± 0.029	1.531 ± 0.131	
TFT_Graphite_395µm_DR0.75	394.9 ± 3.6	9.0 ± 1.4	0.543 ± 0.016	1.461 ± 0.103	
TFT_Graphite_680µm_DR0.75	679.8 ± 8.1	9.0 ± 1.4	0.537 ± 0.016	1.238 ± 0.087	
TFT_HC-C_Al_31µm_DR0.75	31.0 ± 0.8	20.2 ± 0.7	0.649 ± 0.026	0.442 ± 0.124	
TFT_HC-C_Al_94µm_DR0.75	94.4 ± 0.8	20.2 ± 0.7	0.578 ± 0.009	0.425 ± 0.031	
TFT_HC-C_Al_94µm_DR1.5	96.1 ± 1.1	20.2 ± 0.7	0.571 ± 0.012	0.384 ± 0.035	
TFT_HC-C_Al_94µm_DR3	92.3 ± 0.8	20.2 ± 0.7	0.569 ± 0.012	0.418 ± 0.024	
TFT_HC-C_Al_131µm_DR0.75	131.2 ± 2.1	20.2 ± 0.7	0.582 ± 0.013	0.376 ± 0.036	
TFT_HC-C_Cu_98µm_DR0.75_p1	97.9 ± 0.4	11.5 ± 0.3	0.639 ± 0.014	0.363 ± 0.007	
TFT_HC-C_Cu_98µm_DR0.75_p2	79.8 ± 0.4	11.5 ± 0.3	0.583 ± 0.018	0.244 ± 0.005	
TFT_HC-C_Cu_98µm_DR0.75_p3	83.3 ± 0.4	11.5 ± 0.3	0.593 ± 0.017	0.239 ± 0.005	

Table A.6 – continued from previous page

Identifier	s_{co} / µm	s_{cc} / µm	ϕ / -	$\lambda_{co,He}$ / W·m^{-1}·K^{-1}	λ_{co,N_2} / W·m^{-1}·K^{-1}
TFT_HC-C_Cu_95µm_DR1.5	95.1 ± 0.5	11.5 ± 0.3	0.644 ± 0.015	0.353 ± 0.010	
TFT_HC-C_Cu_93µm_DR3	92.9 ± 1.1	11.5 ± 0.3	0.632 ± 0.018	0.349 ± 0.011	
TFT_HC-C_Cu_91µm_DR6_p1	90.9 ± 0.4	11.5 ± 0.3	0.638 ± 0.016	0.344 ± 0.010	
TFT_HC-C_Cu_91µm_DR6_p2	78.4 ± 1.0	11.5 ± 0.3	0.603 ± 0.019	0.232 ± 0.005	
TFT_HC-C_Cu_91µm_DR6_p3	78.0 ± 0.8	11.5 ± 0.3	0.600 ± 0.018	0.233 ± 0.004	
TFT_HC-C_Cu_93µm_DR9	93.3 ± 0.6	11.5 ± 0.3	0.635 ± 0.016	0.347 ± 0.007	
TFT_HC-A_Cu_95µm_DR0.75	94.6 ± 1.0	11.5 ± 0.3	0.595 ± 0.020	0.283 ± 0.005	
TFT_HC-A_Cu_91µm_DR1.5	91.1 ± 0.5	11.5 ± 0.3	0.597 ± 0.016	0.292 ± 0.005	
TFT_HC-A_Cu_95µm_DR3	94.7 ± 0.5	11.5 ± 0.3	0.592 ± 0.016	0.283 ± 0.005	
TFT_HC-A_Cu_94µm_DR6	94.2 ± 0.5	11.5 ± 0.3	0.587 ± 0.016	0.292 ± 0.005	
TFT_HC-A_Cu_94µm_DR9	93.5 ± 0.5	11.5 ± 0.3	0.595 ± 0.016	0.300 ± 0.007	
TFT_HC-Blend_Al_96µm_DR075	96.4 ± 2.5	21.9 ± 0.3	0.547 ± 0.017	0.396 ± 0.012	
TFT_HC-Blend_Al_77µm_DR6	76.6 ± 0.5	21.9 ± 0.3	0.549 ± 0.006	0.376 ± 0.018	
TFT_LFP400_67µm_DR0.75	67.5 ± 2.1	19.2 ± 1.9	0.599 ± 0.018	0.408 ± 0.023	
TFT_LFP400_109µm_DR0.75	109.0 ± 2.1	19.2 ± 1.9	0.560 ± 0.014	0.379 ± 0.017	
TFT_LFP400_109µm_DR1.5	109.3 ± 2.0	19.2 ± 1.9	0.559 ± 0.008	0.347 ± 0.021	
TFT_LFP400_109µm_DR3	104.3 ± 2.0	19.2 ± 1.9	0.559 ± 0.013	0.355 ± 0.012	
TFT_LFP400_170µm_DR0.75	170.4 ± 2.0	19.2 ± 1.9	0.542 ± 0.005	0.354 ± 0.014	
TFT_LFP200_198µm_DR0.75_p1	198.2 ± 1.4	22.0 ± 0.5	0.533 ± 0.009	0.320 ± 0.005	
TFT_LFP200_198µm_DR0.75_p2	180.3 ± 1.3	22.0 ± 0.5	0.483 ± 0.012	0.311 ± 0.004	
TFT_LFP200_198µm_DR0.75_p3	162.0 ± 1.0	22.0 ± 0.5	0.419 ± 0.005	0.361 ± 0.002	
TFT_LFP200_198µm_DR0.75_p4	153.2 ± 1.2	22.0 ± 0.5	0.384 ± 0.021	0.407 ± 0.006	

Table A.6 – continued from previous page

Identifier	s_{co} / µm	s_{cc} / µm	ϕ / -	$\lambda_{co,He}$ / W·m^{-1}·K^{-1}	λ_{co,N_2} / W·m^{-1}·K^{-1}
TFT_LFP200_198µm_DR0.75_p5	152.3 ± 1.3	22.0 ± 0.5	0.373 ± 0.011	0.441 ± 0.004	
TFT_LFP200_198µm_DR3_p1	197.6 ± 2.2	22.0 ± 0.5	0.547 ± 0.012	0.328 ± 0.007	
TFT_LFP200_198µm_DR3_p2	177.6 ± 1.2	22.0 ± 0.5	0.489 ± 0.019	0.321 ± 0.006	
TFT_LFP200_198µm_DR3_p3	162.2 ± 0.7	22.0 ± 0.5	0.467 ± 0.006	0.348 ± 0.004	
TFT_LFP200_198µm_DR3_p4	162.2 ± 0.7	22.0 ± 0.5	0.433 ± 0.014	0.376 ± 0.005	
TFT_LFP200_198µm_DR3_p5	154.0 ± 0.9	22.0 ± 0.5	0.411 ± 0.015	0.362 ± 0.003	
TFT_LFP400_222µm_DR0.75_p1	222.0 ± 1.0	22.0 ± 0.5	0.545 ± 0.005	0.357 ± 0.006	
TFT_LFP400_222µm_DR0.75_p2	203.2 ± 0.8	22.0 ± 0.5	0.487 ± 0.008	0.331 ± 0.004	
TFT_LFP400_222µm_DR0.75_p3	177.1 ± 1.2	22.0 ± 0.5	0.407 ± 0.013	0.390 ± 0.003	
TFT_LFP400_222µm_DR0.75_p4	175.5 ± 0.7	22.0 ± 0.5	0.397 ± 0.007	0.403 ± 0.005	
TFT_LFP400_222µm_DR0.75_p5	165.4 ± 1.5	22.0 ± 0.5	0.381 ± 0.007	0.449 ± 0.004	
TFT_LFP400_222µm_DR0.75_p6	165.3 ± 2.4	22.0 ± 0.5	0.373 ± 0.014	0.471 ± 0.007	
TFT_LFP400_205µm_DR3_p1	205.2 ± 4.2	22.0 ± 0.5	0.548 ± 0.017	0.346 ± 0.008	
TFT_LFP400_205µm_DR3_p2	181.4 ± 1.0	22.0 ± 0.5	0.471 ± 0.017	0.381 ± 0.022	
TFT_LFP400_205µm_DR3_p3	167.4 ± 0.7	22.0 ± 0.5	0.417 ± 0.006	0.420 ± 0.010	
TFT_LFP400_205µm_DR3_p4	156.0 ± 1.5	22.0 ± 0.5	0.369 ± 0.016	0.423 ± 0.009	
TFT_LFP400_205µm_DR3_p5	149.1 ± 1.2	22.0 ± 0.5	0.369 ± 0.027	0.408 ± 0.013	
IAM_Graphite_70µm_p1	70.0 ± 1.6	10.3 ± 1.2	0.606 ± 0.063	1.594 ± 0.109	1.340 ± 0.181
IAM_Graphite_70µm_p2	61.6 ± 1.6	10.3 ± 1.2	0.586 ± 0.071	1.260 ± 0.109	1.053 ± 0.0621
IAM_Graphite_70µm_p3	55.8 ± 1.6	10.3 ± 1.2	0.544 ± 0.078	1.182 ± 0.055	1.017 ± 0.053
IAM_Graphite_70µm_p4	48.5 ± 1.6	10.3 ± 1.2	0.471 ± 0.088	1.237 ± 0.079	1.080 ± 0.048
IAM_Graphite_70µm_p5	40.8 ± 1.6	10.3 ± 1.2	0.376 ± 0.102	1.584 ± 0.069	1.422 ± 0.091

Table A.6 – continued from previous page

Identifier	s_{co} / µm	s_{cc} / µm	ϕ / -	$\lambda_{co,He}$ / W·m^{-1}·K^{-1}	λ_{co,N_2} / W·m^{-1}·K^{-1}
IAM_Graphite_70µm_p6	37.0 ± 1.8	10.3 ± 1.2	0.328 ± 0.113	2.071 ± 0.117	1.797 ± 0.146
IAM_Graphite_117µm_p1	117.2 ± 1.7	11.0 ± 1.2	0.597 ± 0.038	1.356 ± 0.160	
IAM_Graphite_117µm_p2	108.2 ± 1.7	11.0 ± 1.2	0.585 ± 0.041	1.439 ± 0.261	
IAM_Graphite_117µm_p3	102.9 ± 1.7	11.0 ± 1.2	0.569 ± 0.043	1.279 ± 0.203	
IAM_Graphite_117µm_p4	89.1 ± 1.7	11.0 ± 1.2	0.514 ± 0.049	1.078 ± 0.078	
IAM_Graphite_117µm_p5	86.3 ± 1.8	11.0 ± 1.2	0.412 ± 0.049	1.279 ± 0.095	
IAM_Graphite_117µm_p6	71.0 ± 1.7	11.0 ± 1.2	0.291 ± 0.058	1.538 ± 0.078	
IAM_Graphite_117µm_p7	59.9 ± 1.7	11.0 ± 1.2	0.211 ± 0.068	2.127 ± 0.173	
IAM_NMC622_55µm_p1	54.9 ± 1.6	16.7 ± 1.2	0.513 ± 0.012	0.714 ± 0.032	0.622 ± 0.013
IAM_NMC622_55µm_p2	50.4 ± 1.6	16.7 ± 1.2	0.469 ± 0.013	0.640 ± 0.019	0.559 ± 0.019
IAM_NMC622_55µm_p3	47.1 ± 1.6	16.7 ± 1.2	0.427 ± 0.015	0.590 ± 0.10	0.520 ± 0.016
IAM_NMC622_55µm_p4	43.2 ± 1.7	16.7 ± 1.2	0.379 ± 0.018	0.579 ± 0.016	0.515 ± 0.018
IAM_NMC622_55µm_p5	41.4 ± 1.7	16.7 ± 1.2	0.349 ± 0.019	0.599 ± 0.015	0.530 ± 0.016
IAM_NMC622_55µm_p6	39.6 ± 1.7	16.7 ± 1.2	0.303 ± 0.021	0.621 ± 0.026	0.606 ± 0.012
CC_NMC811_80µm_p1	79.5 ± 1.6	16.2 ± 1.2	0.507 ± 0.008	0.498 ± 0.007	0.389 ± 0.006
CC_NMC811_80µm_p2	75.5 ± 1.6	16.2 ± 1.2	0.494 ± 0.011	0.467 ± 0.021	0.367 ± 0.019
CC_NMC811_80µm_p3	73.6 ± 1.6	16.2 ± 1.2	0.488 ± 0.008	0.465 ± 0.008	0.361 ± 0.006
CC_NMC811_80µm_p4	73.5 ± 1.6	16.2 ± 1.2	0.483 ± 0.009	0.460 ± 0.007	0.356 ± 0.009
CC_NMC811_80µm_p5	73.0 ± 1.6	16.2 ± 1.2	0.472 ± 0.009	0.449 ± 0.009	0.350 ± 0.006
CC_NMC811_80µm_p6	69.6 ± 1.6	16.2 ± 1.2	0.454 ± 0.010	0.437 ± 0.007	0.341 ± 0.005
CC_NMC811_80µm_p7	65.4 ± 1.6	16.2 ± 1.2	0.372 ± 0.012	0.368 ± 0.008	
CC_NMC811_80µm_p8	58.6 ± 1.7	16.2 ± 1.2	0.319 ± 0.015	0.405 ± 0.013	

Table A.6 – continued from previous page

Identifier	s_{co} / µm	s_{cc} / µm	ϕ / -	$\lambda_{co,He}$ / $W \cdot m^{-1} \cdot K^{-1}$	λ_{co,N_2} / $W \cdot m^{-1} \cdot K^{-1}$
IAM_NMC622_dry_GF	68.7 ± 10.0	-	0.327 ± 0.019	0.509 ± 0.139	
IAM_NMC622_dry_GL	71.5 ± 6.0	17.5	0.340 ± 0.023	0.447 ± 0.066	
IAM_NMC622_dry_GD	44.2 ± 4.7	17.5	0.223 ± 0.038	0.741 ± 0.132	

Table A.7: Thermal conductivity in $W \cdot m^{-1} \cdot K^{-1}$ of the electrodes measured with the guarded hot plate method at different pressures. Uncertainty according to the least square residuals of the linear regression.

Identifier	2 bar	3 bar	4 bar	5 bar	6 bar
IAM_Graphite_70µm_p1	0.522 ± 0.057	0.479 ± 0.025	0.540 ± 0.027	0.613 ± 0.026	0.690 ± 0.027
IAM_Graphite_70µm_p2	0.412 ± 0.020	0.479 ± 0.030	0.590 ± 0.018	0.640 ± 0.033	0.709 ± 0.045
IAM_Graphite_70µm_p3	0.395 ± 0.010	0.832 ± 0.399	0.840 ± 0.256	0.869 ± 0.194	0.909 ± 0.128
IAM_Graphite_70µm_p4	0.398 ± 0.009	0.667 ± 0.051	0.722 ± 0.056	0.763 ± 0.052	0.795 ± 0.062
IAM_Graphite_70µm_p5	0.356 ± 0.015	0.865 ± 0.117	0.909 ± 0.106	0.956 ± 0.084	0.980 ± 0.066
IAM_NMC622_55µm_p1	0.165 ± 0.002	0.172 ± 0.002	0.183 ± 0.001	0.195 ± 0.003	0.215 ± 0.010
IAM_NMC622_55µm_p2	0.175 ± 0.006	0.252 ± 0.050	0.253 ± 0.042	0.253 ± 0.031	0.256 ± 0.025
IAM_NMC622_55µm_p3	0.227 ± 0.055	0.245 ± 0.061	0.258 ± 0.049	0.267 ± 0.032	0.274 ± 0.027
IAM_NMC622_55µm_p4	0.188 ± 0.033	0.219 ± 0.066	0.231 ± 0.060	0.242 ± 0.043	0.265 ± 0.040
IAM_NMC622_55µm_p5	0.200 ± 0.022	0.195 ± 0.038	0.220 ± 0.037	0.243 ± 0.035	0.263 ± 0.032
IAM_NMC622_55µm_p6	0.213 ± 0.002	0.200 ± 0.009	0.221 ± 0.006	0.243 ± 0.006	0.267 ± 0.004

Table A.8: Names and manufacturers of the used materials. The raw materials of the CC_NMC811 electrode are unknown.

	AM	CMC	SBR	PVDF	CB	CG
MVM_Graphite	Mechano-Cap ® 1P1	Na-CMC salt	SBR	–	C-NERGY Super C65	–
	(HC Carbon GmbH)	(Carl Roth)	(Nanografi Nano Technology)	–	(Nanografi Nano Technology)	–
TFT_Graphite	SMG-A	Sunrose MAC500LC	SBR	–	C-NERGY Super C65	–
	(Hitachi Chemical Co.Ltd.)	(Nippon Paper Industries)	(Zeon Europe GmbH)		(Imerys Graphite & Carbon)	
TFT_HC	HC	Sunrose MAC500LC	SBR	–	C-NERGY Super C65	–
	(Kuranode, kuraray)	(Nippon Paper Industries)	(Zeon Europe GmbH)		(Imerys Graphite & Carbon)	
TFT_LFP	LFP200 | LFP400	Sunrose MAC500LC	SBR	–	C-NERGY Super C65	–
	(ibu-Tec)	(Nippon Paper Industries)	(Zeon Europe GmbH)		(Imerys Graphite & Carbon)	
IAM_Graphite	SMG-A	Na-CMC, CRT 2000	TRD 2001	–	C-NERGY Super C65	–
	(Hitachi Chemical Co.Ltd.)	(DOW Wolff)	(JSR Micro)		(Imerys Graphite & Carbon)	
IAM_NMC622	HED NMC622	–	–	Solef 5130	C-NERGY Super C65	C-NERGY KS6L
	(BASF)			(Solvay S.A.)	(Imerys Graphite & Carbon)	(Imerys Graphite & Carbon)

Table A.9: Reciprocal specific feed load within the extruder for the differently mixed electrodes obtained from the simulation by Meza Gonzalez et al. [244]

Identifier	**SFL^{-1} / -**
MVM_Graphite_TSE11_n300_m0.4	89.84
MVM_Graphite_TSE11_n300_m0.8	44.92
MVM_Graphite_TSE11_n600_m0.4	179.7
MVM_Graphite_TSE11_n600_m0.8	89.84
MVM_Graphite_TSE11_n900_m0.4	269.5
MVM_Graphite_TSE11_n900_m0.8	134.8
MVM_Graphite_TSE16_n300_m1.2	92.16
MVM_Graphite_TSE16_n300_m2.4	46.08
MVM_Graphite_TSE16_n600_m1.2	184.3
MVM_Graphite_TSE16_n600_m2.4	92.16
MVM_Graphite_TSE16_n900_m1.2	276.5
MVM_Graphite_TSE16_n900_m2.4	138.2
MVM_Graphite_TSE18_n300_m2	78.73
MVM_Graphite_TSE18_n300_m4	39.37
MVM_Graphite_TSE18_n600_m2	157.5
MVM_Graphite_TSE18_n600_m4	78.73
MVM_Graphite_TSE18_n900_m2	236.2
MVM_Graphite_TSE18_n900_m4	118.1
MVM_Graphite_TSE24_n300_m4	93.31
MVM_Graphite_TSE24_n300_m8	46.65
MVM_Graphite_TSE24_n600_m4	186.6
MVM_Graphite_TSE24_n600_m8	93.31
MVM_Graphite_TSE24_n900_m4	279.9
MVM_Graphite_TSE24_n900_m8	140.0

A.2 Additional Figures

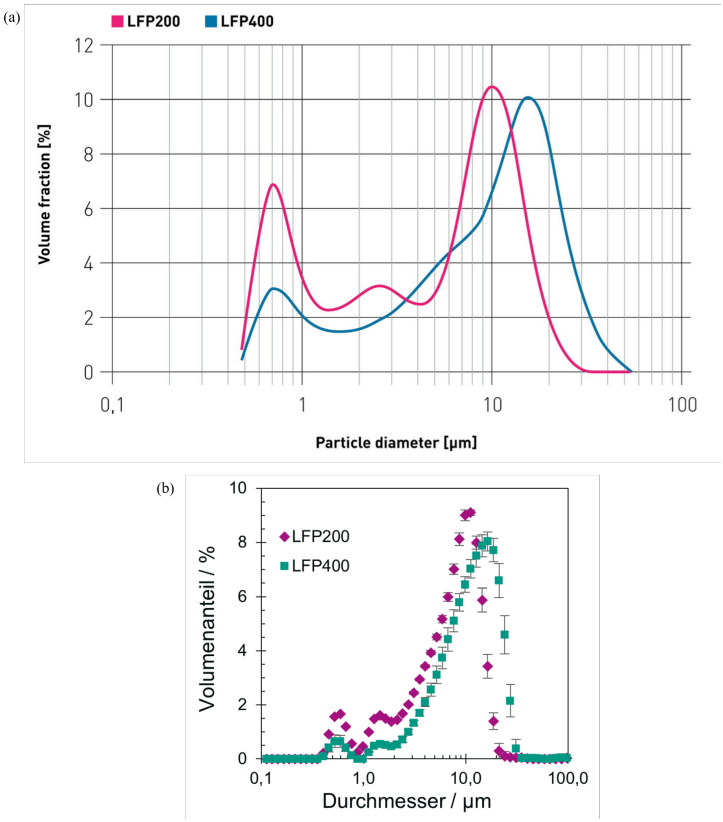

Figure A.1: Particle size distribution of LFP200 and LFP400 (a) according to manufacturer IBU-tec [211] and (b) measured by Janning at KIT [255].

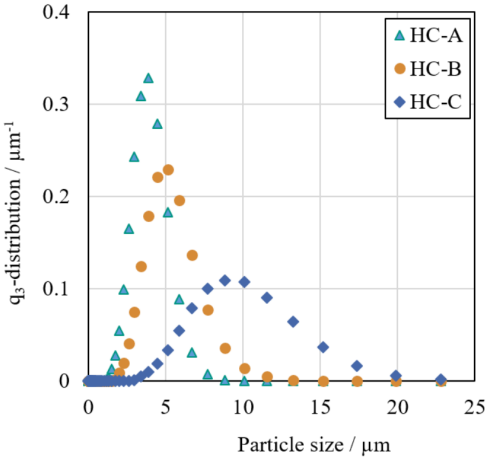

Figure A.2: Particle size distribution of HC-A, HC-B and HC-C. The HC-B material was not investigated in the present work (reproduced from Klemens et al. [256], Creative Commons Attribution 4.0 License CC BY).

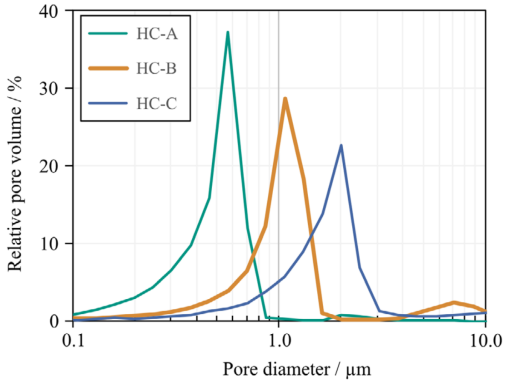

Figure A.3: Pore size distribution of HC-A, HC-B and HC-C. The HC-B material was not investigated in the present work (reproduced from Klemens et al. [73], Creative Commons Attribution 4.0 License CC BY).

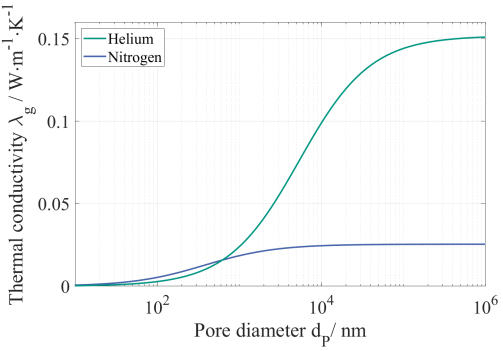

Figure A.4: Thermal conductivity of helium and nitrogen within pores with a varied pore size according of the Knudsen effect following the derivation by Schlünder and Tsotsas [240].

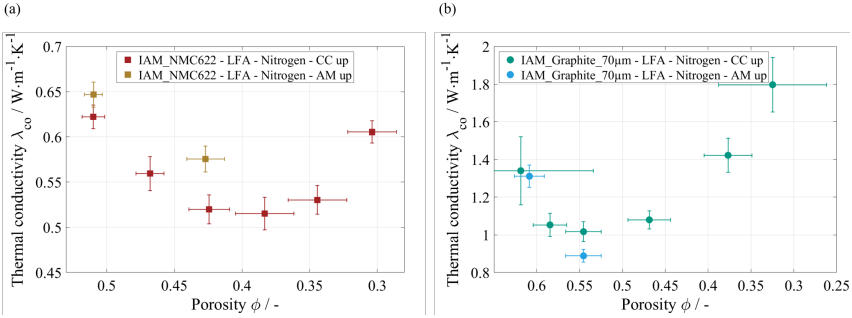

Figure A.5: Effective thermal conductivity of the coatings of (a) the IAM_NMC622 electrodes and (b) the IAM_Graphite_70µm electrodes. "AM up" describes the electrodes with the current collector facing the light pulse. For the investigated electrodes no sound conclusion can be drawn from the results. The differences between the two approaches are minimal for the uncalendered electrodes and do not show a clear trend for lower porosities.

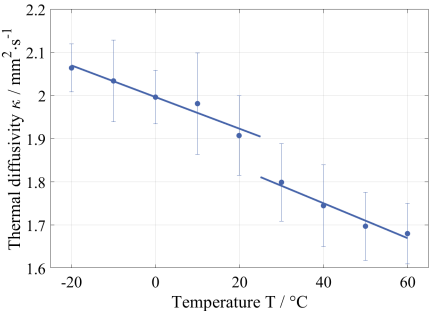

Figure A.6: Thermal diffusivity of the electrode IAM_Graphite_70µm_p1 measured in helium in dependence on the temperature and linear fits for the temperature ranges $T \leq 20\,°C$ and $T \geq 30\,°C$. A jump between 20 °C and 30 °C is visible (reproduced from Gandert et al. [216], Creative Commons Attribution 4.0 License CC BY).

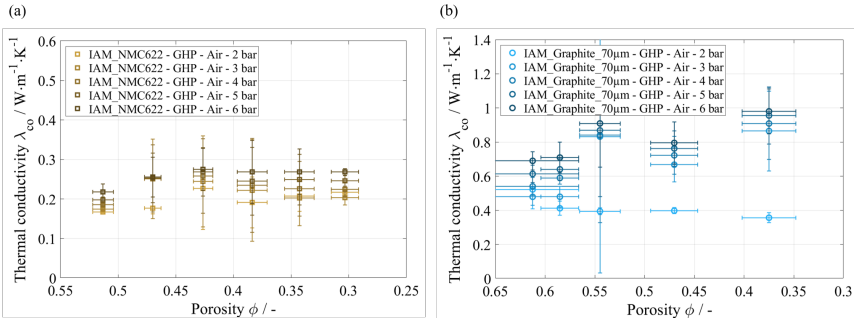

Figure A.7: Thermal conductivity of the electrode coating of (a) the IAM_NMC622 electrodes and (b) the IAM_Graphite_70µm electrodes obtained with the GHP method at different pressures (adjusted from Gandert et al. [216], Creative Commons Attribution 4.0 License CC BY).

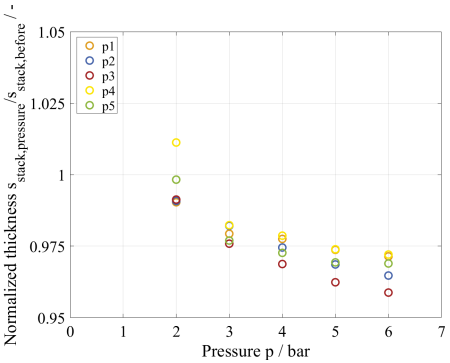

Figure A.8: Thickness of the graphite samples measured during the compression referred to the thickness measured outside of the rig before the thermal conductivity measurement.

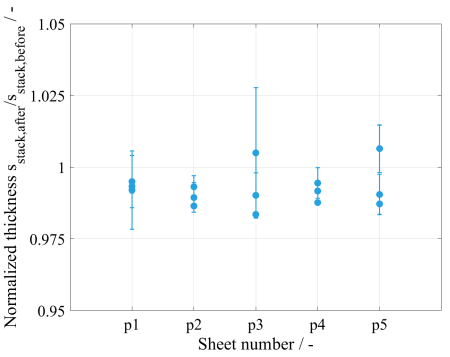

Figure A.9: Comparison of the measured sample thickness of the graphite electrodes before and after the GHP measurements for different sheets with increasing degree of calendering.

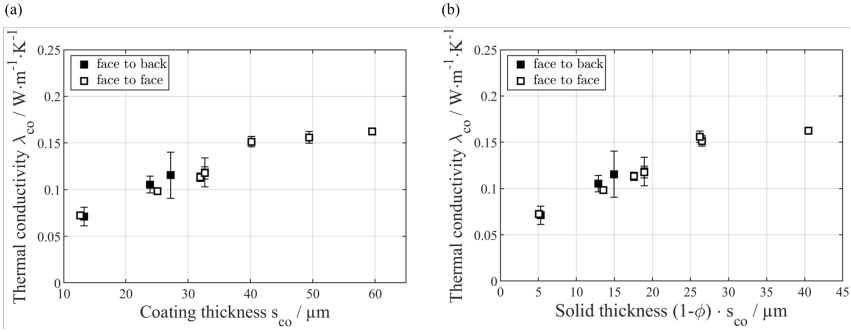

Figure A.10: Effective thermal conductivity of the face to face and face to back stacks for NMC111 electrodes with varying coating thicknesses, shown with double standard deviations. The data is either referred to (a) the thickness of a single coating layer or (b) to the effective thickness of only the solid material. The measurements were conducted at 5 bar.

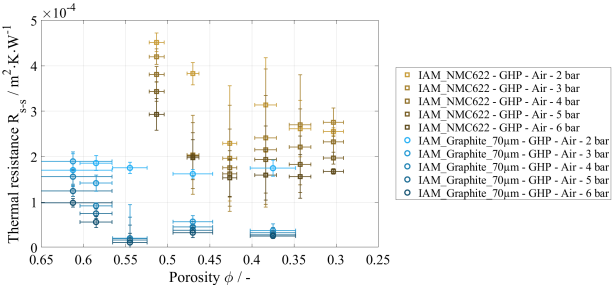

Figure A.11: Internal thermal contact resistances between the electrode coatings of the IAM_NMC622 electrodes and the IAM_Graphite_70µm electrodes within the GHP measurement rig at all measured pressures between 2 bar and 6 bar. The values were calculated with the assumption that the thermal conductivity obtained with the LFA is correct.

List of Figures

2.1 Examples for (a) an incremental and (b) a cumulative pore size distribution for graphite electrodes at different compression rates (adjusted from Froboese et al. [50], Copyright 2017, Elsevier, reproduced under the license number 6135241071637). 10
2.2 Schematic depiction of (a) the pull-off test and (b) possible failure mechanisms: (1) adhesion failure, (2) cohesion failure and (3) failure of the adhesive (adjusted from Haselrieder et al. [66], Copyright 2015, Elsevier, reproduced under the license number 6135250046122). 16
2.3 Connection between the force P during loading and unloading and the indentation depth h. The areas under the curves represent the total (W_t), plastic (W_p) and elastic (W_e) indentation work (reproduced from Bartali et al. [76], Copyright 2010, Elsevier, reproduced under the license number 6135250724496). . . 17
2.4 Capacity retention of a full cell: (a) percentage of the usable discharge capacity at different C-rates referred to the capacity at C/10 and (b) percentual capacity retention of different cells after cyclization with 1C (adjusted from Bockholt et al. [80], Copyright 2016, Elsevier, reproduced under the license number 6135251325427). 20
2.5 Schematic depiction of the measurement device used for the guarded hot plate method (reproduced from Gandert et al. [93], Creative Commons Attribution 4.0 License CC BY). 23

2.6 Schematic depiction of the laser flash method (a, reproduced from Gandert et al. [93], Creative Commons Attribution 4.0 License CC BY) and exemplary voltage profile which is directly proportional to the temperature change on the backside of the sample (b). 25
2.7 Schematic depiction of a one-sided coated electrode consisting of the active material coating and the current collector. 27
2.8 Schematic depiction of the DSC setup and operating principle (inspired by NETZSCH-Gerätebau GmbH [105]). 28
2.9 Schematic depiction of the setup and operating principle of the gas pycnometry (inspired by Lowell et al. [108]. 30
2.10 Literature data for the thermal conductivity of the dry electrode coating of battery electrodes measured with LFA, GHP and photothermal deflection spectroscopy [26, 30–34, 39, 41–44, 110, 112, 113] (reproduced from Gandert et al. [93], Creative Commons Attribution 4.0 License CC BY). 32
2.11 Literature data for the thermal conductivity of the dry and soaked electrode coating of battery electrodes measured with the GHP [39, 41–44]. 33
2.12 Evaluation of literature data for the thermal conductivity of electrode coatings at different pressures measured with the guarded hot plate method. (a) Absolute values and (b) data normalized to the thermal conductivity at 2 bar or 2.3 bar of the dry electrodes. (c) Absolute values and (d) data normalized to the thermal conductivity at 2 bar or 2.3 bar of the soaked electrodes. . . 35
2.13 Thermal conductivity factor of the electrodes measured with the GHP method in the literature describing the ratio of the thermal conductivity of the electrodes soaked with electrolyte solvent to the thermal conductivity of the dry electrodes $\lambda_{co,soaked}/\lambda_{co,dry}$. . . . 36
2.14 Schematic depiction of the sequence of the processes used for electrode production. Left: wet processing route. Right: dry manufacturing. 37

2.15 Adhesion strength of HC anodes with different AM particle sizes (HC-A < HC-B < HC-C) dried with different drying rates and constant heat transfer coefficients of (a) 35 $W \cdot m^{-2} \cdot K^{-1}$ and (b) 80 $W \cdot m^{-2} \cdot K^{-1}$ (reproduced from Klemens et al. [73], Creative Commons Attribution 4.0 License CC BY). 43
2.16 SEM images of a ruptured surface (top) and an ion-etched cross-section (bottom) of NMC cathodes produced with conventional dissolver mixing (left) and additional dry preprocessing (right) of the NMC and CB (reproduced from Bauer et al. [61], Copyright 2015, Elsevier, reproduced under the license number 6135260942067). 46
2.17 Adhesion strength of HC, PBA, LFP and graphite electrodes (reproduced from Klemens et al. [73], Creative Commons Attribution 4.0 License CC BY). 51
2.18 Schematic depiction of the binder migration during electrode drying (reproduced from Westphal and Kwade [64], Copyright 2018, Elsevier, reproduced under the license number 6135261301190).53
2.19 Results of the EDX analysis of a graphite anode showing the distribution of fluorine from the PVDF binder within the coating and the derived concentration within the different layers (adjusted from Westphal and Kwade [64], Copyright 2018, Elsevier, reproduced under the license number 6135261301190). . . . 54
2.20 Adhesion strength of graphite anodes with PVDF binder processed with different mass loadings and drying temperatures (adjusted from Westphal and Kwade [64], Copyright 2018, Elsevier, reproduced under the license number 6135261301190). . . . 56
2.21 Adhesion strength of HC, PBA, LFP and graphite electrodes referred to the value at the lowest drying rate (reproduced from Klemens et al. [74], Creative Commons Attribution 4.0 License CC BY). 57
2.22 Relative electrical resistance of graphite anodes with PVDF binder processed with different mass loadings and drying temperatures (adjusted from Westphal and Kwade [64], Copyright 2018, Elsevier, reproduced under the license number 6135261301190).59

2.23 SEM images of NMC electrodes with increasing degree of calendering from left to right. A penetration of the AM particles into the current collector foil can be observed for the most strongly calendered electrode (reproduced from Mayer et al. [60], License: Creative Commons Attribution 4.0 License CC BY). 64
2.24 Simulated effective thermal conductivity of the electrode coating for different porosities obtained by calendering and different mean particle sizes of the AM (reproduced from Sangrós et al. [49], License: Creative Commons Attribution 4.0 License CC BY-NC). 67
2.25 Schematic depiction of the free-standing electrode production with subsequent lamination onto the current collector foil and the dry manufacturing by direct calendering of the electrodes (inspired by Degen and Krätzig [25]). 69
3.1 Foil sample holder used for all the LFA measurements featured in this work (reproduced from Gandert et al. [216], Creative Commons Attribution 4.0 License CC BY). 78
3.2 Relative deviation of the stack thickness measured with the dial indicator by Mitutoyo Corporation in comparison to the micrometer screw by Mahr GmbH (adjusted from Gandert et al. [36], Creative Commons Attribution 4.0 License CC BY). 82
3.3 Impact of a variation in the thickness of the electrode stack on (a) the effective thermal diffusivity κ, (b) the porosity ϕ and (c) the effective thermal conductivity λ of the electrode stack for the uncalendered electrodes IAM_Graphite_70µm_p1, IAM_Graphite_117µm_p1, IAM_NMC622_p1 and CC_NMC811_p1 (adjusted from Gandert et al. [36, 220], Creative Commons Attribution 4.0 License CC BY). 84
4.1 Schematic depiction of the model introduced by Oehler et al. [32, 34, 113] (reproduced from Oehler et al. [32], Creative Commons Attribution 4.0 License CC BY). 92

4.2 Graphic depiction of the considered model geometries. For a better visibility, the thickness ratio of the different components does not reflect the reality. Exemplarily, the different geometries are shown for the cases with graphite paint on the backside of the metal foil (adjusted from Gandert et al. [93], Creative Commons Attribution 4.0 License CC BY). 97
5.1 Impact of the mean particle size of the active material on (a) the effective thermal conductivity and (b) the porosity of the LFP and HC electrode coatings. 101
5.2 Impact of the specific feed load on (a) the porosity and (b) the thermal conductivity of the coating for different extruders by Thermo Fisher Scientific (TSE11, TSE16 and TSE24) and varied settings for the rotation speed and mass flow. 105
5.3 Impact of the specific feed load on (a) the porosity and (b) the thermal conductivity of the coating for the TSE11 and TSE18 extruder with different screw geometries. 106
5.4 Impact of the coating thickness on the effective thermal conductivity of the electrode coating for graphite, HC and LFP processed with a drying rate of 0.75 $g \cdot m^{-2} \cdot s^{-1}$. 106
5.5 (a) Impact of the drying rate on the effective thermal conductivity of the electrode coating with a dry film thickness of approx. 67 µm for graphite, 94 µm for HC and 109 µm for LFP. (b) Combined impact of drying rate and mean particle size on the thermal conductivity of the HC electrodes and (c) the LFP electrodes. 108
5.6 Thermal conductivity of the coating of varyingly strong calendered NMC electrodes. Besides the experimental data, quadratic fit functions and the corresponding equations are given. 110
5.7 SEM images of the ion-milled cross-sections of (a) the IAM_NMC622 cathodes and (b) the IAM_Graphite_117µm anodes: Uncalendered sample (top), sheet at the minimum of the thermal conductivity (center), and most strongly calendered sample (bottom) (adjusted from Gandert et al. [36], Creative Commons Attribution 4.0 License CC BY). 111

5.8 Thermal conductivity of the coating of varyingly strong calendered graphite electrodes with different starting thicknesses. Besides the experimental data, quadratic fit functions and the corresponding equations are given. 114
5.9 Effective thermal diffusivity and volumetric heat capacity of (a) the IAM_NMC622 cathode stacks, (b) the CC_NMC811 cathode stacks, (c) the IAM_Graphite_70µm anode stacks, and (d) the IAM_Graphite_117µm anode stacks in dependence on the porosity at a set temperature of 20 °C (adjusted from Gandert et al. [36], Creative Commons Attribution 4.0 License CC BY). . . . 115
5.10 Thermal conductivity of the coating of HC electrodes calendered with different forces. The porosity could not be varied in a wide range here, as a further increase of the force did not lead to a further compression of the coating. 116
5.11 Thermal conductivity of the coating of LFP electrodes with different AM particle sizes x_{50} of 5.8 µm (LFP200) and 11.1 µm (LFP400), dried at a rate of 0.75 $g \cdot m^{-2} \cdot s^{-1}$ and calendered to different porosities. Besides the experimental data, quadratic fit functions and the corresponding equations are given. 117
5.12 Thermal conductivity of the coating of LFP electrodes with different AM particle sizes x_{50} of 11.1 µm (LFP400) and 5.8 µm (LFP200), dried at a rate of 3 $g \cdot m^{-2} \cdot s^{-1}$ and calendered to different porosities. 118
5.13 Experimental data and results of the analytical model by Oehler et al. [32, 34, 113] for the effective thermal conductivity of the coatings of (a) the NMC electrodes, (b) the graphite electrodes and (c) the LFP electrodes dried at 0.75 $g \cdot m^{-2} \cdot s^{-1}$ as a function of the porosity ((a) and (b) adjusted from Gandert et al. [36, 220], Creative Commons Attribution 4.0 License CC BY). 119
5.14 SEM image of the BCB phase in the IAM_NMC622_p6 cathode (reproduced from Gandert et al. [220], Creative Commons Attribution 4.0 License CC BY). 120

5.15 Comparison of the effective thermal conductivity of the electrode coating of (a) the differently strong calendered IAM_NMC622 cathodes and (b) the IAM_Graphite_70µm anodes obtained with the laser flash analysis (LFA) in helium and nitrogen atmosphere and the guarded hot plate method (GHP) in air at 2 bar and 6 bar. The LFA data were evaluated with the penetration model for porous samples in the NETZSCH software. The most strongly calendered graphite sheet could not be measured with the GHP method due to material scarcity. The data is plotted versus a decreasing porosity, which is equivalent to an increasing degree of calendering (adjusted from Gandert et al. [93], Creative Commons Attribution 4.0 License CC BY). 123
5.16 Comparison of the sample thickness of (a) the IAM_NMC622 cathode stacks and (b) the IAM_Graphite_70µm anode stacks measured with a micrometer for the LFA at KIT and with a micrometer within the GHP rig at NTNU for different layer numbers and porosities (adjusted from Gandert et al. [216], Creative Commons Attribution 4.0 License CC BY). 124
5.17 Effective thermal conductivity of the coating of (a) the IAM_NMC622 cathodes and (b) the IAM_Graphite_70µm anodes measured in nitrogen resulting from the evaluation with different models in the NETZSCH software. The value obtained with the penetration model for the IAM_Graphite_p2 electrode at a porosity of $\phi = 0.58$ is hidden behind the data point calculated with the standard model (adjusted from Gandert et al. [93], Creative Commons Attribution 4.0 License CC BY). 127
5.18 Effective thermal conductivity of the coating of (a) the IAM_NMC622 cathodes and (b) the IAM_Graphite_70µm anodes measured in helium resulting from the evaluation with different models in the NETZSCH software. 128

5.19 SEM images of the ion-milled cross sections of (a) the NMC622 electrodes at a porosity of 0.51, 0.38 and 0.30 and (b) the graphite electrodes at a porosity of 0.61, 0.48 and 0.33 and pore depth distributions of (c) the NMC622 electrodes and (d) the graphite electrodes (reproduced from Gandert et al. [93], Creative Commons Attribution 4.0 License CC BY). 129
5.20 (a) Effective thermal conductivity of uncalendered graphite anode coatings with varied thickness measured with the LFA in helium and evaluated with the penetration model. (b) Expected slope of the effective thermal conductivity with varied thickness considering the effect of the light penetration and the effect of binder migration (reproduced from Gandert et al. [216], Creative Commons Attribution 4.0 License CC BY). 130
5.21 Comparison of the effective thermal conductivity of the coating layer of graphite anodes measured with and without current collector and calculated according to a series connection of the two layers. 132
5.22 Effective thermal conductivity of the face to face and face to back stacks for NMC111 electrodes with varying coating thicknesses, shown with double standard deviations. The data is either referred to (a) the thickness of a single coating layer or (b) to the effective thickness of only the solid material. The measurements were conducted at 2.5 bar (adjusted from Gandert et al. [216], Creative Commons Attribution 4.0 License CC BY). . . . 137
5.23 Internal thermal contact resistances between the electrode coatings within the GHP measurement rig. The values were calculated with the assumption that the thermal conductivity obtained with the LFA is correct (adjusted from Gandert et al. [216], Creative Commons Attribution 4.0 License CC BY). 141
5.24 Specific electrical conductivity of (a) the differently strong calendered IAM_NMC622 electrodes and (b) the IAM_Graphite_70µm electrodes with respect to the porosity. 146

5.25 Comparison of the thermal conductivity of the IAM_Graphite_70µm electrode coatings obtained by LFA measurements in helium and calculated from the data of the specific electrical conductivity according to the Wiedemann Franz Law. 147
5.26 Effective thermal conductivity of the dry-manufactured NMC622 electrodes in comparison to the wet-processed electrodes with the same composition at different degrees of calendering measured in helium. 149
5.27 Thermal conductivity of the coating of the differently calendered electrodes of all the investigated AMs. For LFP only the electrodes produced with a drying rate of 0.75 $g \cdot m^{-2} \cdot s^{-1}$. 152
A.1 Particle size distribution of LFP200 and LFP400 (a) according to manufacturer IBU-tec [211] and (b) measured by Janning at KIT [255]. 219
A.2 Particle size distribution of HC-A, HC-B and HC-C. The HC-B material was not investigated in the present work (reproduced from Klemens et al. [256], Creative Commons Attribution 4.0 License CC BY). 220
A.3 Pore size distribution of HC-A, HC-B and HC-C. The HC-B material was not investigated in the present work (reproduced from Klemens et al. [73], Creative Commons Attribution 4.0 License CC BY). 220
A.4 Thermal conductivity of helium and nitrogen within pores with a varied pore size according of the Knudsen effect following the derivation by Schlünder and Tsotsas [240]. 221
A.5 Effective thermal conductivity of the coatings of (a) the IAM_NMC622 electrodes and (b) the IAM_Graphite_70µm electrodes. "AM up" describes the electrodes with the current collector facing the light pulse. For the investigated electrodes no sound conclusion can be drawn from the results. The differences between the two approaches are minimal for the uncalendered electrodes and do not show a clear trend for lower porosities. 221

A.6 Thermal diffusivity of the electrode IAM_Graphite_70µm_p1 measured in helium in dependence on the temperature and linear fits for the temperature ranges $T \leq 20\,°C$ and $T \geq 30\,°C$. A jump between 20 °C and 30 °C is visible (reproduced from Gandert et al. [216], Creative Commons Attribution 4.0 License CC BY). 222
A.7 Thermal conductivity of the electrode coating of (a) the IAM_NMC622 electrodes and (b) the IAM_Graphite_70µm electrodes obtained with the GHP method at different pressures (adjusted from Gandert et al. [216], Creative Commons Attribution 4.0 License CC BY). 222
A.8 Thickness of the graphite samples measured during the compression referred to the thickness measured outside of the rig before the thermal conductivity measurement. 223
A.9 Comparison of the measured sample thickness of the graphite electrodes before and after the GHP measurements for different sheets with increasing degree of calendering. 223
A.10 Effective thermal conductivity of the face to face and face to back stacks for NMC111 electrodes with varying coating thicknesses, shown with double standard deviations. The data is either referred to (a) the thickness of a single coating layer or (b) to the effective thickness of only the solid material. The measurements were conducted at 5 bar. 224
A.11 Internal thermal contact resistances between the electrode coatings of the IAM_NMC622 electrodes and the IAM_Graphite_70µm electrodes within the GHP measurement rig at all measured pressures between 2 bar and 6 bar. The values were calculated with the assumption that the thermal conductivity obtained with the LFA is correct. 224

List of Tables

3.1 Exact recipe for the different electrode formulations in wt.%. 73
3.2 Conducted variations for the different basic electrode formulations. . . 73
4.1 Values of the thermal conductivity λ and the density ρ of the materials contained in the investigated electrodes that were used in the model. 93
5.1 Solid density and specific heat capacity of the different formulations of the electrode coatings at 20 °C to 25 °C used for the evaluation of the effective thermal conductivity. For the AMs with different particles size, the specific heat capacity was measured separately. The uncertainties of the measured values are given with a coverage factor of $k = 2$. 100
5.2 Obtained thermal conductivity of the coating in $W{\cdot}m^{-1}{\cdot}K^{-1}$ for the most strongly calendered graphite anode sheet IAM_Graphite_70µm_p6 with different model geometries and boundary conditions. Either no graphite spray at all or a 3 µm thin layer was considered. 133
5.3 In-plane and through-plane thermal conductivity on cell level in $W{\cdot}m^{-1}{\cdot}K^{-1}$ for the combination of both p1 electrodes and both p5 electrodes, respectively. Furthermore, it was varied between the values obtained by LFA in helium (He), LFA in nitrogen (N_2), GHP at 6 bar in air and estimated values for the soaked electrodes by multiplying the GHP values by factor 3. 144
A.1 Thermal conductivity data of dry electrodes in $W{\cdot}m^{-1}{\cdot}K^{-1}$ measured with the LFA. 205
A.2 Thermal conductivity data of dry electrodes in $W{\cdot}m^{-1}{\cdot}K^{-1}$ measured with the GHP. 206

A.3 Thermal conductivity data of dry electrodes in $W \cdot m^{-1} \cdot K^{-1}$ measured with additional methods. All data were obtained from the graphs by Loges et al. [110]. 207
A.4 Thermal conductivity data in $W \cdot m^{-1} \cdot K^{-1}$ measured with the GHP for varied pressure by Richter et al. [41, 42]. 208
A.5 Thermal conductivity data in $W \cdot m^{-1} \cdot K^{-1}$ measured with the GHP for varied pressure by Spitthoff et al. [44]. 209
A.6 List of all electrode sheets measured in the context of this thesis. Identifier of the electrode sheets with the corresponding coating thickness, current collector thickness, porosity and thermal conductivity obtained with the laser flash analysis in helium and nitrogen at 20 °C. Uncertainties according to GUM A with a coverage factor of $k = 2$. Due to a lack of available data for the uncertainty analysis, double standard deviations are given for the dry manufactured samples. 210
A.7 Thermal conductivity in $W \cdot m^{-1} \cdot K^{-1}$ of the electrodes measured with the guarded hot plate method at different pressures. Uncertainty according to the least square residuals of the linear regression. . 216
A.8 Names and manufacturers of the used materials. The raw materials of the CC_NMC811 electrode are unknown. 217
A.9 Reciprocal specific feed load within the extruder for the differently mixed electrodes obtained from the simulation by Meza Gonzalez et al. [244] 218